Drag Amplification and Fatigue Damage in Vortex-Induced Vibrations

by

Vikas Gopal Jhingran

Submitted to the Department of Mechanical Engineering
in partial fulfillment of the requirements for the degree of

Doctor of Philosophy in Ocean Engineering

at the

MASSACHUSETTS INSTITUTE OF TECHNOLOGY
[June 2008]
April 2008

Author .....
Department of Mechanical Engineering
April 24, 2008

Certified by .....
J. Kim Vandiver
Professor of Mechanical and Ocean Engineering, MIT
Thesis Supervisor

Accepted by .....
Lallit Anand
Chairman, Department Committee on Graduate Students

Drag Amplification and Fatigue Damage in Vortex-Induced Vibrations

by

Vikas Gopal Jhingran

ABSTRACT

Fatigue damage and drag force amplification due to Vortex-Induced-Vibrations (VIV) continue to cause significant problems in the design of structures which operate in ocean current environments. These problems are magnified by the uncertainty in VIV prediction, particularly with regard to fatigue damage. Although the last fifteen years has seen significant advancement in VIV prediction, important fatigue and drag related questions remain unanswered.

This research addresses two important problems. The first is the difficulty in measuring local drag coefficients on long flexible cylinders, excited by VIV. At best engineers are forced to use spatially averaged drag coefficients. This is especially inaccurate when the pipe and flow properties change, either due to partial coverage with VIV mitigation devices, such as strakes or fairings, or shear in the incident current profile. The second problem is the lack of design procedures that account for the effect on fatigue damage due to the higher harmonics in the VIV strain response.

To address these problems, two experiments were performed to collect data, the first in October of 2004 and the second in October of 2006. Both of these experiments were designed specifically to collect strain measurements from a densely instrumented pipe undergoing VIV at high mode numbers when subjected to current profiles with varying amounts of shear.

Data from these experiments was used to develop a method to extract local drag forces from the measured mean strain. This method, when applied to a partially faired pipe undergoing VIV, successfully and accurately distinguished the dissimilar local drag coefficient between the bare pipe region and the region with fairings. In bare pipes, for the first time the method allowed for the measurement of the variation of local drag coefficient along the length of a flexible pipe undergoing VIV in sheared current.

Further by using filtering techniques, the higher harmonics were isolated and analyzed, particularly for their magnitude and phase response characteristics. Interesting features about the phase relationships between the first, second and third harmonics were observed when the primary VIV response was in the form of a traveling wave. Finally, data revealed some inaccuracies in the fatigue estimation techniques currently being used by the oil and gas industry. Two methods are suggested to incorporate the higher harmonics in VIV related fatigue design while correcting the observed inaccuracies in the current methods.

The results revealed limitations in the commonly used, vibration-amplitude based methods of calculating local drag coefficients and may lead to modifications to correct these limitations. These findings also provide tools for researchers to include the higher harmonics in VIV related fatigue damage calculations and remove some of the uncertainty involved in VIV fatigue estimation and could lead to smaller safety factors in VIV fatigue design.

ACKNOWLEDGMENTS

Though I am the face of this thesis, I could not have accomplished this work without the help of a number of people. First, I thank Dr. J. Kim Vandiver for the opportunity to learn from him and others at MIT. I also thank my committee members, Dr. Michael Triantafyllou and Dr. Ronald Ballinger for their guidance and support during this process.

I thank all its members of the SHEAR7 JIP, which supported my research at MIT, and DEEPSTAR for sponsoring the Gulf Stream experiments.

A special mention to the students (current and former) involved with VIV research at MIT. Thank you for providing a great learning environment that ultimately benefited all of us. In particular, Mr. Vivek Jaiswal for his help and stimulating conversations, Dr. Harish Mukundan and Dr. Jason Dahl for sharing their research ideas and insights, Dr. Susan Swithenbank and Dr. Hayden Marcollo for helping out with Gulf Stream data and experiments.

Many thanks to Sheila McNary for her help and guidance and Barbara Keesler for her help in arranging my committee meetings.

During the last three and a half years, my wife Anjali has been patient and very supportive. This work would not have been possible without her strength, perseverance and understanding.

Finally, I had the opportunity to meet and work with some very knowledgeable people during my research, among which Dr. Owen Oakley and Dr. Steve Leverette deserve special mention for their help.

To my Parents, Mr. Manoj Gopal Jhingran and Mrs. Ranjana Jhingran:

Your sacrifice and foresight has made this day possible.

This page is dedicated to my Sister, Dr. Ekta Jhingran

CONTENTS

LIST OF TABLES

LIST OF FIGURES

1. Introduction and Motivation

1.1 Introduction

Most unexplored oil and gas reserves of significance are offshore, miles away from any coastline. Having exhausted much of the onshore and near-shore reserves, the oil and gas industry is moving into deeper waters to find large reserves to meet the growing energy demands. Figure 1 shows the timeline of the oil and gas industries progression into deeper waters. They are also drilling in harsher environments for oil and gas. In their quest, one of the many challenges they face is that of Flow-Induced Vibrations (VIV).

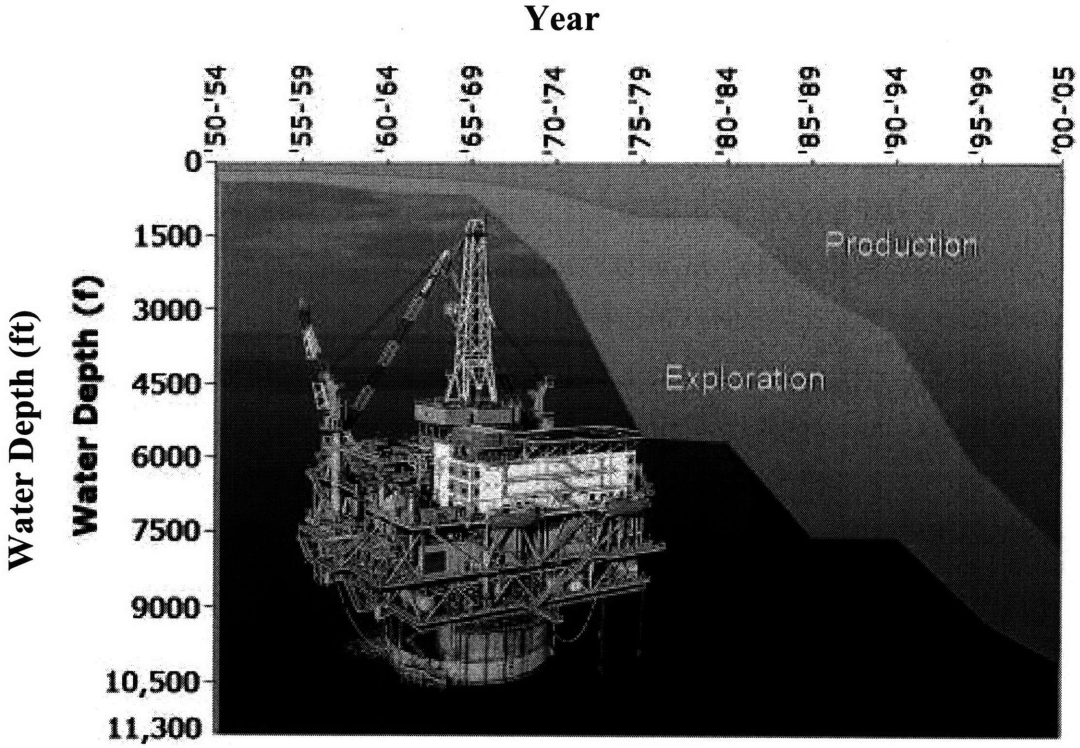

Figure 1 - The progression of the oil and gas drilling and production operations into deeper water

For many years, amplification in drag and fatigue damage due to vortex-induced-vibrations (VIV) has caused significant problems for offshore platforms and risers operating in strong ocean current environments. The problem has been aggravated in recent years as water depths increase and the risers are excited at higher modes. In just

the last few years there have been several high profile rig failures because of reasons that can, at least partially, be attributed to Flow-Induced vibration [1].

Expectedly, extensive VIV research has been carried out over the last fifteen years. This has led to significant understanding of the physics behind VIV and the occurrence and behavior of these vibrations in constant and sheared current profiles. This understanding has resulted in the development of VIV prediction programs like SHEAR7[1] that estimate the effects of VIV on slender structures.

Despite these advances, VIV is still not clearly understood and many important questions regarding it, especially in sheared current profiles, remain unanswered. As a result, the oil and gas industry uses design safety factor of ten or higher for VIV related fatigue damage in spite of predictive programs generally giving conservative estimates of displacement response due to VIV.

1.2 Background

It has long been observed that flow of a viscous fluid past a bluff body creates vortices in its wake, which are shed alternately from both sides in a pattern called the Karman Vortex Street. This phenomenon is quiet ubiquitous, see Figure 2, and can be seen when air flows past thin strings, like the Aeolian harp, or in the clouds when their flow is interrupted by a mountain or island. These alternating vortices create a periodic forcing on the bluff body which becomes important only when their shedding frequency is close to one of the natural frequencies of the bluff body. Then the bluff body shows resonant behavior and vibrates with large amplitudes. The resulting vibrations are known as Vortex Induced Vibrations or Flow-Induced Vibrations.

[1] SHEAR7 is a VIV prediction program owned and maintained by Dr. J. Kim Vandiver at MIT. For details visit http://web.mit.edu/SHEAR7/SHEAR7.html

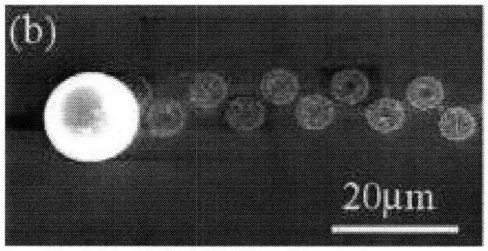

$Re \sim 10^{-2}$ - An image from a Scanning Electron Microscope (SEM) showing the formation of the Von Karman Vortex street behind a Tin particle in flow of Argon gas. The application in this case is growing Silicon nanowires [2]

$Re \sim 10^{2}$ – The Saint Louis wind harp is 13 feet high in Blind Boone park located 60 miles east of Kansas City, MO.

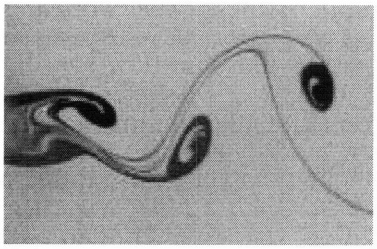

$Re \sim 10^{4}$ – A typical vortex shedding pattern seen behind a cylinder placed in fluid flow. Experiments at these Reynolds numbers are common with VIV researchers.

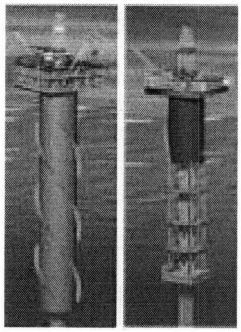

$Re \sim 10^{7}$ - Spar platforms, used in the oil and gas industry due to their low heave response to ocean waves, are prone to Vortex-Induced Motion (VIM).

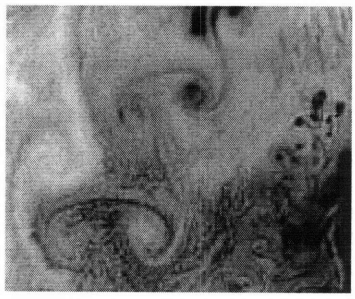

$Re \sim 10^{11}$ – Von Karman Vortex streets seen behind small islands in the Alutian Islands in the northern Pacific ocean. The image, acquired by Landsat 7's Enhanced Thematic Mapper plus (ETM+) sensor, shows the wake behind the islands when fast moving clouds encounter them.

Figure 2 - VIV is a ubiquitous phenomenon that is seen over a wide range of Reynolds numbers and wide ranging physical situations.

1.2.1 Brief History of VIV

Centuries ago, Leanardo Da Vinci painted the Karman vortex street he observed behind some pilings in a stream. Later, Strouhal, in 1878 measured the acoustical notes from vertical wires revolving about a parallel axis and expressed the frequency as $f = (0.185 \times U)/D$, where U is the speed of air flow onto the wire and D is the diameter of the wires. This suggested that the non-dimensional number $(f \times D)/U$ is a constant and is called the Strouhal number. This formula has been subsequently modified by Lord Rayleigh in 1915 (see [3]) and again by Roshko in 1954 ([4]) to account for slight variations in the Strouhal number with viscosity but it remains remarkably constant for a wide range of Reynolds number and shapes of bluff bodies. The vortex shedding frequency, f_S, is expressed as $f_S = (St \times U)/D$, where U is the fluid flow speed, D is the diameter of the bluff body and St denotes the Strouhal number with a value of around 0.2. During "lock-in", the response frequency of the body is very close to the predicted vortex shedding frequency.

Von Karman's theoretical work in early 20th century, which explained the stable alternating vortex shedding pattern behind bluff bodies, laid the theoretical groundwork for VIV research. However, it was not until the 1960s and 1970s that extensive work was undertaken to explain VIV and incorporate its effects into engineering design. Results from field experimental in the 1980s, by Vandiver et al. [5] and others, provided greater understanding about the drag and lift aspects of VIV, and paved the way for empirical programs for the prediction of VIV.

The 1990s and the first half of this decade has been filled with carefully done research in laboratory environments, which have shed light on the subtleties of VIV. For example, in 2003, Jauvtis and Williamson [6] showed that VIV amplitude response of a rigid cylinder was larger when both in-line and cross-flow motion were allowed as opposed to just cross-flow motion. Similarly, Triantafyllou et al. [7] in 2004 examined the amplitude response in the in-line and cross-flow direction for rigid and flexible cylinders in constant currents and found that in flexible cylinders, unlike rigid cylinders, the peak

displacement response in the in-line direction did not occur at the same reduced velocity and the peak displacement response in the cross-flow direction.

The study of long flexible cylinders, the kinds used in the oil and gas industry, has just begun. Only recently have Vandiver et al. [8-10]performed a series of experiments that approximate the large length-to-diameter ratios seen in real oil and gas structures, albeit at lower Reynolds numbers. These experiments have were key in identifying important areas of research like the higher harmonics, their affect on strain and traveling waves response of long flexible cylinders responding at high modes to highly sheared current profiles. Just when the VIV research community was beginning to believe that they understood the complex nuances of VIV, these experiments provided a stark reminder that much work still needs to be done.

1.2.2 Complicating Issues

A sense of the complicated nature of VIV can be obtained from the general equation of motion for any point on a pipe undergoing VIV, shown in Equation(1.1). In most cases, Equation(1.1) is simplified by decoupling the x and y motion. Even then, the dependence of added mass and damping on displacement, axial position, and frequency makes it difficult to solve the equations without making simplifications. The dependence of the forcing on the displacement adds further complications to the problem requiring an iterative process to solve the equation [11]. Further difficulties are posed by the three dimensionality of the problem. The forcing due to a three dimensional wake can be significantly different from the two dimensional wake which is assumed to simplify the problem.

$$
\begin{aligned}
&(m(z)+m_a(x,y,z,\omega))y_{tt}+c(x,y,z,\omega)y_t+(EI(z)y_{zzzz}-T(z)y_{zz})=F(x,y,z,t)\\
&\textit{where}\\
&m(z)=\textit{local mass density}\\
&m_a(x,y,z,\omega)=\textit{local added mass}\\
&c(x,y,z,\omega)=\textit{local damping}\\
&EI(z)=\textit{local bending stiffness}\\
&T(z)=\textit{local Tension}\\
&F(x,y,z,t)=\textit{local forcing in phase with velocity}
\end{aligned}
\qquad (1.1)
$$

Secondly, the structures in the oil and gas industry to which the VIV problem most applies further complicate the problem. Deepwater risers can have length-to-diameter (*L/D*) ratios greater than 5000, Spar and deepwater semi-submersible platforms operate in the Reynolds number regime of 10^7 or greater. These massive sizes, and the non-dimensional parameters associated with it, make it difficult to build and test models that effectively represent the actual structure.

Thirdly, the hydrodynamics of the vortices are difficult to theoretically predict and visualize. The vortex shedding patterns change with various non dimensional parameters like reduced velocity and Reynolds number. Figure 3 shows the various vortex shedding patterns from laboratory experiments done by Williamson and Roshko [12] in which the in-line motion was restricted. Each of these patterns produces a different hydrodynamic force, lift and drag, on the structure. Moreover, the vortex shedding patterns are different if in-line motion is not restricted for the structure.

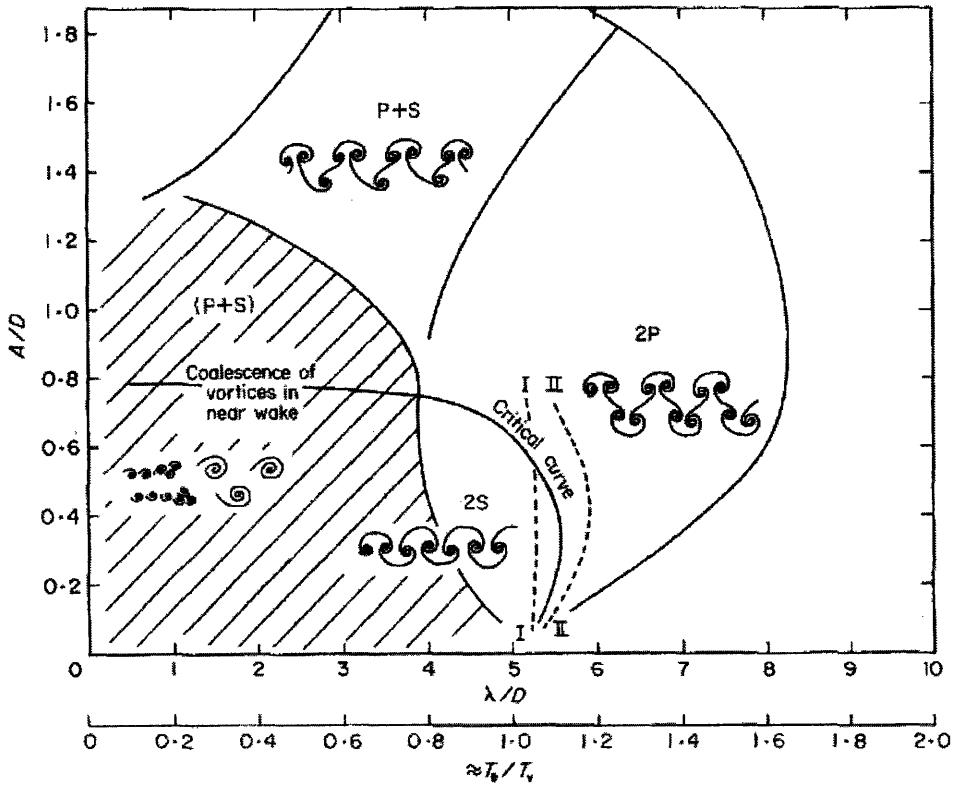

Figure 3 - Map of vortex synchronization patterns near the fundamental lock-in region; from Williamson and Roshko [10].

Visualizing the vortex pattern in the wake of a cylinder is a difficult, expensive and time consuming task. Some of the experimental techniques are Digital Particle Image Velocimetry (DPIV), pressure-sensitive color dyes and time resolved PIV. Recent progress in Computational Fluid Dynamics (CFD) has also made it possible to visualize the formation and propagation of these vortices as shown in Figure 3. They too, however, come with a staggering cost in terms of computation time, modeling and coding effort, and computing power. Furthermore, in spite of the phenomenal increase in computation speeds in recent years, CFD methods still have difficulty solving the Navier-Stokes equation at Reynolds numbers encountered in the offshore oil and gas industry. This motivates research in finding other ways that provide information about the wake without the time and cost penalty associated with the techniques mentioned above.

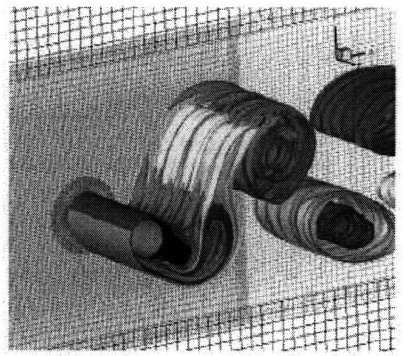

Figure 4 – Recent advances in CFD programs has led to accurate predictions of the vortex dynamics in the near wake of a cylinder undergoing VIV

Finally, the current profiles that are seen by the real structures pose additional problems. Most laboratory experiments, motivated by simplicity in the experimental setup and analysis, introduce a constant velocity fluid flow on a spring mounted rigid cylinder. The reduced velocity is varied by changing the current velocity. In realistic current flows, shear in the current can cause the local reduced velocity to vary along the riser. Further, VIV data from laboratory experiments is dominated by rigid cylinder motion or standing waves in flexible pipes. However, in deepwater risers in sheared currents, the response is mostly traveling waves. This discrepancy in the experimental data and the reality has not been studied in detail.

1.2.3 Things that matter most to the oil and gas industry

While it is important to recognize the complexity of the VIV problem, it is imperative to remember the physical quantities that are most useful in design of offshore structures. It may be that the quantities of interest can be approximately predicted without incorporating all the details of the physics of the VIV problem. The quantities that are of most interest to the offshore oil and gas industry are displacement response of a structure due to VIV, drag force amplification due to VIV and the fatigue damage caused to VIV.

1.2.3.1 Displacement response of a structure due to VIV

The offshore industry uses a lot of cylindrical structures in their operations that are prone to VIV. Moreover, many of these structures are close to other structures and their displacements due to VIV or VIM have to be predicted accurately, making the VIV displacement response prediction a key area of research.

Recent work indicates that VIV predictive programs do a good job in predicting the cross-flow displacement response due to VIV [10]. The prediction process is hampered by the difficulties discussed earlier, but programs like SHEAR7 are able to estimate the region and magnitude of the maximum response fairly accurately.

A critical step in the VIV prediction process is estimating correctly the "power-in" region, where the structure takes energy from the fluid. Though laboratory experiments have developed guidelines where "power-in" regions should occur, more research is underway to identify the position and length of these regions on structures placed in realistic ocean currents. Further, identifying and defining these regions becomes harder when traveling waves are present. The current thought is that a standing wave forms in the "power-in" region and energy is dissipated as traveling waves from the ends of the "power-in" region. This theory is being questioned based on data from the Gulf Stream experiments. Figure 5 uses test data from the second Gulf Stream experiments and shows regions of traveling wave and standing wave VIV response. More research is required to identify the "power-in" regions in the traveling wave environments.

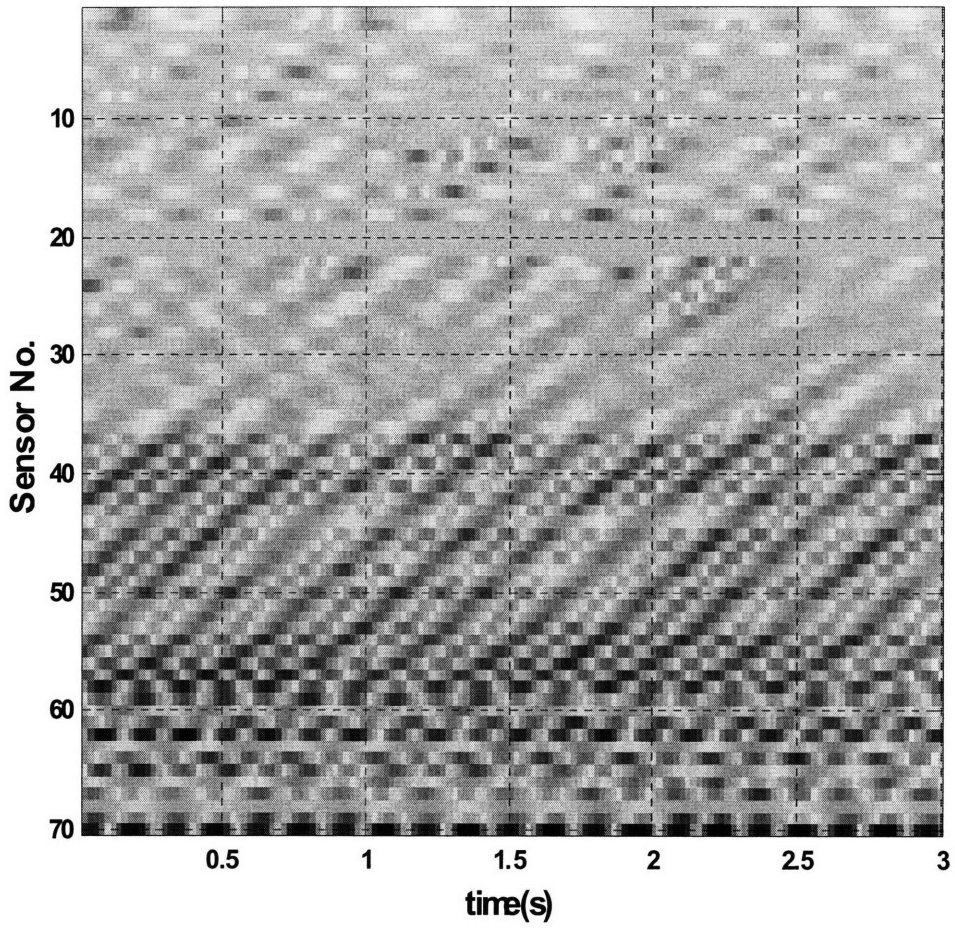

Figure 5 – A plot of amplitude of VIV with time for each sensor clearly reveals the existence of traveling waves. Following peaks, shown in red, and troughs, shown in blue, in time indicate regions of standing and traveling waves. The example was from the Test – 20061023203818 from the second Gulf Stream experiments.

1.2.3.2 Drag forces amplification due to VIV

Accurate force estimates are required for any structural design and the marine risers and offshore structures are no different. Drag forces are estimated by semi-empirical formulations used in VIV prediction programs like SHEAR7. These formulations were developed many decades ago based on field and laboratory experiments. However, many aspects of VIV, especially traveling wave response, were not fully understood then. The formulations therefore were developed based on data that did not represent the response of an offshore structure. These drag force formulations were obtained by using force

measurements at the ends of the flexible cylinder and thus producing spatially averaged forces. However, estimating drag forces when the local reduced velocity changes and the response is mostly in the form of traveling waves has not been researched primarily because it has not been possible to measure the local drag coefficients in long pipes where the local reduced velocity changes due to shear in the current.

1.2.3.3 Fatigue damage due to VIV

The offshore oil and gas industry uses the SN curve method of fatigue damage estimation fatigue damage, which is arguably the most important consequence of VIV. The thinking for a long time has been that if the displacement response due to VIV is predicted correctly, then the stress response computed from this displacement response can be calculated easily making the assumption that the response is at the fundamental frequency of VIV, which corresponds to the Strouhal frequency. However, recent experiments [8, 10] have indicated that stress spectra obtained from VIV strain measurements contain energy at frequencies that are multiples of the Strouhal frequency. Moreover, the strain at these higher frequencies is caused due to the high curvature associated with these high modes and not due to high displacement amplitude of vibration. This means that these higher harmonics could contribute greatly to the fatigue damage due to VIV without significantly affecting the displacement response due to VIV. This provides the motivation to understand these higher harmonics so that they can be predicted and their effects incorporated into fatigue damage estimates used in the industry.

Even before the effects of the higher harmonics are incorporated, the current estimation fatigue damage calculation process has to be reevaluated. Various assumptions, like VIV strain being a Gaussian process, have never been carefully verified. However, these assumptions are used as justification for the use of the Rayleigh formulation [13] in the fatigue estimation process.

1.3 Motivation for this Work

The above descriptions of the problems we face in solving VIV problems coupled with the quantities the oil and gas industry is most interested in provides some very

interesting areas for research that will have the maximum impact on VIV related engineering design procedures in use today. The first of these is the need to be able to predict the "power-in" regions in traveling wave environments. The scarcity of well instrumented data sets showing traveling waves makes it difficult to move forward on this front. However, innovative methods that can indirectly point out the "power-in" regions can be very helpful moving forward. This is particularly true because the currently accepted theory of the "power-in" having standing waves does not seem to work when most of the vibrations are in the form of traveling waves.

The second area that clearly needs more insight is the variation of drag coefficients in traveling wave environments. A plethora of drag-related data is available on rigid cylinder experiments where the variation of drag coefficients has been established with reduced velocity. However, little is known about the variation of reduced velocity in sheared current environments where the reduced velocity changes with the spatial location on a pipe. Further, the drag coefficient formulations in use today were developed using data from rigid cylinder laboratory experiments or field experiments that had standing wave VIV response. They, however, are used in sheared current environments for existing projects where the response is dominated by traveling waves. No research has been carried out verifying their accuracy in such environments. Further, no established methods exist to compute drag coefficients using data from highly instrumented pipes undergoing VIV.

Such a method offers promise to address the concerns of finding the "power-in" region as well. Laboratory research has shown relations between high drag coefficients and wake patterns. A similar correlation may exist between wake patterns and displacement amplitudes, phase difference between in-line and cross-flow motion and lift coefficients. Using time-averaged mean drag, or local drag coefficients, as a method to identify the wake patterns in sheared flows with traveling wave VIV response has never been proposed.

Finally, fatigue damage remains one of the most important yet least understood aspects of VIV. Recent research indicates the existence of higher harmonics in strain data measurements from VIV field experiments. When do these higher harmonics occur? What is the fatigue implication of these higher harmonics? Are the current fatigue

formulations used in the oil and gas industry adequate or will there be a need to modify them based on these new findings? The answers to these questions could have a significant impact current design procedures in use today.

1.4 A preview of the chapters that follow

This thesis is organized in seven chapters. So far, a brief history of VIV, the important VIV related parameters that most impact the oil and gas industry and the motivation for this work, which follows from the earlier discussions, have been presented. The contents of the chapters that follow are summarized below.

Chapter 2 contains the summary of previous research that is related to this work. Due to the plethora of research done on VIV, this literature survey has been limited to the topics that pertain to the work presented in this thesis, which are higher harmonics, drag amplification due to VIV and the fatigue implications of VIV.

Chapter 3 explains the details of the experiments that provided most of the data analyzed for this research. The details of these experiments have been previously published in various reports, which is why this chapter gives a broad overview and presents details of only the aspects of the experiments that had significant contributions from the author.

Chapter 4 deals with drag amplification due to VIV. It presents a new way of calculating local mean drag coefficients, and then suggests how this could be used to infer information like the "power-in" region in pipes and the local wake structure behind the pipe.

Chapter 5 explains the observation of and research on the higher harmonics of VIV. The chapter represents the findings of the author about when the higher harmonics exist, their magnitude and properties that are used in Chapter 6 to build a preliminary model for the higher harmonics.

Chapter 6 goes into the details of fatigue damage due to VIV. This chapter examines the fatigue damage due to the higher harmonics and presents two methods of incorporating them in VIV predictions..

Chapter 7 is a summary of the main results presented in this thesis. It also contains some suggestions for future work.

2. Literature Survey

Research on VIV dates back four decades and volumes of research exist on the subject. A good understanding of the subject can be developed by reading the various books that have been written on the subject [11, 14, 15], or studying the many reviews that have been published in various journals [16-18]. Therefore, the purpose of this chapter is not give the reader a review of all the significant research done in the field of VIV but only to limit the review to the topics most relevant to this thesis. Even in that, the approach is to give the reader an understanding of the history and significant work that led to the current state-of-the-art and which forms the foundation that this work builds upon. For example, the field of fatigue damage estimation has two distinct schools of thought; the people who favor the S-N curve and Miner's rule approach and those that swear by the crack propagation and fracture mechanics methods. As the oil and gas industry, and the work in this thesis, primarily uses the S-N curve approach, the fatigue aspect of the literature survey only summarizes the main contributions that led to the current state-of-the-art in the S-N curve approach.

2.1 Drag

Early research on the amplification of drag forces due to VIV was done by Bishop and Hassan [19]. In forced cylinder experiments, which allowed only cross-flow motion of the 1 inch diameter test cylinder, they measured the mean drag forces while varying the frequency of oscillation so that the ratio of the forcing frequency to the Strouhal frequency changed from below 1.0 to more than 1.0. The mean drag force peaked at a certain frequency and then decreased. They however, did not report their findings in terms of, now commonly used, dimensionless parameters like drag coefficients or reduced velocity. Moreover, the 9 inch wide and 11.25 inch deep water channel used for the experiments made it necessary for corrections due to end and blockage effects.

Griffin and Ramberg[20], among others, studied the drag amplification of a cylinder oscillating in the cross-flow direction. They used a theoretical formulation of drag force based on work by Milne Thompson[21] and Kochin et. al.[22] which required vortex strength and spacing as inputs. They computed these inputs for experiments at Re=144 and

Re=400 and reported drag amplifications compared to stationary cylinders of around 2. Using their own and other data available at the time, they gave the empirical formula shown in Equation(2.1) for the drag amplification due to VIV. Griffin and Ramberg also correlated the length of the vortex formation region with the drag coefficients, showing that changes in the wake structure were closely mirrored by changes in the mean drag coefficients. Similar, amplifications were reported in forced vibration tests by Sarpkaya [23] and Schragel [24].

$$C_D/C_{D0} = 0.124 + 0.933\, w_r$$

where w_r = *wake response parameter*

$$w_r = (1 + 2\frac{\overline{Y}}{D})(St.V_r)^{-1} \qquad (2.1)$$

St= Strouhal No. (~0.2)

$V_r = \frac{V}{f \times D}$; V = Flow Velocity ; f =response frequency; D=Pipe Diameter

In the early 1980s, the first drag amplification values became available from spring-mounted cylinders undergoing free vibrations in uniform fluid flow. Overvik [25] plotted the drag coefficient of a freely oscillating cylinder against reduced velocity, where the motion was allowed only in the cross-flow direction. The plot, shown below in Figure 3, also had a peak amplification of 2.2, similar to forced vibration tests reported earlier.

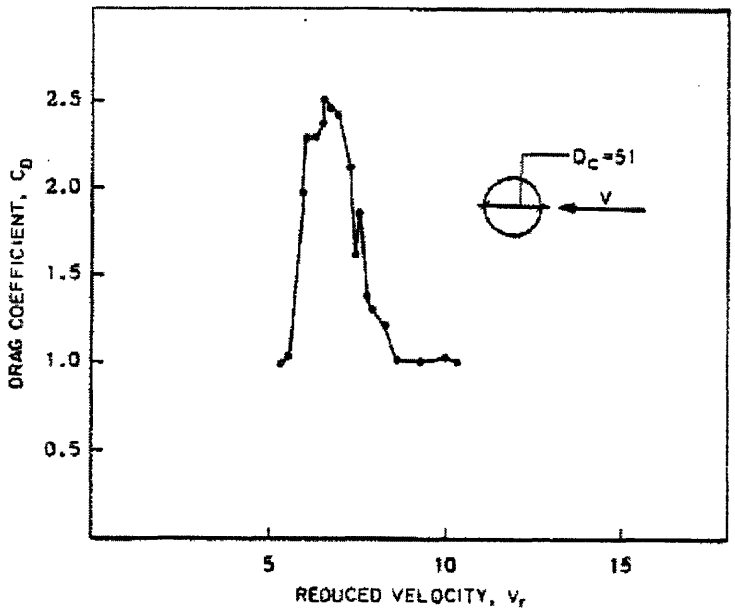

Figure 3 - Free vibration experiments with a 1 degree-of-freedom rigid cylinder by Overvik (1982) (taken from Sarapkaya, 2004)

Field experiments performed in the early 1980s with flexible pipes gave further credibility to the drag amplification values. In the early 1980's, Vandiver et al. conducted the first field experiments to confirm these reported drag amplifications, only observed in laboratory settings till then, for long flexible pipes in realistic current environments. Their experiments were done on a steel pipe, 75 feet in length with typical VIV excitations around modes 3 to 5. These experiments conducted by Vandiver et al. were characterized by standing waves being generated in the pipe due to the "lock-in" region covering almost the entire length of the pipe. This enabled the authors to get meaningful results from spatially averaged values of drag coefficients. Using their measurements, Vandiver et. al were able to correlate the amplitude to diameter ratio (*A/D*) with the amplification of drag (Equation (2.2)). It states that the predicted local $C_D(z)$ is the product of the stationary cylinder drag coefficient, C_{Do} , for the cylinder at the operating Reynolds number and an amplification factor which is dependent on the local RMS vibration amplitude, $Y_{rms}(z)$. The character "z" is the axial position coordinate along the length of the cylinder. As mentioned earlier, in the original formulation [26] the $Y_{rms}(z)$ term was taken to be the maximum anti-node response

amplitude. This has proven to be too conservative, and therefore the current use of the formula [27] is to take $Y_{rms}(z)$ as the local response amplitude.

$$C_D(z) = C_{Do} * C_{D,amp}(z)$$
$$C_{D,amp}(z) = 1.0 + 1.043 * (2\frac{y_{rms}(z)}{D})^{0.65} \quad (2.2)$$

In the early 1990s, Gopalkrishnan [28] did a series of experiments forced experiments with a 2.54 cm diameter pipe. The experiments, which had Reynolds numbers of 10,000, forced the cylinder in sinusoidal cross-flow motion. The amplitude and frequency of the motion were varied to develop a matrix of experiments. In each case, mean drag coefficients were calculated and presented in the contour plot shown in Figure 1. Though the results were similar to past work, this was the first time such a rich drag coefficient dataset was generated. It showed regions, at high reduced velocities and amplitude-to-diameter ratios in which the drag coefficient could be larger than 3.0.

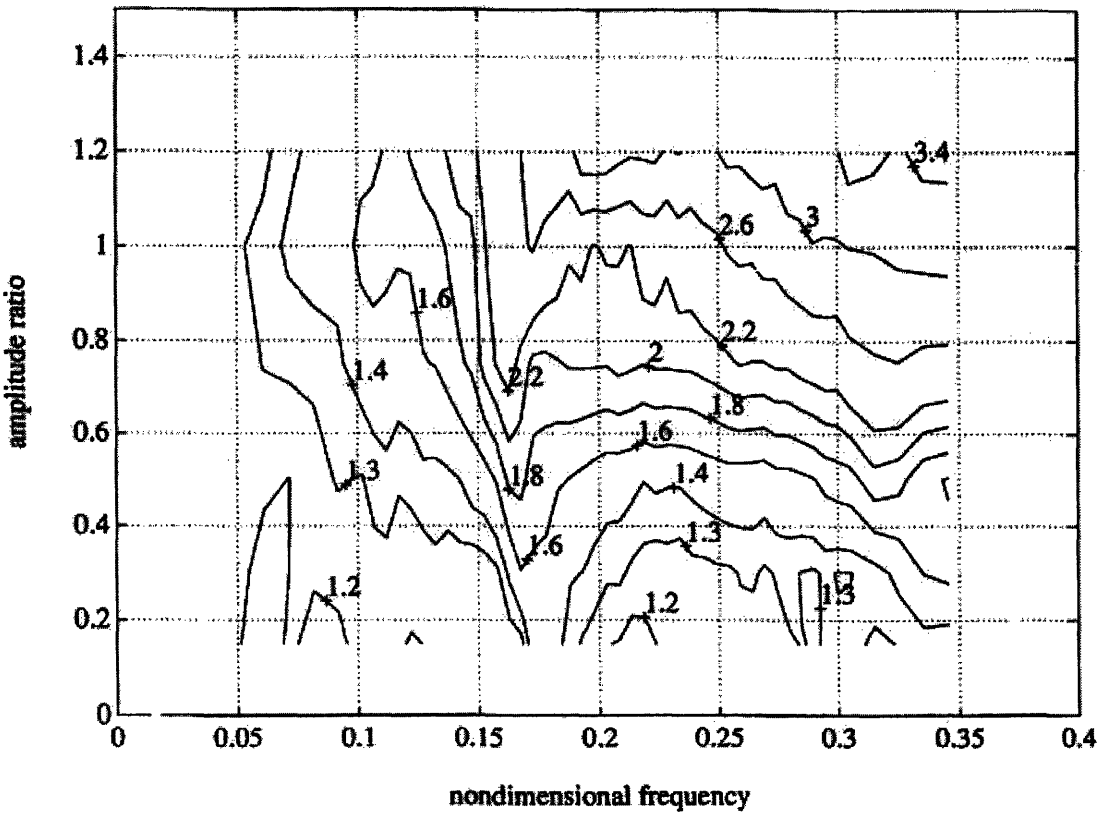

Figure 4 - Drag Coefficient contours for force experiments at Re=10,000. (From [28])

Though Gopalkrishnan's work was the most comprehensive drag coefficient dataset available at the time, it acknowledged the need for mean drag coefficient data from experiments that allowed both in-line and cross-flow motion in the future. This research was further explored by Charles Williamson in free vibration experiments, first with cross-flow motion only ([29, 30]) and then with both cross-flow and in-line motion [6]. Though he found dramatic differences in other VIV related parameters, his mean drag coefficient values, both from cross-flow motion only and in-line and cross-flow motion experiments were similar to the values observed in the forced oscillation experiments performed by Gopalkrishnan. Figure 5 shows the plots from the Williamson paper.

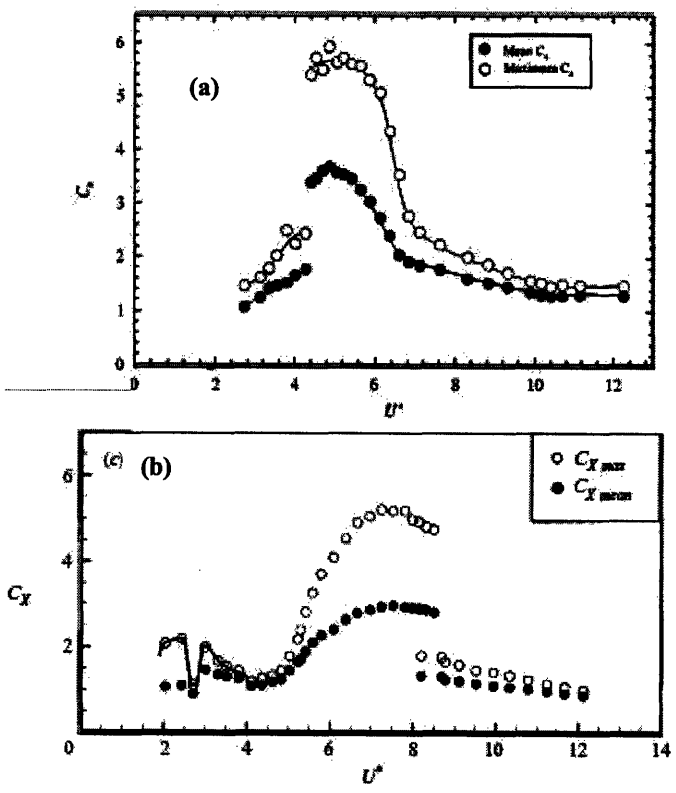

Figure 5 - (a) Mean drag coefficients from 1-D free vibration, rigid cylinder experiments (from [29]) and (b) Mean drag coefficients from 2-D free vibration, rigid cylinder experiments (from [6]).

2.2 Fatigue Damage

Due to the implications of fatigue damage in a wide variety of subjects, it has been studied extensively over the last 150 years. Therefore, the purpose here is not to present

all the work that has been done on fatigue but to highlight some of the key developments [31, 32]that have led to how VIV fatigue damage is calculated in the offshore oil and gas industry today.

According to Walter Schultz in "The History of Fatigue" [32], the first published work on fatigue was by Wilhelm August, a German mining engineer, who in 1937 carried repeated tests on chains and winches. Schultz also mentions that the Englishman Braithwaite was the first to use the word "fatigue" in a publication in 1854 where he discussed many fatigue related failures like water pumps, railway axles and propeller shafts.

Other early work includes the study of axle failures in German railway cars by Wöhler [32, 33], who was the first to suggest that different safety factors were needed for fatigue related design and strength related design. At that time, railway accidents due to failed railway axles were commonplace. Wöhler, measured the stress these axles saw during service and put forward some key observations about fatigue life like the importance of stress amplitude and mean load. He was also the first to put forward the concept of fatigue life based design, as opposed to design for infinite fatigue life, and developed tables of stress amplitude vs number of cycles to failure. These tables were the beginnings of the S-N curves that are used extensively in fatigue design. These concepts are central to the methodology used for fatigue related designs used by the oil and gas industry today.

G. Kirsh, in 1898, calculated the stress concentration around a circular hole in a large plate in tension. His finding, that stress around the hole could be as high as 3 times the value at other regions of the plate, led others like Russian mathematician Gury Vasilyevich Kolosov (1907) and British engineer Charles Edward Inglis (1914) to calculate the stress concentrations for elliptical holes. This helped engineers realize the importance of sharp corners and notches in engineering design.

In 1924, the Swedish researcher A. Palmgren introduced the concept of fatigue damage accumulation. In 1945, M.A. Miner wrote a paper "Accumulative damage in Fatigue" [34] where he also presented essentially the same hypothesis for fatigue life summation. He also performed the first fatigue experiments to check his hypothesis. The Miner-Palmgren rule of fatigue accumulation, which states that the fatigue damage at

different frequencies can be linearly added, is extensively used today in fatigue related design. The rule is shown in mathematical form in Equation(2.3).

$$\sum_{i=1}^{k} d_i = \sum_{i=1}^{k} \frac{n_i}{N_i} = 1$$

where

n_i = number of cycles at ith stress range

N_i = number of cycles for failure at ith stress range (2.3)

Matsuishi and Endo [35] proposed the rain-flow counting method to get ranges for a random signal, making it easy to apply the Palmgren-Miner rule for fatigue calculations of structures responding to random loading. Their method was based on pairing tensile and compressive peaks to give stress range distributions. Downing and Socie [36], among others, have written popular algorithms to implement rain-flow counting techniques in fatigue life estimation. Even though several different counting methods are available now and they differ slightly in their algorithm, the rain-flow method still remains the most popular and is regarded as the most accurate way to estimate stress ranges for fatigue life calculations.

In the mid-twentieth century, the need for spectral fatigue techniques became relevant as the fatigue calculation procedures became more complex and performing them in the time domain became more and more time consuming. Longuet-Higgins [37] and Cartwright and Longuet-Higgins [38] showed that for a narrow banded sea spectrum, which is Gaussian distributed based on work done by Rice [39, 40], the extremes can be shown to be Rayleigh distributed [13]. This, combined with the assumption that for narrow-banded signals a peak is followed by a trough of equal magnitude, lead to the description of a stress range probability distribution for narrow-banded Gaussian processes. Statistical formulations for the extremes of a non-Gaussian distributed time series data have been derived by, among others, Weibull [41]. These formulations are more complex and require the tweaking of two parameters for the time series at hand.

Though the extremes of broad-banded Gaussian spectra are also Rayleigh distributed, the range can not be obtained from the extremes as was the case for the narrow banded spectrum. The initial temptation was to "correct" the narrow banded

fatigue estimate by using factors based on the "broadbandedness" of the signal. Wirsching [42], Chaudhury and Dover [43] and Hancock and Gall, among others, proposed empirical corrections to the narrowbanded formulations. However, Dirlik [44] proposed an empirical formulation to calculate the broad band stress range PDF directly from the stress PSD. He considered seventy different PSDs, varing from narrow banded to almost white noise, and developed time series representations for each. He then used monte carlo techniques to find coefficients for the empirical model that had the zeroth, first, second and fourth spectral moments as parameters. A good match between fatigue damage estimates using Dirlik's formulation with those obtained using the Rainflow counting methods have been reported by many researchers. Bishop and Sherratt [45] developed a closed form solution for the stress range PDF of a broadband stress PSD. Their formulation, however, is time consuming to implement and the accuracy of the results are not much better than the Dirlik formulation. For these reasons, the Dirlik method is regarded as the best method for broadband spectral fatigue calculations.

2.3 Higher Harmonics

Vandiver et al. [46] in field experiments from 1981 reported the first 'figure 8' displacement response, which is now common in laboratory experiments that allow both in-line and cross-flow motion. Figure 6, a figure from their work, shows the mid span displacement at the 3rd mode cross-flow and 5th mode in-line.

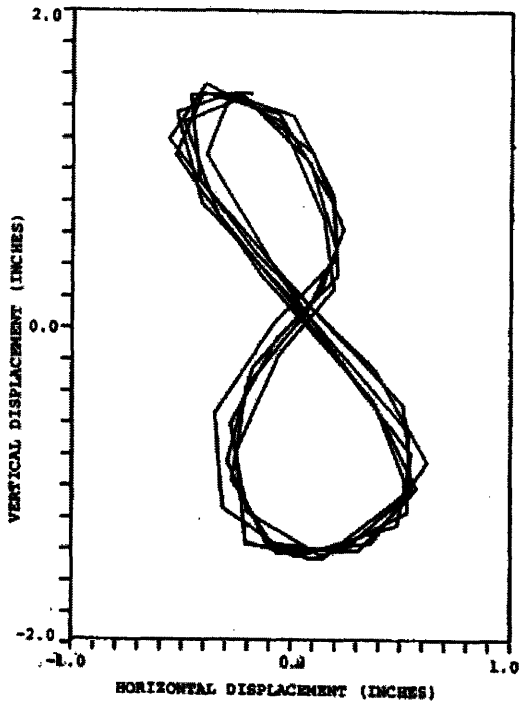

Figure 6 – The figure 8s were noticed by Vandiver in the lock-in regions in a flexible pipe undergoing VIV.

Recently, Jauvtis and Williamson [6] studied VIV for spring mounted cylinders having relatively low mass ratios (<6) and two degrees of freedom. They found the excitation at the 3x harmonic is associated with the shedding of three vortices in the wake behind the cylinder during each VIV half cycle. They call this the '2T' mode of vortex shedding. They report that the switch to the 2T mode happens around Vr=5 and persists until Vr=8. They observed large A_y/D_o ratios associated with the 2T mode and call it the SuperUpper (SU) region in the plot of A_y/D_o versus reduced velocity. The 2T mode is associated with a relatively large third harmonic lift force component in the cross-flow direction. Figure 7 shows Jauvtis and Williamson's A_y/D_o versus reduced velocity data. This plot has been constructed from data shared by Williamson. The horizontal axis is reduced velocity and the plot shows the variation of A_y/D_o based on the observed vibration frequency reduced velocity. The region labeled as SU is the response branch associated with a strong 3x harmonic force component.

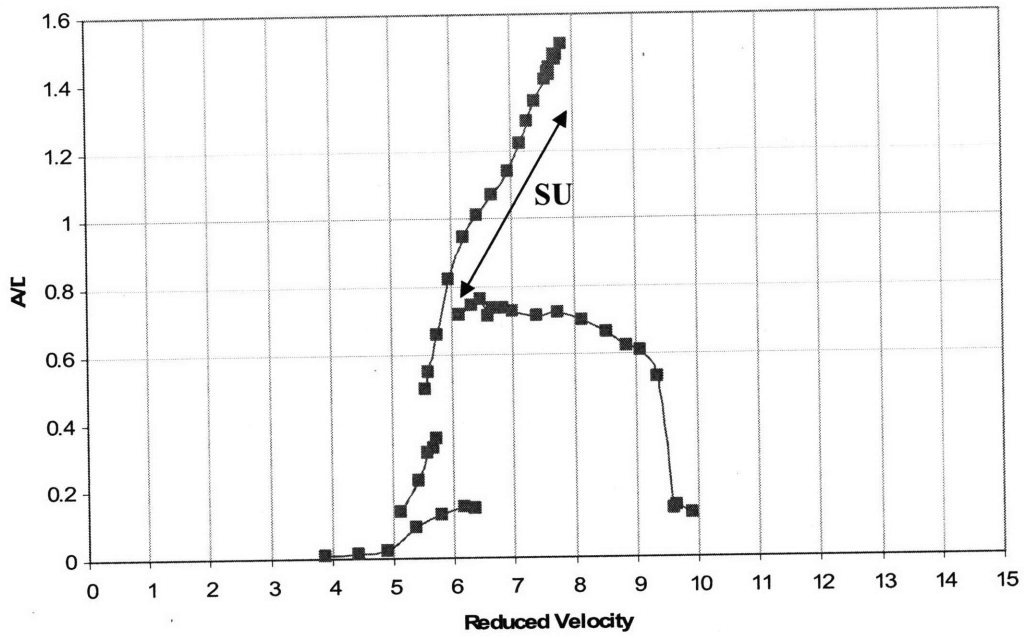

Figure 7 – The A/D of a spring mounted rigid cylinder in free vibration with both in-line and cross-flow degrees of freedom. For the x-axis, reduced velocity is based on the measured response frequency of the cylinder.

Aronsen [47], using forced vibrations on a painted Aluminum cylinder 15 cm in diameter and 3 m long, observe the 3rd harmonic in tests that utilized only in-line motion. He suggests that the 3rd harmonic is due to instability in the wake caused by the in-line motion, making it impossible for the 3rd harmonic to exist without in-line motion. A similar conclusion has been arrived at by Dahl [48] who explains the existence of forcing at the 3rd harmonic by the interaction of a cylinder undergoing large in-line VIV motion with the vortices in its wake.

To the author's knowledge, the 4th and 5th harmonics have not been clearly observed in the laboratory experiments with rigid cylinders. The clearest measurement of the 5th harmonic is in the Gulf Stream experiments.

3. Experiments and Data Analysis

In four decades of VIV research, experimenters have led the way with new observations, and theoretical work has followed in explaining the physics behind the observations. The importance of experiments to VIV research cannot be understated.

3.1 Brief History

3.1.1 Laboratory and towing tank experiments

Over the years, many different VIV experiments have been performed, each with different underlying constrains, limitations and benefits. Most of the laboratory or towing tank experiments have been with rigid cylinders, many of which have been forced VIV experiments [28, 30] and a few free vibrations experiments [6, 25]. In the last decade has there been a realization that both in-line and cross-flow degrees of freedom are important in VIV and only the recent rigid cylinder laboratory experiments have reflected this understanding by allowing both in-line and cross-flow degrees of freedom [6, 47, 48]. The handful of laboratory experiments with flexible cylinders has revealed interesting differences between VIV of rigid and flexible cylinders. For example, experiments done by Triantafyllou et al. [7]showed that the maximum VIV displacement in the cross-flow direction happens at different reduced velocities for rigid and flexible cylinders.

Among the advantages of VIV experiments in the laboratory or towing tanks are the ability to closely control and monitor the design variables like fluid flow velocity and tension. Further, the option of doing a second set of experiments to confirm an unexpected finding is a clear benefit. Lastly, the ability of experimenters to slowly vary parameters and cover an entire range of Reynolds numbers, reduced velocity and *A/D* ratios is essential for understanding the underlying physics of VIV. These advantages, coupled with the availability of visualization techniques, have helped researcher use laboratory experiments to understand difficult problems related to VIV.

Primary disadvantages of laboratory settings include the difficulty in doing VIV experiments with flexible pipe, particularly at high mode numbers. Further, the inability to produce realistic shear current profiles in laboratory setting is also a drawback, as is

the inability to perform tests at *L/D* ratios of 1000 or higher. Finally, the relatively short lengths of test pipes do not allow a pure traveling wave response like those observed in long risers

3.1.2 Field Experiments

Various researchers have gone beyond the laboratory settings to performed VIV experiments in order to better replicate the current profiles, L/D ratios and excited modes of the model to match those of actual risers. J. Kim Vandiver, from MIT, has led the way in this area and has made important observations like the figure 8 motions of a flexible pipe under "lock-in" when both in-line and cross-flow degrees of freedom were allowed [46] and the importance of the higher harmonics in VIV strain measurements [8, 10].

Though field experiments are difficult to perform and calibrate, they are more representative of real risers in the field. This enables researchers to study VIV in pipes vibrating at high mode numbers, effects of different current profiles and directions, and the traveling wave VIV response of long pipes. Difficulties range from cost of doing the experiments, to deployment challenges, inability to look at and study the details of the flow and the inability to go back and redo problem tests.

3.2 Experiments performed as part of this research

The experimental data used in this thesis is from a series of field experiments carried out at Lake Seneca in upstate New York and in the Gulf Stream offshore of Miami. Together, these experiments form one of the first data sets that measure VIV in large length-to-diameter ratio pipes, where a high mode numbers (20+) are excited. Further, the Gulf Stream experiments belong to a small but growing group of data sets that made VIV strain measurements.

3.2.1 Lake Seneca Experiments

Two experiments were performed at Lake Seneca, the first in November of 2003 and the second in June of 2004. The Lake Seneca test facility, in upstate New York, was selected because it is a fully equipped field test station moored in calm, deep water, making it ideal for conducting a controlled test on a long circular pipe in uniform flow.

The purpose of these experiments was to study VIV in pipes with large length-to-diameter ratio, vibrating at high mode numbers (10^{th} mode or above). Further, it also offered an opportunity to investigate the mean drag forces on pipes vibrating at high mode numbers and study the drag and efficiency of strakes as VIV mitigating devices.

The experimental utilized a 1.31 in OD pipe, 400 ft long but constructed in 100 ft sections so that shorter length pipes could also be tested. The pipe was filled with a flexible epoxy compound to exclude water and to hold the wires in place. A railroad wheel, with fins mounted on it to prevent pitching and rotating, was connected to the bottom end to provide tension. The tension was carefully chosen such that the pitch and roll natural frequencies of the weight, which were approximately 0.68 Hz, were lower than the lowest VIV response frequency of interest. The main pipe properties are shown in Table 1.

Table 1 - Lake Seneca Pipe Properties

Outer Diameter	1.310 in (0.0333m)
Inner Diameter	0.980 in (0.0249m)
Lengths tested	201 & 401 ft (61.26 & 122.23m)
Effective tension	805 lbs submg. bottom weight (3581N)
Modulus of Elasticity (E)	1805.0 ksi (1.276E10 N/sq m)
Moment of Inertia (I)	3.994E-06 ft^4 (3.447E-8 m^4)
EI	149489.3 [lb-in^2](429.0 N-m^2)
Mass / Displaced Mass of water	1.35
Weight in air	0.79 [lb/ft](11.53 N/m),(1.176 kg/m)
Manufactured by	FiberSpar

Each 100 ft long section of pipe contained six evenly spaced tri-axial accelerometers, which were sampled at 60 Hz by analog to digital converters and micro-processors located locally at each accelerometer unit. Towing speed was measured by two mechanical current meters, one suspended underneath the towed weight and the other hung over the side of the towing vessel. At the top of the pipe, a load cell and tilt meter were attached to allow the measurement of the tension in the pipe and the top angle of inclination. The experimental set-up is shown in Figure 8.

The length, diameter and tension of the pipe were chosen so as to permit cross-flow excitation of up to the 25th mode. The maximum speed possible at Lake Seneca was limited by the maximum allowable deflection angle of the pipe. Typical towing speeds were approximately 1.0 to 3.5 ft/s, (0.3 to 1.1m/s). The curvature of the pipe did change the incident velocity perpendicular to the pipe. However, as the top angles of the pipe were less than 30 degrees, this angle changes the incident current by less than 15%.

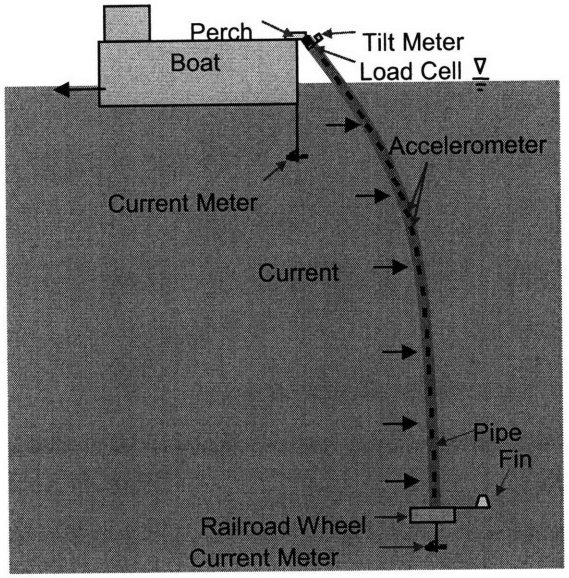

Figure 8 - Setup for the Lake Seneca experiments.

3.2.2 The Gulf Stream Experiments

The Seneca experiments were followed by the more extensive Gulf Stream experiments. Though the basic setup was similar to the Lake Seneca experiments, these experiments faced several new challenges including non-uniform current profiles, the use of fiber optic strain gauges and spooling and deployment on site.

The Gulf Stream experiments were conducted in October of 2004 and October of 2006 offshore of Miami, Florida. Since the experiments attempted to study the effects of current shear and directionality, they were done in the Gulf Stream. The boat then oriented itself into, across, and with the Gulf Stream so that different types of current shear could be seen.

The goals of the overall test program were to understand the different aspects of the dynamics of a pipe undergoing VIV at high mode numbers. These aspects included VIV

suppression with strakes, drag coefficients of bare and straked pipes, in-line and cross-flow VIV, and damping factors. The importance of the higher harmonics to fatigue, as reported in [8], was found in data collected in these experiments.

The experiments were conducted on the Research Vessel F. G. Walton Smith from the University of Miami using pipes instrumented with fiber optic strain gauges to monitor the vibration. The pipe during both experiments was spooled on a drum mounted at the aft portion of the ship. The pipe was un-spooled and lowered into the water using a hydraulic motor and then deployed, which again differed between the two experiments. A railroad wheel weighing 805 lbs (dry weight, 725 lbs in water), was attached to the bottom of the pipe to tension the pipe, an arrangement similar to the Lake Seneca experiment. Figure 9 shows the details of the experiments setup on board the Walton Smith.

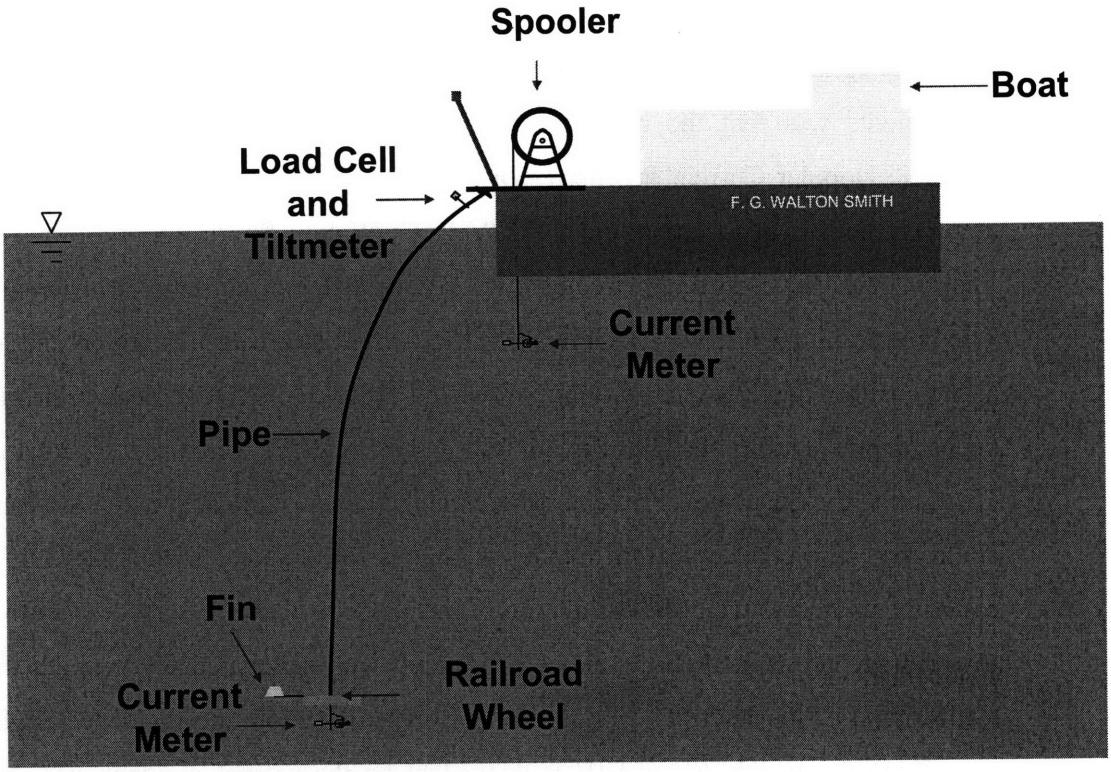

Figure 9 – Stow position and the deployed position during the second Gulf Stream experiment.

Eight optical fibers were embedded into the outer layer of the pipe during manufacture. Two fibers were located in each of the four quadrants of the pipe, and each

fiber contained 35 strain gauges, spaced fourteen feet apart. Though the strain gauges from each fiber in the pair were off-set from each other by seven feet, as seen in Figure 10(b), for convenience, the data from the fibers in the same quadrant were combined as if there was a single fiber with seventy strain gauges, spaced 7 feet apart.

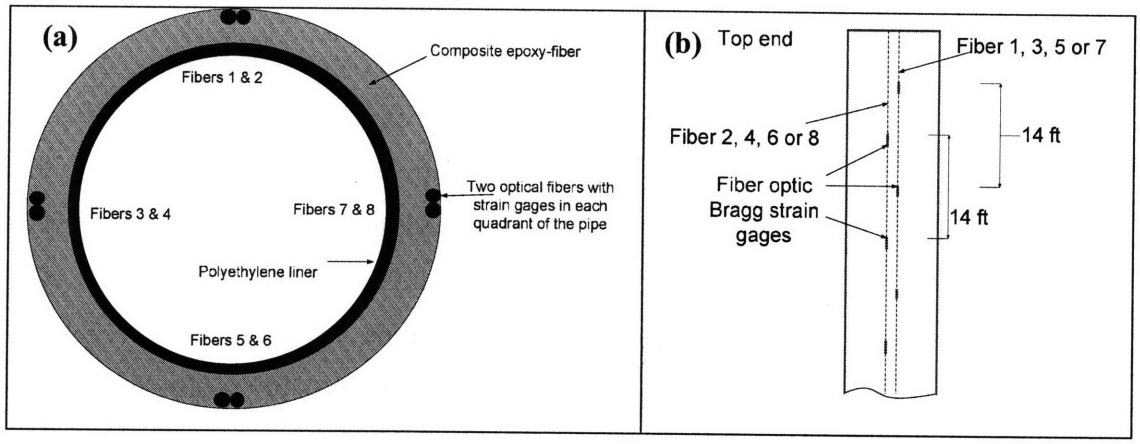

Figure 10 – (a) Cross-Section and (b) Side View of the Pipe from the Gulf Stream Test

One significant difference between the lake Seneca experiments and the Miami experiments was that the current profile was not uniform in the Gulf Stream. An Acoustic Doppler Current Profiler (ADCP) recorded the current velocity and direction along the length of the pipe. On the R/V F. G. Walton Smith, there are two ADCPs. Each ADCP uses a different frequency to obtain different currents at different depths. The broadband (600 kHz) ADCP records the current at greater resolution and accuracy at the shallow depths, whereas the narrowband (150 kHz) ADCP records the current at deeper depths. During the Gulf Stream testing, both ADCPs were used to gather data.

Unlike the Seneca experiments where the incidence angle of the pipe was small and could be ignored, the large incidence angles observed during the Gulf Stream experiments necessitated the estimation of the shape of the pipe with respect to vertical for each experiment. A finite-element program was developed to compute the mean static shape of the riser. The FEM enabled one to estimate the incidence angle of the pipe along the length. Since VIV is dependent on the normal incident velocity on the pipe, the measured velocity profile was converted to the normal incident velocity for VIV analysis. More details are in section 3.3.1

Additional instrumentation included a tilt meter, to measure the inclination at the top of the pipe, a load cell to measure the tension in the pipe, and two mechanical current meters to measure the current speeds at the top and bottom of the pipe.

3.2.2.1 The first Gulf Stream Experiments

The first Gulf Stream experiments were performed in October of 2004. It was done with a 484 ft long pipe made of a composite carbon-glass matrix with an HDPE liner. The pipe properties are found in Table.

Table 2 –Gulf Stream Pipe Properties

Pipe Length	484 ft (147.5m)
Inner Diameter 1.05 in. (0.0267 m)	Outer Diameter 1.40 in.(0.0356 m)
Optical Fiber Position 1.30 in.(0.033 m)	EI 1.7e5 lb.in2 (488 Nm2)
Modulus of Elasticity (E) 2.30e6 lb./in2 (1.586e10 N/m2)	EA 8.5e5 lb. (3.78e6 N)
Weight in Seawater 0.12 lb./ft. (flooded in Seawater)	(1.75 N/m)
Weight in air, w/trapped water 0.83 lb./ft. (12.11 N/m)	Density 0.053 lb/in3 (1.47 g./cc).
Effective Tension 725 lbs submg. bottom weight (3225N)	Material Carbon fiber –epoxy
Length 485.3 ft (147.3 m) (U-joint to U-joint)	Manufactured by Hydril (now Futurepipe)
Inner Diameter 1.05 in. (0.0267 m)	Outer Diameter 1.40 in.(0.0356 m)
Diameter at Optical Fiber Position 1.30 in.(0.033 m)	EI 1.7e5 lb.in2 (488 Nm2)

3.2.3 The Second Gulf Stream Experiments

The experience of the design team with the first Gulf Stream experiments motivated some key design changes in the mechanical design for the Second Gulf Stream experiments in 2006. The most important changes were to the way the pipe was spooled and attached at the top end connection to the pipe when deployed. The first change was motivated by the breakage of several strain gauges due to high stress created in the

spooling and un-spooling procedure. To avoid breaking fibers, a new method of deploying the pipe was designed and implemented for the second Gulf Stream experiment. Details are provided in Appendix A. The second change resulted from the limitations imposed by the universal joint at the top end of the pipe. On several occasions in the first experiment, the top angle was so large that it exceeded the largest angle allowed by the top joint. To avoid this, a new way of holding the pipe when deployed was designed and implemented. Further details are in Appendix A.

The pipe used in the second Gulf Stream experiments was 500 ft long and 1.43 inches in diameter. It was made from glass-fiber epoxy with the fiber optics installed during manufacture. A pressure gauge was also installed on the rail road wheel fin, Figure 11, to measure the depth of the bottom end during an experiment. The depth measurement provided an important check for the pipe shape calculations. Appendix B has details of how the depth sensor designed and installed.

Table 3 – Details of the pipe used in the second Gulf Stream Experiments

Pipe Length	500.04 ft (152.4m)
Inner Diameter	0.98 inch (0.0249 m)
Outer Diameter	1.43 inch (0.0363 m)
EI	1.483e3 lb ft2 (613 N m2)
EA	7.468e5 lb (3.322e6)
Weight in Seawater	0.1325 lb/ft (0.1972 kg/m)
Weight in air	0.511 lb/ft (0.760 kg/m)
Density	86.39 lb/ft3 (1383 kg/m3)
Effective Tension	725 lb
Material	Glass fiber epoxy composite
Length	500.4 ft (152.524 m)
Manufactured by	FiberSpar Inc

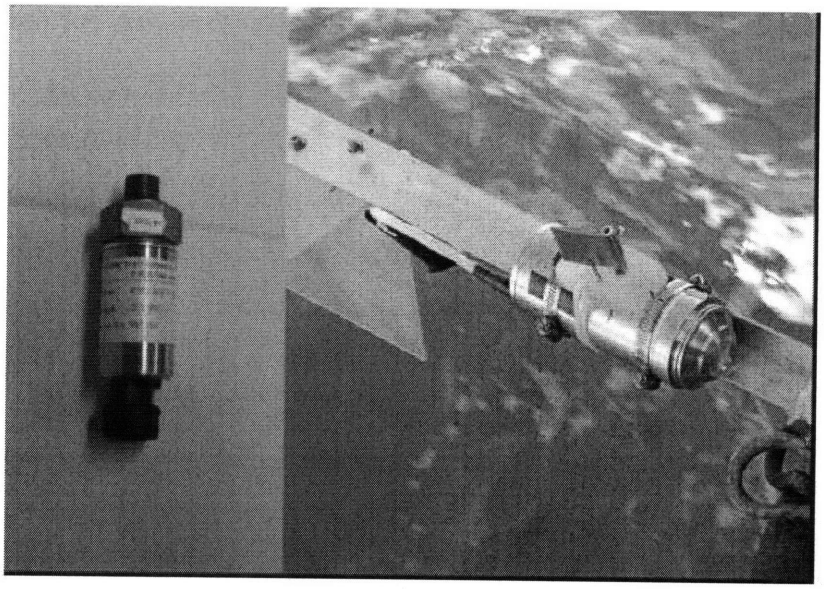

Figure 11 – Pressure Transducer (left) installed in an aluminum casing to the rail road wheel.

3.3 Key data analysis procedures

As with all experiments, the Gulf Stream experiments had their share of problems with the data acquisition system and other instrumentation. Hence, many data processing and analysis procedures were identified to minimize the effects of these problems. The details of the problems and methods can be found in the experiments reports [9]. Some of the key procedures are explained below.

3.3.1 Calculating Normal Incident Current Profiles

When a pipe under tension is towed in water, the drag forces acting on it cause it to assume a curved shape. This change in shape changes the flow velocity components normal to the pipe axis. To estimate this component, the shape of the pipe, which depends on the drag force on the pipe, has to be computed. This problem is further complicated by VIV which causes amplification in the drag force.

A measure of the drag on the pipe is the observed top angle. A combination of SHEAR7, a VIV prediction program, and a finite-element MATLAB program was used to numerically compute the top angle for a current profile. The drag coefficient was changed till the predicted angle matched the measured top angle. The MATLAB

program calculates the shape of the component corresponding to this top angle and uses it to estimate the normal incident current on the pipe.

The finite-element program breaks the pipe into a number of segments. Using the input velocities (ie. velocities measure by the ADCP), it then calculates forces perpendicular to the axis of each segment of the pipe (drag forces for each segment) and forces tangential to the axis of each segment of the pipe. The program then sums up the forces on each of the segments and calculates the total horizontal and vertical force. These are the total drag force and total lift force on the pipe. The shape of the pipe corresponding to this equilibrium position is then calculated. This in turn changes the incident velocity on the pipe. The program then repeats the above process to converge to the final shape of the pipe for the given current profile.

At each stage in the above process, the drag coefficients are estimated using a SHEAR7 model of the pipe. The best estimate of the normal incident velocity profile at that stage of the iteration is used as the velocity profile for SHEAR7.

If the top angle is near vertical, as in the Lake Seneca experiments, the current incident on the pipe remains constant. However, when current varied with depth, as seen in the Miami tests, the incident current, and hence the drag force, on each segment of the pipe changes due to the rise of the pipe during tow. Therefore, the above iterative method must account for the rise of the pipe. The iteration process is repeated till the bottom end does not change between two iterations. Predicted and measured bottom end depth can also be checked.

The inclination of each segment is calculated based on the total horizontal and vertical forces acting on that segment and all the segments below it. The main steps in the calculation are shown in the flow chart below and explained in the next page.

Step1: Using the ADCP profiles we calculate the incident velocity profile on pipe assuming no lift and no inclination angle. This forms a starting estimate of the velocity.

Step 2: Input this velocity profile into the SHEAR7 model of the pipe. When the model is run SHEAR7 will calculate the drag coefficients along the pipe using the predicted local RMS response.

Step 3: Using the calculated drag coefficients and the FE model of the pipe, estimate the top angle, pipe shape and rise of the bottom end. Iterate till the forces are in balance.

Step 4: For the equilibrium shape in Step3, calculate the new incident current profile considering the lift of the pipe. If the lift has not changed then proceed else go back to Step 2.

Step 5: Check to see if the calculated top angle matches the measure top angle. If not multiply drag coefficients by a factor and go to Step 2.

Step 6: End

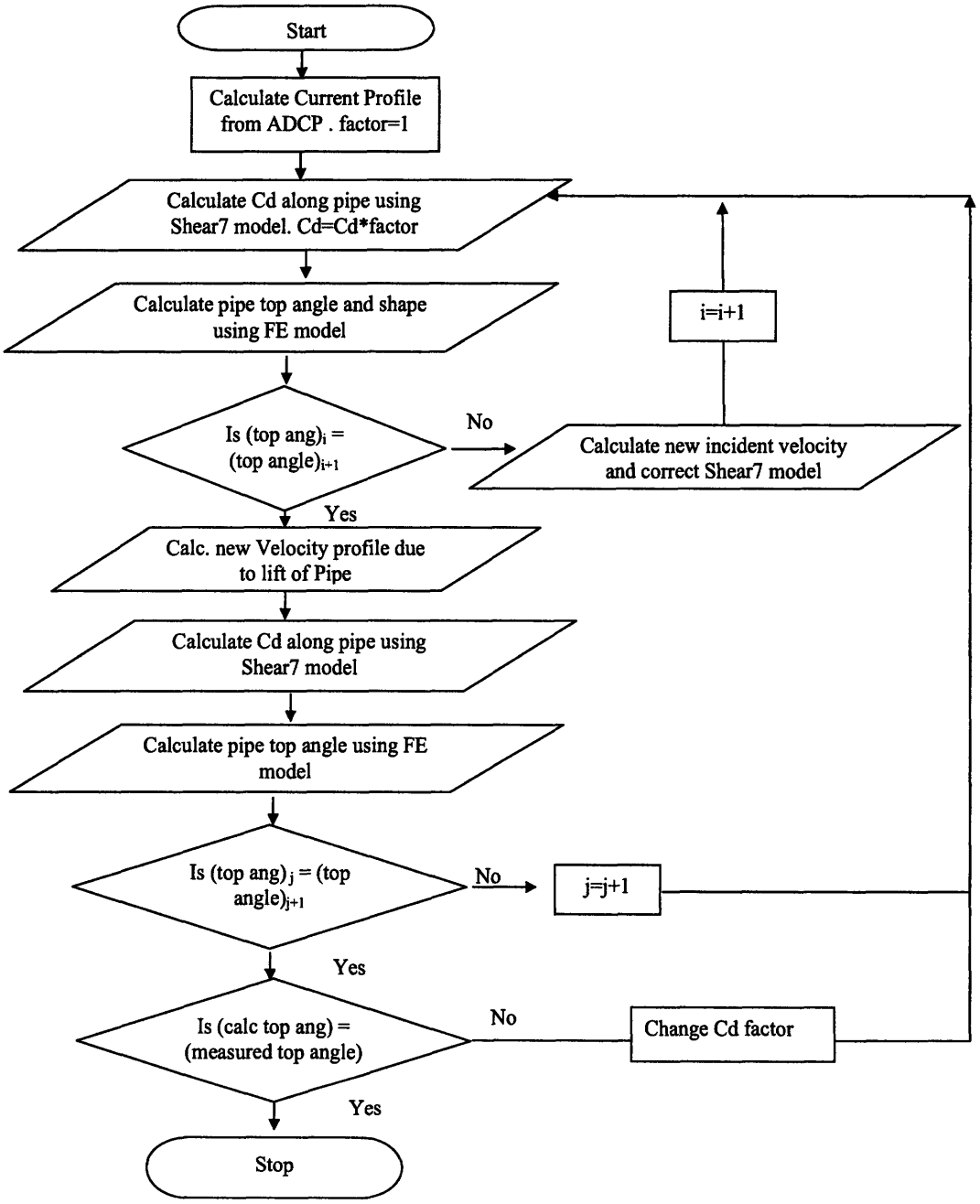

3.3.2 Working in the frequency Domain

In both the Miami experiments, the fibers were not generally aligned with the cross-flow or in-line directions. This happened due to a twist in the pipe, introduced during manufacture, making it impossible for the any fiber to be perfectly aligned with any one direction for the entire length of the pipe. Further, the orientation of the fibers changed during the six day experiment due to the creep introduced in the pipe while stowed on the spooler.

Figure 3 shows the angle calculated in two different ways. The calculations are in general agreement with the manufactures estimate of a 180 degree twist in the pipe but shows that the twist is not linear as earlier thought.

Because of this twist, it became difficult to estimate the total in-line and total cross-flow response. Working in the time domain to rotate sensors was difficult and prone to errors. Hence, the response of two orthogonal signals was combined in the frequency domain. The response at each frequency can be combined as the square root of the sum of the squares, as shown in Equation (3.1) for the 1st harmonic response, but the response at different frequencies have to isolated first before this procedure is employed.

$$\varepsilon_{1total} = \sqrt{(\varepsilon_{1Q1})^2 + (\varepsilon_{1Q4})^2}$$

where $Q1$ and $Q4$ are othogonal sensors and

ε_{1Q1} = RMS strain calculated using Q1 strain

ε_{1Q4} = RMS strain calculated using Q4 strain (3.1)

3.3.3 Establishing steady state regions

Figure 3 (a) presents data from a bare pipe test (Test – 20061023203818) performed during the second Gulf Stream experiment. It shows time-frequency plots, called scalograms, at three locations on the pipe. The frequency range in these plots is chosen to show the Strouhal frequency, called the fundamental VIV frequency or 1x frequency in this paper. Figure 3 (b) shows the mean normal incident current on the pipe during the test. The scalograms were calculated at sensor locations 232.5 ft (sensor 33), 302.5 ft (sensor 43) and 372.5 ft (sensor 53) measured axially from the top of the pipe. Their positions on the pipe are shown by dots in Figure 3 (b).

The scalograms indicate that the fundamental frequency of VIV was not constant for the duration of the test. They suggest that the frequency reached a steady state value only in the last sixty seconds of the test. Since the motion of the pipe is mainly governed by the fundamental VIV frequency, we can make the assumption that steady state conditions are achieved when this frequency is steady with time. Experimental data from these steady-state regions can be used to make comparisons with results from predictive programs, like SHEAR7, which assume steady state conditions in their analysis.

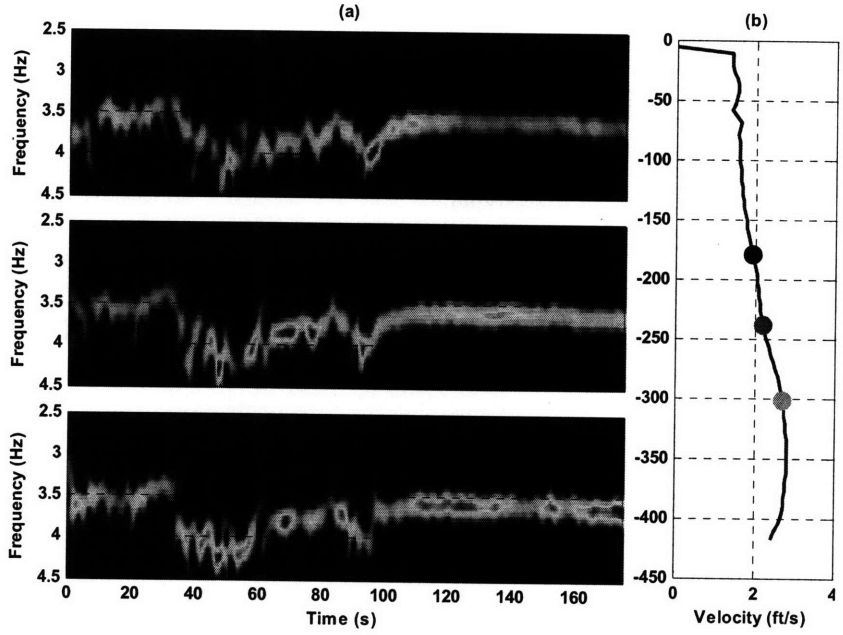

Figure 12 (a) - Time-Frequency plots for test 20061023203818 show that in this example steady state conditions are achieved only in the last 60 seconds. The plots were obtained using the Morlet Wavelet analysis. (b) The normal incident current profile with locations where the wavelet transforms shown in (a) were performed.

In this steady state region, the fundamental frequency of vibration and all its harmonics are narrow banded, almost single frequency responses. Figure 4 shows the strain Power Spectral Density (PSD) for the steady state duration of the test. These PSDs, shown for orthogonal quadrants Q4 and Q1, correspond to the same sensor locations as the scalograms. As expected, the PSDs show energy not only at the fundamental frequency of vibration but also at its harmonics. (See [49] for an excellent discussion on time-frequency analysis)

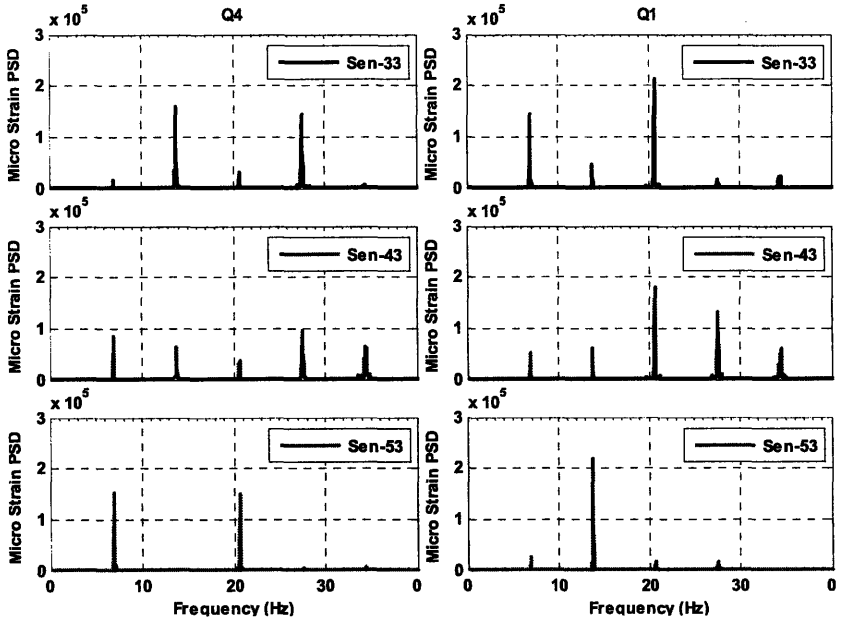

Figure 13 –Strain PSDs, shown for Q4 and Q1, in the steady state region are almost single frequency responses. Each PSD was calculated using the Welch method with 60 seconds of data, a 40 second window length and 95% overlap.

4. Drag Coefficients

Researchers have known for decades that drag forces are enhanced due to VIV. Comparing two cylinders placed in fluid flow – one undergoing VIV and the other stationary – the former experiences greater drag forces. Significant research has been done to explain this "amplification" in drag forces due to VIV. This has led to empirical formulations for an amplification factor, a multiplier that accounts for the enhanced drag. Hence, the total drag force for a cylinder undergoing VIV is calculated as the drag force of a stationary rigid cylinder in fluid flow multiplied by this amplification factor.

Several formulations have been derived for the amplification factor using both field experiments [46] laboratory tests [23] (Chapter 2 has details of past work). All these formulations represent the drag amplification as a function of amplitude of vibration. Some have other parameters in the formulation as well. The most commonly used formulation in the oil and gas industry has been proposed by Griffin and Vandiver ([27]) using data from experiments conducted in tidal currents in Castine, Maine. The formulation is shown in Equation(4.1). An estimate of the amplification can be obtained by assuming an RMS *A/D* value of 0.707, which represents a peak amplitude-to-diameter ratio of 1.0. Such amplitudes are observed in lightly damped pipes undergoing VIV, as is common in the oil and gas industry. The amplification factor comes out to be 2.31, implying a greater than doubling of the drag forces due to VIV.

$$C_D(z) = C_{Do} * C_{D,amp}(z)$$

$$C_{D,amp}(z) = 1.0 + 1.043 * (2\frac{y_{rms}(z)}{D})^{0.65}$$

$C_D(z)$ = *Local Drag Coefficient*

$C_{D,amp}(z)$ = *Drag Amplification*

C_{Do} = *Drag Coefficient of a stationary cylinder* (4.1)

$y_{rms}(z)$ = *Local Amplitude of vibration*

D = *Diameter of pipe*

The formulation in Equation(4.1) has been derived using experimental data for a flexible pipe undergoing VIV at low mode numbers and the response was dominated by standing waves. Further, the drag force measurements were made at the ends (supports) of a flexible pipe undergoing VIV. Therefore, Equation(4.1) represents a spatially averaged value of the drag amplification factor.

The above approach of calculating spatially averaged drag coefficients is perfectly acceptable for spring mounted rigid cylinder laboratory experiments because the wake structure is the same over the entire length of the rigid cylinder undergoing VIV. However, when these results have to be verified for flexible cylinders, the above approach has limited applicability. If the pipe is placed in constant current with the "lock-in" region occupying most of the length of the pipe and generating a standing wave pattern, spatially average mean drag force is relevant. However, spatially averaged mean drag coefficients are inadequate when discussing VIV of long pipes in sheared flows because they are increasingly characterized by energy propagation in the form of traveling waves. In these situations the "lock-in" region comprises of only a small portion of the length of the pipe and the local response, especially when it is away from the "power-in" region, is dominated by waves propagating from other spatial locations on the pipe. Further, there may be several spatially removed "lock-in" regions in the pipe which generate vibrations with different frequencies [50] which then travel along the pipe and combine with locally generated VIV. The resulting response is very different from the locally generated response in rigid cylinder laboratory experiments and constant current VIV field experiments. When formulations that correlate response amplitude to drag amplifications are used in these conditions, they are bound to give erroneous results.

This chapter analyzes VIV related drag coefficients for both standing and traveling wave responses in flexible pipes and presents the following results. First, it validates the use of Equation(4.1) to estimate spatially averaged mean drag coefficients at high mode numbers when the response is of the standing wave type. Second, it an effort to study the drag coefficients when the response is of the traveling wave type, it develops a method to extract local drag coefficients from densely instrumented VIV strain data is developed in this chapter. This method is shown to capture large variations in local drag

coefficients in pipes with partial coverage of VIV mitigation devices (like fairings). Third, this above method is used to study the spatial variation of drag forces in bare pipes where the dominant VIV response is in the form of traveling waves. This study reveals interesting characteristics of local drag coefficients in such situations, including the need to modify Equation(4.1) for traveling wave VIV response. Finally, this chapter looks at mean drag coefficients for pipes covered in varying amounts with VIV mitigation devices, both fairings and strakes.

4.1 Spatially averaged mean drag Coefficients at High Mode Number: Lake Seneca Experiments

The Castine experiments excited the pipe in its second and third mode in the cross-flow direction. In recent times, the drag amplification formulation based on those experiments, Equation (4.1), is being used for pipes excited at very high modes, (sometimes higher than one hundred) without much research indicating the validity of the drag amplification formulation for flexible pipes excited at very high modes.

There are numerous reasons to be cautious about the unconditional applicability of Equation (4.1) at high mode numbers. First, at high mode numbers, there is considerable overlap in reduced velocity "power-in" bandwidth, usually considered from Vr=5 to Vr=7. This means that the "power-in" region corresponding to Vr=5 to Vr=7 for mode n-1, where n is a high mode, will overlap with the "power-in" region corresponding to Vr=5 to Vr=7 for mode n. This was not the case in the Castine experiments. Second, unlike the Castine experiments which were dominated by stationary wave response with distinct nodes and antinodes, the response for most risers vibrating at high modes in the field is dominated by traveling wave response. Later in this thesis, it is shown that traveling wave response produces different displacement patterns from a standing wave response, leading to different drag characteristics.

The Lake Seneca experiments, preformed in upstate New York in November 2003 and June 2004, provide one of the first highly instrumented data sets for flexible cylinders vibrating at high mode numbers. The experiments, which were done in the Reynolds number regime of 1.3×10^4 to 2×10^4, are used here to check the drag formulation presented in Equation (4.1). Though the primary VIV response of the pipe

corresponded to mode numbers of 15 to 25, like the Castine experiments, the response is dominated by standing waves due to the constant current profile in the experiments. Twenty bi-axial accelerometers, distributed spatially along the length of the pipe, are used to measure the VIV response of the pipe in both in-line and cross-flow directions. The vertical angle made by the pipe is measured using a tilt meter (see Figure 14)

4.1.1 Methodology to calculate spatially averaged Mean C_D using Observed Top Inclination Angle

The only indicator of drag force, albeit indirect, in the Lake Seneca experiments is the top tilt angle obtained from two accelerometers placed just below the top U-Joint, as shown in Figure 14. A procedure is developed to estimate the drag force distribution on the pipe using the measured current velocity, the measured top tilt angle and a SHEAR7 model of the pipe.

The result is a finite-element program[2] to estimate the top tilt angle of the pipe based on static force equilibrium. The pipe is divided into small segments, and using drag coefficients obtained from SHEAR7 and the normal incident velocity, the time-averaged mean forces acting normal to each segment is calculated. The weight-per-unit-length of the pipe and the tension estimates give the axial forces acting on each segment of the pipe. The static equilibrium configuration for each of the segments, starting from the bottom end (where the RRW was attached) and moving upwards, is then calculated. This process gives the static shape of the pipe during tow and also the inclination angle of each of the segments. When these inclination angles are large, the normal component of the incident velocity is much less than the actual current value. Further, the inclination angle of the uppermost segment corresponds to the predicted top inclination angle.

In some instances, especially when the inclination angle is large enough to produce substantial differences between the incident current velocity and the normal component of the incident current, the finite-element model is used in an iterative fashion to estimate the predicted top angle. Each iteration uses the corrected normal incident current profile, based on the predicted inclination angles of the previous iteration,

---

[2] The first version of the program was written by Dr. Hayden Marcollo, AMOG Counsulting.

continuing till the predicted top angle of the final iteration is within acceptable error, usually 0.1 degrees, of the predicted top angle of the previous iteration. This procedure was performed for each of the tests done at Lake Seneca, providing an estimate of the spatially averaged mean drag coefficient at different tow velocities. Further, to understand the reasons behind the observed differences between the predicted and measured values, the calculations are done in two slightly different ways.

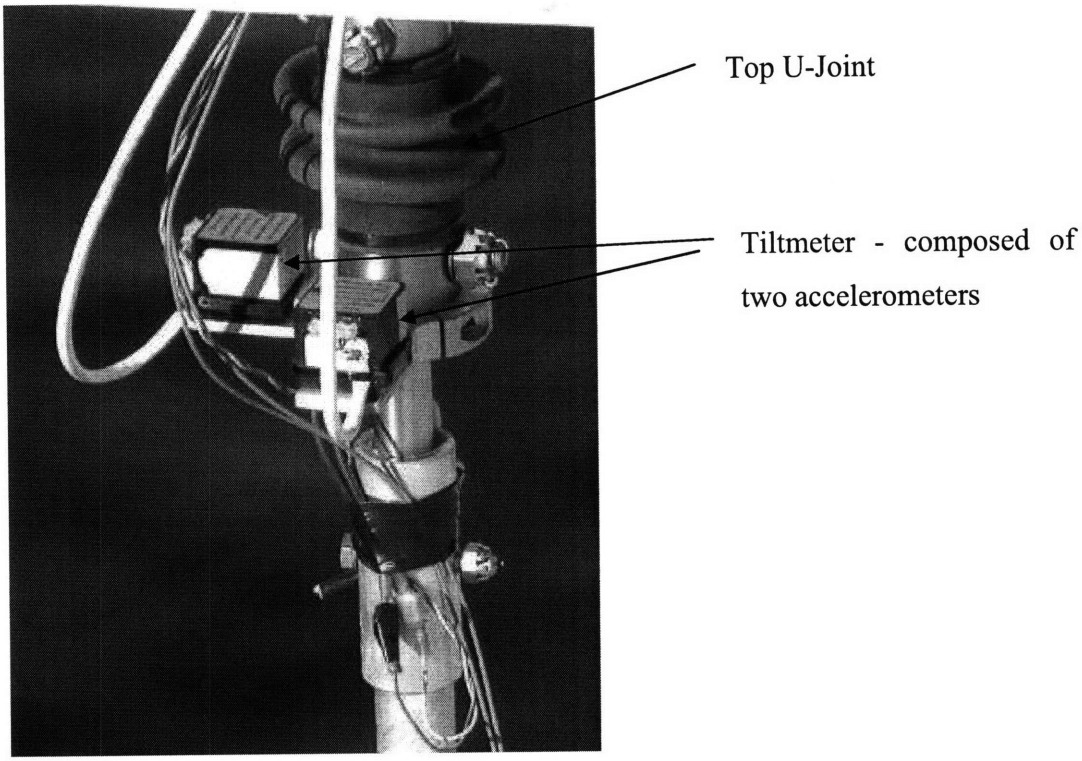

Figure 14 - Accelerometers in the Lake Seneca experiments were used to get top tilt angles.

Method 1: Using the structural properties of the pipe and the normal incident current profile $V_n(z)$, SHEAR7 is used to predict the local RMS response amplitude, $\underline{Y_{rms}(z)}$. The SHEAR7 program uses $Y_{rms}(z)$ to compute the local drag coefficient amplification factor using Equation (4.1). The stationary cylinder drag coefficient, C_{Do}, at the experimental Reynolds numbers is approximately 1.2. As shown in Equation(4.1), the product of this value and the amplification factor provides an estimate of the local

normal incidence drag coefficient. The predicted $C_D(z)$ is then used in a finite-element model of the pipe and railroad wheel to achieve the static shape of the riser under tow. In this configuration of static equilibrium, the top tilt angle and the spatially averaged drag coefficient are calculated. A tangential drag coefficient of 0.01 is assumed.

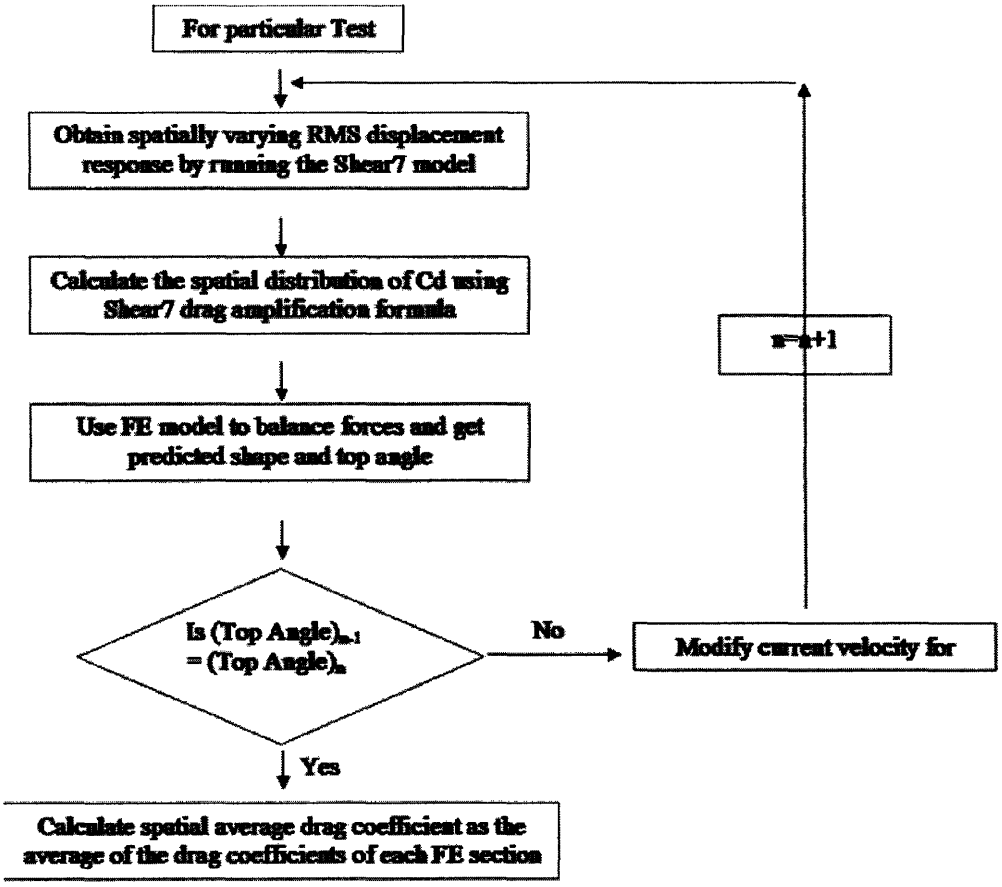

Figure 15 - Method 1: Spatially averaged mean C_D values calculated using SHEAR7 predicted displacement response. Note n indicates the iteration number.

Method 2: The measured RMS response amplitude, $Y^M_{rms}(z)$ is estimated by double integrating the acceleration data. Equation (4.1) is used to compute the local drag coefficients corresponding to the calculated $Y^M_{rms}(z)$ and used in the finite-element model to obtain static shape of the riser under tow. For this configuration of static equilibrium,

the top tilt angle and the spatially averaged drag coefficient are calculated. A tangential drag coefficient of 0.01 is assumed.

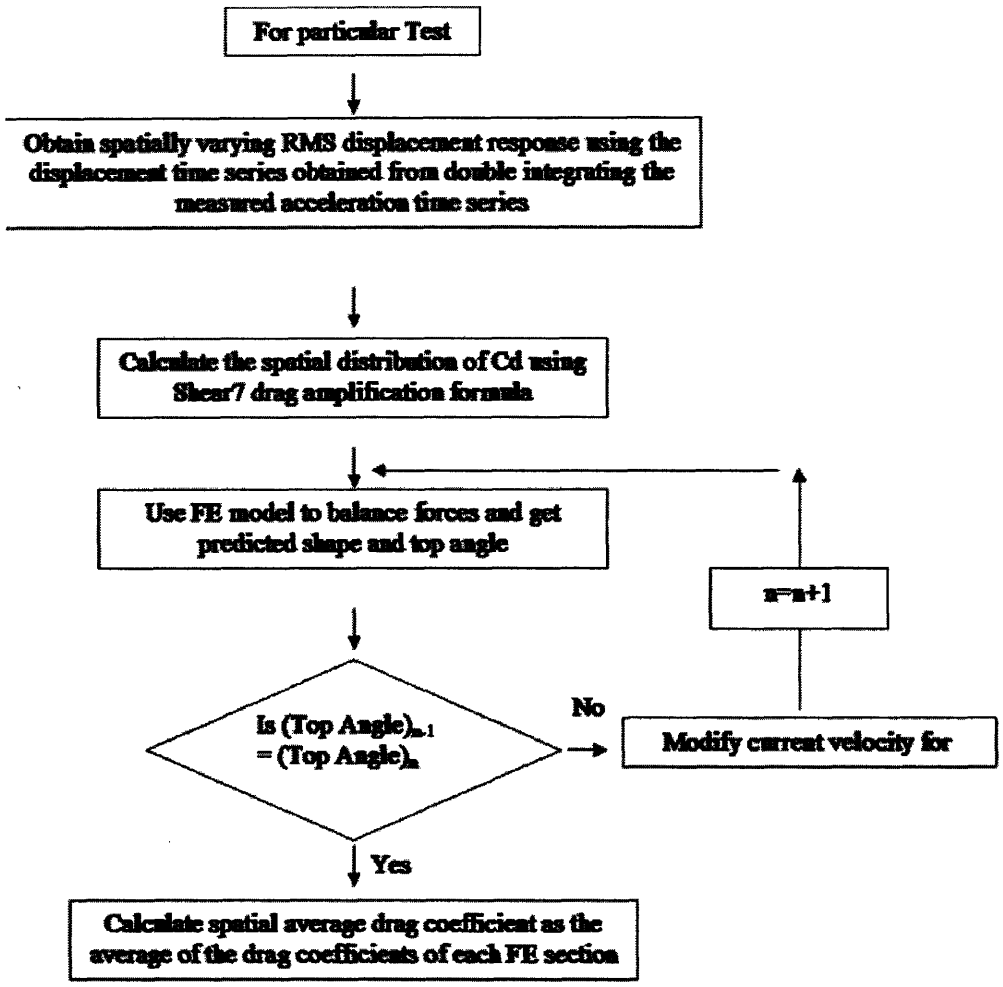

Figure 16 - Method 2: Spatially averaged mean C_D values are calculated using measured displacement response (calculated from acceleration data). Note n indicates the iteration number.

4.1.2 Results

A finite-element model of the 401 ft long pipe tested at Lake Seneca is developed. The C_{Do} value of 1.2 is used as the experiments were carried in the Reynolds number range of $1.3x10^4$ to $2x10^4$. The results were developed using the static equilibrium approach discussed earlier.

In Figure 17, the top inclination angle versus tow speed is shown on the primary scale while the variation of drag coefficient (C_D) with tow velocity is shown on the secondary scale to the right. The curves plotted are :-

- The red line (Top Tilt angle – Observed) is the time-averaged top tilt angle vs time-averaged tow speed, measured for each experiment.
- The green line (Top tilt angle – SHEAR7 predicted) is obtained using Method 1 (described earlier) to give the predicted spatially averaged mean drag coefficient (shown as the deep blue line).
- The light blue line (Top tilt angle – Mean C_D from observed Y_{rms}/D) is based on Method 2 to calculate the spatially averaged mean drag coefficient (shown as the pink line).

The SHEAR7 predicted RMS response and drag amplification factors are 10% to 15% higher than the observed values. Inclination angles using the SHEAR7 drag amplification formula with observed spatially averaged RMS displacement $\overline{Y_{rms}^{M}}^{z}$, are about 5% to 10% higher than observed values. This suggests that Equation (4.1) accurately predicts the C_D amplification of a bare pipe at high mode numbers when used with the observed RMS response values. Since SHEAR7 is by design conservative in response amplitude prediction, it will yield conservative predictions of drag coefficient amplification. In this example, it was still within 15% of the observed values.

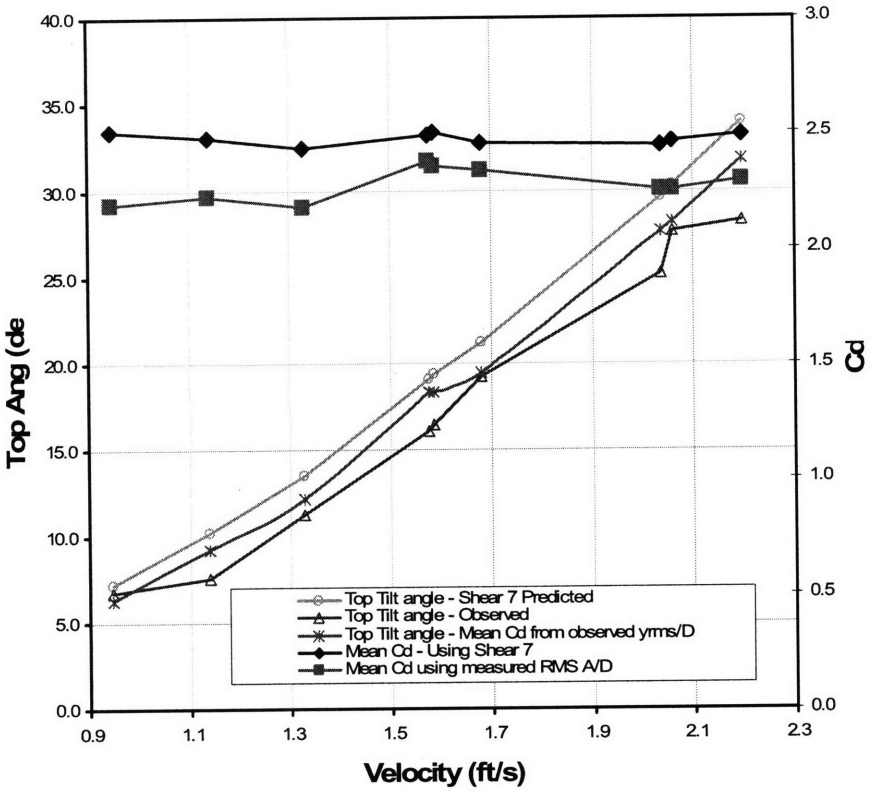

Figure 17 – Estimated drag coefficients (left axis) and top tilt angles (right axis) for different tow speeds using data from the Lake Seneca experiments with 401 ft long pipe.

Similar analysis of the data for the experiments performed on the 201 foot long bare pipe at Lake Seneca provides several useful results regarding the prediction of drag coefficients at high mode number. In these tests, performed in November of 2003, only the current and top angles were measured. Hence, SHEAR7 is used to produce drag coefficients and predict top inclination angles using the FE program described earlier in the section. These predictions are compared to the measured top angles and the corresponding mean drag is tabulated. Figure 18 shows that the top angles predicted using drag coefficients obtained from SHEAR7 compares well with measured values for a range of top angles. The corresponding spatially averaged drag coefficients are between 2.2 and 2.5.

In summary, the spatially averaged drag coefficients obtained from Lake Seneca experiments validated the use of Equation (4.1) for flexible pipes undergoing VIV at high mode numbers.

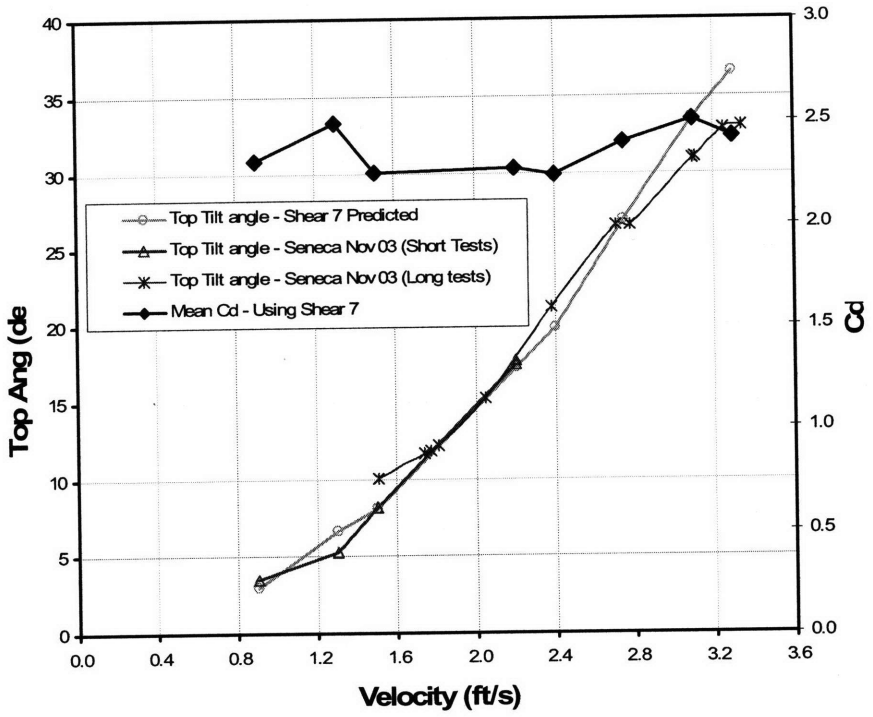

Figure 18 - Drag coefficients estimated from Lake Seneca experiments - 201 ft long pipe

4.2 Drag in traveling wave environments

As mentioned earlier, Equation (4.1) was derived from VIV in flexible pipes with standing wave response. In these situations a spatially averaged drag coefficient is meaningful. However, this is not the case when the dominant local VIV response of a pipe is due to traveling waves generated elsewhere on the pipe.

4.2.1 Drag as a indicator of the wake

Many researchers have proposed that changes in mean drag forces represent a change in the wake structure. Griffen and Ramberg [20] investigate this idea in a series of papers in the late 1970s and early 1980s. More recently, laboratory experiments by

Gopalkrishnan [28] and Jauvtis and Williamson [6] also indicate a close relationship between drag, reduced velocity, and the vortex pattern in the wake, lending support to the idea that changes in the mean drag force reflect changes in the vortex shedding pattern in the wake of the structure.

To date, however, this idea has not been investigated. Recently, researchers have been studying how vortices shed in the wake of a cylinder interact with the vibrating cylinder, where some vortex patterns lead to a higher mean drag force than others [48]. Therefore certain vortex shedding patterns, or wake patterns, may reasonably be associated with a mean drag coefficient.

Such a relationship between drag and vortex shedding patterns becomes particularly useful when long slender pipes are placed in sheared current environments. Under these conditions, "power-in" regions comprise a small fraction of the pipe length and the response is dominated by traveling waves. A traveling wave response does not allow sudden changes in VIV amplitude, because energy transferred from one location to another reduces only due to damping, which is small for the VIV problem. However, wake patterns are very dependent on the local reduced velocity and can change suddenly as reduced velocity changes in sheared flow. This means that for flexible cylinders in sheared flow, sudden changes in local drag coefficients and not the local response amplitudes may better indicate changes in the vortex shedding pattern in the wake of the cylinder. Usually, vortex patterns behind a cylinder are identified in laboratory experiments using time consuming and expensive techniques like Particle Induced Velocimetry (PIV) or pressure-sensitive dyes.

4.2.2 Drag in Sheared Current Environments

A possible method for estimating mean drag of a pipe in sheared flow could be to compute spatial distribution of vibration amplitude, usually from double integration of measured acceleration, and then to use existing formulations that relate the measured local RMS A/D of the pipe to local drag coefficients. This approach however is not accurate in the presence of traveling waves because of reasons discussed above. This limitation motivates us to look for methods of calculating mean drag force in realistic

settings that are independent of the affects of traveling waves and are more a representation of the wake dynamics behind the cylinder.

4.3 Using Strain to calculate mean drag force

4.3.1 Theory

Recent experiments, sponsored by DEEPSTAR, have used strain gauges to measure VIV response in a flexible pipe. The primary reason for this is that strain translates directly to stress making fatigue calculations easy and more accurate. Acceleration on the other hand has to be converted to displacements which in turn are used to compute strain before fatigue analysis can be done. A closer look at the VIV fundamentals reveals another benefit; that of strain being used to measure local drag coefficients. As a mean force on the pipe results in a mean strain (see next section for details), strain can be used to estimate mean drag coefficients for a flexible pipe undergoing VIV. Further, as traveling waves influence only the dynamic component of response, the local mean strain will not be influenced by energy propagating from the other regions of the pipe.

The equation of motion for a pipe undergoing VIV can be written as

$$(m(z)+m_a(z,\omega))y_{tt}+c(z)y_t+(EI(z)y_{zzzz}-T(z)y_{zz})=F(z,t)$$

where

$m(z)$ = *local mass density*

$m_a(z)$ = *local added mass*

$c(z)$ = *local damping* (4.2)

$EI(z)$ = *local bending stiffness*

$T(z)$ = *local Tension*

$F(z,t)$ = *local forcing in phase with velocity*

On taking a temporal mean of each term in Equation(4.2), the acceleration and velocity terms vanish because they are zero-mean oscillatory processes. Further, for a tension dominated beam undergoing VIV, as was the case in the Miami and Seneca experiments (Table 4), the term corresponding to EI can also be dropped. This reduces Equation(4.2) to

$$-T(z)\overline{y_{zz}^{\,t}}=\overline{F(z)^t} \tag{4.3}$$

where $^{-t}$ denotes a temporal mean. The local temporal averaged in-line force $\overline{F(z)^t}$ is equal to the local mean drag force per unit length.

The physical interpretation of Equation(4.3) is shown in Figure 19

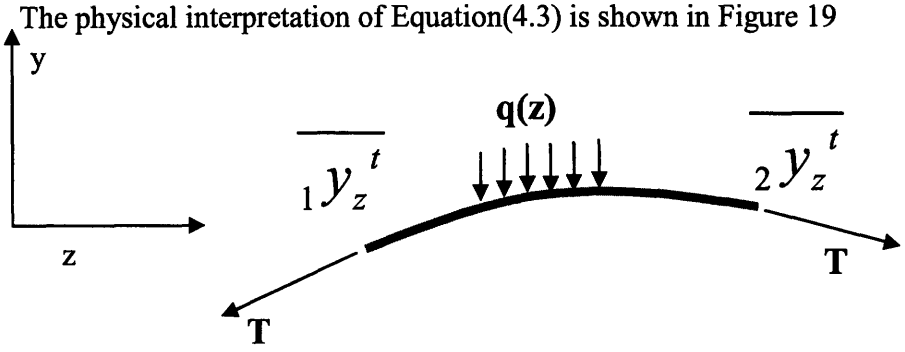

In a tension dominated pipe, the change in slope from location 1 to location 2 can only be caused by a force acting normal to the pipe.
Further, the **T** . $\overline{y_{zz}{}^t} = q(z)$

Figure 19 – Schematic showing that the mean normal force can be found if the tension and curvature are known

As the Gulf Stream experiments measured strain, Equation (4.3) can be rewritten as

$$-T(z).\overline{\varepsilon(z)^t}.\frac{2}{D} = \overline{F(z)^t} \tag{4.4}$$

where

$$\varepsilon = \frac{D/2}{R}; \quad \varepsilon = Strain \quad D = Diameter of Pipe \quad R = Radius of curvature$$

$$R = \frac{1}{\sigma}; \quad \sigma = curvature$$

$$F = T \times \sigma; \quad T = Tension$$

The drag force per unit length can be written using a drag coefficient as $F(z) = \frac{1}{2}\rho D V(z)^2 C_D(z)$. Therefore, we can express $C_D(z)$ as

$$C_D(z) = \frac{4T(z)\overline{\varepsilon(z)^t}}{\rho D^2 V(z)^2} \tag{4.5}$$

Equation(4.5) gives the local drag coefficient, unlike the spatial average drag coefficient obtained for the Lake Seneca experiments.

Table 4 – Calculations using nominal values for the second Gulf Stream experiments show that pipe was stiffness dominated.

$EI = 613\,N/m^2\,; c = 40\,m/s; f = 4\,Hz$
$k = \frac{\omega}{c} = 0.6\,; T = 3500\,N$
$\frac{EIk^4}{Tk^2} = 0.063$

4.3.2 Implementation

Though the theory behind getting local drag coefficients seems relatively simple, implementation is made difficult by the presence of several non-bending related mean strains that make it difficult to extract the static bending strain from the measured strain response.

4.3.2.1 Identification of non-bending related strains

Residual Stress

When the fiber optics, with the strain gauges, was embedded in the pipe during the manufacturing process, large residual strains developed in them. Further, the magnitude of the residual strains differed from fiber to fiber, as well as spatially along a single fiber. The residual strains, coupled with the axial strains due to the weight of the RRW and pipe, had magnitudes as large as 800 micro strain in certain locations of the pipe as shown in Figure 20. These large values resulted in measured strains sometimes exceeding the measuring limit of the fiber optic system, shown as zero strain marks in Figure 20, when the dynamic strains due to VIV were superimposed on the static strains resulting in a null value being assigned to the sensor.

To add to this, the handling and stowage of the pipe introduced creep in the pipe resulting in the residual stresses changing over the course of the experiments. Figure 21 shows the residual stress on three different days of the experiments and the difference between them is substantial. As shown here, the stresses increase due to creep.

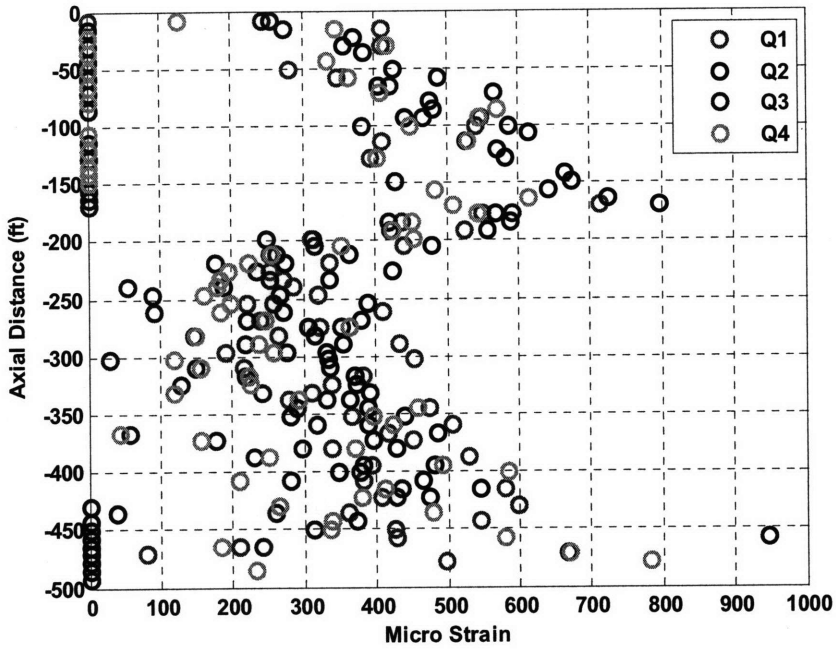

Figure 20 – The sum of Residual Strains and axial strains due to the weight of the RRW and pipe for bare pipe tests performed on the 23rd of October, 2006, the 4th day of testing. Q1, Q2, Q3 and Q4 indicate the quadrants where the fibers are located.

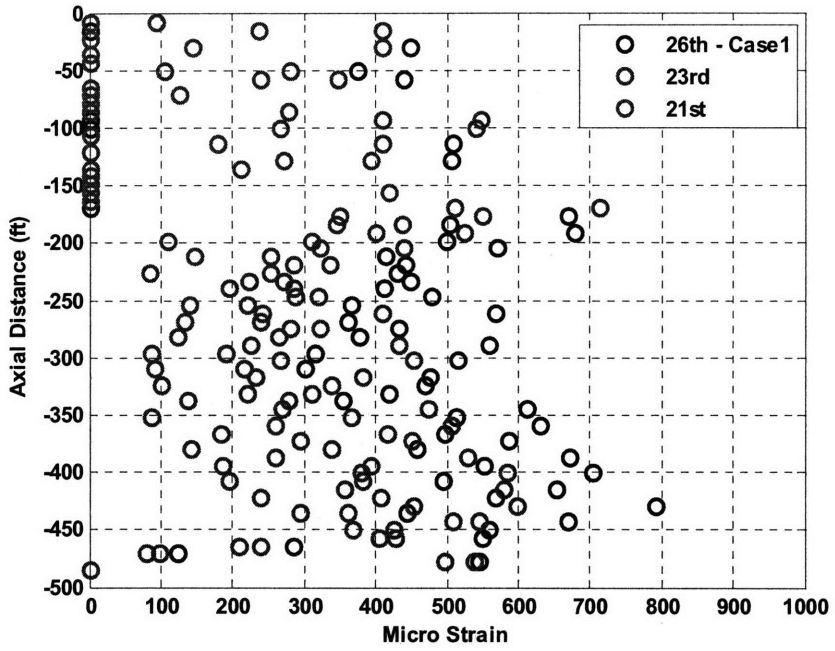

Figure 21 - The sum of residual strains and axial strains due to the weight of the RRW and pipe for quadrant 1 on three different days of testing. Their difference shows how creep changed the residual stresses during the Gulf Stream experiments

Stresses due to the weight of RRW and the weight of the pipe.

The weight of the RRW, about 725 lb (329 kg) in seawater, introduced tensile stresses in the pipe which were spatially constant and equal for all the fibers in the pipe. The weight of the pipe, however, introduced a higher stress at the top than at the bottom. Fortunately, the pipe was almost neutrally buoyant, having a weight per unit length of 0.197 kg/m, and the stresses due to the weight of the pipe were small.

Tensile Stresses developed during experiments

During the experiment, small angles of the RRW to the incident fluid flow resulted in additional tensile forces on the pipe, which were spatially constant for a fiber and the same for all the fibers. Further, additional strains were developed in the pipe due to the tangential fluid forces acting in the axial direction at the perimeter of the pipe. Both these forces could be removed by taking the difference of opposite quadrants (Q1 and Q3 for example), to isolate the mean strain. Since bending does not introduce any mean strains, these had to be due to tensile forces generated during the experiments.

4.3.2.2 Removing non-bending related strains

For the Gulf Stream experiment, the strain measurements for each sensor is time averaged to remove the dynamic components as shown by Equation(4.6)

$$\varepsilon_{Measured} = \varepsilon_{Dynamic} + \varepsilon_{Mean} \tag{4.6}$$

Time averaging the measured strain removes the dynamic components

$$\overline{\varepsilon_{Measured}}^{t} = \varepsilon_{Mean} \tag{4.7}$$

The ε_{Mean} consists of strains from many different sources. These can be shown in mathematical form as

$$\varepsilon_{Mean} = \varepsilon_{Static\ bending} + \varepsilon_{Axial\ due\ to\ tow} + \varepsilon_{Creep} + \ldots \\ \varepsilon_{Residual} + \varepsilon_{Axial\ due\ to\ RRW} + \varepsilon_{Axial\ due\ to\ pipe\ weight} \tag{4.8}$$

where,

$\varepsilon_{Static\ bending}$ is the mean bending strain due the shape of the pipe.

$\varepsilon_{Axial\ due\ to\ tow}$ is the mean axial strain developed during the experiment. This was discussed in detail earlier.

ε_{Creep} is the strain developed due to creep when the pipe was stowed or handled during the experiments. The creep strain just added to the residual strain.

$\varepsilon_{Residual}$ is the strain in the pipe that was developed during the manufacturing process.

$\varepsilon_{Axial\ due\ to\ RRW}$ and $\varepsilon_{Axial\ due\ to\ pipe\ weight}$ are the axial strains developed due to the weight of the RRW and the self weight of the pipe.

Removing the residual strain and axial strain due to the weight of the pipe and RRW

As mentioned earlier, the pipe developed residual strains during manufacture, transportation and handling and they had to be removed from the measured experimental strains. Moreover, the weight of the RRW and pipe introduced additional strains in the

pipe that are not caused by VIV. All of these strains are removed with the help of a 'Zero'.

A 'Zero' is an experiment that provides the base values of the variables being measured, which in our case were fiber strains. 'Zero' tests were done during the Gulf Stream tests before every set[3] of experiments to measure the starting values of mean strains at each sensor and after the set of experiments to make sure that the mean strain values did not change during the experiments. The end 'Zeros' also acted as backup incase the start 'zero' files were corrupted or were found to have errors. Equation (4.9) puts the strains captured by a zero file in mathematical form.

$$\varepsilon_{Zero} = \varepsilon_{Creep} + \varepsilon_{Residual} + \varepsilon_{Axial\ due\ to\ RRW} + \varepsilon_{Axial\ due\ to\ pipe\ weight} \qquad (4.9)$$

The 'Zero' experiments were performed by slowing down the boat to zero speed such that there was no relative speed between the boat and the ambient current. Sometimes, this did not lead to a near-zero tilt meter reading due to strong variation of current magnitude with water depth. In these cases, the boat speed had to be modified to ensure a small top angle. For example, most 'zero' cases in the second Gulf Stream experiments have top angles of 10 degrees or less, which is small considering the ocean wave environment. The small top angle should imply a small incident velocity on the pipe resulting in relatively little or no VIV. This can be ensured by checking the top end of the pipe for any VIV related vibrations. It the pipe is vibrating substantially, it indicates very strong deep currents and the boat position may have to be changed for the zero. Once the positioning was done, strain measurements were taken, as if performing a normal test.

As Equation (4.9) shows for the Gulf Stream experiments, a 'zero' captured the residual strains as well as the strains due to the weight of the RRW and the pipe, which could then be removed from mean strain measurements from other test measurements (Equation(4.10))

$$\varepsilon_{Mean} - \varepsilon_{Zero} = \overline{\varepsilon}^{t}_{Static\ bending} + \overline{\varepsilon}^{t}_{Axial\ due\ to\ tow} \qquad (4.10)$$

---

[3] A 'set' of experiments was a group of experiments performed without spooling the pipe or changing the configuration of the experiment (by adding strakes or fairings).

Unfortunately, creep in the pipe resulted in the 'Zero' changing every time the pipe was stowed on the drum. Therefore, a good 'Zero' was required for every set of experiments.

Removing strains due to tension developed during tow

During an experiment, additional time-averaged axial forces are developed that produce strains unrelated to the static bending of the pipe. In pure bending, fibers in opposite quadrants, Q1 and Q3 for example, will experience strains of equal magnitude but opposite signs as the strain at the neutral axis for a pipe in pure bending is zero. The axial forces generated during the experiment results in a net strain at the neutral axis which has to be removed from the experimental mean strain measurements in order to extract the static bending related strains. The commonly used procedure for finding the strain at the neutral axis is to average the temporal mean strains at each axial location for all the four orthogonal fibers as shown in Equation(4.11)

$$average(\bar{\varepsilon}^{t}_{Q1} + \bar{\varepsilon}^{t}_{Q2} + \bar{\varepsilon}^{t}_{Q3} + \bar{\varepsilon}^{t}_{Q4}) = \bar{\varepsilon}^{t}_{Axial\ due\ to\ tow} \tag{4.11}$$

When this mean axial strain is removed, in addition to the 'zero', from the measured temporal mean strain value, the remaining mean strain represents the mean strain due to the static bending of the pipe.

$$\varepsilon_{Mean} - \varepsilon_{Zero} - \bar{\varepsilon}^{t}_{Axial\ due\ to\ tow} = \bar{\varepsilon}^{t}_{Static\ bending} \tag{4.12}$$

Finding total static bending strain

As the fibers in the Gulf Stream experiments are not aligned with the in-line or cross-flow direction, static bending strains from two orthogonal fibers had to be combined to derive the total mean bending strain at any location.

$$\bar{\varepsilon}^{t}_{Total\ Static\ bending} = \sqrt{(\bar{\varepsilon}^{t}_{Q1-Static\ bending})^2 + (\bar{\varepsilon}^{t}_{Q4-Static\ bending})^2} \tag{4.13}$$

The temporal total static bending strain at each sensor location due is used with Equation(4.5) to derive the local drag coefficients along the length of the pipe.

4.3.3 Error Analysis and discussion

The approach discussed in this chapter to extract local drag coefficients from densely instrumented strain data is novel. Consequently, there is no previous research on the accuracy of this technique and the conditions under which the results are accurate. This section attempts to estimate the error in predicting local drag coefficients from strain data and discuses the sources and magnitudes of the error.

An error analysis for any proposed method provides two important insights. First, it gives guidance on the certainty of the results obtained from the method. The analysis will identify regions or conditions when the proposed method is most applicable and provide confidence intervals for the results. Second, it will identify parameters that cause the largest error in the drag calculations. This second insight could potentially minimize overall error in local drag estimates by helping researchers choose appropriate instrumentation for their experiments.

The error in the predicted C_D is calculated using the theory of error propagation [51]. Consider a function $f(x,y,z)$. The standard deviation of error, $S_{f(x,y,z)}$, of $f(x,y,z)$ is given by

$$S_{f(x,y,z)} = \sqrt{(\frac{\partial f}{\partial x})^2 S_x^{\,2} + (\frac{\partial f}{\partial y})^2 S_y^{\,2} + (\frac{\partial f}{\partial z})^2 S_z^{\,2}} \tag{4.14}$$

where;

S_x=Standard Deviation of variable x

S_y=Standard Deviation of variable y

S_z=Standard Deviation of variable z

The error in the various variables such as incident velocity and tension propagate into the drag estimate. Using Equations (4.5) and (4.14), the standard deviation in C_D is given by

$$S_{C_D(T,\bar{\varepsilon}^t,V)} = \frac{4}{\rho D^2}\sqrt{\frac{(\bar{\varepsilon}^t)^2}{V^4} S_T^{\,2} + \frac{T^2}{V^4} S_{\bar{\varepsilon}^t}^{\,2} + \frac{4.T^2(\bar{\varepsilon}^t)^2}{V^6} S_V^{\,2}} \tag{4.15}$$

where;

$S_{C_D(T,\bar{\varepsilon}',V)}$ = Standard Deviation of estimated C_D

S_T = Standard Deviation of measured tension

$S_{\bar{\varepsilon}'}$ = Standard Deviation of measured static bending strain

S_V = Standard Deviation of measured incident velocity

Equation (4.15) can be used at each spatial location of a pipe undergoing VIV to provide the standard deviation of estimated C_D at that location. Ideally, local values of tension, static bending strain and normal incident velocity should be used to estimate local error in estimated C_D. However, this is not always possible.

For the Gulf Stream experiments, tension measurements were available only at the top of the pipe. Since the time variation of tension at different location on the pipe was not available, it is assumed that the standard deviation of tension remains the same everywhere on the pipe and is equal to the value of the standard deviation of observed tension at the top of the pipe. Since the mean value of tension does not change drastically along the length of the pipe (most of the tension is provided by the RRW at the bottom of the pipe), this is a reasonable assumption for the Gulf Stream experiments.

The standard deviation of the static bending strain is difficult to estimate. Since static strain is obtained using time averaged means of the measured strain, the individual measurements of strain can not be used to estimate the standard deviation of static strain. Therefore, a different approach is taken. The dynamic component of strain in the "Zero" file represents the noise in the dynamic strain. This is because an ideal "Zero" should have no dynamic strain components. Assuming that the magnitude of error in dynamic strain is about the same as the magnitude of error in the static strain, the standard deviation in the "Zero" dynamic strain represents the expected standard deviation of the static bending strain.

The last component of error is due to velocity. In the Gulf Stream experiments, the spatial distribution of velocity is obtained using an ADCP. These ADCP measurements are obtained every 3 to 4 seconds. In order to remove the influence of boat motion from the measured ADCP current profiles, the mean from several of these measurements (15

to 18 second temporal averages) are calculated. A typical Gulf Stream test lasting 180 seconds can be divided into ten or eleven such 15 to 18 second zones; each zone providing an average current profile. These ten or eleven profiles are then used to calculate the standard deviation in the current for the particular test. (The normal incident current profiles were calculated using estimated incidence angles from an FE program. This process also has errors that affect the estimates of normal incident velocity. These errors are neglected in these calculations.)

4.3.4 Example

The following example shows the process of going from the measured strain to the local drag coefficients for Test 20061023205043. This was a bare pipe test performed on the 23rd of October, 2007 which was the 4th day of testing during the second Gulf Stream experiments. The maximum velocity for the test was 1.1 m/s and the top angle was about 55 degrees.

4.3.4.1 Step 1 – Getting Zero Values

The first step is to identify the zero values that would apply to this set of experiments. For the bare pipe experiments on the 23rd, test 20031023201203 was the zero file. The strains in the zero file contain the residual stresses from the manufacturing and handling of the pipe and the tension strains due to the RRW and the weight of the pipe. These strains are shows for all the four quadrants in Figure 22.

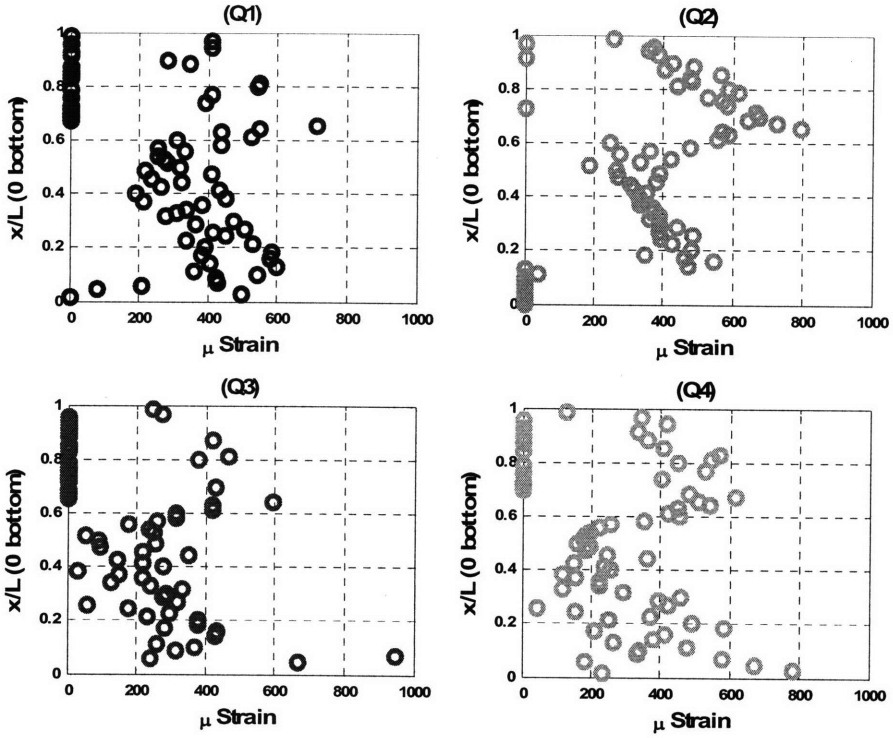

Figure 22 – The mean strains for each quadrant from the zero file 200623201203. The zero file gives the residual strains and tension strains that have to be removed from the measured mean strains for a particular experiment.

4.3.4.2 Step 2 - Measure Mean Strains for the experiment

Mean strains are temporal averages over the entire experiment at each spatial location of the pipe. Mean strains do not contain any influence from the oscillating component of strain, either from VIV or boat motion, but is the strain introduced due to the mean static shape of the pipe during the experiment in addition to the residual and mean tension related stresses. The zero strains are shown in Figure 23(a) and the experiments mean strains are shown in Figure 23(b).

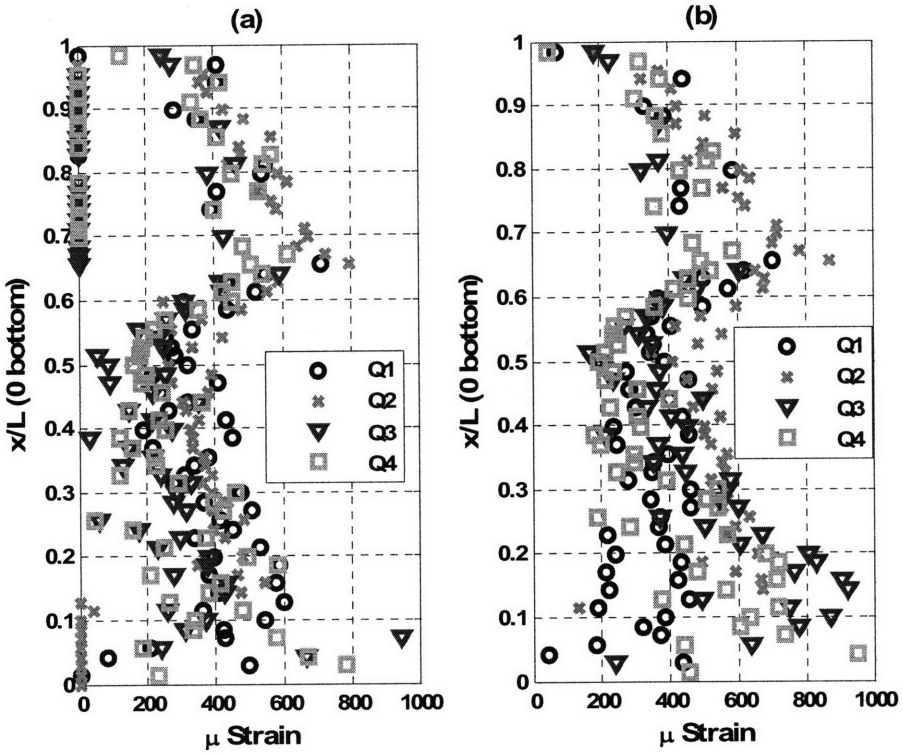

Figure 23 – (a) The zero for this test has to be removed from the temporal mean of the measured experimental strain, shown in (b).

4.3.4.3 Step 3 – Remove strain due to axial forces developed during the experiment

Once the Zero has been removed from the measured temporal mean strains, what remains are the static strains developed only during the experiment as shown in Figure 24(a). However, these are both due to static bending of the pipe and mean tension developed during the experiments. The effect of the mean tensions can be seen in Figure 24(a) where opposite quadrants (Q1&Q3) and (Q2&Q4), which should have bending strain components of same magnitudes but of opposite signs, seem to be shifted from there zero-mean value. The mean strain can be calculated using any of the two pairs of opposite sensors, (Q1&Q3) and (Q2&Q4). Both pairs were used to estimate the spatial distribution of the strain due to mean tension developed during the experiments, as shown in Figure 24 (b). The final mean strain was an average of the strains obtained from both pairs where available (Equation(4.11)), or the value of the strain for the pair that was available.

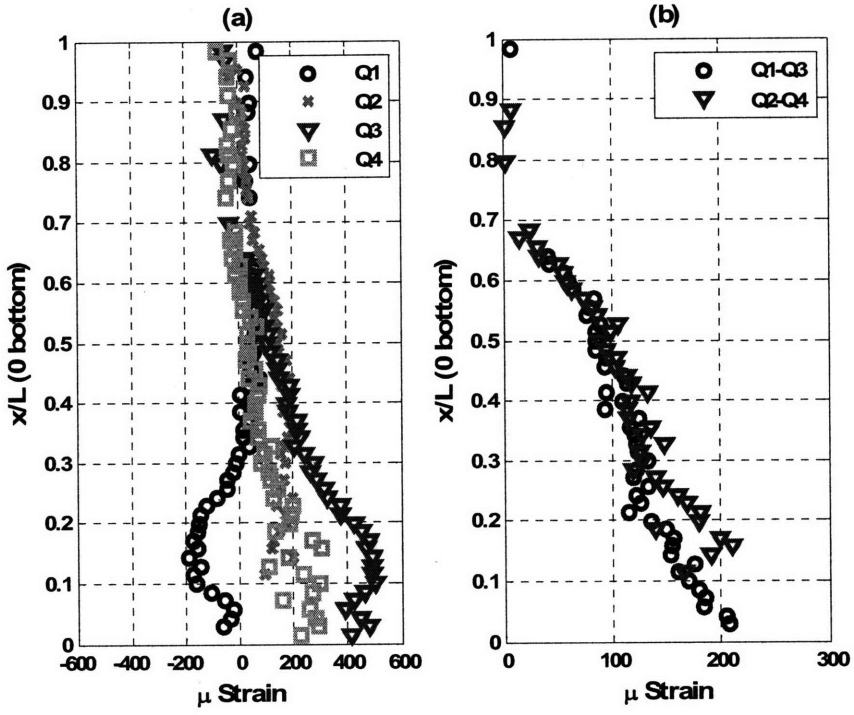

Figure 24 –(a) The (measured–Zero) strain for each fiber includes the static bending strain and changes in local mean tension during tow (b) fiber pairs (Q1,Q3) and fiber pairs (Q2,Q4) are used to estimate mean tension during tow.

4.3.4.4 Step 4 – Calculate mean strain due to bending

Once the axial tension has been removed, what remains is the strain due to bending in each of the fibers (Equation(4.12)). The total strain due to bending can now be calculated using the square root-of–the-sum-of-the-squares for orthogonal sensors at every spatial location (Equation(4.13)). This process is shown in Figure 25, which shows the final strains for two pairs and the final values of the mean strain. This strain can now be converted to force using Equation(4.4). The spatial distribution of the mean force acting on the pipe is then converted to drag coefficients using Equation(4.5).

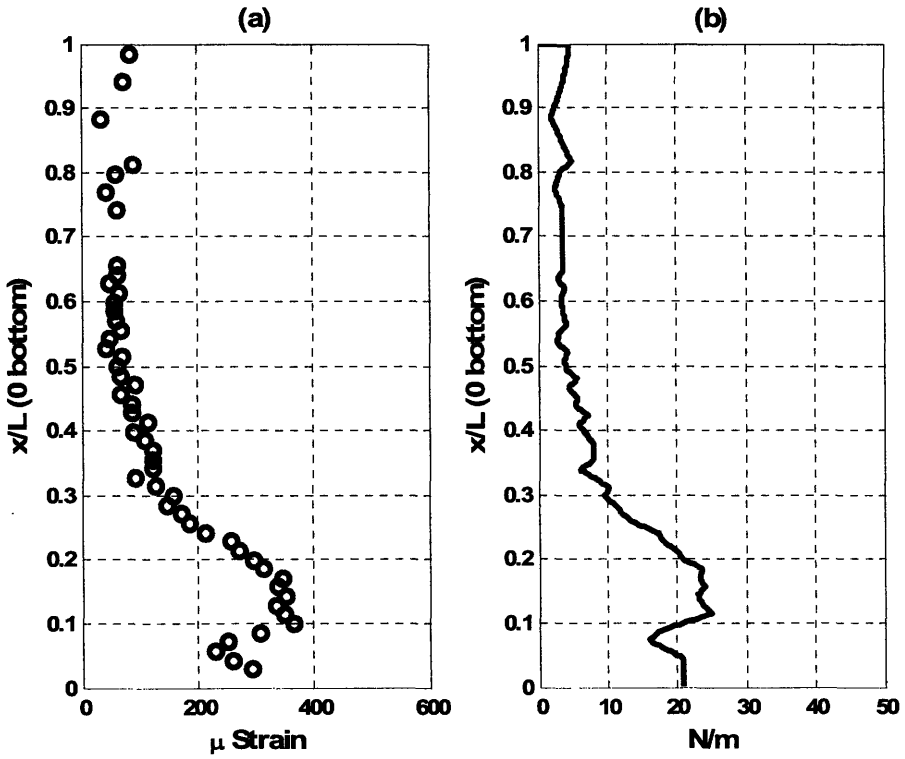

Figure 25 – (a) The total static bending strain of the pipe and (b) the associated drag force.

4.3.4.5 Step 5 – Estimate local distribution of drag force

The final step in the process is converting the local mean drag force calculations into local drag coefficients using Equation(4.5). The correct estimation of the normal incident velocity is essential for the correct estimation of the drag force. The method of estimating the normal incident velocity has been discussed in previous chapters. Figure 26 shows the axial distribution of the drag force per unit length, the normal incident velocity profile and the final local mean drag estimates.

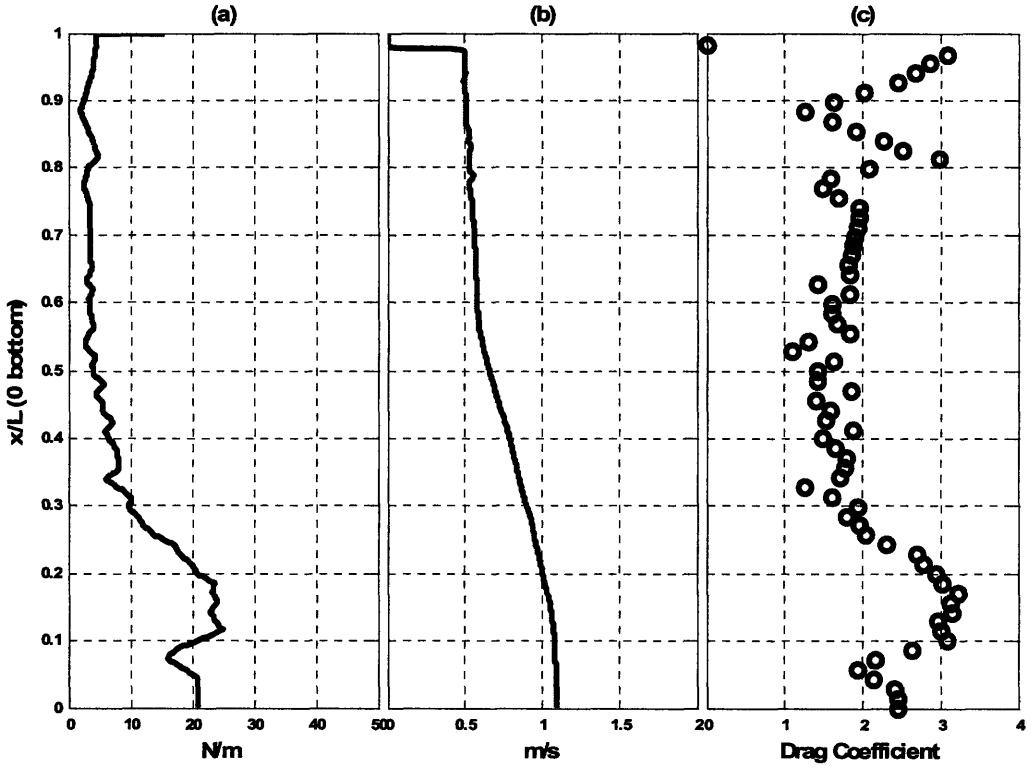

Figure 26 – The distribution of local drag force, shown in (a), is used in conjunction with the normal incident velocity profile, shown in (b), and the properties of the pipe to estimate the local drag coefficient along the length of the pipe

4.3.4.6 Error estimate and discussion

The standard deviation of the drag calculations can be estimated using Equation(4.15). Figure 27 shows the results for local C_D for case 20061023205043. The red lines indicate $C_D \pm 1$ standard deviation of the error. The large error bands towards the top of the pipe show the uncertainty in the calculated C_D in this region. This region

corresponds to low flow velocity (due to large incidence angles) and small values of static bending strains (Figure 25). It is best to neglect the results in this region (z/L=0.4 to z/L=1.0).

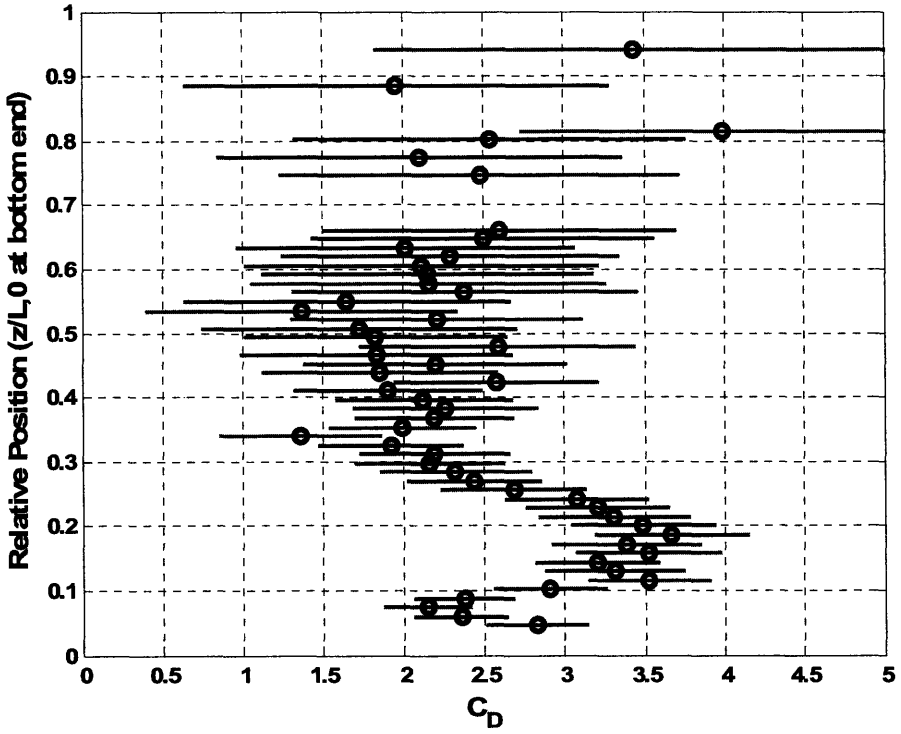

Figure 27 – The spatial distribution of local C_D for Test-20061023205043. The red lines indicate $C_D \pm 1$ standard deviation of the error.

Figure 28 shows the variation of the three error components (see formulation of standard deviation of drag in Equation(4.15)) along the length of the pipe. The largest contribution to the error in the local C_D comes from the error in measuring the mean bending strain. This is because the spatial variation in mean bending strain is large (50 μStrain to 400 μStrain as seen in Figure 25) while the velocity varies by only a factor of 2 or 3 and the tension is assumed constant over the entire length. Therefore the errors due to noise in the system, though small compared to the maximum observed static bending strain, become large in areas were the static bending strain is small and cause large error in C_D in these locations. This is the primary reason why the region (z/L=0.4 to z/L=1.0) has large error in this particular example and should be neglected. A secondary reason is the small normal incidence velocities towards the top of the pipe. Since the variability in the measured ADCP velocity does not change substantially over the length

of the pipe, the error in velocity contributes more to the error in estimated C_D towards the top of the pipe (where the velocity is lower).

The analysis shows that for the Gulf Stream experiments, regions that have small static bending strains and small velocities will have large error in the estimated local C_D values. This is seen in the large variations in the C_D estimates in these region and these values should be neglected. Luckily, the areas of small static bending strains are regions away from the primary VIV response and consequently not very important for the understanding of VIV.

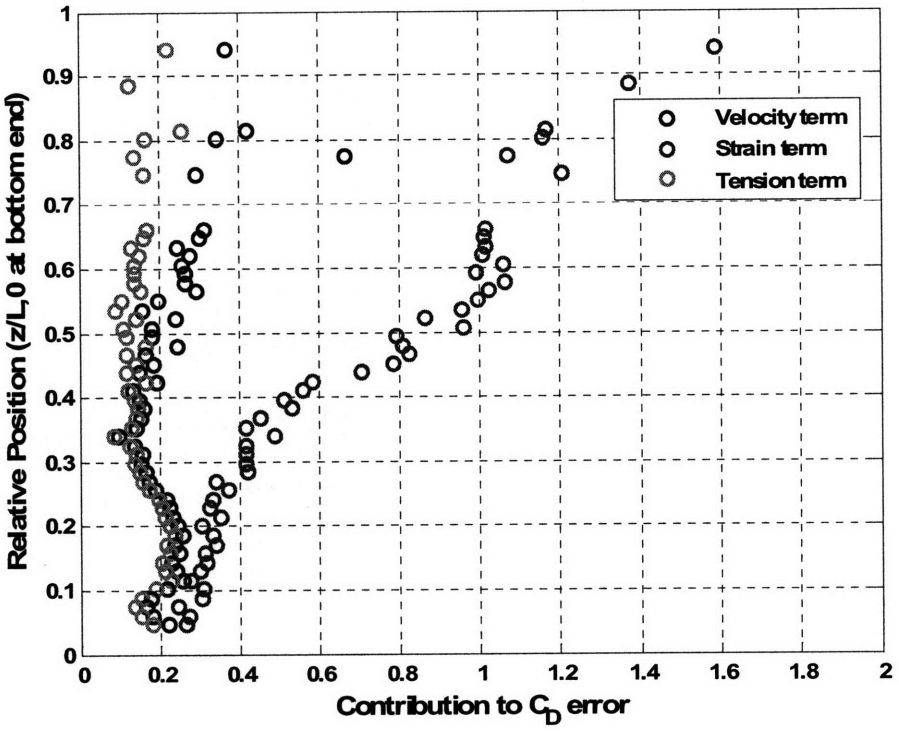

Figure 28 – The contribution of the three parameters to the standard deviation of C_D shows that the main cause of the large error in C_D towards the top end of the pipe is the error in strain measurements.

4.3.5 Proof of Concept

One of the configurations during the Second Gulf Stream experiments consisted of the partial coverage with fairings, donated by AIMS International, placed on the bottom 40% of the pipe. The schematic in Figure 29 shows this configuration. Also shown is a picture of the fairing that was used during the experiments. This configuration is

interesting because fairings are known to have very low drag coefficients. Therefore, this condition offers a sudden transition of drag coefficient, from that of vibrating pipes (~ 2.5) to that of a pipe with fairings (~1.0). Such sharp changes in drag coefficient are ideal to test the methodology for calculating local drag coefficients. Further, these fairings had been tested in the laboratory by AIMS, providing values that could be used to check the estimates obtained from the second Gulf Stream field estimates.

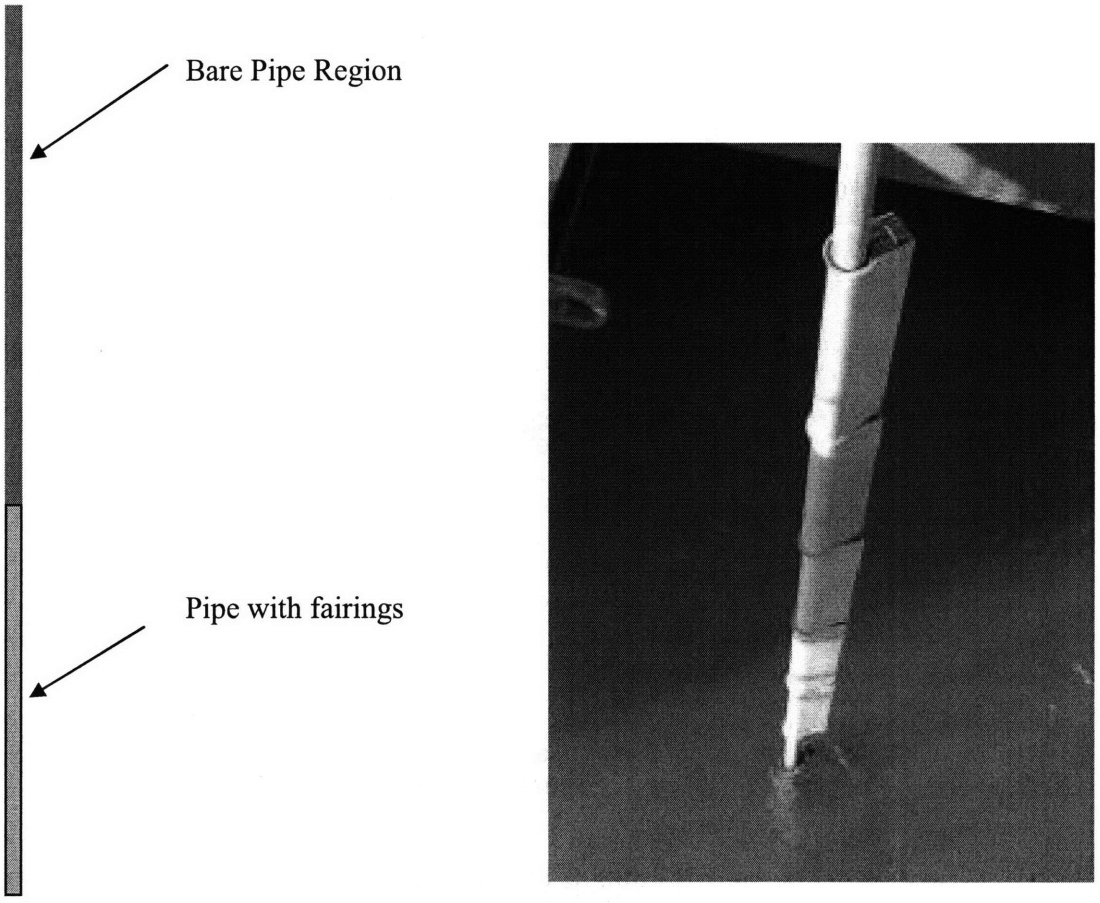

Figure 29 - (a) A schematic showing the 40% fairings setup. (b) A picture of the fairings during the experiments

The drag coefficients were calculated using the method described earlier for four different cases. Figure 30 shows the current profiles for the four cases that were analyzed. The velocities range from 0.7 m/s to 1.4 m/s. Moreover, the profiles cover the

range of velocities tested, and vary from constant velocities. The current directional variation for all the cases was small.

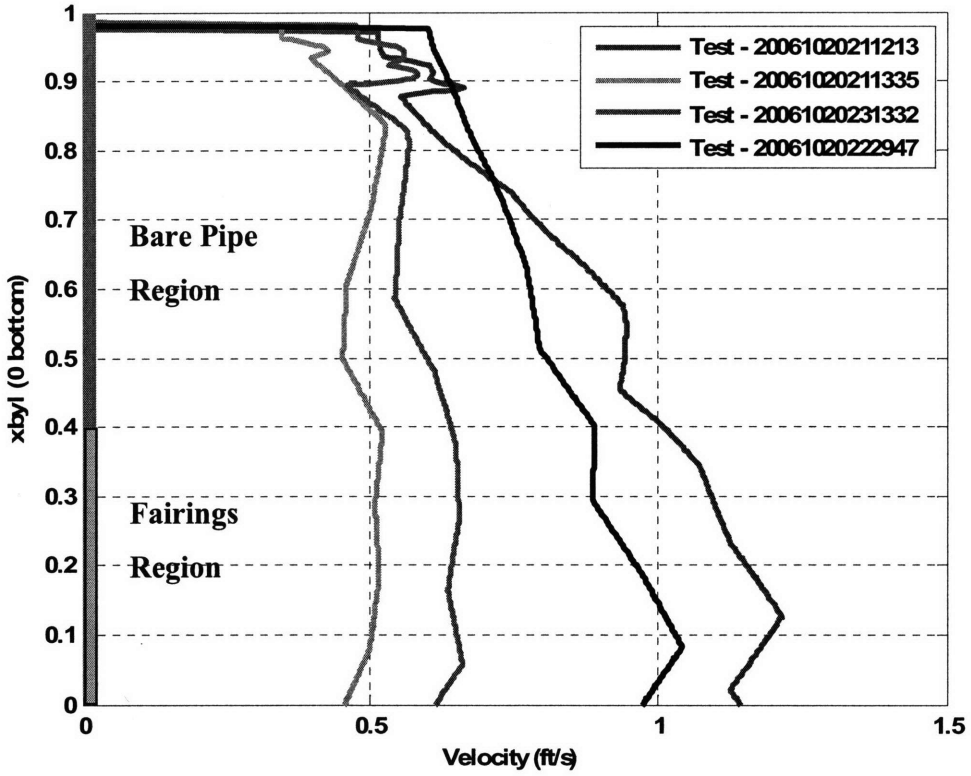

Figure 30 – Four different velocity profiles for the 40% fairing cases. The Fairings were attached at the end of the pipe (as shown in the figure). The profiles were chosen to cover the range of velocities tested during the experiments.

The drag coefficients for four cases are shown in Figure 31. The dramatic change in drag coefficients at the transition from bare pipe to pipe with fairings is captured accurately by the method. This validates the accuracy of this method in calculating the local drag coefficients for a pipe undergoing VIV. The region from z/L=0.75 to z/L=1.0 shows large oscillations in drag coefficients. This is to be expected because of the large error bounds of the calculation in this region. The drag forces are small and many sensors were not functioning in this region. Further, the value of the normal incident velocity is reduced significantly in this region due the large inclination angles of the pipe towards the top end. For all these reasons, significant errors are to be expected in the

local C_D estimates at the top end of the pipe. It should however be noted that this region of the pipe is furthest from the region of interest (the faired region in these cases and the "power-in" regions in bare pipe cases), where the results are not significantly affected by the errors in drag estimation in the top 25% of the pipe.

The sharp change in the drag coefficients indicates that the calculated drag coefficients are not very sensitive to traveling wave vibration in the region with fairings.

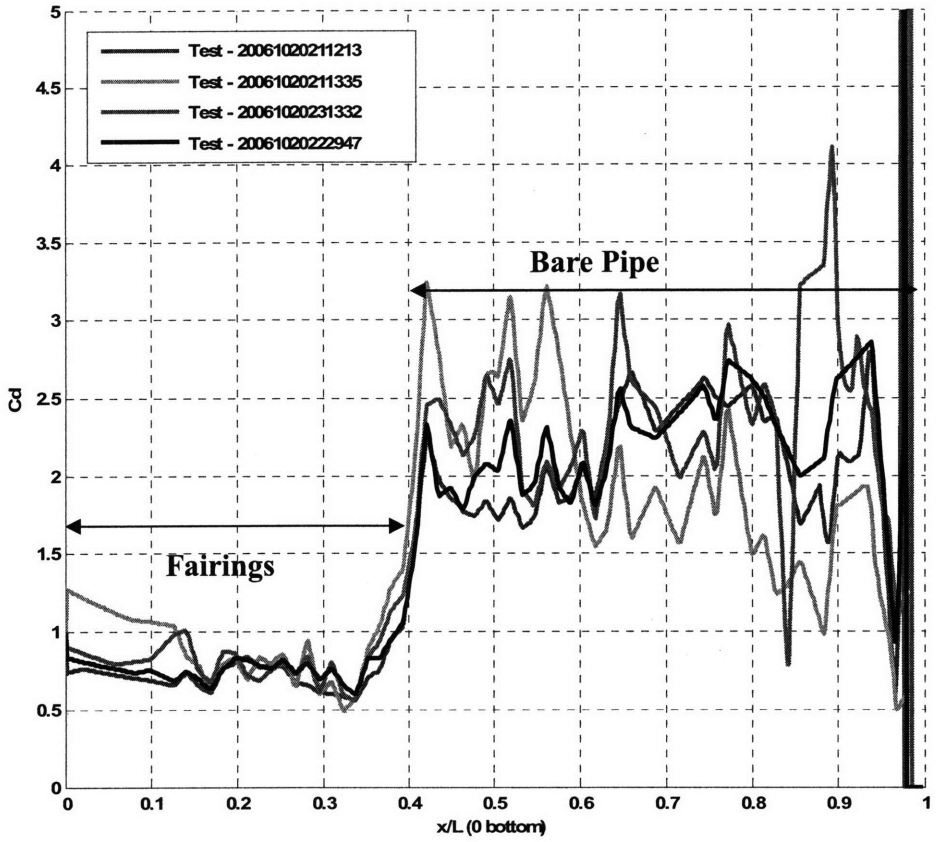

Figure 31 – C_D variation along the length of the pipe for four Gulf Stream experiments with fairing covering the bottom 40% of the pipe.

4.3.6 Drag Coefficients for bare pipe in Shear Currents

The mean drag coefficients predicted for the 40% fairing cases from the second Gulf Stream experiments provide confidence in the method developed for predicting local drag coefficients from strain measurements. Therefore a more ambitious goal, that of predicting the variation of local drag coefficients in sheared currents, can now be attempted. As indicated in the earlier sections, various researchers have studied the variation of drag with *Vr* and *A/D* using lab and field experiments. However, the more difficult task of measuring the variation of local drag coefficients along a pipe in sheared flows has never been studied, because of the lack of strain gauge data from many closely spaced sensors.

The bare pipe Test 20061023203818 was chosen to study in detail the variation of drag coefficients along the length of the pipe. This test had a maximum current velocity of 3.6 ft/s and the current profile and pipe inclination angle combine to produce a large shear in the incident current profile.

The axial distribution of drag coefficient for the test is shown in the Figure 32. Three regions of drag are clearly visible. They can now be described in terms of reduced velocity as :-

Region I – A region of reduced velocity, around 5.2 to 6.8 in this case, where the drag coefficient is greatly amplified.

Region II – A region of reduced velocity lower than 5.2 where the drag coefficient is between 1.5 and 2.0

Region III – A region of reduced velocity higher than 6.8 where the drag coefficient is between 2.0 and 2.5.

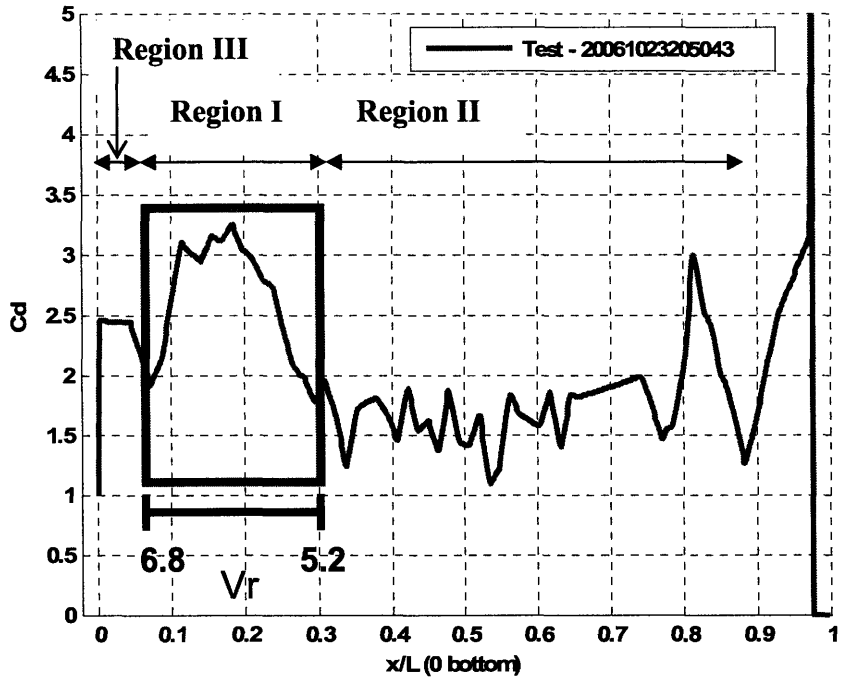

Figure 32 – Local drag coefficient along the length of a bare pipe in a typical Gulf Stream case.

The drag coefficients in region I are plotted against reduced velocity in Figure **33**(a). This variation of drag coefficients with reduced velocity is very similar to the variation seen in a plot developed in 1982 by Overvik (from [16]), shown in Figure **33**(b), using free vibration experiments with spring mounted rigid cylinders. It is extraordinary that even though the two sets of experiments are so different, the Gulf Stream experiments are with flexible cylinders vibrating at high mode numbers with the reduced velocity changing due to the shear in the current while the Overvik experiments are laboratory experiments where the velocity was varied to change reduced velocity, the patterns of drag variation with reduced velocity is similar. There are differences in the magnitude of the drag coefficients; the Gulf Stream experiments have a peak drag coefficient of 3.2 while the Overvik experiments show a peak drag of 2.5. This difference could be attributed to the limitation in the Overvik experiments whereby only cross-flow oscillations were allowed. Recent work by Jauvtis and Williamson [6] has indicated that drag coefficients greater that 3.0 are observed when both in-line and cross-flow degrees

of freedom are allowed in free oscillation laboratory experiments with spring mounted rigid cylinders.

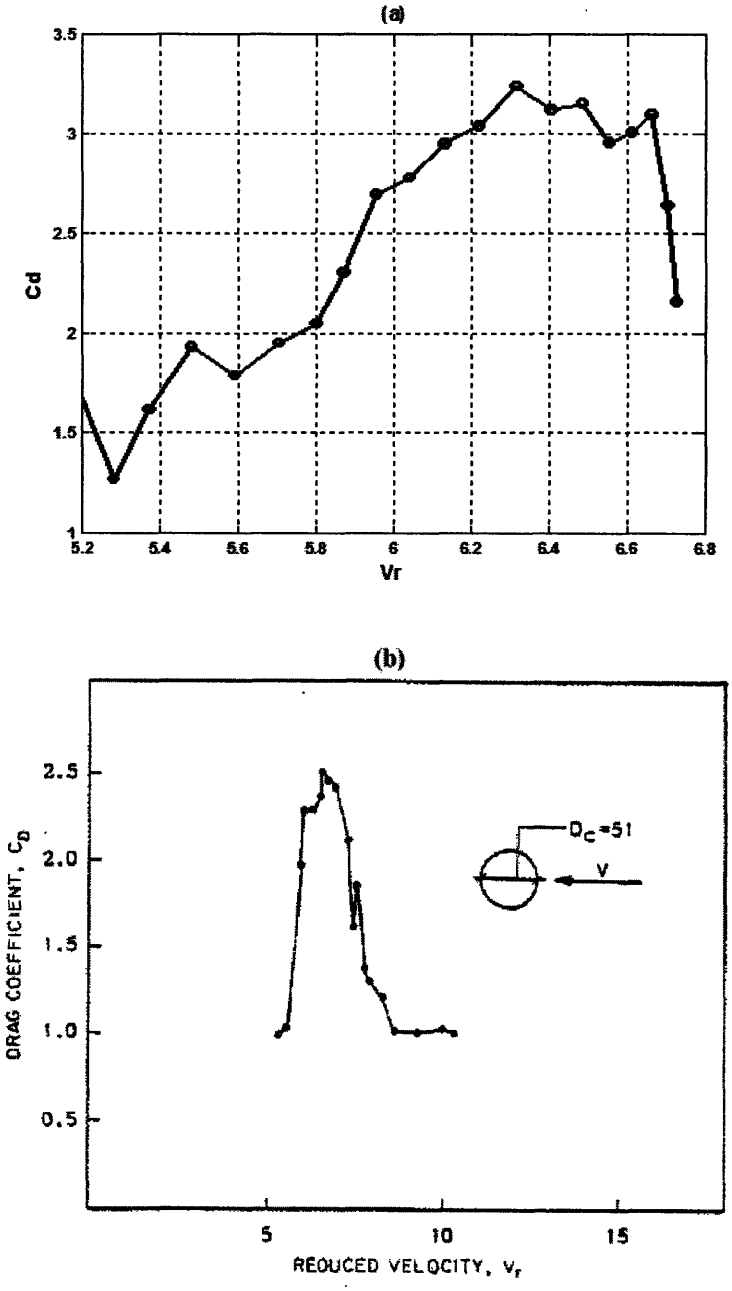

Figure 33 – Drag coefficient plotted against reduced velocity in (a) for Test – 20061023205043 from the Gulf Stream experiments where the reduced velocity changed due to the shear in the current (b) free vibration experiments with a 1 degree of freedom rigid cylinder by Overvik (1982) (taken from [16]).

Similar variations as seen in Test 20061023205043 discussed above were seen when other bare pipe cases from the second Gulf Stream experiments were studied. Figure 34 shows the local mean drag coefficients along the length of the pipe and the regions of drag amplification are seen in all the cases. The drag coefficients away from the maximum velocity, between z/L=0.75 and z/L=1.0 should be ignored because of the higher possibility of error, as explained earlier. Moreover, these regions are away from the reduced velocities of interest for the VIV problem. Again, the drag can be separated into three zones a) A region in reduced velocity where the drag force is greatly amplified and drag coefficients of 3 or more are observed. b) For reduced velocities greater than in region a, the drag coefficient seems to be between 2.0 and 2.5. c) For reduced velocities smaller than in region a, the drag coefficients are between 1.5 and 2.0.

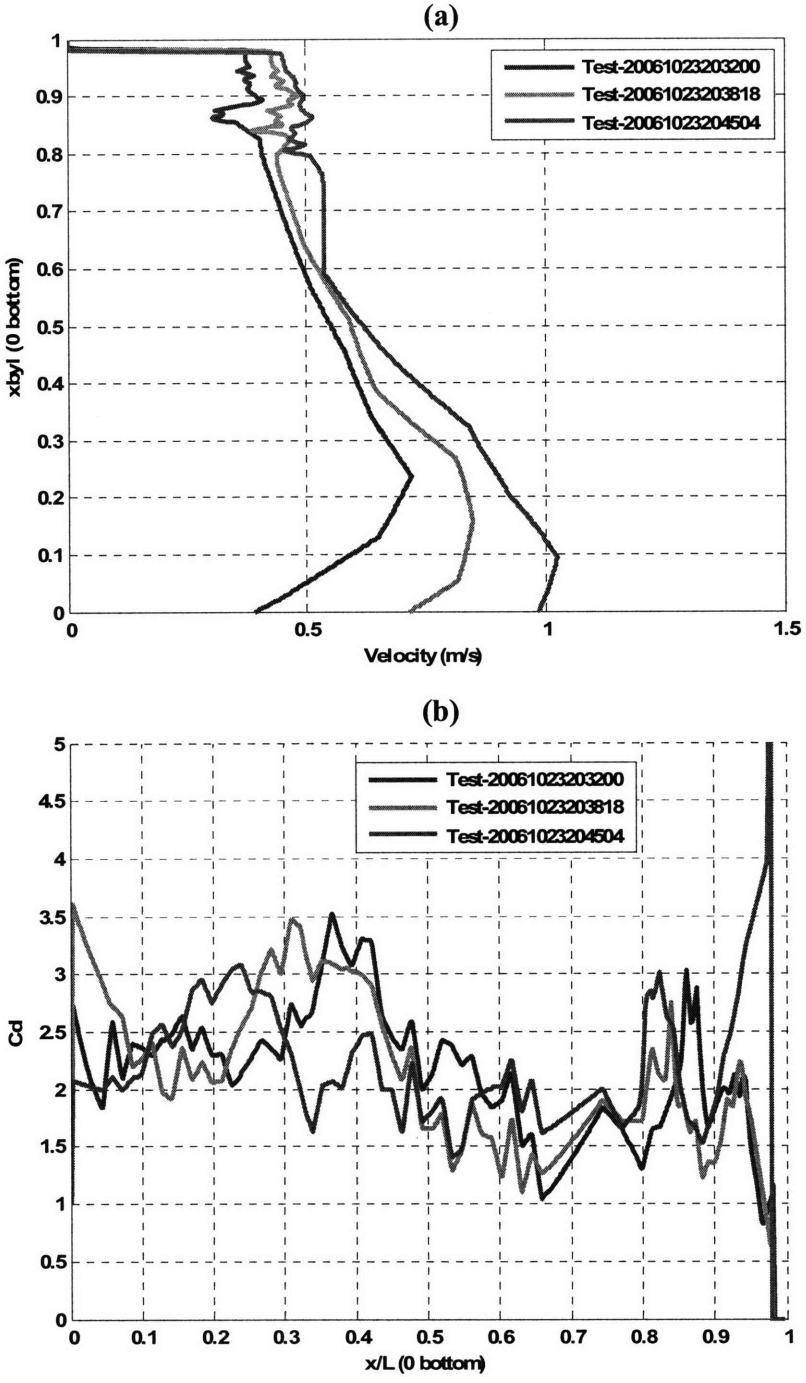

Figure 34 - (a) The velocity profile and (b) the associated local drag coefficients for three bare pipe tests from the second Gulf Stream experiments. The region of pronounced drag is clearly seen in all the experiments.

Drag variations calculated using data from high mode number experiments with a 38m long pipe in linearly sheared currents corroborates the observations from the second Gulf Stream experiments. These experiments, performed by NDP at Marintek in Trondhiem (see [52]), also used strain gauges to measure VIV related vibrations, making it possible to apply the procedure developed earlier. Moreover, since the experiments were carried out in more controlled environments, the current velocity measurements during the experiments were more reliable than those obtained from ADCP measurements during the Gulf Stream experiments, resulting in better estimates of local reduced velocity. Figure 35(a) shows the variation of drag coefficient along the length of the test pipe for two tests. The axial variation of the local drag coefficient is similar to the Gulf stream experiments discussed earlier. Further, when the local drag coefficient is plotted against local reduced velocity in Figure 35(b), the variation is remarkably similar to Figure **33**. The drag coefficient peaks around Vr=6.0. As the NDP experiments were performed on a shorter pipe (38 m) than the Miami experiments, there were significant standing waves. However, the mean drag coefficients were not affected by the standing waves.

An error analysis was performed using the method described earlier (Equation (4.15)). The error in C_D for Tests – 2450 and 2490 are shown in Figure 36. However, since there were no "Zero" files available for the NDP experiments, the error in C_D due to the "noise" in strain measurements is neglected.

The error is large away from the region of maximum velocity (and the "power-in" region). This trend is similar to what was observed in the Gulf Stream experiments. The small error-bounds in the regions of maximum local drag estimates provide confidence in the estimated local C_D values.

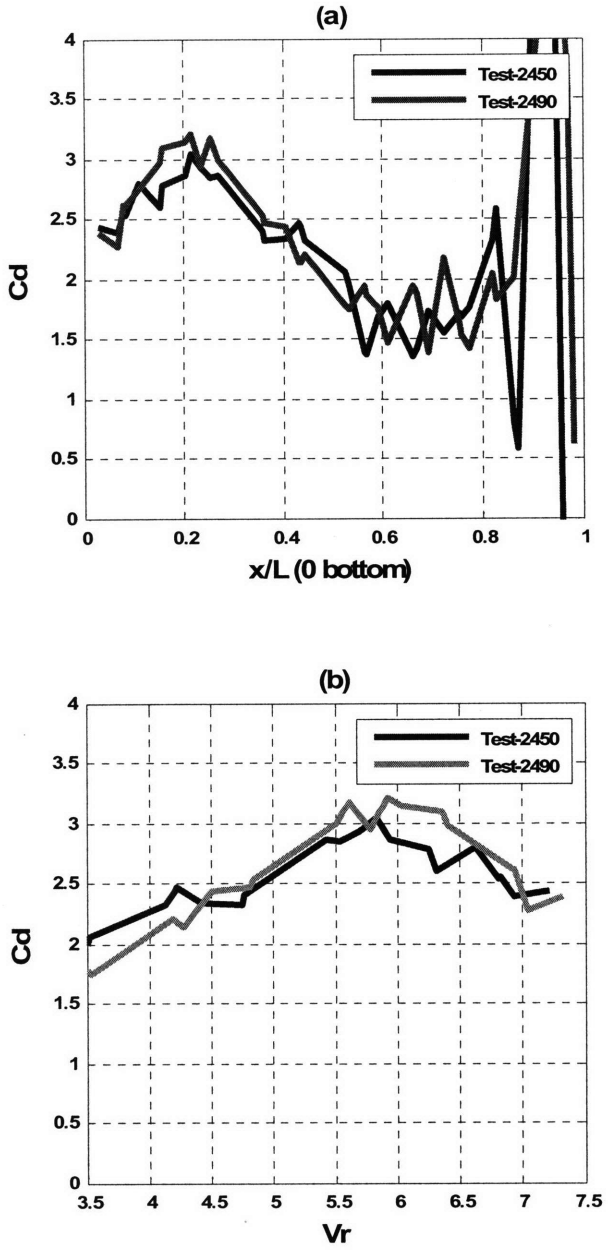

Figure 35 – The variation of local drag coefficient (a) along the axial length of the pipe and (b) with local reduced velocity. The results are for Test-2450 and Test-2490 from the NDP experiments. Bottom indicates the end where the velocity was high.

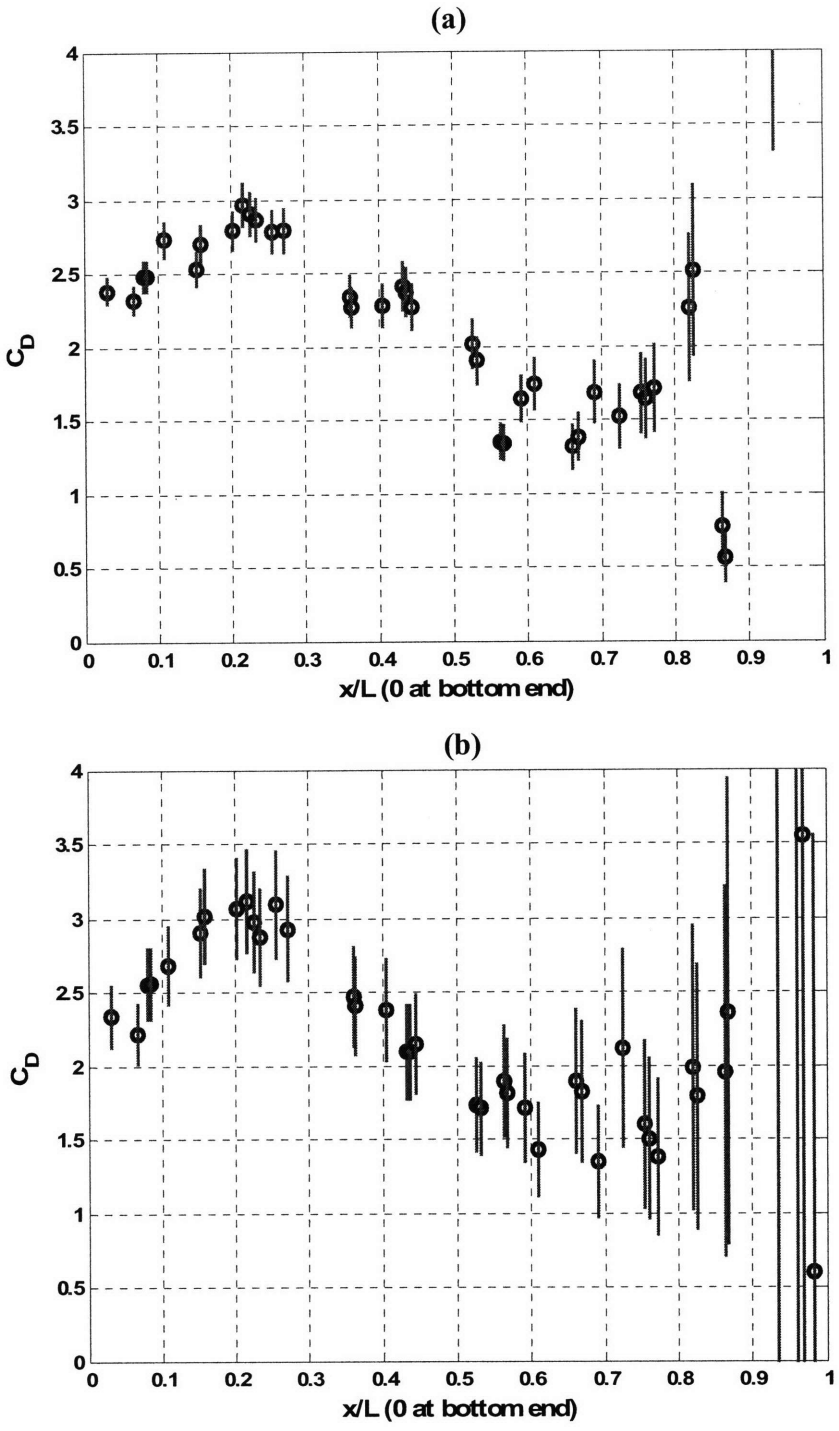

Figure 36 – Local drag coefficients with error bars (shown with red lines) (a) Test-2450 (b) Test-2490 from the NDP experiments. Bottom indicates the end where the velocity was high.

4.4 Spatially averaged Drag coefficients

Even though the drag coefficients vary with reduced velocity, the mean drag coefficient for the whole pipe is close to the observed values in the Lake Seneca experiments. Figure 37 shows the mean drag coefficients obtained for tests conducted during the Miami experiments. Each value is for a particular test and was obtained by spatially averaging the local drag coefficients obtained for that test using the analysis explained in the previous sections. This mean drag coefficients are close to those predicted by drag formula of Vandiver et. al.

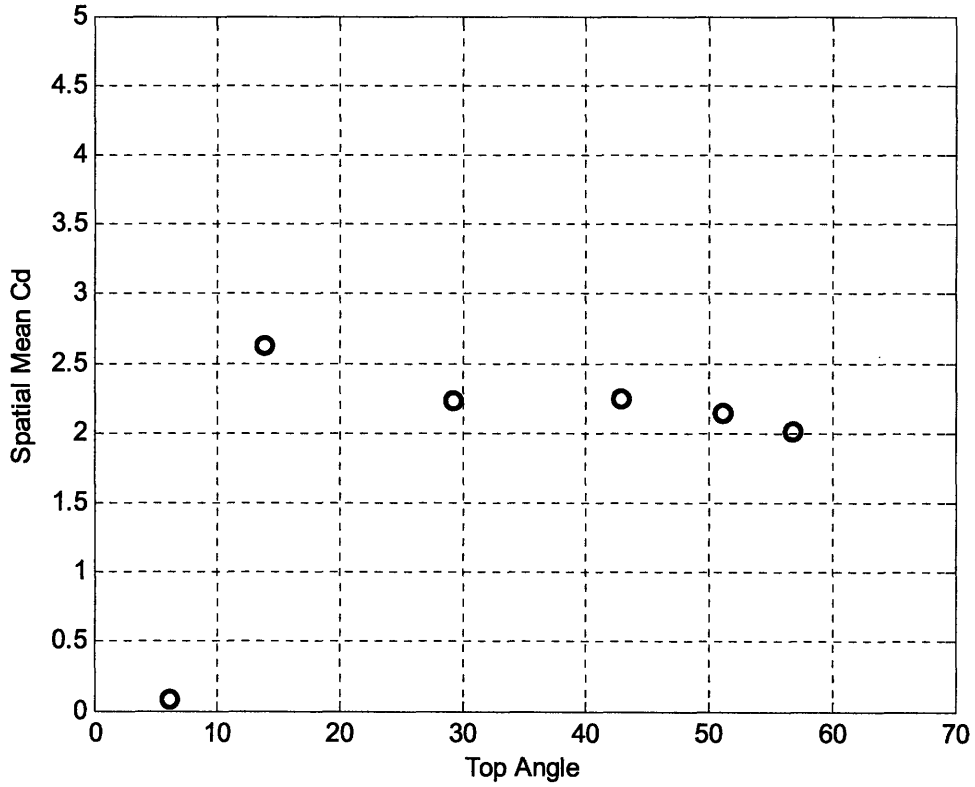

Figure 37-Spatially averaged drag coefficients for bare pipe tests performed during the Gulf Stream experiments have values similar to those observed in the Lake Seneca experiments.

4.5 Drag Coefficients of Strakes and Fairings

The offshore oil and gas industry uses suppression devices like strakes and fairings on risers to mitigate the effects of VIV. It is therefore important for them to understand the drag implications of using mitigation devices.

4.5.1 Strakes

Straked tests were performed both at Lake Seneca and the Gulf Stream experiments. The Lake Seneca experiments were almost uniform current while the Gulf Stream experiments had various degrees of shear in them. The spatially averaged drag coefficients computed for the Lake Seneca experiments used the same method for the bare pipe cases. These methods are explained in detail at the beginning of this chapter. The results from this analysis are plotted in Figure 38.

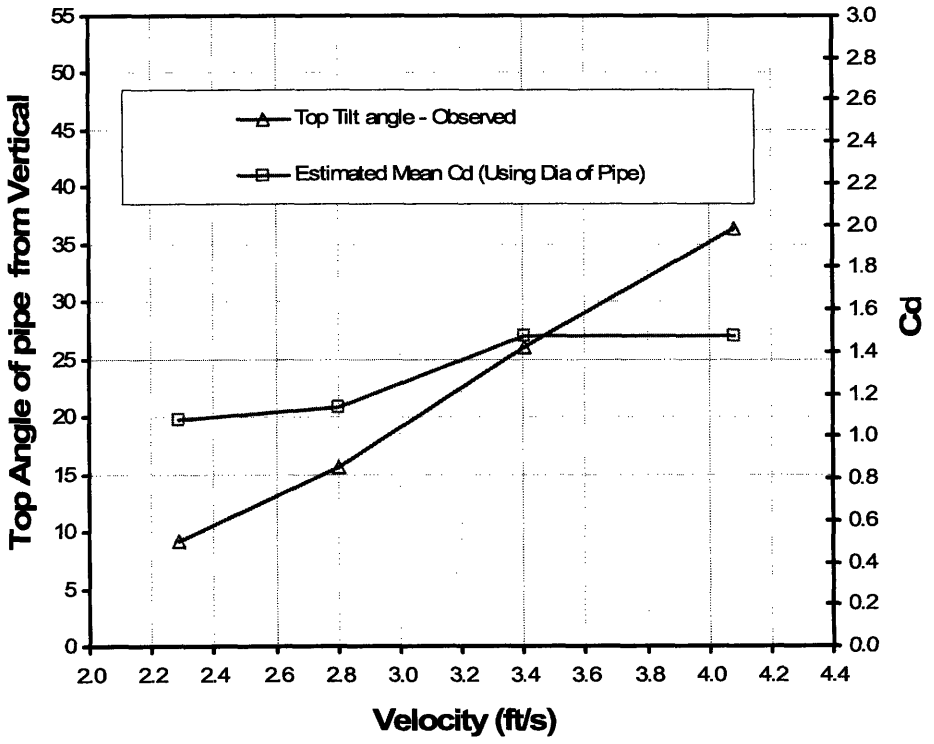

Figure 38 – The drag coefficients for strakes used in the Lake Seneca experiments, 0.25 D height and 17.5 D pitch, were found to be between 1.1 and 1.5

The drag coefficients are in the range of 1.1 to 1.5, which is similar to results published by manufacturer, AIMS International.

An objective of the Gulf Stream experiments was to investigate the changes in spatially averaged drag coefficients when the percentage of strake coverage on the pipe was varied. The fully staked condition was equivalent to 84% coverage because real risers have practical limitations to the amount of riser coverage possible. Other coverage

amounts tested were 62% coverage and 50% coverage. A schematic of the coverage pattern is shown in Figure 39.

The mean drag coefficients for the straked cases are shown in Figure 40. Interestingly, the spatially averaged drag coefficients increase from around 1.5 (or lower) to more than 3.0 as the peak velocity of the tests increase (indicated by the increase in top angle). This trend is observed in both the 50% and 62% pipe coverage cases. Moreover, there is not a lot of difference in spatially averaged drag between the 50% coverage cases and the 62% coverage cases, implying that both are effective in mitigating VIV. The reason for the increase in drag coefficients with inclination angle is not clear but may be due to changes in flow around the strakes at non-perpendicular incidence angles.

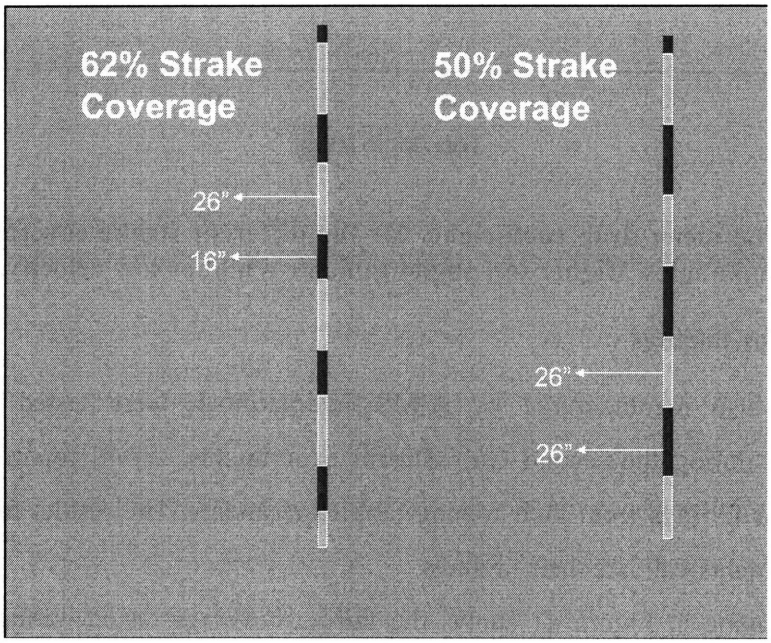

Figure 39- Two different stake coverages were tested during the second Gulf Stream experiments

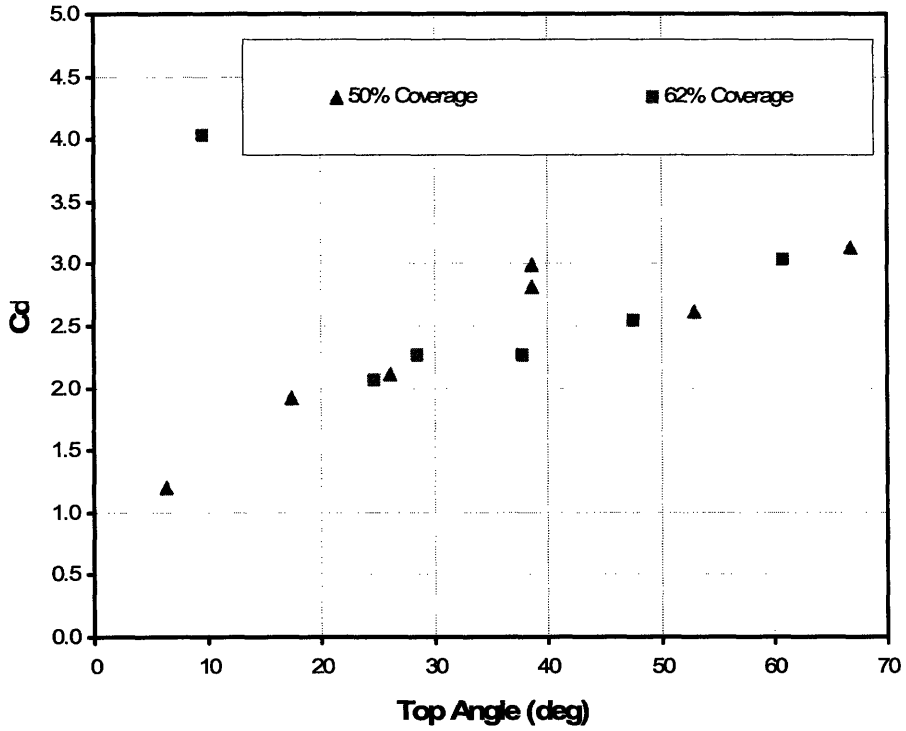

Figure 40 - The mean drag coefficients for the different strake coverage amounts for different top angles. Higher top angles indicate a higher tow velocity.

4.5.2 Drag for fairings

Fairings, also manufactured by AIMS International, were tested in different configurations during the second Gulf Stream experiments. AIMS reported low drag coefficients for fairings from their towing tank experiments. The results from the Gulf Stream experiments validate their findings.

The schematic in Figure 41 shows the fairing coverage tested during the second Gulf Stream experiments.

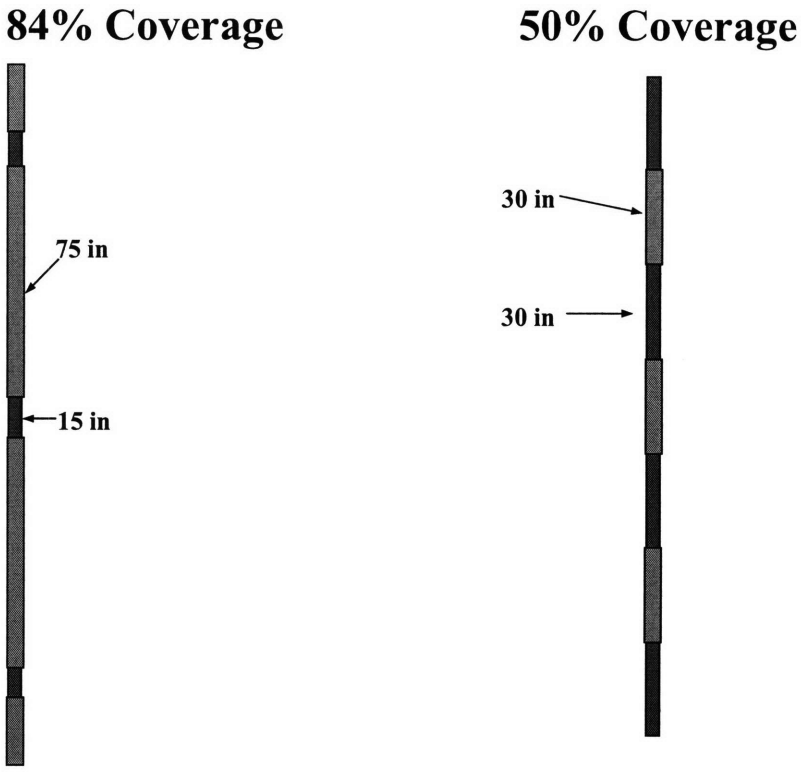

Figure 41 - Two different amounts of fairing coverage were tested during the second Gulf Stream experiments

The spatially averaged drag coefficients for the fairing configurations are shown in Figure 42. Neglecting the cases which have small top angles (low speed cases) and are prone to large error in the calculations, the mean drag coefficients do not vary with increasing velocity. This indicates that, contrary to the strakes, the drag coefficients for fairings are not greatly affected by the angle made by the incident velocity to the pipe. The mean drag coefficient increased slightly to 1.5 when the percentage of fairing coverage was reduced from 84% to 50%.

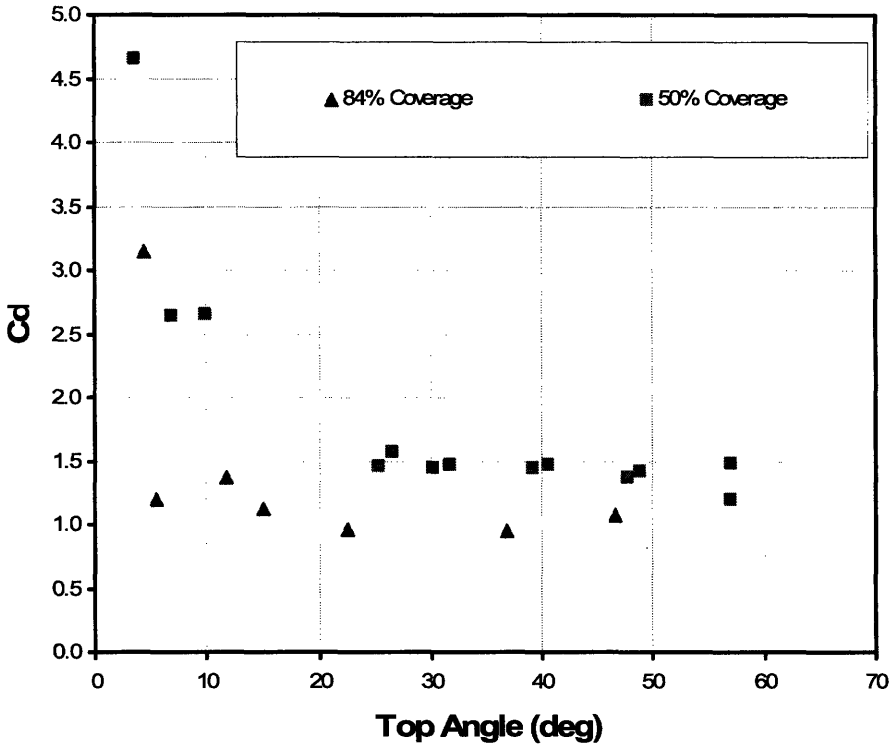

Figure 42 – The mean drag coefficients for the different fairing coverage amounts for different top angles. Higher top angles indicate a higher tow velocity.

4.6 Summary and Conclusions

Though drag coefficients and drag amplification due to VIV have been studied for many years, only recently has data been available that can correlate the steady-state local wake dynamics to the measured local drag coefficient of the pipe. Such experiments have been done in the laboratory with rigid and flexible cylinders. Further, this work presents for the first time, local drag coefficients have been extracted for field experiments using strain measurements. Together, they provide useful insight into how drag varies with reduced velocity and with fairing and strake coverage.

For many years, empirical formulations have predicted drag amplification due to VIV using the response amplitude of the pipe undergoing VIV. These formulations have been based on data obtained in the laboratory using rigid cylinder tests or field experiments performed in uniform current profiles. In these cases the response reflects the wake dynamics and the drag coefficient can be directly correlated to the response

amplitude. With long flexible pipes in sheared currents, the response is dominated by traveling waves. In such a situation, the response amplitude may not be a reflection of the wake because of vibration energy being transferred from one part of the pipe to another by traveling waves.

The Miami experiments provided one of the first opportunities to study local drag coefficients in the presence of traveling waves. The results indicate that local drag coefficients are strongly dependent on reduced velocity, and hence the wake dynamics, and not as much on the response amplitude. Indeed, when the local drag coefficients were calculated for tests carried out by NDP at Marintek, the results were remarkably similar to those obtained from the second Gulf Stream experiments. This was in spite of standing waves generated in these tests due to the relative short length of the test pipe.

An analysis of the source and magnitude of error in the estimated local C_D showed that the proposed method works best in the regions of the pipe where the static bending strain is the largest. The error is also large in regions of small incident velocity.

These results indicate that the currently used drag prediction methodologies, which mostly depend on response amplitude, will have to be modified so that the strong dependence of local drag on reduced velocity is correctly captured.

The Gulf Stream experiments also support laboratory test results that fairings (at least the type tested) have a lower drag coefficient than strakes. Moreover, it was found that the drag coefficient of strakes increased as the incident angle of the flow increased as shown in Figure 40. This was not the case for fairings, where the drag coefficient was found to be independent of the angle made by the pipe to the incident flow (Figure 42).

5. The Higher Harmonics in VIV

Research on the higher harmonics in VIV response is relatively new and few definitive results exist about them. The research presented in this chapter is one of the first studies on the higher harmonic strain response in flexible pipes responding at high mode numbers. As a result, several new methods were developed to study the higher harmonic strain response and better understand their properties. Since these methods are not commonly used, it is helpful to start with the main conclusions from this chapter so that the reasons behind the methods are easily understood when they are introduced.

5.1 Main Conclusions

- The maximum RMS strain response for all the higher harmonics were observed in regions dominated by traveling wave response and not near the ends of the pipe, where the response is dominated by standing waves.
- In a particular test, the maximum RMS strain response in the 2^{nd} harmonic was observed when the pipe responded in 'figure c' displacement patterns at that location while the maximum RMS strain 3^{rd} harmonic response was observed when the pipe responded in a 'figure 8'and 'figure c'.
- A large 1^{st} harmonic RMS response is likely in experiments when a large 2^{nd} harmonic RMS response is also present. However, maximum 1^{st} harmonic response does not occur at the same location as the maximum 2^{nd} harmonic response.
- A large 3^{rd} harmonic RMS response is likely when a high 2^{nd} harmonic RMS response is also present. Again, the maximum 3^{rd} harmonic response does not occur at the same location as the maximum 2^{nd} harmonic response.
- A large 2^{nd} harmonic RMS response is not required for a large 4^{th} harmonic RMS response, even thought they both occur in the in-line direction. Large 4^{th} harmonic RMS response is likely in tests that have a large 5^{th} harmonic response.
- In a particular test on average, the maximum observed magnitude of the 3^{rd} harmonic RMS strain response is likely to be 1.25 times the maximum observed magnitude of the 1^{st} harmonic RMS strain.

- In a test on average, the maximum observed magnitude of the 5th harmonic RMS strain response is likely to be 0.57 times the maximum observed magnitude of the 1st harmonic RMS strain.

5.2 Introduction

Most researchers and engineers associate VIV with displacement response in the cross-flow direction at the fundamental VIV frequency, which corresponds to the Strouhal frequency. However, vibrations at the fundamental VIV frequency are accompanied by vibrations at multiples of the fundamental VIV frequency. These higher harmonics were noticed in Power Spectral Density (PSD) plots of measured acceleration data from early VIV experiments and subsequent research showed that the odd harmonics, 3rd, 5th etc., occur in the cross-flow direction while the even harmonics, 2nd,4th etc., occur in the in-line direction. Though the displacement response of the pipe undergoing VIV is dominated by the 1st and the 2nd harmonic, the importance of the higher harmonics are amplified in measured acceleration and strain response time histories. Figure 43 explains this amplification using the 3rd harmonic as an example.

5.3 Experimental observations of the higher harmonics

Though early research showed the 2nd harmonic forcing to be the in-line component of the same hydrodynamic force that caused the vibrations at the fundamental VIV frequency, the in-line response at the 2nd harmonic was considered less important than the cross-flow response at the fundamental VIV frequency. This was primarily because the observed in-line displacement amplitude was less than the displacement amplitude in the cross-flow direction. In the late 1990's, it became clear that the displacement in the in-line direction, though not as large as the cross-flow direction, was significant. Further, extensive research on the 2nd harmonic revealed important properties about VIV motion that only happen when in-line motion was allowed. In laboratory experiments using rigid cylinders, researchers found that the amplitude of VIV displacement response in the cross-flow direction increased when in-line motion was allowed [6].

Consider a VIV travelling wave displacement response in the cross-flow direction comprising of the 1st and 3rd harmonics

$$y(t) = A_{x1}Sin(\omega_{x1}t + k_{x1}z) + A_{x3}Sin(3\omega_{x1}t + k_{x3}z) \quad ; \quad \frac{(\text{Displacement Amplitude})_{3x}}{(\text{Displacement Amplitude})_{1x}} = \frac{A_{x3}}{A_{x1}}$$

Acceleration response becomes

$$\ddot{y}(t) = A_{x1}(w_{x1})^2 Sin(\omega_{x1}t + k_{x1}z) + A_{x3}(3\omega_{x1})^2 Sin(3\omega_{x1}t + k_{x3}z); \frac{(\text{Acc. Amplitude})_{3x}}{(\text{Acc. Amplitude})_{1x}} = \frac{9A_{x3}}{A_{x1}}$$

The strain is dependent on curvature, which is given by

$$y_{zz}(t) = A_{x1}(k_{x1})^2 Sin(\omega_{x1}t + k_{x1}z) + A_{x3}(k_{x3})^2 Sin(3\omega_{x1}t + k_{x3}z)$$

In tension dominated systems, $k_{x3}=3k_{x1}$ leading to

$$y_{zz}(t) = A_{x1}(k_{x1})^2 Sin(\omega_{x1}t + k_{x1}z) + A_{x3}(3k_{x1})^2 Sin(3\omega_{x1}t + 3k_{x1}z); \frac{(\text{Strain Amplitude})_{3x}}{(\text{Strain Amplitude})_{1x}} = \frac{9A_{x3}}{A_{x1}}$$

The third harmonic response amplitude is increased by a factor of 9 in both the acceleration and strain response

Figure 43 – The amplitude of the 3rd harmonic, when compared to the amplitude of the 1st harmonic, is nine times greater in acceleration or strain data than in displacement data.

The 3rd harmonic response, though noticed decades ago, was largely ignored because its contribution to the displacement in the cross-flow direction was very small. A 3rd harmonic component in VIV forcing was first noticed in 2004 when Jauvtis and Williamson [6], in VIV experiments with spring mounted cylinders having relatively low mass ratios (<6) and both in-line and cross-flow degrees of freedom, found a reduced velocity range where three vortices, instead of the single vortex that is commonly observed, were shed in the wake behind the cylinder during each VIV half cycle. Moreover, the same research found this vortex-shedding pattern to be stable and it coincided with the largest cross-flow displacements. They named this new pattern the '2T' mode, T implying vortex triplets, of vortex shedding, and the associated region of large A/D ratios as the "SuperUpper" region. Their research found the switch to '2T' mode at a reduced velocity (based on the natural frequency of the pipe not the response frequency) of five and the pattern persisted till a reduced velocity of eight. Though the

authors did not specifically discuss it, their research may have offered the first hydrodynamic explanation for the existence of the third harmonic in VIV response.

Some energy at the 4th and 5th harmonic frequencies was also noticed in early measured data. Jong [5] reported them in acceleration PSDs in the early 1980s but their minimal contribution to the displacement response undermined their importance. The 4th and 5th harmonics have not been studied extensively and no hydrodynamic explanations exist for why and when they occur, except that they may simply be necessary Fourier components of the fundamental periodic vortex-induced force.

5.3.1 Lake Seneca experiments

The 2004 VIV experiments at Lake Seneca in upstate New York [8]revealed significant energy in the acceleration Power Spectral Density (PSD) at frequencies corresponding to the higher harmonics of the fundamental VIV frequency. The high acceleration response was observed not only at the 2nd and 3rd harmonics, but also the 4th and 5th harmonics. For test 0407141557, Figure 44 shows the acceleration Power Spectral Density (PSD) at two axial locations on the pipe, z/L=0.19 and z/L=0.77, for two orthogonal accelerometers, one aligned with the in-line direction (shown as a red dashed line) and the other with the cross-flow direction (shown in blue solid line). As expected, the odd harmonics appear in the cross-flow direction while the even harmonics occur in the in-line direction.

The striking feature of the acceleration PSDs in Figure 44 is the energy content at the higher harmonics, both in-line and cross-flow, which in some cases is more than the spectral energy at the Strouhal frequency. RMS strain values accounting for only the first harmonic would under-predict total RMS strain by a factor of two or more. This has important consequences in fatigue damage incurred by the pipe (Chapter 6).

The Seneca experiments highlighted the importance of the higher harmonics, especially in high mode number VIV experiments and led the way for the Gulf Stream experiments.

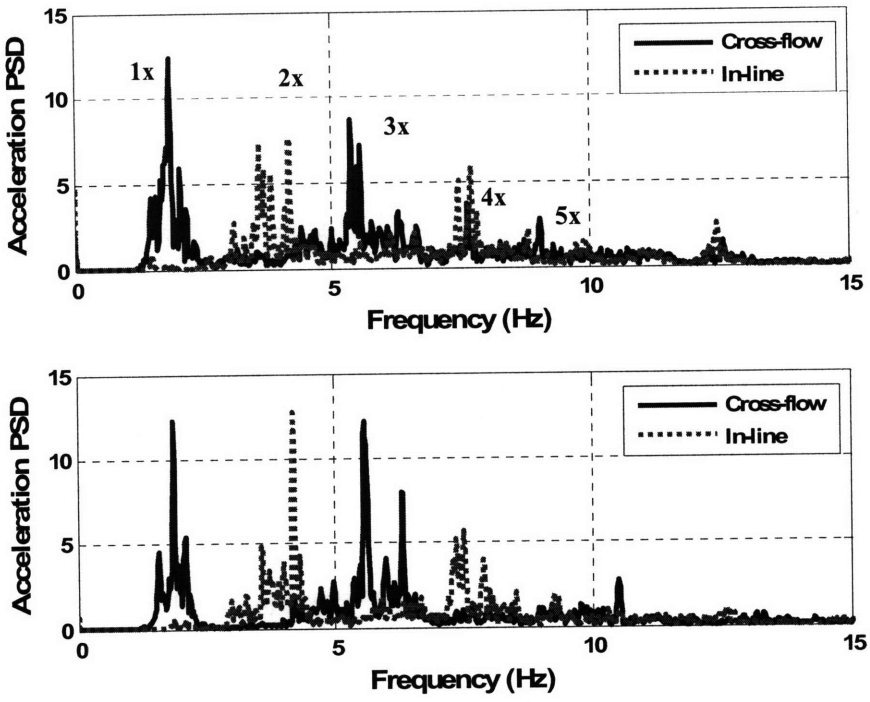

Figure 44 - Cross-flow and in-line acceleration PSDs showing the energy at the 1st and the higher harmonics observed in the lake Seneca experiments. The harmonics are indicated as 1x, 2x etc. (a) z/L = 0.19 from the top end and (b) z/L = 0.77 from top end. The units for both (a) and (b) are $(m/s^2)^2/Hz$

5.3.2 The Gulf Stream experiments

These experiments, carried out in October of 2004 and October of 2006, are one of the few data sets that contain strain measurements from densely instrumented pipes undergoing VIV at high mode numbers in realistic current environments. Figure 45(a) presents data from a bare pipe test (Test – 20061023203818) performed during the second Gulf Stream experiment. It shows time-frequency plots, called scalograms (see [49, 53]), at three locations on the pipe. The frequency range in these plots is chosen to show only the Strouhal frequency, called the fundamental VIV frequency or 1x frequency in this thesis. Figure 45(b) shows the mean normal incident current on the 500.4 ft long pipe during the test. The scalograms were calculated at sensors located at z/L=0.53 (sensor 33), z/L=0.40 ((sensor 43) and z/L=0.26 (sensor 53), where z/L=0 was the bottom end of the pipe. Their positions on the pipe are shown by dots in Figure 45(b).

The scalograms indicate that the fundamental frequency of VIV was not constant for the duration of the test. They suggest that the frequency reached a steady state value only in the last sixty seconds of the test. Since the cross-flow motion of the pipe is mainly governed by the response at the fundamental VIV frequency, we can make the assumption that steady state conditions are achieved when this frequency is steady with time.

In this steady state region, the fundamental frequency of vibration and all its harmonics are narrow banded, almost single frequency responses. Figure 46 shows the strain PSD for the steady state duration of the test. These PSDs, shown for orthogonal quadrants Q4 and Q1, correspond to the same sensor locations as the scalograms. The PSD peaks are labeled as 1x, 2x, etc. where the "x" should be interpreted as "times the fundamental VIV frequency of vibration." This terminology will be used for the rest of the thesis.

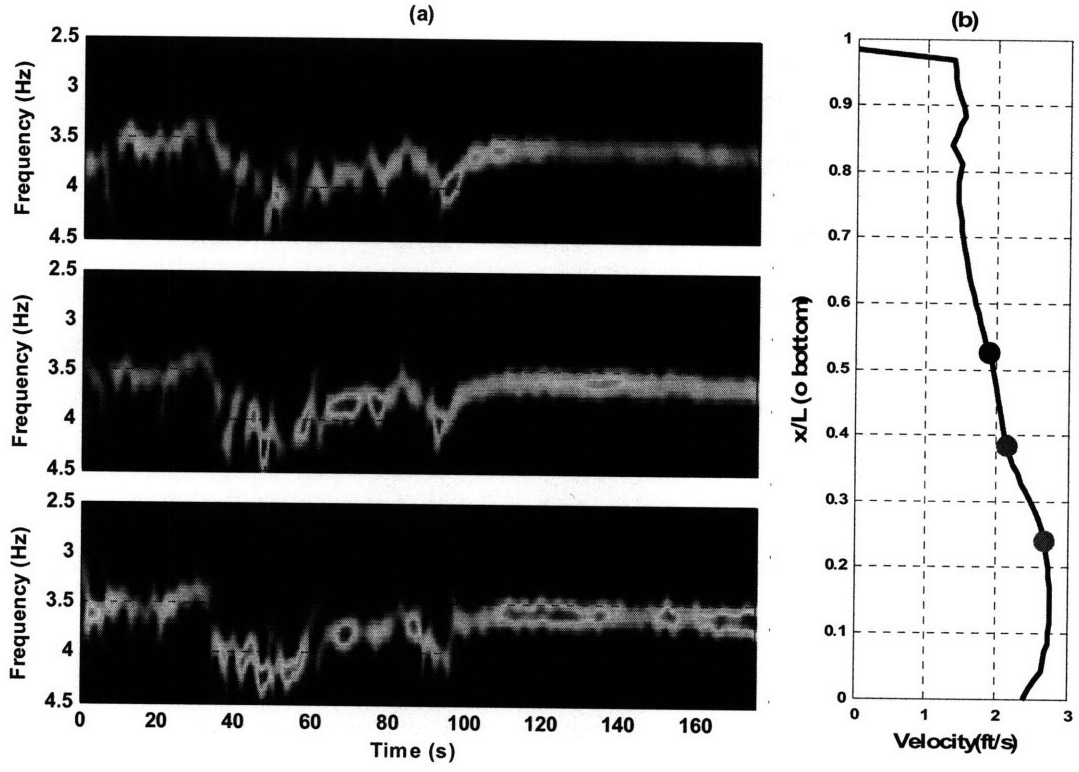

Figure 45 - (a) - Time-Frequency plots for test 20061023203818 show steady state conditions are achieved only in the last 60 seconds. (b) The normal incident current profile with locations of the time-frequency analysis shown in (a).

As expected, the PSDs show energy not only at the fundamental frequency of vibration but also at its harmonics. Of these, the 3rd harmonic and the 5th harmonic are of particular interest because they occur in the cross-flow direction and can have important implications for fatigue life estimates in the cross-flow direction.

When a sensor in the Gulf Stream experiment was exactly aligned with the cross-flow direction, the odd harmonics dominated in the PSD. However, the twist in the fibers along the pipe resulted in sensor orientations which were neither in-line nor cross-flow. This explains why the PSDs in Figure 46 contain energy in both the odd and even harmonic frequencies.

In order to compute the total cross-flow response, the response measured by a pair of orthogonal sensors should be transformed to a new co-ordinate system aligned with the cross-flow and in-line directions. However, this was not always possible because data from some fibers was not perfectly synchronous during the experiments, making it difficult to rotate the strain data into new co-ordinate systems because orthogonal strain measurements were not available at the same time instant. It was more feasible to calculate total energy at a particular frequency using PSDs from two orthogonal fibers.

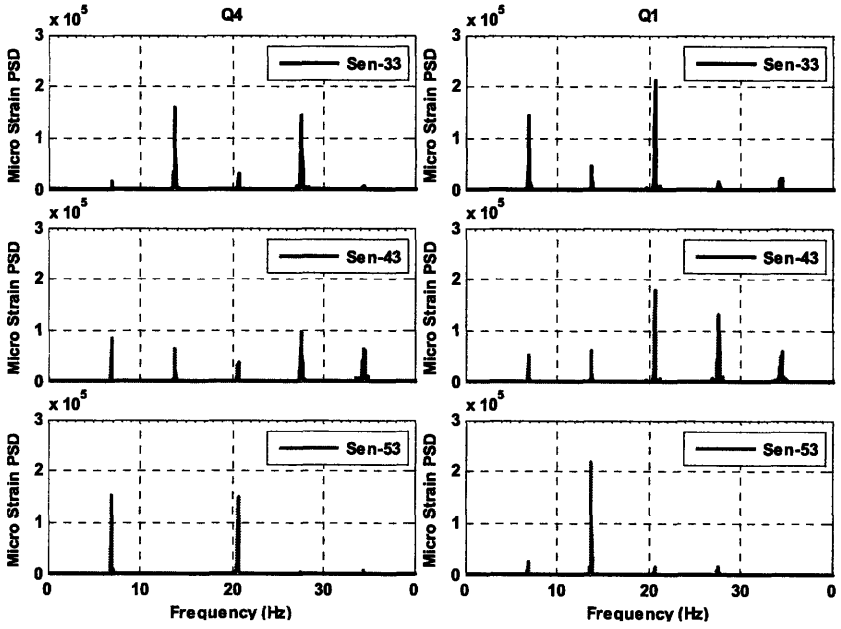

Figure 46 – Strain PSDs for Quadrants 1 and 4 at 3 different axial locations show the higher harmonics in the VIV response. Test – 200623203818

The strain data from each quadrant was filtered to isolate the signal corresponding to each of the harmonics. Spectra for 1x components from orthogonal quadrants were then summed to produce a spectrum that represents the total spectral response in the 1x component. This was done for each of the harmonics. Finally, the spectral response for each of the odd harmonics i.e. 1st, 3rd and 5th, were summed to produce the spectral representation of the total cross-flow strain response. Similarly, the spectral response for each of the even harmonics was summed to produce the spectra for the total in-line strain response. Figure 47 shows the PSDs for the total cross-flow and in-line strain response, developed using the Q1 and Q4 strain spectra shown in Figure 46, at locations corresponding to sensors 33, 43 and 53.

The filtered signals from orthogonal quadrants, Q1 and Q4 in this case, can be used to find the total response at each harmonic frequency. For example the total RMS strain response at the 1st harmonic at a particular axial location is given by the following formulation.

$$\varepsilon_{1total} = \sqrt{(\varepsilon_{1Q1})^2 + (\varepsilon_{1Q4})^2}$$

where

ε_{1Q1} = RMS strain calculated using Q1 strain

ε_{1Q4} = RMS strain calculated using Q4 strain (4.16)

Equivalent formulations are used to calculate the total RMS strain response corresponding to the 2nd, 3rd, 4th and 5th harmonics.

When the total RMS cross-flow strain from a typical Gulf Stream test is plotted against axial position on the pipe, a strong peak is observed in some regions of the pipe. However, when the data is filtered to remove the higher harmonics, the peak is no longer present indicating that it was caused by the higher harmonics. In the example case shown in Figure 48, the strain peak in the total cross-flow RMS strain is seen at z/L=0.4 while the RMS strain response corresponding to just the 1st harmonic does not have a prominent peak. These are the first indications of the localized nature of the higher harmonics, a finding that is confirmed by further analysis.

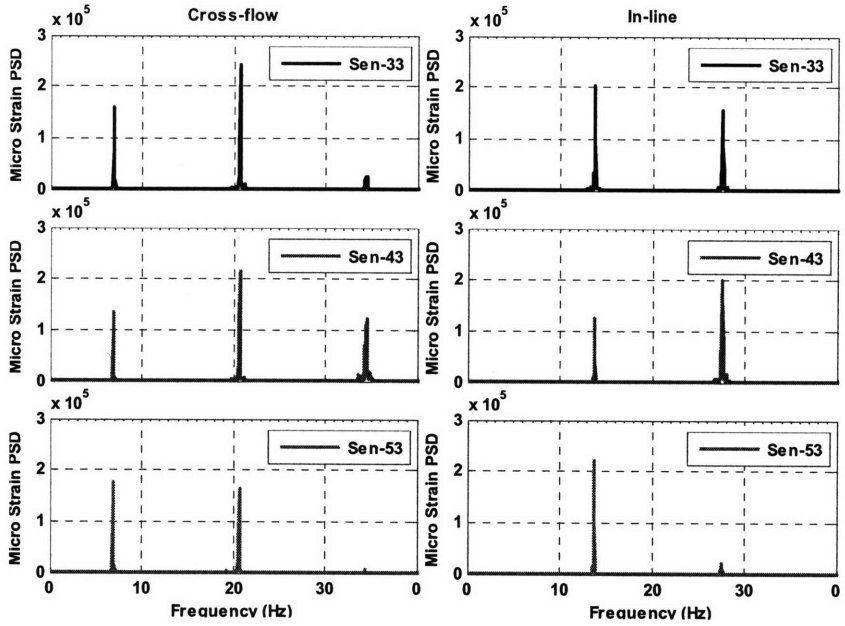

Figure 47 - The total cross-flow strain spectrum (odd harmonics) and the total in-line strain spectrum (even harmonics) at 3 different locations on the pipeTest - 200623203818

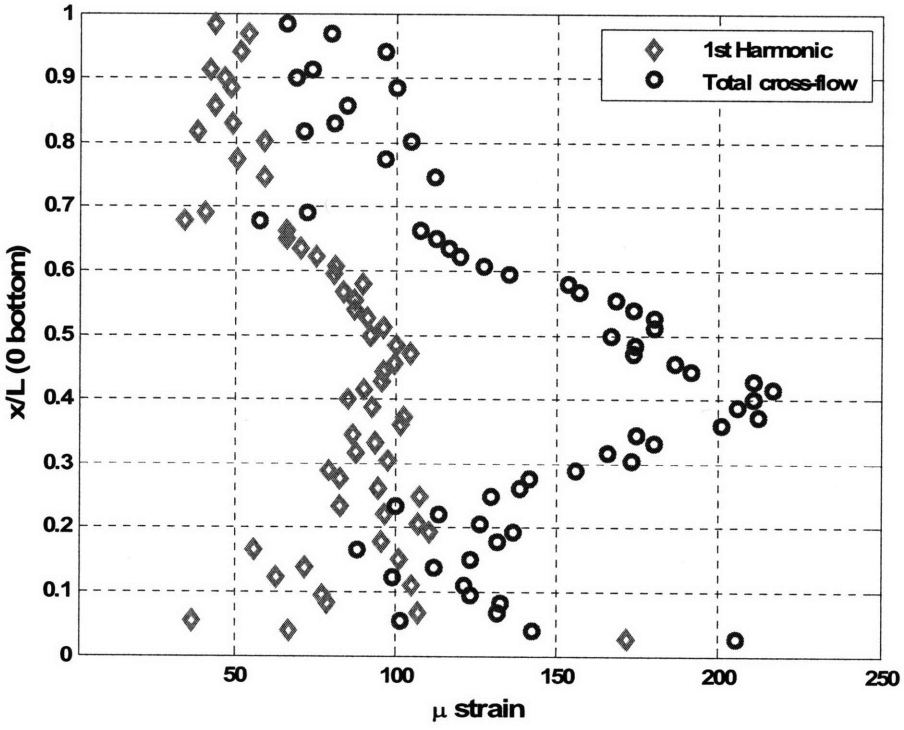

Figure 48 – The axial distribution of total cross-flow RMS strain and the RMS strain from only the 1st harmonic for Test-200623203818

Apart from confirming the occurrence of the higher harmonics in VIV strain measurements, the Gulf Stream experiments provide the data to analyze each of the higher harmonics and study their properties with the final objective of being able to incorporate their effects into VIV prediction tools.

5.4 Properties of the Higher Harmonics

The data from the second Gulf Stream experiment provides an opportunity to investigate the nature of the higher harmonics in flexible pipes where the response is predominantly in the form of traveling waves. In this section, the relationship between the X,Y trajectories and the higher harmonics is investigated. Such a relationship is suggested by various researchers [6, 48].

Further, trends, in the form of correlations, and properties, like amplitude response, are investigated for each of the higher harmonics. As the response data has no information about the wake, it cannot be used to develop hydrodynamic explanations for the observed trends and properties. Mention is made when an observed trend or property have been studied previously and either verify or differ with existing work.

To help study the higher harmonics and identify trends and properties, the measured strain data is processed in a number of ways.

1) The contribution of each of the harmonics to the total RMS strain response is isolated, using the methods described earlier, and the contribution to the total RMS strain is identified at a particular spatial location. The reduced velocity corresponding to that spatial location is found using the frequency of the 1x response and the normal incident velocity at that location.
2) The VIV strain response depends on the amplitude of the displacement response and the modal curvature corresponding to response frequency. As the modal curvature at a particular frequency is dependent on the properties of the vibrating pipe, it changes from experiment to experiment. This makes it impossible to compare RMS strain results from two different experiments where the primary VIV frequency is different. The strains corresponding to each of the harmonics could be converted to displacements but that has additional problems. First, the displacements of the higher harmonics are very small and working with small numbers is inconvenient and prone

to error. Second, the importance of the higher harmonics is in their contribution to strain and fatigue, not in the displacement. Thus, a new approach is developed to make the strain measurements useful.

For a flexible pipe

$$\text{Curvature } \sigma = \frac{\partial^2 y}{\partial z^2} \quad ; \quad \text{Moment } M = EI\frac{\partial^2 y}{\partial z^2} \quad ; \quad \text{Strain } \varepsilon = \frac{D}{2}\times\sigma$$

D = Pipe Diameter ; y=cross-flow displacement ; z=axial distance along pipe

Solving for ε gives :-

$$\varepsilon = \frac{M\times\frac{D}{2}}{EI} = \frac{D}{2}\times\sigma \tag{4.17}$$

Consider an un-damped VIV response at the 1st harmonic

$$y_{x1}(z,t) = A_{x1}^{+}Sin(k_{x1}z - \omega_{x1}t) + A_{x1}^{-}Sin(k_{x1}z + \omega_{x1}t) \tag{4.18}$$

The amplitudes A_{x1}^{+} and A_{x1}^{-} determine if the response is a traveling wave, a standing wave or a combination of the two. ω_{x1} is the 1st harmonic frequency and k_{x1} is the 1st harmonic wave number. Restating Equation (4.17)

$$\varepsilon_{x1}(z,t) = \frac{D}{2}\times\frac{\partial^2 y(z,t)}{\partial z^2} \quad ; \quad \varepsilon_{x1} = \text{Strain response of the 1st harmonic} \tag{4.19}$$

Using Equation (4.18) in Equation (4.19) gives

$$\varepsilon_{x1}(z,t) = \frac{D}{2}\times[-A_{x1}^{+}k_{x1}^{2}Sin(k_{x1}z - \omega_{x1}t) - A_{x1}^{-}k_{x1}^{2}Sin(k_{x1}z + \omega_{x1}t)] \tag{4.20}$$

The wave number for the 1x response, k_{x1}, can be written in terms of the mode number corresponding to the 1st harmonic, n_{x1}, and the wave number of the 1st mode, $k_{1^{st}\text{mode}}$, as $k_{x1} = n_{x1}\times k_{1^{st}\text{mode}}$. Using these in Equation (4.20) gives

$$\varepsilon_{x1}(z,t) = \frac{D}{2}\times[-A_{x1}^{+}n_{x1}^{2}k_{1^{st}mode}^{2}Sin(k_{x1}z - \omega_{x1}t) - A_{x1}^{-}n_{x1}^{2}k_{1^{st}mode}^{2}Sin(k_{x1}z + \omega_{x1}t)] \tag{4.21}$$

For a tension dominated pipe $\omega_{x1} = n_{x1}\times\omega_{1^{st}\text{mode}}$ and Equation(4.20) becomes

$$\varepsilon_{x1}(z,t) = \frac{D}{2}\times[-A_{x1}^{+}(\frac{\omega_{x1}}{\omega_{1^{st}\text{mode}}})^{2}k_{1^{st}\text{mode}}^{2}Sin(k_{x1}z - \omega_{x1}t) - A_{x1}^{-}(\frac{\omega_{x1}}{\omega_{1^{st}\text{mode}}})^{2}k_{1^{st}\text{mode}}^{2}Sin(k_{x1}z + \omega_{x1}t)] \tag{4.22}$$

At a given location on the pipe, the RMS 1st harmonic strain from Equation(4.22) is

$$\overline{\varepsilon_{x1}}^{rms} = \frac{D}{\sqrt{2}} \times (\frac{\omega_{x1}}{\omega_{1^{st}mode}})^2 \times k_{1^{st}mode}{}^2 \times A^* \tag{4.23}$$

A^* is the amplitude at the location. Re-organizing the terms of Equation(4.22)

$$\frac{\overline{\varepsilon_{x1}}^{rms}}{(\frac{\omega_{x1}}{\omega_{1^{st}mode}})^2} = \frac{D}{\sqrt{2}} \times k_{1^{st}mode}{}^2 \times A^* \tag{4.24}$$

The term $\frac{D}{\sqrt{2}} \times k_{1^{st}mode}{}^2 \times A^*$ is equal to the RMS strain in the pipe for a response at the 1^{st} mode with amplitude A^*. Therefore, $\frac{\overline{\varepsilon_{x1}}^{rms}}{(\frac{\omega_{x1}}{\omega_{1^{st}mode}})^2}$ is a "normalized RMS 1^{st} harmonic strain" which is independent of the primary VIV frequency, making comparisons between the 1^{st} harmonic strain responses possible between tests with different fundamental VIV frequencies.

A similar mathematical analysis leads to the following relationship for the 3^{rd} harmonic strain response.

$$\frac{\overline{\varepsilon_{x3}}^{rms}}{(\frac{\omega_{x1}}{\omega_{1^{st}mode}})^2} = \frac{D}{\sqrt{2}} \times 9k_{1^{st}mode}{}^2 \times A^{\oplus} \tag{4.25}$$

The term $\frac{D}{\sqrt{2}} \times 9k_{1^{st}mode}{}^2 \times A^{\oplus}$ is equal to the strain in the pipe for a response at the 3^{rd} mode with amplitude $A^{\oplus}$. $\frac{\overline{\varepsilon_{x1}}^{rms}}{(\frac{\omega_{x1}}{\omega_{1^{st}mode}})^2}$ is called "normalized RMS 3^{rd} harmonic strain" which is independent of the VIV frequency, making comparisons possible between the strain response at the 3^{rd} harmonic of two different experiments with different 3^{rd} harmonic frequencies. Equivalent "normalized" strains are derived for the 2^{nd}, 4^{th} and 5^{th} harmonics. These "normalized" strains are used to identify correlations between the higher harmonics.

3) The trends and relationships between the "normalized" strains are studied using correlation coefficients, in addition to plots. The correlation coefficient is defined as

Correlation Coefficient

$$rho = \frac{\sum_{i=1}^{n}(X_i - \overline{X})(Y_i - \overline{Y})}{\sqrt{\sum_{i=1}^{n}(X_i - \overline{X})^2 + \sum_{i=1}^{n}(Y_i - \overline{Y})^2}}$$

where

X_i and Y_i represent the terms of two data sets

$\overline{X}$ and $\overline{Y}$ represent the mean value of the data sets

4) The reduced velocity, *Vr*, is always calculated using the measured frequency response of the 1st harmonic, even when the higher harmonics strain amplitudes are plotted against reduced velocity.

5) The strain measurements from the Gulf Stream experiments are modified to represent the displacement trajectories of the pipe at a particular location. Since the optical fibers were not perfectly aligned with the in-line or cross-flow directions, the strains from orthogonal fibers are filtered and combined to find the total 1x and 2x RMS strains (Equation(4.16)). The displacement trajectories, called X,Y trajectories in this chapter, are constructed using the total RMS magnitudes of the 1x and 2x strain response during a 3 second time interval from the steady-state portion of a test. The filtered 1x and 2x strain time series from Q1 and Q4 for the same 3 second time interval is used to determine the phase relationship. This is shown in mathematical form in Equation(4.26).

$$X(t) = \frac{\varepsilon_{1total}}{\varepsilon_{1Q1}} \times \varepsilon_{1Q1}(t)$$

$$Y(t) = (\frac{1}{4}) \times \frac{\varepsilon_{2total}}{\varepsilon_{2Q4}} \times \varepsilon_{2Q4}(t)$$

where

$X(t)$ = Time series representing the cross-flow motion

$Y(t)$ = Time series representing the in-line motion

ε_{1Q1} = RMS strain calculated using Q1 strain (4.26)

ε_{2Q4} = RMS strain calculated using Q4 strain

$\varepsilon_{1Q1}(t)$ = Time series of measured Q1 strain

$\varepsilon_{2Q4}(t)$ = Time series of measured Q4 strain

The 2x strain response is divided by 4 so that the shapes are representative of the displacement response of the pipe at a particular location. Finally, to show the direction of motion, the first 8 points of the trajectory were represented as red dots, going from the largest to the smallest. This means that the motion direction can be calculated by connecting all the dots starting from the largest and continuing to the smallest.

5.4.1 The spatial variation of X,Y trajectories and its influence on the Higher Harmonics

Recent researchers, like Jauvtis and Williamson [6], have studied the phase relationships of the in-line and cross-flow motion and established the X,Y trajectory plots for different phase differences between the 1x and 2x response time histories. Figure 49 shows a plot from their paper where the trajectories and the direction of motion are shown for an assumed motion time-history of $y = Sin(\omega t)$ (cross-flow) and $x = 0.3Sin(\omega t + \theta)$ (in-line), where θ is the phase difference between the in-line and the cross-flow motion. Also shown on the plot are some terms used to refer to certain displacement profiles in this thesis. Recent work by Dahl et al. [29] has tried to explain the existence of the higher harmonics, particularly the third harmonic, on the interaction of the X,Y trajectory of the pipe and the vortices in its wake.

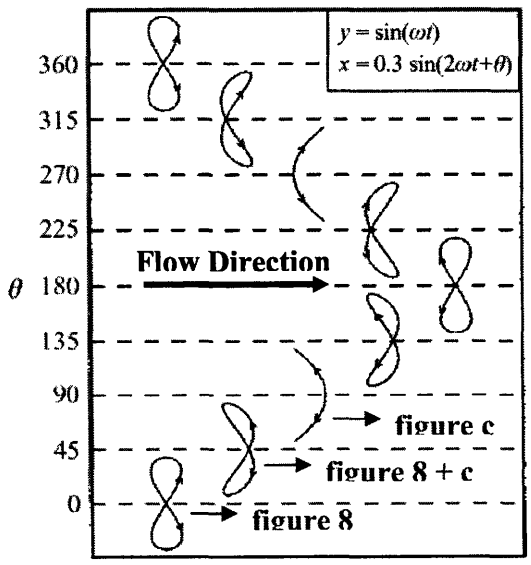

Figure 49 – The phase relationship between the in-line and cross-flow motion leads to different displacement patterns.

For second Gulf Stream flexible cylinder experiments, relationships between the trajectories and the region of maximum responses were also observed. This was despite the significant differences between rigid cylinder laboratory experiments mentioned above and flexible cylinder experiments in terms of reduced velocity of the maximum 1st and maximum 2nd harmonic peak responses.

The phase relationships between the higher harmonics can best be explained by examining a particular test from the second Gulf Stream experiments. This particular experiment, Test – 200623203818, had an extraordinary sixty second steady-state period during which the fundamental VIV frequency did not change, as shown in Figure 45. This steady-state region provides an opportunity to explore the phase relationships between in the in-line and cross-flow motion and their relationship with the higher harmonics.

In this steady-state region, the measured strain time series can be filtered to isolate the contributions of the each of the harmonics to the total strain RMS response. The method of doing this has been discussed previously in this chapter. Figure 50 (b) shows the temporal variation of strain at each sensor location for a three second response window (seconds 117 to 120), after it has been filtered to remove all the frequencies except the response at the 1st harmonic. Such a plot allows us to follow the peaks in the 1st harmonic response and establish regions of standing and traveling waves. Figure 50 (a) shows the axial variation of the 1x, 2x and 3x RMS strain response during this 3 second period. Note that sensor 70 corresponds to the bottom end of the pipe.

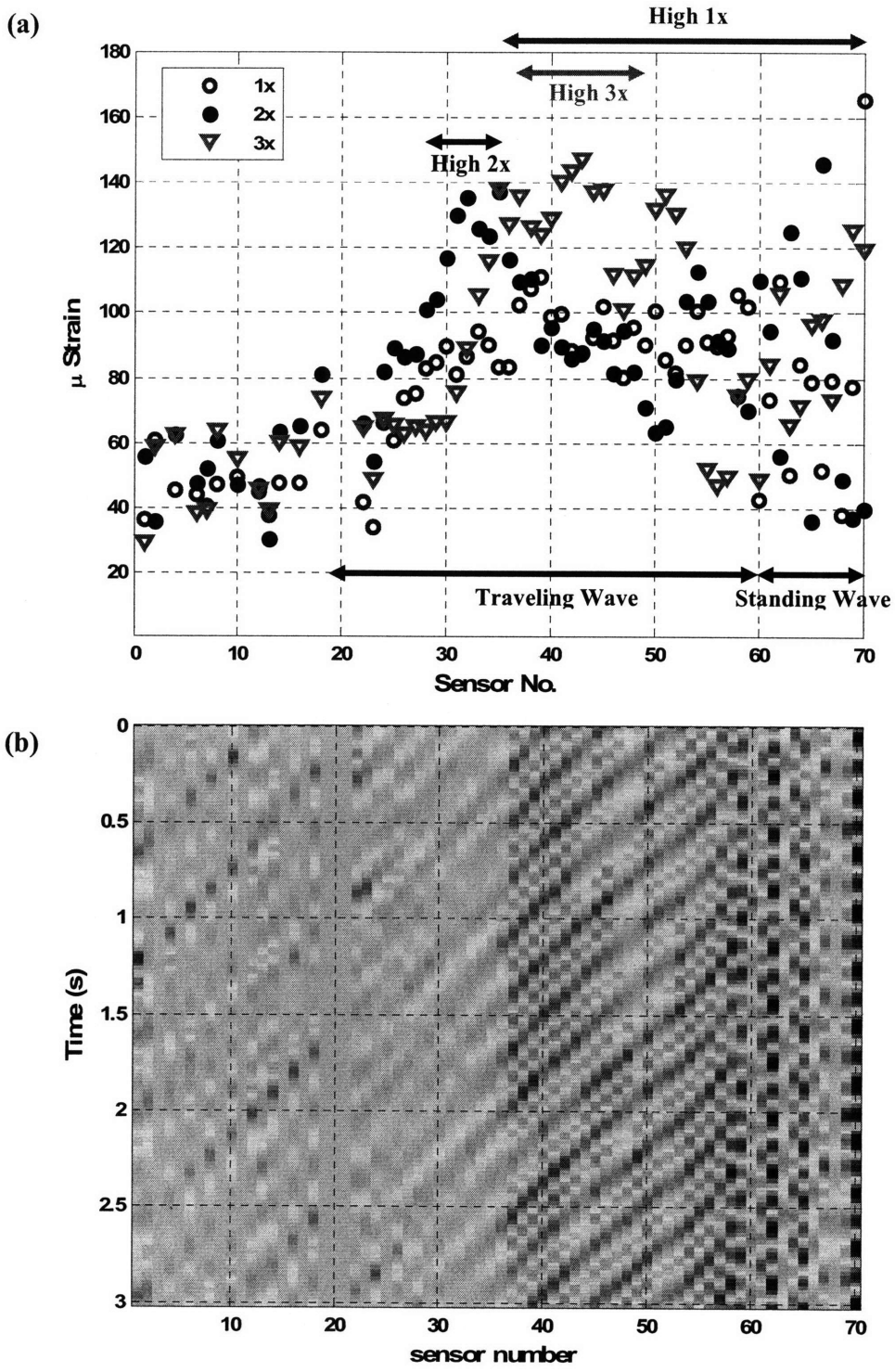

Figure 50 – (a) The RMS strain response at the 1x, 2x and 3x frequencies during a 3 second time period (b) The magnitude of the 1st harmonic clearly shows regions of standing and traveling waves (red=peak, blue=trough)

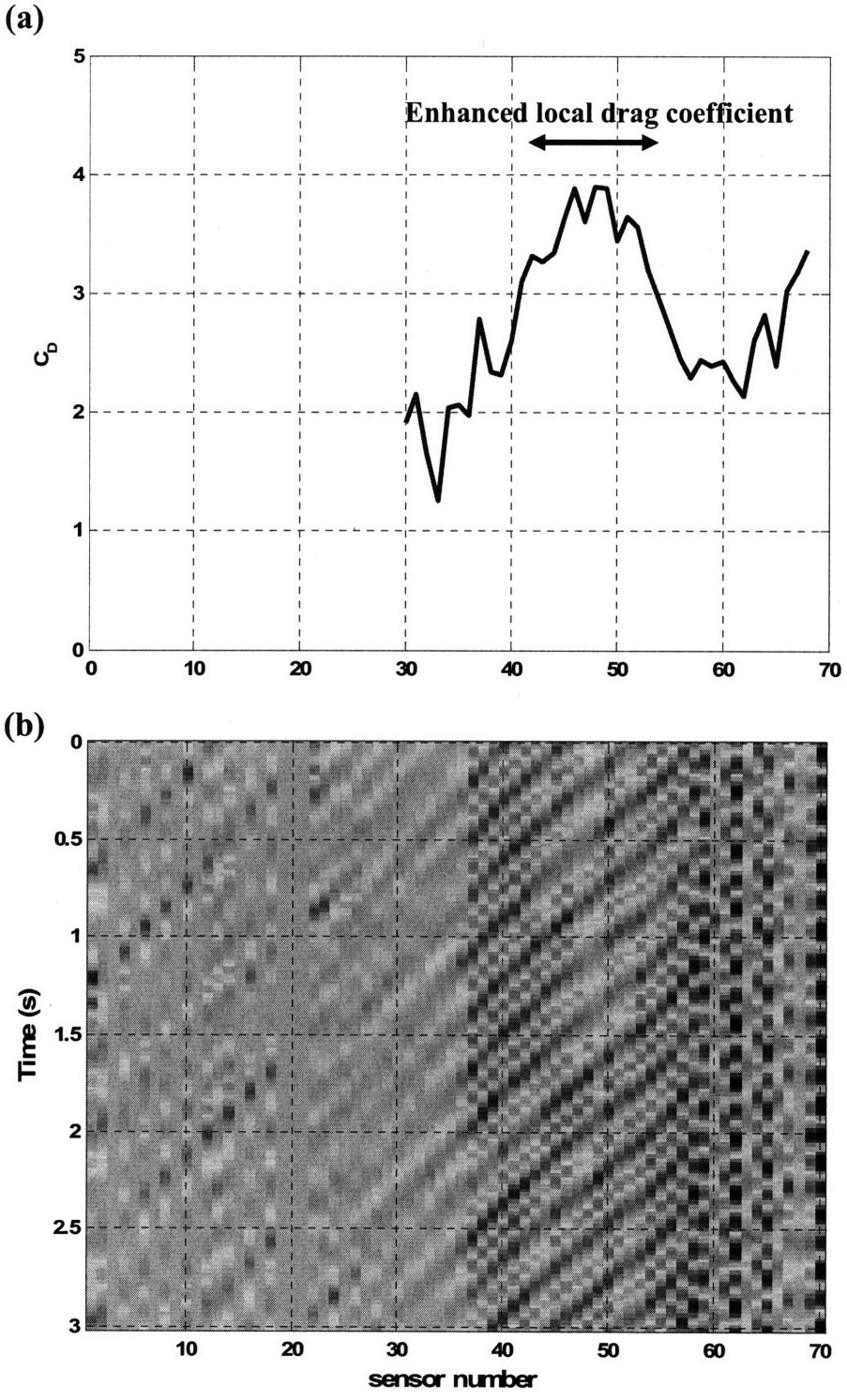

Figure 51 – The region of enhanced local drag coefficient (shown in (a)) is also the region where the traveling wave is starts propagating along the pipe (shown in (b)).

From Figure 50 (a) and (b), the following observations can be made

- Sensor 60-Sensor 70 - a predominantly standing wave region of the pipe where the 1x waves are reflected from the boundary causing nodes and antinodes
- Sensor 58- Sensor 50 – a predominantly traveling wave region where the 1x RMS response is large, the 2x RMS strain response is comparable in magnitude and the 3x RMS response is small but starts to build up towards sensor 50.
- Sensor 38-Sensor 48 – a predominantly traveling wave response where the 1x and 2x response remain the same but the 3x RMS strain response is consistently high.
- Sensor 38 – Sensor 28 – Predominantly traveling wave response where the 1x response starts to decrease, the 3x decreases after sensor 35 and the 2x peaks at sensor 32 before decreasing rapidly.

To calculate the 1x, 2x and 3x RMS strain response, the measured strain signal shown in Figure 50 (b) was filtered to extract the strain response at 1x and 2x harmonics from two orthogonal quadrants (Q1 and Q4 in this case). From these filtered time series data, the X,Y plots were constructed using the total magnitude of the 1x and 2x response in combination of their phase relationship contained in the filtered time series measurements. The process is shown in Equation(4.26). The 2x strain response is divided by 4 so that the shapes are representative of the displacement response of the pipe at a particular location. Finally, to show the direction of motion, the first 8 points of the trajectory were represented as red dots, going from the largest to the smallest. This means that the motion direction can be traced by connecting all the dots starting from the largest and continuing to the smallest.

5.4.1.1 Standing wave region

The waves generated during VIV are reflected at the boundary to form a region where the dominant response is a standing wave. The phase and amplitude of a standing wave depends on the distance from a node and since the in-line and the cross-flow response have different wave numbers, it can be expected that in this region the displacement response pattern will change in magnitude, shape and direction of motion as the amplitude and phase of the in-line and cross-flow response changes with changing axial position. This is exactly what is seen in Figure 52.

5.4.1.2 Traveling wave region

A little further away from the bottom of the pipe, the amplitude of the standing wave reduces considerably and the final response can be said to be predominantly composed of traveling waves. In this region, assuming that the waves are non-dispersive, the displacement response of the pipe will retain its shape and move spatially as the waves travel away from the region where they were generated. This is clearly seen in Figure 53. The 'figure 8' patterns are seen over consecutive sensor locations. Moreover, the phase difference which corresponds to the 'figure 8' pattern and the observed direction of motion of the pipe is 0 degrees.

5.4.1.3 The region of high 3x RMS response and region of high 2x response

The region between sensor 30 and sensor 40 shows the change in trajectories as the response moves from a high 3rd harmonic RMS strain response to a high 2nd harmonic RMS strain response. Around sensor 35, a close look at the X,Y trajectories indicates that as the wave travels further up the pipe, the phase relationship between the 1x and 2x time histories are slightly modified resulting in a pattern that looks like a combination of the 'figure c' shape and a 'figure 8'. This, along with the direction of motion, corresponds to an approximate phase difference between the 1x and 2x time histories of 45 degrees. The region between sensor 30 and sensor 34 corresponds to the highest 2x RMS strain response, with the 2x RMS strain centered on sensor 32. The traveling wave has moved further from where it was generated and the phase difference between the 1x

and 2x responses has also increased. In this region, the phase difference is around 90 degrees, with sensor 32 showing an almost exact phase difference of 90 leading to a perfect 'figure c' pattern. It is very interesting that this is also the sensor that corresponds to the center of the region of maximum 2x RMS strain response. Another remarkable phenomenon that is seen is the reversing of direction of the trajectories as the phase difference goes from slightly above 90 degrees to slightly below 90 degrees (Sensor 30). Figure 49, which is based on theoretical calculation, also shows this reversal in direction of motion.

5.4.1.4 The region of high drag coefficient

The region where the traveling wave starts propagating towards the top end of the pipe, around sensor 55, also shows the largest value of local drag coefficient (Figure 51). This region shows the 'figure 8' patterns with the direction of motion being 'downstream at the extreme cross-flow displacement' and corresponds to a phase difference of 0 degrees between the 2x and 1x strain response.

This region of enhanced drag also corresponds to the growing of the 1x and 3x RMS response. This makes it a likely 'power-in' region for the pipe, where energy is transferred from the fluid to the pipe. This finding makes local drag coefficients a good indicator of the 'power-in' region when the VIV response is in the form of traveling waves.

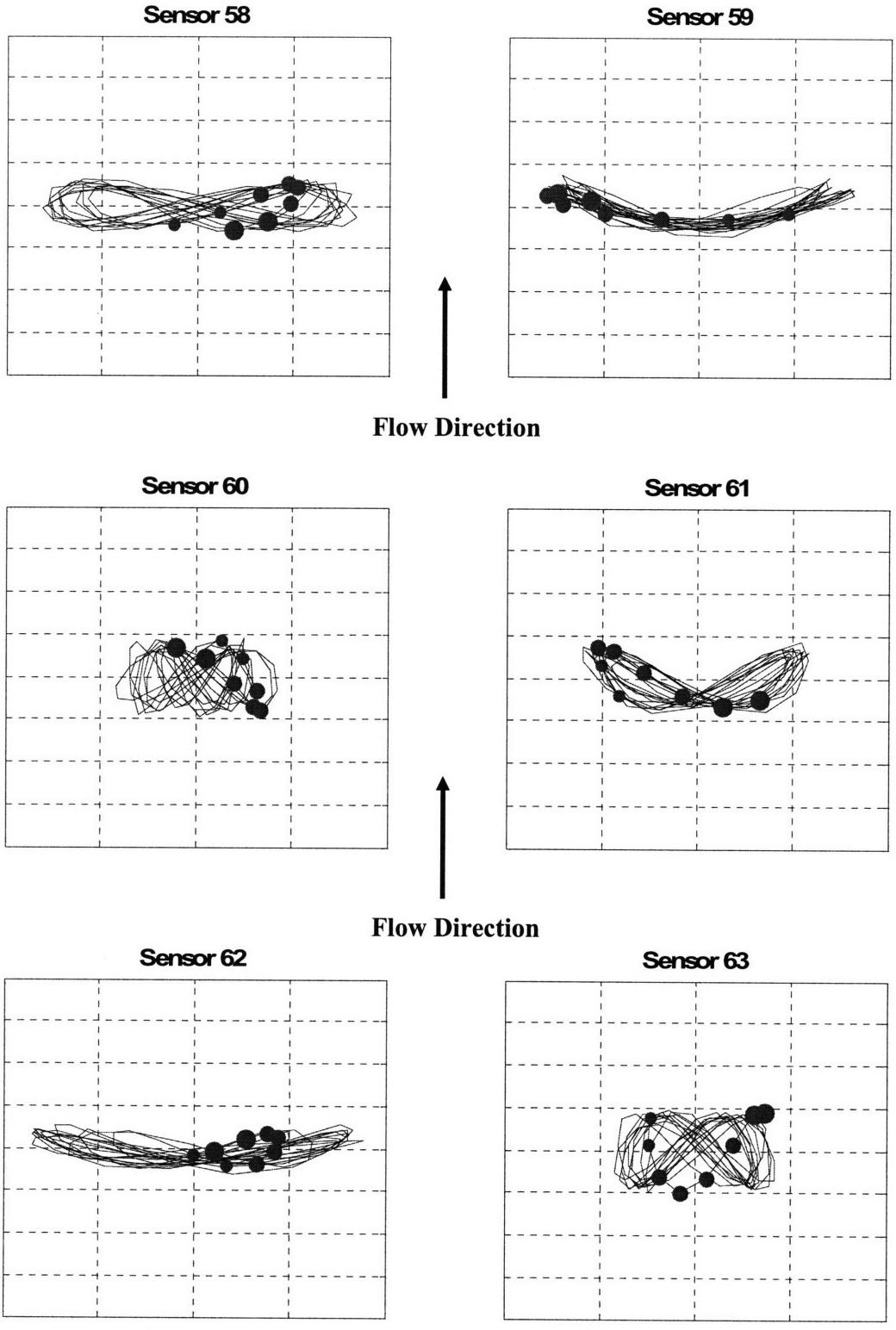

Figure 52 - X,Y plots in the standing wave region. Current direction is from bottom to top.

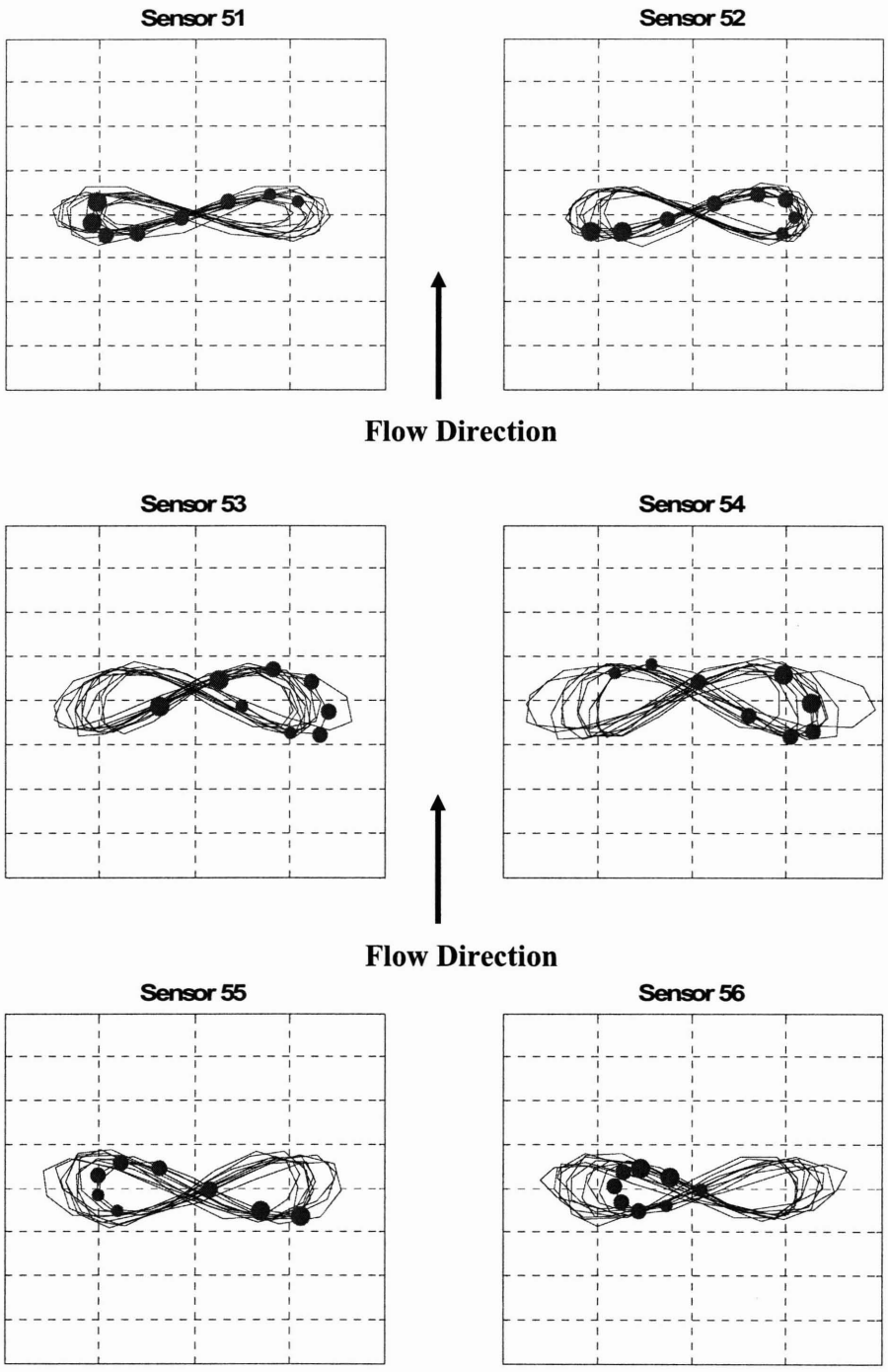

Figure 53 – The X,Y trajectories in the traveling wave region of the pipe where the phase difference between the 1x and 2x motion is 180 degrees. Current direction is from bottom to top.

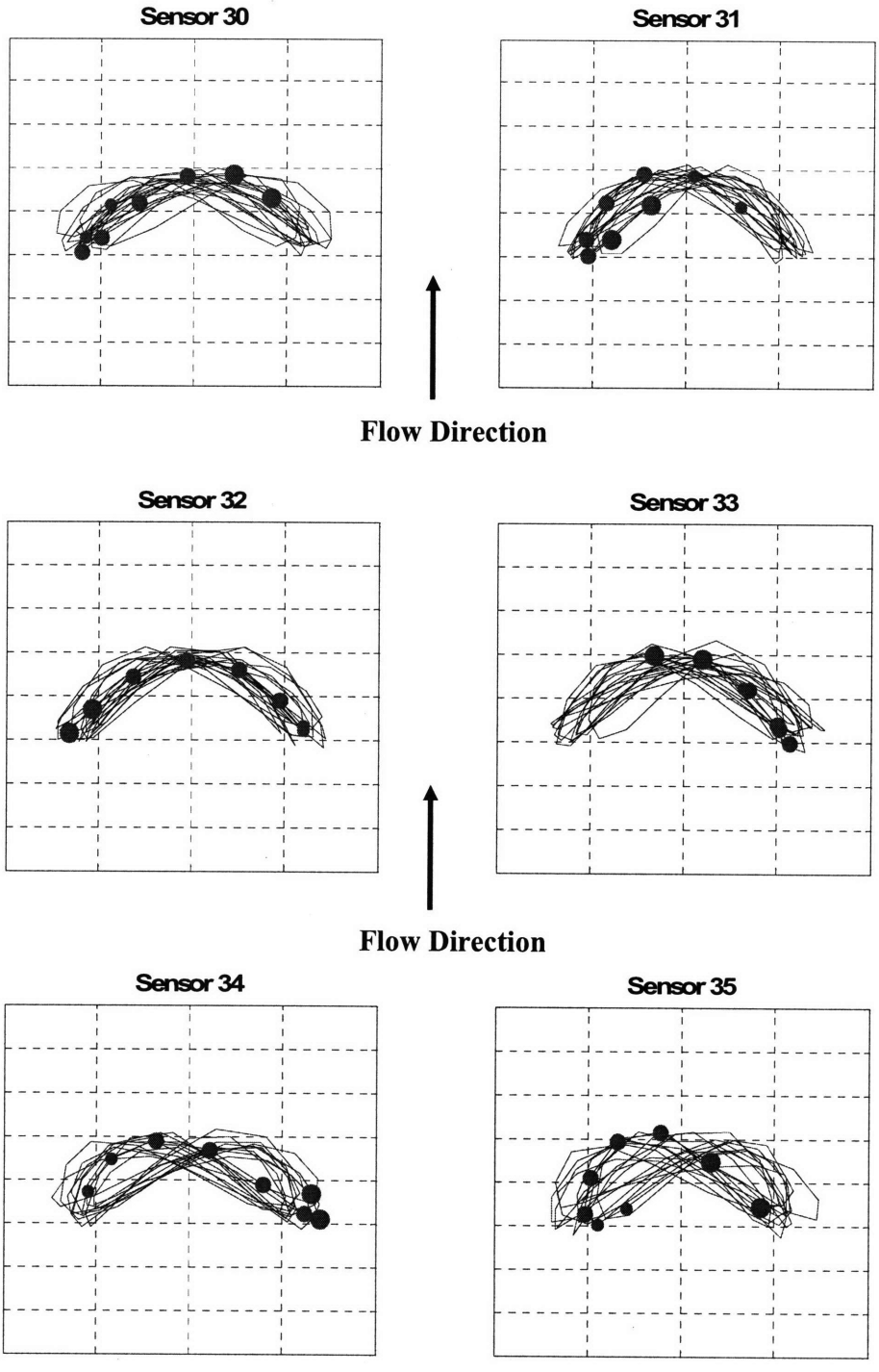

Figure 54 - The X,Y trajectories show a 'figure c+8' pattern (Sensors 34,35) which corresponds to a 45 degree phase difference and a large 3x response. The phase changes to 90 degrees leading to a 'figure c' pattern (sensor 32,33) and large 2x response. Finally the trajectory direction is reversed as the phase crosses 90 degrees (sensor 30,31). Current direction is from bottom to top.

5.4.2 Properties of the Cross-Flow Harmonics

Various correlations and trends were developed for the for the cross-flow harmonics. The important findings are presented here (see Appendix C for more results).

5.4.2.1 The Third Harmonic

Location of the maximum RMS strain

Recent research by Jauvtis [6] has found that a large 3rd harmonic component in the forcing exists in the reduced velocity region where the cross-flow displacement response was the largest. Few such experiments have been performed for flexible cylinders, and fewer have looked at the 3rd harmonic response in field experiments. For test – 200623205557, which is also analyzed in the second harmonic section, the spatial distribution of the 1st and 3rd harmonic RMS strain response is shown in Figure 55. The RMS strain peaks for both the 1st and 3rd harmonics occur at the same spatial location, confirming the observations made by Jauvtis et al.

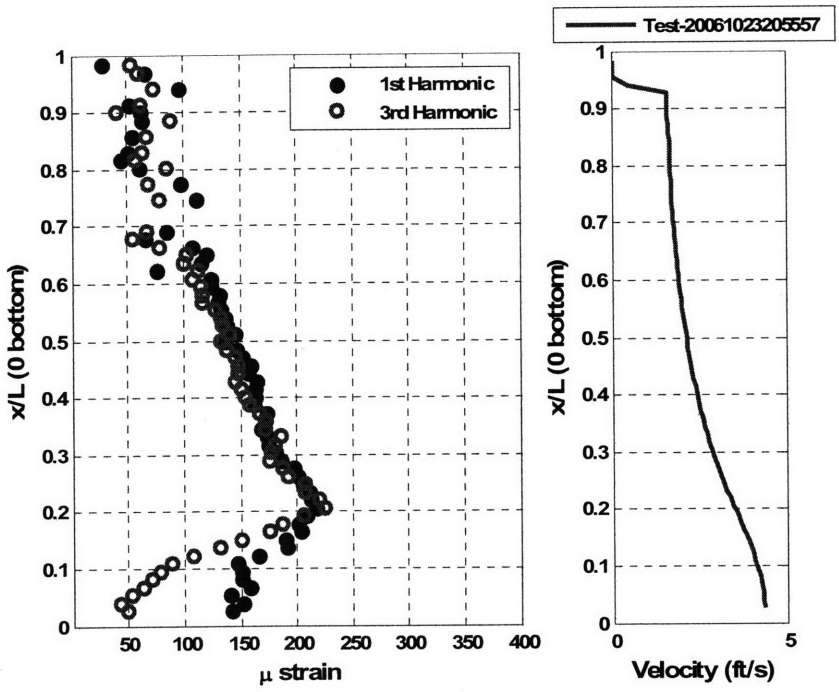

Figure 55 - RMS 1st and 3rd harmonic strain for test 20031023205557

This observation is further confirmed by analyzing multiple tests done during the Second Gulf stream experiments. For eleven[4] different tests from the Gulf Stream experiments, the reduced velocity was calculated at the spatial locations where the largest 1x and 3x RMS strain response was observed. The results are plotted in Figure 56 and confirm that the largest 3x RMS strain responses occurs at or very close to the reduced velocity at which the largest 1x RMS strain response is observed.

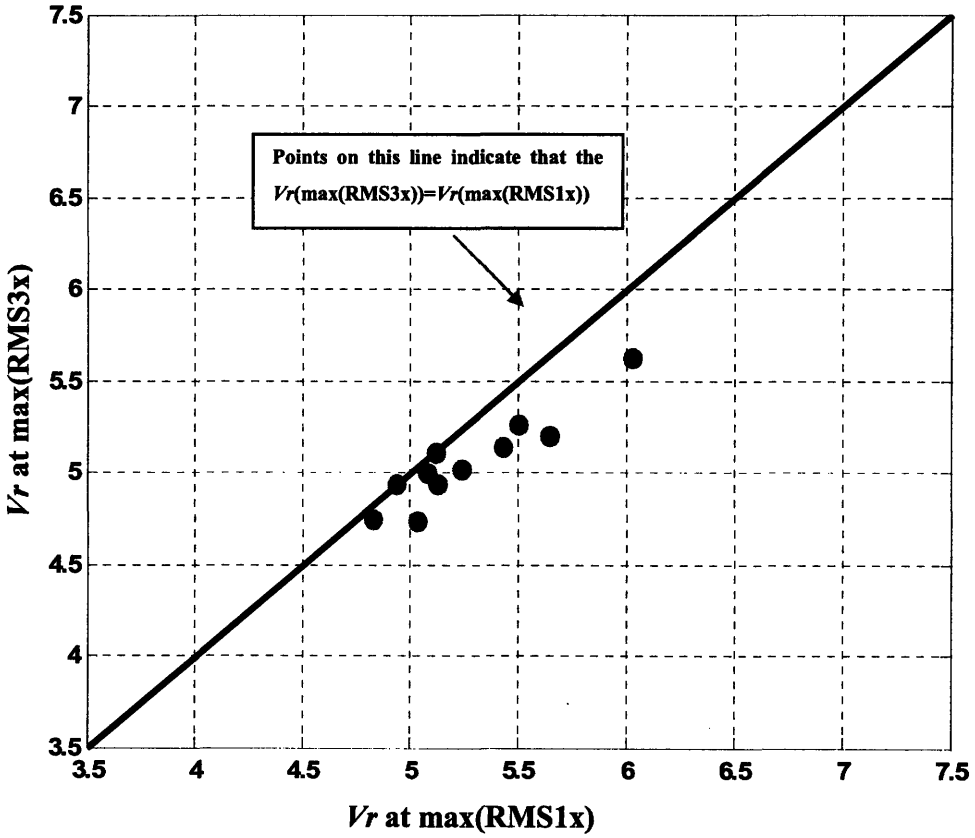

Figure 56 – The reduced velocity of the maximum RMS strain in the 1x and 3x frequencies are very close to each other

Experiments in the laboratory have shown a clear relation between the 3x forcing and reduced velocity. However in the Gulf Stream flexible cylinder experiments, no

[4] These tests, listed in Table 6, were selected because the reduced velocity monotonically increased in the region of the highest 1x and 3x response, similar to the velocity profile shown in Figure 55, enabling the reduced velocity in the region of the maximum RMS 1x and 3x strain responses to be accurately calculated.

clear relationship could be developed. After analyzing data from multiple tests, the 3x peak was found to be in the Vr=5.0 to Vr=6.0 range for a number of cases.

Expected Amplitude response

Since VIV predictive programs estimate only the 1st harmonic response, it is helpful to represent the measured amplitude of the 3x response in terms of the measured 1x response. Further, as discussed earlier, representing the 3x RMS response as a ratio of the 1x RMS response removes the influence of mode number on strain.

The ratio of the maximum 3x RMS strain response to the maximum 1x RMS strain response for any given test, referred to as 3x-to-1x ratio from here on, was calculated for two different categories of experiments.

1. The first category considered tests where the primary VIV frequency was not completely constant in time, but the 1x, 2x and 3x harmonics could still be clearly identified in the strain PSD and filtered out. These cases do not allow the third harmonic to develop fully because of the fluctuating 1x frequency. Typical results, along with the test names, are shown in Table 5. The values of the 3x-to-1x ratio of strains vary from 0.96 to 1.48 and have a mean value of 1.25.
2. The second category considered time intervals within tests that are at least twenty seconds long during which steady-state conditions were achieved i.e. the primary VIV frequency did not fluctuate. An example of such a time interval is shown in Figure 45 where the last 60 seconds of the test were steady-state. These cases allow the third harmonic to develop fully leading to large 3x-to-1x ratios. The test names, the start and end of the steady-state regions in seconds and the calculated 3x-to1x ratios are shown in Table 6. The average ratio is 1.46.

As expected, the third harmonic response is stronger when it is allowed to develop fully in the steady state regions. However, using the values of the 3x-to-1x ratio obtained from the steady-state regions are too conservative in design because the steady state regions occur only a small fraction of the time. Therefore, these ratios provide an upper bound of values for an engineer to use when incorporating the effects of the higher harmonics.

Table 5 – The ratio of the RMS 3x strain to RMS 1x strain for all tests

Test name	Ratio
20061023203818	1.28
20061023204504	1.37
20061023205043	1.48
20061023205557	1.03
20061022154633	0.96
20061022153702	1.31
20061022153003	0.96
20061023204504	1.37
20061020182045	1.24
20061020175715	1.41
20061020174124	1.27
20061020172900	1.32
Mean Value	**1.25**
Standard Deviation	0.17

Table 6 – The ratio of RMS 3x strain and RMS1x strain for steady-state regions in the second Gulf Stream experiments

Test name	Start Sec	Stop Sec	Ratio
20061020175715	0	35	1.35
20061020175715	125	155	1.49
20061020180904	35	65	1.41
20061021142015	1	35	1.40
20061023203818	110	170	1.37
20061023205043	85	125	1.61
20061021174641	20	50	1.56
		Mean Value	**1.46**
		Standard Deviation	0.10

Correlation Plots

When the maximum amplitude of the 'normalized 3rd harmonic RMS strain' and the maximum amplitude for the 'normalized 2nd harmonic strain' was plotted for multiple Gulf Stream tests, a clear trend is observed which resulted in a correlation coefficient of 0.84. In Figure 57 which shows this correlation, each point of the plot indicates a separate experiment. The clear trend indicates that in the Gulf Stream experiments, a large 3rd harmonic amplitude response is likely when a large 2nd harmonic amplitude response is observed.

This relation has been established in the laboratory where it has been observed that when rigid cylinders have both cross-flow and in-line degrees of freedom, their response may include a wake pattern called the '2T' pattern that corresponds to the shedding of 3 vortices per VIV half cycle [6]. The displacement response is also larger in the '2T' mode compared to the displacement response if only the cross-flow response was possible.

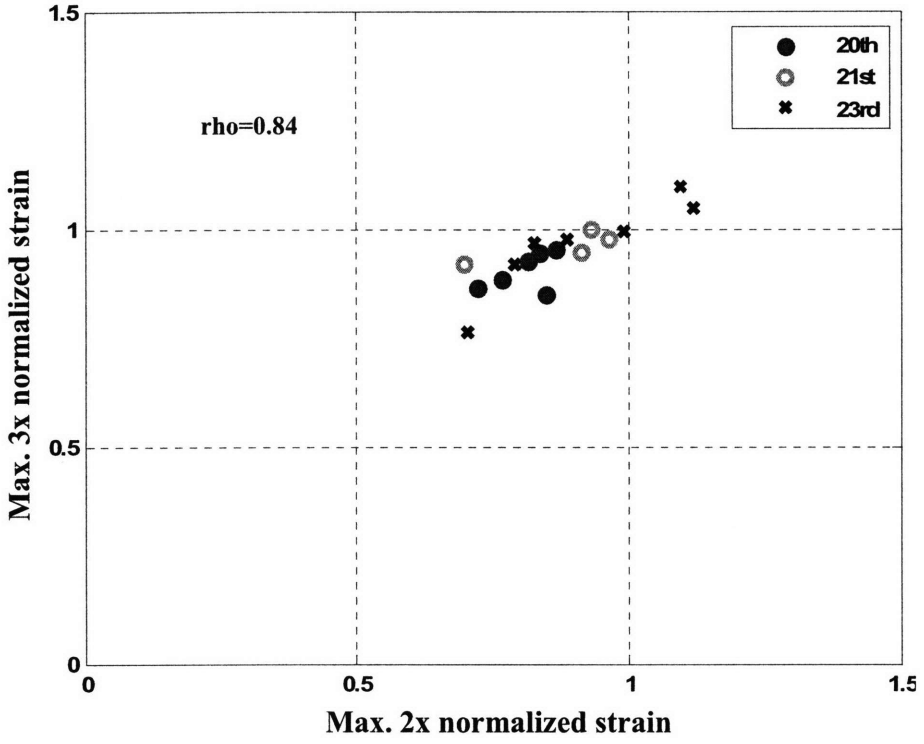

Figure 57 - The cross-flow components 3x and 1x RMS strain show no trends. The 3x RMS and 2x strain, which are in the cross-flow and in-line direction, show a clear dependence on one another. The data is from experiments on the 20th, 21st and 23rd of October, 2006.

5.4.2.2 The 5th Harmonic

Not much is known about the forcing and response at the 5th harmonic for either spring mounted rigid cylinders or flexible pipes undergoing VIV. In fact, many tests performed with spring mounted rigid cylinders show very little 5th harmonic forcing [29]. The Lake Seneca, and the Gulf Stream experiments in particular, measured large RMS strain at the 5th harmonic frequency. However, the response was localized and did not always occur.

Location of the maximum RMS strain

Similar to the 3rd harmonic, the reduced velocity of the maximum 5x RMS response is seen to occur close to that of the maximum RMS 1x response. Figure 58 shows the reduced velocity at the spatial location of the maximum RMS 5th harmonic response plotted against the reduced velocity at the spatial location of the maximum RMS 3rd harmonic response. They seem to occur at the same reduced velocities.

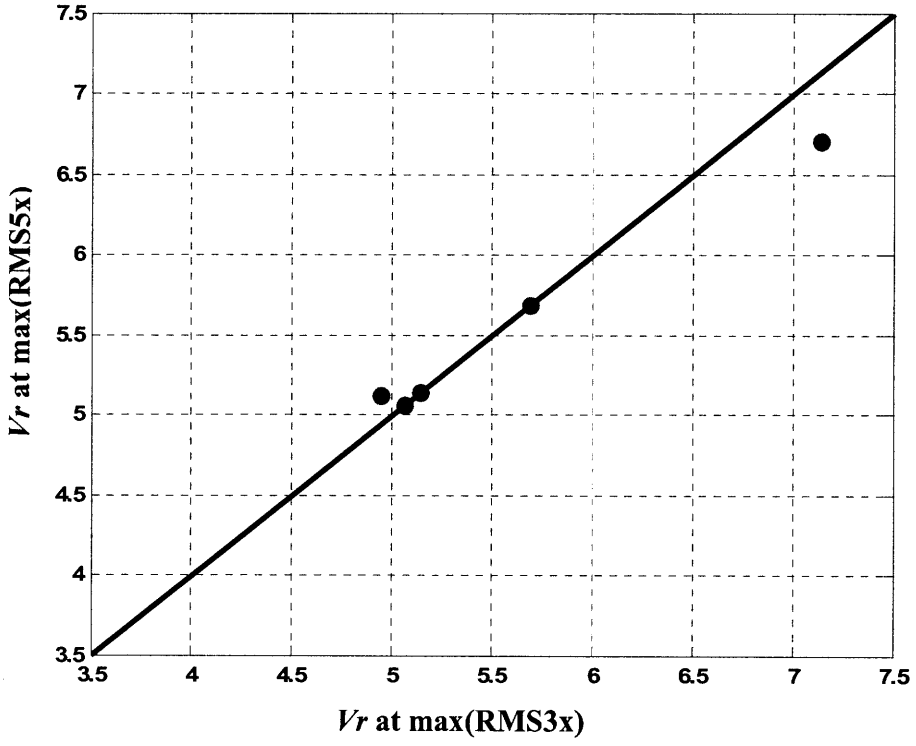

Figure 58 – Comparison of the reduced velocity of the maximum 3rd harmonic response and the maximum 5th harmonic response.

Expected Amplitude response

Among the additional difficulties in analyzing the fifth harmonic amplitude are :-

- When the VIV frequency was not steady, it becomes difficult to distinguish the 5^{th} harmonic from the other harmonics because the frequencies of the 5^{th} harmonic response are likely to overlap with the frequencies of the 4^{th} harmonic response in the PSD even if the frequencies of the 2^{nd} and 3^{rd} harmonics can be clearly distinguished in unsteady response conditions.
- In some high speed tests where steady-state conditions were achieved, the 5^{th} harmonic frequency was greater than the Nyquist frequency, which was about 25 Hz for the second Gulf Stream experiments. These cases had to be discarded for the analysis of the 5^{th} harmonic response.

The strain response amplitudes for the 5^{th} harmonic were studied in terms of the 1^{st} harmonic RMS strain response, for reasons discussed earlier. Further, the amplitude of the 5^{th} harmonic was studied using two different approaches.

1. Steady state cases were considered to provide a conservative estimate of the 5^{th} harmonic RMS strain response, assuming that they allowed the 5^{th} harmonic to fully develop. The results are shown in Table 7. The value of the ratio of 0.77 is a conservative estimate; the standard deviation of 0.23 indicates the variation in the 5^{th} harmonic response.
2. Use many samples where the 1^{st} harmonic frequency did not change much but only lasted for a few seconds. These samples indicate the regions where the 5^{th} harmonic, though present, did not have the time to develop fully. These results, shown in Table 8 represent a mean estimate of the 5^{th} harmonic response. The standard deviation is still very large.

Table 7 – The analysis of steady state cases reveals a conservative estimate of the 5th harmonic strain response. The ratio refers to the ratio of the maximum RMS 5th harmonic response to the maximum RMS 1st harmonic response

Test Name	Start Sec	Stop Sec	Ratio
20061020175715	0	35	0.77
20061020175715	125	155	0.46
20061020180904	35	65	0.81
20061021142015	1	35	0.71
20061023203818	110	170	1.10
		Mean Value	**0.77**
		Standard Deviation	0.23

Table 8 - The analysis of small time length steady state cases provided a mean estimate of the maximum RMS 5th harmonic strain response. Ratio is the maximum RMS 5th harmonic strain response divided by the maximum RMS 1st harmonic strain response.

Test Name	Start Sec	Stop Sec	Ratio
20061020172900	25	35	0.83
20061020174124	27	32	0.33
20061020174124	83	88	0.23
20061020174124	142	148	0.38
20061020175715	10	30	0.96
20061020175715	132	142	0.77
20061021140802	107	112	0.47
20061021142015	42	47	0.66
20061021174641	110	115	0.60
20061021174641	22	27	0.73
20061023203200	160	170	0.55
20061023203818	17	22	0.90
20061023203818	62	67	0.34
20061023204504	27	35	0.41
20061023204504	140	150	0.32
20061023205043	52	58	0.58
		Mean Value	**0.57**
		Standard Deviation	0.23

Correlation Plots

No clear relationships for the existence of the higher harmonics could be developed with reduced velocity but observations in most cases show 5x response amplitude as more localized than the 3x response amplitude. Further, some cases indicate the 5th harmonic peak to occur between Vr=5.25 to Vr=5.75.

Analysis of the tests performed during the second Gulf Stream experiments reveals that the 5th harmonic response does not always occur and its strength varies greatly, unlike the 3rd harmonic response. When correlations were studied for "normalized" strains, no clear trends were observed with the "normalized" 1st harmonic and 3rd harmonic strains. However, when the maximum RMS 4th harmonic strain, which is in the in-line direction, and the maximum RMS 5th harmonic strains are compared, they show a clear correlation. This suggests that the 4th and 5th harmonics are causally related and perhaps result from the same hydrodynamics in the wake of the oscillating cylinder. There are other reasons to believe that the 4th and 5th harmonics may be related as discussed in the section on the 4th harmonic.

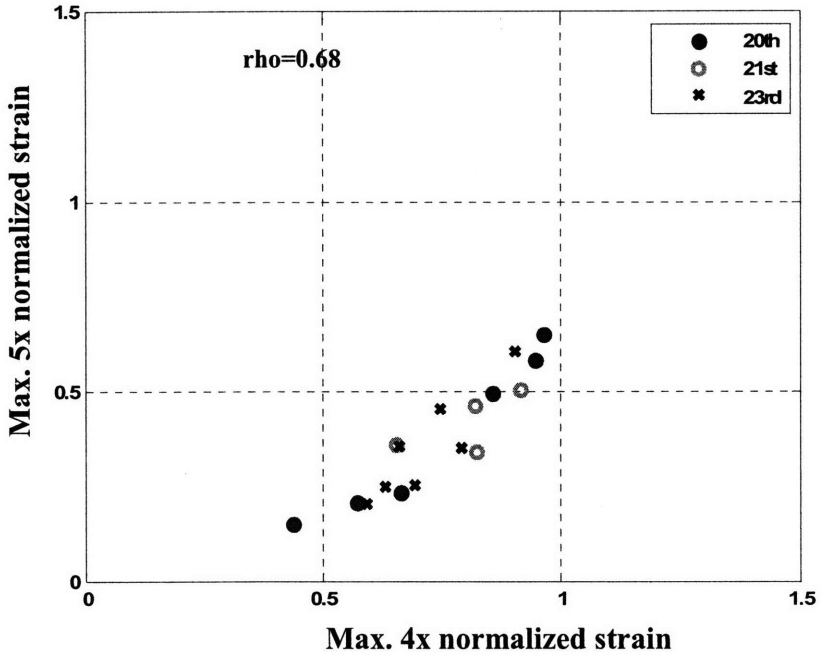

Figure 59 – The maximum normalized RMS 5x strain shows a clear trend when plotted against the maximum normalized RMS 4x strain. The data is from experiments on the 20th, 21st and 23rd of October, 2006.

In a 1993 paper, J. Kim Vandiver [54] proposed that a shear parameter could be important in VIV. Vandiver's shear parameter was

$$Shear\ Parameter = \frac{D}{V}\frac{\partial V}{\partial x}$$

It was of interest to ascertain if the how the higher harmonics depended on current shear. The shear parameter used in the calculation was a modified version of the parameter suggested by Vandiver

$$\beta_1 = \frac{D}{V}\frac{\partial V}{\partial x}$$

Since, $St = \frac{fD}{V}$, then $\frac{D}{V} = \frac{St}{f} = \frac{1}{V_r f}$ and $\beta_1 = \frac{1}{V_r f_{x1}}\frac{\partial V}{\partial x}$; f_{x1} is the measured 1x frequency of the test. As Vr is approximately the same in the power-in region for every test, the shear parameter can be written as

$$\beta_2 = V_r \beta_1 = \frac{1}{f_{x1}}\frac{\partial V}{\partial x} \tag{4.27}$$

The rate of change of velocity was measured as the average value over 5 sensors (28 feet) in the region of the maximum 5x response. The maximum 5x RMS strain response, which was plotted against the shear parameter, was normalized using the procedure reported earlier to remove the effects of frequency on the strain response.

Figure 60 show that there is a clear increase in the normalized 5x RMS response with increasing shear in the current, as indicated by a correlation coefficient of 0.97. When a similar analysis was done for the normalized 3x RMS strain response and normalized 1x RMS strain response, no clear trends were observed. This surprising result suggests that the magnitude of vibration at the 5th harmonic is influenced by the amount of shear in the current.

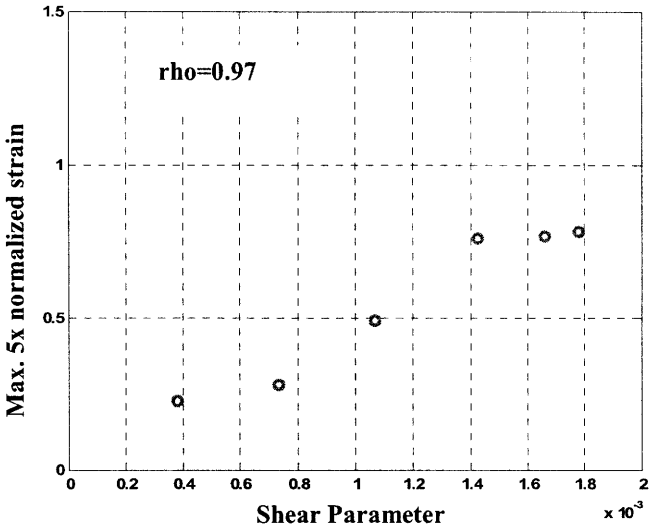

Figure 60 – The normalized RMS 5x strain shows clear trends when plotted against the shear parameter.

This variation with shear could help explain why a prominent 5th harmonic has not been seen in free vibration laboratory experiments with spring mounted rigid cylinders. It could also explain the high standard deviation in the magnitudes of the 5x-to-1x ratio studied earlier. Further, a similar trend was observed for the 4th harmonic providing further indications that the 4th harmonic and the 5th harmonic forcing are related and may be coming from the same hydrodynamics in the wake.

5.4.3 The in-line harmonic components

5.4.3.1 The second harmonic

The 2nd harmonic occurs because vortices shed in the wake of a cylinder cause a force every half VIV cycle that alternates in the cross-flow direction. The in-line component of this force is always in the same direction causing a forcing at twice the frequency of the cross-flow oscillating force.

Figure 61(a) shows the axial distribution of the RMS 1x and 2x strain responses for Test-20061023205557 from the second Gulf Stream experiments. The high incident velocity, as seen in Figure 61(b), resulted in a top angle of 62 degrees and a primary VIV frequency of about 5.9 Hz which corresponded to the 40th modal frequency of the pipe. The total 1x and 2x RMS strain responses were calculated using the methods described earlier.

The 1x and 2x RMS strain peaks do not happen at the same axial location on the pipe. The region between z/L=0.1 and z/L=0.5, which contains the maximum 1x and 2x RMS strain response, is plotted against reduced velocity in Figure 62. The peak in the 2nd harmonic occurs at a Vr=4 while the 1st harmonic peak is seen at a higher Vr of 5.

This observation, that the 2x RMS strain peak occurs at a lower reduced velocity than the 1x RMS strain peak, holds true for most tests from the Second Gulf Stream experiments. Figure 63 plots the reduced velocity at which the maximum RMS 1x strain response is seen against the reduced velocity at which the maximum RMS 2x strain response is seen in eleven[5] different tests. The 1x and 2x RMS strains were calculated using the method described earlier.

[5] These tests were chosen because they had strong 1x and 2x responses, making it easy to identify the region of maximum RMS response, and unidirectional change in current, that is increasing current or decreasing current, in the region of maximum RMS 1x and 2x response which made it easier to correctly identify the reduced velocity in the region of interest.

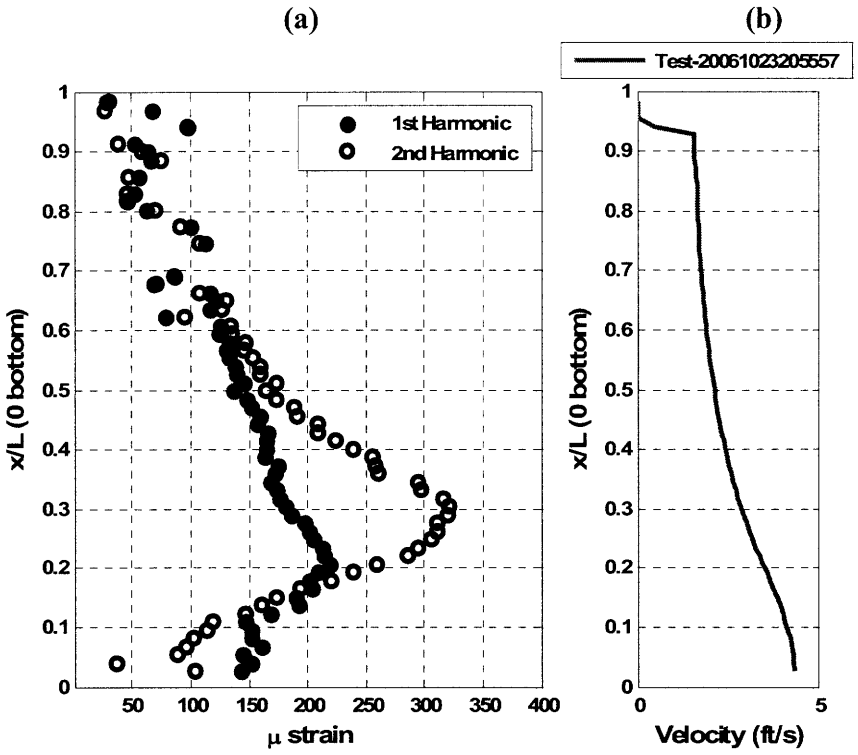

Figure 61 - RMS 1st and 2nd harmonic strain for test 20031023205557.

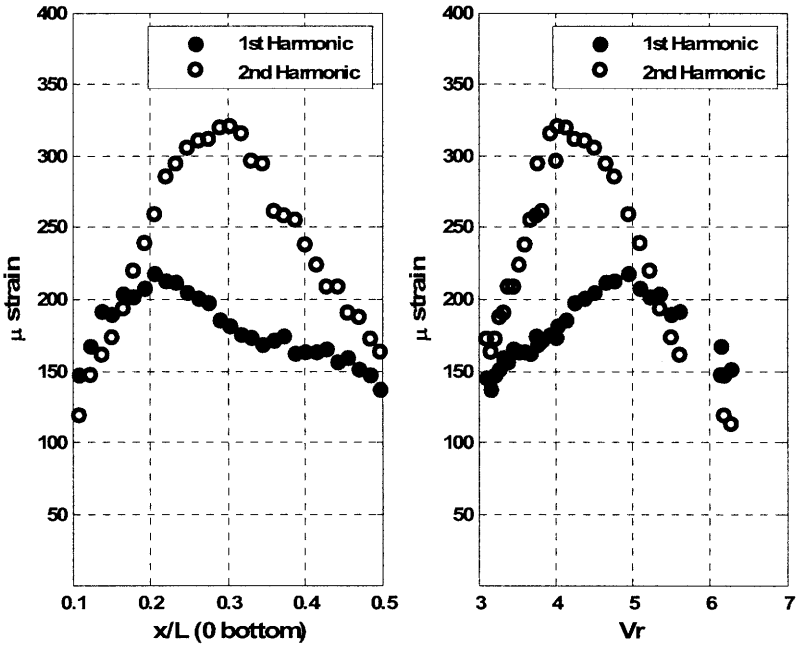

Figure 62 – The region of maximum response of the 1x and 2x RMS strain for Test 20061023205557 is plotted against (a) axial position of the pipe where 0 is the bottom end and (b) reduced velocity

The sensors corresponding to the maximum 1x and 2x RMS strain were identified and the corresponding reduced velocity was calculated. This was done for all the eleven tests reported in Figure 63. The black line represents the condition when both the 2x and 1x RMS strain response happen at the same reduced velocity. The scatter in Figure 63 indicates that the 1x and 2x RMS strain peaks do not happen at the same reduced velocity for every test. The reason for this is not clear. The scatter in the reduced velocity at the 1x peak can partially be due to errors in identifying a clear peak in the 1x RMS strain response. In most cases, the 1x RMS strain response amplitude varies slowly and there can be many sensors with approximately the same response amplitude in the region of maximum 1x response.

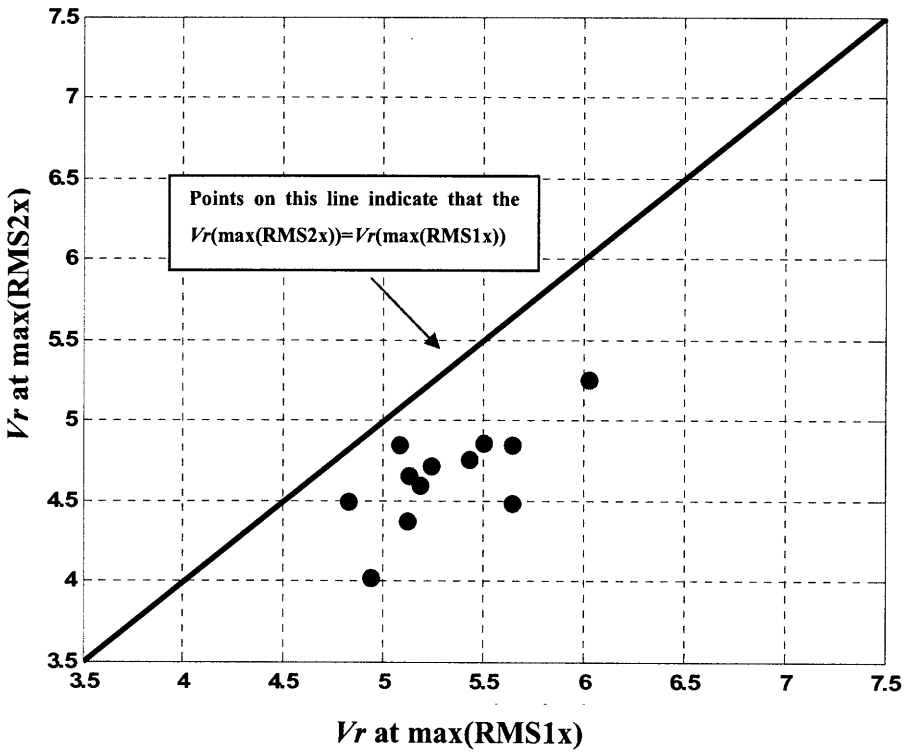

Figure 63 – The reduced velocity at which the maximum 1x RMS strain is always higher than the reduced velocity at which the maximum RMS 2x strain occurs. Results from 11 different tests are shown here.

The topic of where the 2x maximum occurs is revisited when the X,Y trajectories are analyzed and observations are made regarding the phase relationships between the 1x and 2x harmonics.

Many laboratory free vibration experiments with spring mounted rigid cylinders have found that the cross-flow motion amplitude is larger when the in-line motion of the oscillating cylinder is not restricted. Similar results were found for the second Gulf Stream experiments. When the maximum normalized amplitude of the cross-flow motion was compared with the maximum normalized amplitude of the in-line a high correlation of 0.97 was found. Figure 64 shows this result, which used tests from three different days of the second Gulf Stream experiments.

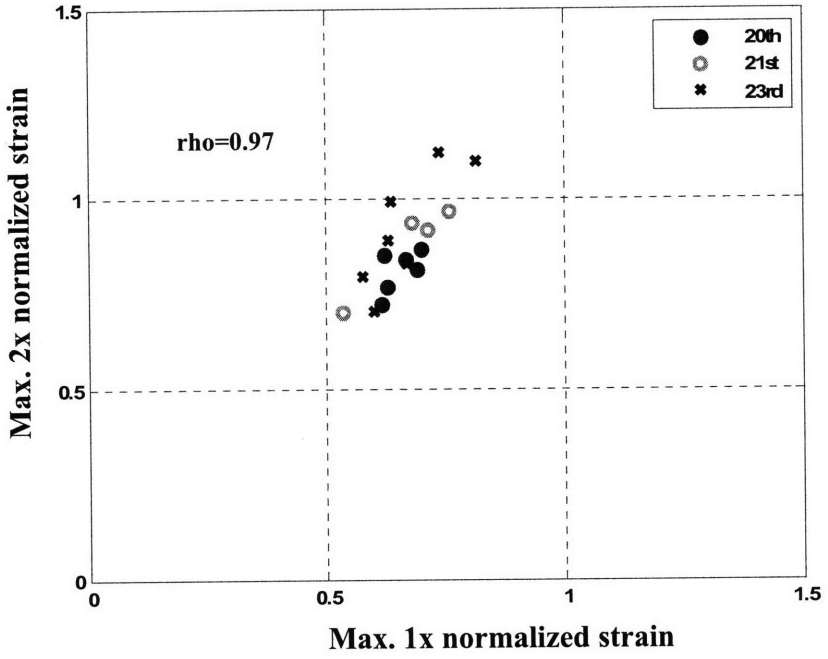

Figure 64 – A strong correlation is observed between the peak 1st harmonic response and the peak 2nd harmonic response. The data is from experiments on the 20th, 21st and 23rd of October, 2006.

5.4.3.2 4th Harmonic

Little research has been carried out on the 4th harmonic and few papers are available on the subject in the VIV literature. It is known that they occur in the in-line direction making their strain contributions add to the 2nd harmonic strains which has implications in calculating fatigue damage in the in-line direction.

Location of the maximum RMS strain

In most of the tests from the second Gulf Stream experiments, the location of the strongest 4th harmonic corresponds to a higher reduced velocity than at the location of

the 2nd harmonic maximum response. The peak in the 4th harmonic RMS strain occurs closer to the region of the peak in the 3rd harmonic RMS strain. Figure 65 shows the reduced velocity in the region of the maximum observed 4th harmonic RMS strain response against the region of the maximum RMS 2nd harmonic response (blue dots) and the maximum RMS 3rd harmonic response (red x's). This may be an indication that the hydrodynamic cause of the 4th harmonic response is more related to the hydrodynamic cause of the 3rd harmonic response and not the 2nd harmonic response, even though the 2nd harmonic is in the in-line direction and the 3rd harmonic is in the cross-flow direction.

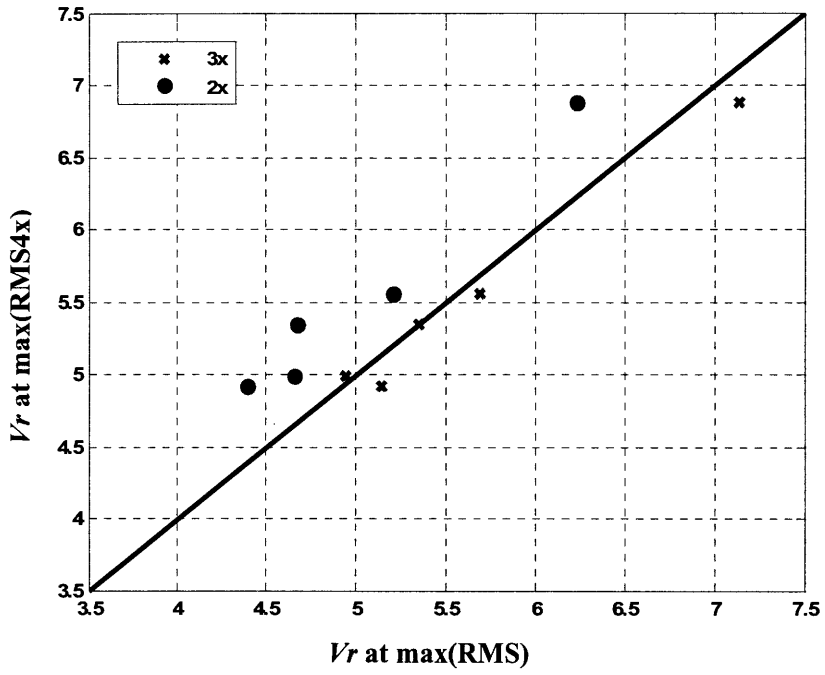

Figure 65 – The reduced velocity at which the peak RMS 4th harmonic strain is observed is close to the reduced velocity at which the peak RMS 1st harmonic strain is observed.

Correlation Plots

Since the 4th harmonic is in the in-line direction, it would be reasonable to expect some relation between the amplitude of strain response of the 2nd harmonic and the 4th harmonic. However, when the normalized maximum 2x RMS strain response is plotted against the normalized maximum 4x response in Figure 66, no clear relationships are seen as indicated by the correlation coefficient of 0.25. As the plot considers tests from

three different days of testing, it suggests that there are other parameters that influence the development of the 4th harmonic which do not affect the 2nd harmonic. Earlier it was shown Figure 59 that the magnitude of the maximum 4th harmonic response is correlated to the magnitude of the maximum 5th harmonic response, thought they occur in the in-line and cross-flow directions respectively.

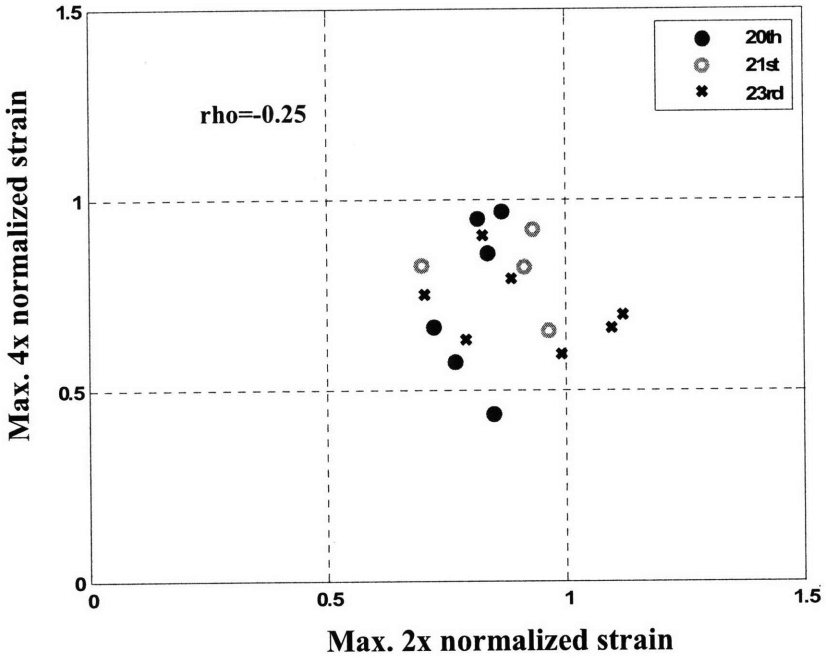

Figure 66 – Maximum normalized 4x and 2x RMS strains show no dependence on each other. The data is from experiments on the 20th, 21st and 23rd of October, 2006.

5.4.4 Higher harmonics magnitudes at the boundary

The second Gulf Stream experiments revealed that the peak in the higher harmonic strain response never occurred near the end of the pipe (near the boundary). Table 9 shows for eleven different second Gulf Stream experiments, the maximum observed RMS strain for the 2nd and 3rd harmonics in the ten sensors nearest to the bottom boundary as a fraction of the maximum RMS 2x and 3x strains observed anywhere on the pipe. The results show that the magnitude of the 2x and 3x response near the boundary is much smaller than the maximum observed 2x and 3x response. Similarly, the 4th and 5th harmonics are not observed near the boundaries.

This observation has important implications since VIV prediction programs like SHEAR7 predict a standing wave response at the boundary. This usually results in the

maximum 1x strain being predicted at the boundaries. The observation that the higher harmonics do not occur near the boundaries is important. Near boundaries, no corrections to strain and fatigue damage will be required to account for the higher harmonics.

Table 9 – The maximum 2x and 3x RMS strain response is a fraction of the maximum observed 2x and 3x RMS response for a test.

Test Names (11 tests from the second Gulf Stream experiments)	Max RMSx2 (sensor 60 to 70)/ Max RMSx2 (sensor 1 to 70)	Max RMSx3 (sensor 60 to 70)/ Max RMSx3 (sensor 1 to 70)
20061023203818	0.82	0.69
20061023204504	0.64	0.44
20061023205043	0.74	0.54
20061023205557	0.61	0.79
20061022154633	0.73	0.79
20061022153702	0.52	0.52
20061022153003	0.70	0.62
20061020182045	0.64	0.55
20061020175715	0.57	0.57
20061020174124	0.61	0.60
20061020172900	0.53	0.45

5.5 Results and conclusions

The higher harmonics have been observed for many decades but their contribution to the over strain response and their importance to fatigue damage have only recently become clear. There is however, little data in the literature that will allow an engineer to incorporate the effects of the higher harmonics. This chapter provides some guidance on the relative magnitudes of these harmonics, when they occur, where they occur, phase

relationships and displacement patterns that favor particular harmonics and other properties observed during the second Gulf Stream experiments.

The main results in this chapter are :-

1. The peak in the 2nd harmonic RMS strain is usually observed at a lower reduced velocity than the peak in the 1st harmonic VIV strain. A high 1x peak response usually translates to a high 2x peak response and a high 2x peak response usually occurs when there is a high 3x peak response. The 1x and the 2x responses are phase locked at any particular location and the maximum response in the 2x direction occurs when the phase difference between the 1x and the 2x response is 90 degrees, which results in a 'figure c' response.
2. The peak in the 3rd harmonic RMS strain is usually observed at or close to the peak in the 1st harmonic response. A large 1x response does not always correspond to a large 3x response. The conservative estimate of the peak magnitude of the 3x strain response is 1.45 times the peak magnitude of the 1x strain response while an average estimate is 1.24 times the peak magnitude of the 1x strain response. The 3x response is also phase locked with the 1st harmonic and the highest 3rd harmonic response is seen with the displacement X,Y shape is a 'figure 8' or a "figure 8+c' indicating a phase difference between the cross-flow and in-line motion between 0 and 45 degrees.
3. The 4th and the 5th harmonics seem to occur together and a good correlation was found between their maximum RMS amplitude responses. The 5th harmonic was found to be unrelated to the 1st and 3rd harmonics and large variations were found in the observed maximum 5x RMS strain response from one test to another.
4. A careful analysis of the traveling wave in the pipe provided insight into why and where the higher harmonics are observed. The traveling wave is generated with the X,Y trajectory plots looking like 'figure 8's'. Due to the non-dispersive nature of the pipe used in the second Gulf Stream experiments, this shape is maintained as the wave travels down the pipe. As

the wave propagates, the phase relations between the in-line and cross-flow motions begin to change, probably due to slight differences in propagation speeds between the 1st and the 2nd harmonics. The peak in the 3rd harmonic occurs in the region where the phase is between 0 degrees and 45 degrees leading to a 'figure 8' or a 'figure 8+c' pattern. As the wave propagates, the phase relations between the in-line and cross-flow motions change further until they result in a 'figure c' pattern. This is the region where the peak response in the second harmonic is observed.

These results raise important questions that have not yet been addressed by the VIV community. If the phase difference is so important in determining the regions of the higher harmonics, will any significant higher harmonics be observed in highly dispersive pipes where the phase relationships change very quickly with time? How dependent are the higher harmonics on reduced velocity in traveling wave environments?

6. Incorporating the higher harmonics in VIV fatigue estimates

One of the most important consequences of Vortex-Induced Vibrations (VIV) is increased fatigue damage. The current state-of-the-art in VIV prediction for marine risers, accurately estimates the RMS cross-flow displacement response of VIV but makes no attempt to estimate the VIV displacement amplitudes in the in-line direction or include the higher harmonics in the total response in the cross-flow direction. In light of the significant strain energy at the higher harmonic frequencies found in recent experiments (discussed in Chapter 5), this chapter presents the fatigue contribution of the higher harmonics and confirms that they cannot be ignored.

Further, skepticism about the accuracy of predicted VIV results coupled with the severe consequences of failures in the oil and gas industry has prompted the use of high safety factors in VIV fatigue design. This chapter reviews the current methods adopted by the VIV community, identifies the assumptions that lead to overly conservative results, and suggests modifications using results from the recent Gulf Stream experiments to remove some of the unnecessary conservatism in VIV prediction.

Finally, two different methods of incorporating the higher harmonics are proposed in this chapter. Both methods use currently existing programs and procedures, providing a riser engineer with tools that can be immediately implemented to incorporate the contributions of the higher harmonics in VIV related fatigue damage calculations.

6.1 Higher Harmonic Contributions to fatigue in experimental data

As shown in chapter 5, the contributions of the higher harmonics to total cross-flow strain can be substantial. In some regions of the pipe the higher harmonics contribute more that half of the total cross-flow RMS strain (refer Figure 48 in Chapter 5). Since fatigue damage is proportional to $(\text{stress})^m$, where m is the slope of the S-N curve (usually between 3 and 4) and stress is proportional to strain, the increase in the RMS strain due to the higher harmonics has a significant impact on the fatigue damage of the pipe. Assuming an API X' S-N curve and the Young's Modulus of Steel (Es) as 200×10^6 MPa, the fatigue damage calculated from the measured data for Test 20061023203818 from the second Gulf Stream experiments is much larger than the fatigue damage

predicted using Shear7 (Figure 67). If the Shear7 predictions in Figure 67 were used in design, the maximum predicted fatigue damage would occur in the standing wave at the bottom boundary. SHEAR7 would not have predicted the location of the measured peak damage rate correctly because it only accounts for the 1x contribution and not the 3x and 5x components which are significant closer to the middle of the pipe.

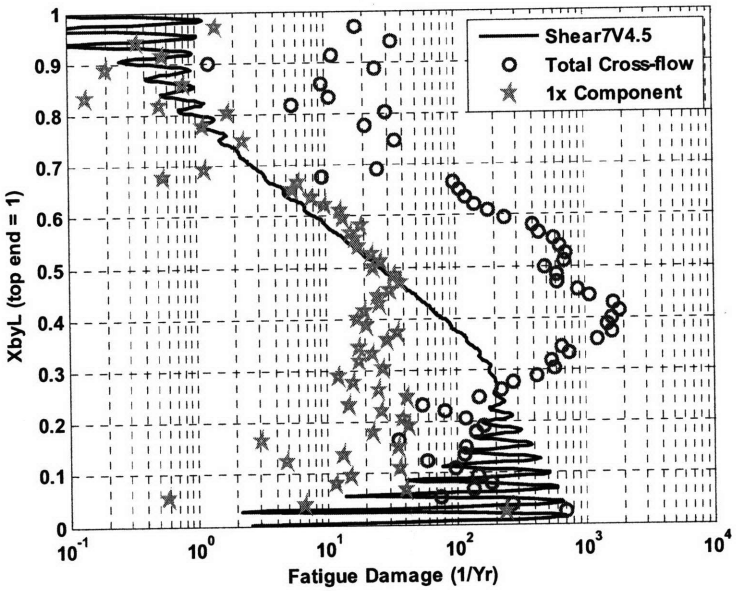

Figure 67- Comparison of fatigue damage predicted by Shear7V4.5 to that calculated from measured data using the Dirlik method. Young's modulus for steel and API-X' S-N curve were used.

As mentioned earlier, the location of the maximum predicted damage by Shear7V4.5 is near the boundary (Figure 67) due to the standing wave. If the total damage rate, calculated using measured strain along the pipe is normalized by the maximum Shear7V4.5 predicted damage anywhere on the pipe, measured fatigue damage exceeds the maximum predicted by Shear7 by a factor of 3 (Figure 68). Although the actual damage rate is greater than the maximum predicted by a factor of 3, this is within the factor of safety normally used in the industry and could be a possible reason that failures in actual practice have not been observed.

However, fatigue results presented as above may understate the significance of the higher harmonic contributions to fatigue. The highest fatigue damage occurs in the region of maximum 3x and 5x response, not at the boundary as predicted by Shear7. It

is more realistic to examine the region of maximum stress due to the higher harmonics, and compute the ratio of the total damage rate to the maximum 1x damage rate in the same region. The result, shown in Figure 69, indicates that the higher harmonics can increase fatigue damage by a factor of 40 or more in certain regions of the pipe. Note that in both Figure 68 and Figure 69, sensors 33, 43 and 53 are marked in solid dots. The spectra at these sensor locations are studied in more detail later in this chapter.

Clearly, there is a need to incorporate the higher harmonics in VIV fatigue estimates. However, in order to constructively suggest methods of doing so, it is important that we understand the fatigue estimation methodology currently in use in the oil and gas industry.

6.2 Data properties that are important for fatigue calculations

The damage caused by a stress time series depends on its statistical and spectral properties. However, if is helpful to understand the steps involved in fatigue life prediction before we study the important properties of stress time histories.

a) Predictive programs, like Shear7, are used to estimate the RMS amplitude response of a pipe undergoing VIV. These programs utilize user defined structural models of the pipe, user input current profiles and data banks of empirical lift and added mass coefficients to model the response of the pipe. The predicted RMS amplitude response is converted to RMS stress response using the structural properties of the modeled pipe.

b) A stress range Probability Distribution Function (PDF), calculated using the predicted RMS stress response, is used to estimate the fatigue damage per unit time. The stress range PDF is developed either by using standard formulations, like the Rayleigh formulation or by using Rainflow cycle counting techniques.

c) S-N curves are used to establish a relationship between the stress range distribution and fatigue damage rate. This widely used method is based on empirical formulations determined from many years of fatigue experiments.

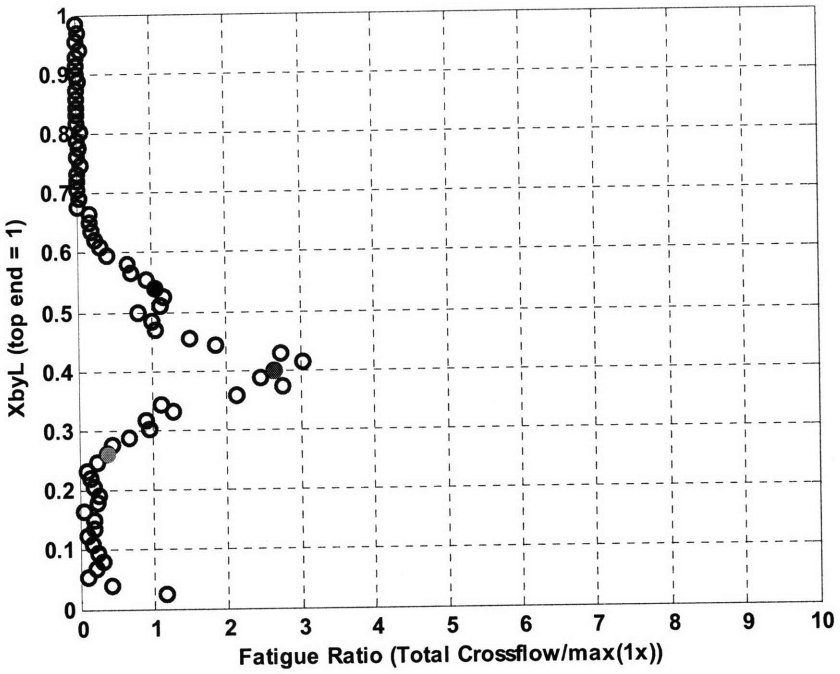

Figure 68 - The ratio of the total cross-flow damage to the maximum damage by SHEAR7-V4.5. The ratio at sensors 33, 43 and 53 are shown by solid dots.

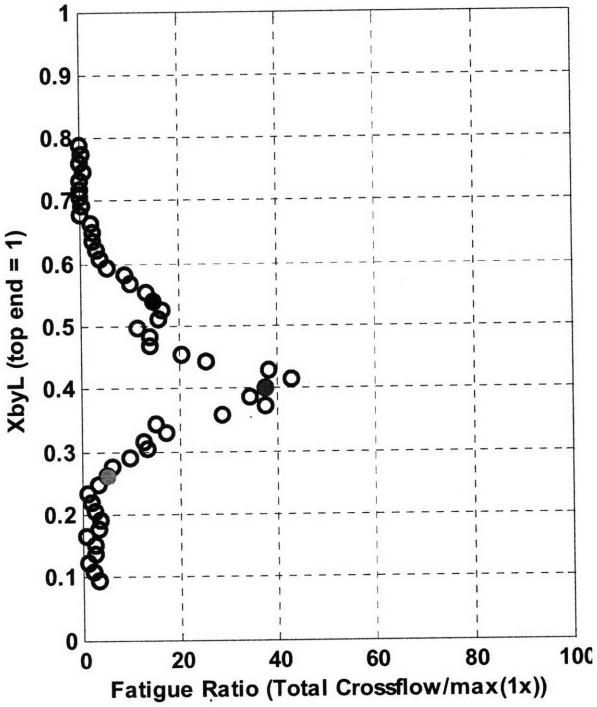

Figure 69 - The ratio of the total damage rate to the maximum 1x damage rate in the same region, which occurs at z/L=0.2. The ratio at sensors 33, 43 and 53 are shown by solid dots.

The critical step in this process, apart from the prediction of the response, is the calculation of a stress range PDF from the RMS stress response or time histories. There are two important data properties that influence the formulations used in calculating the stress range PDFs.

6.2.1 Probability Distribution Function (PDF) from zero-mean time series

The first property is the probability distribution of the VIV data time series measurements. The most common PDF for a zero mean time series is the Gaussian distribution. It follows from the central limit theorem that a sum of independent variables with the same probability distribution will result in the final data to have a Gaussian distribution. Until recently, VIV prediction programs like Shear7 describe the VIV response of a pipe in terms of a superposition of independent variables or modes. It is commonly assumed that the time history of stress at each spatial location is Gaussian distributed. Figure 70 shows the probability distribution of a response of a typical flexible cylinder as modeled in the VIV response prediction program SHEAR7.

The data shown in Figure 70 was generated using modal amplitude and phases calculated by Shear7. The response was normalized to have a variance of 1. Also shown in the figure is the Gaussian probability distribution with unit variance. The good match indicates that when many signal components with different frequencies are summed, the result is a Gaussian process.

The Gaussian nature of the predicted time history of VIV allows the use of established statistical properties, such as the distribution of maxima, for such distributions.

6.2.2 Spectral content of the data time series

Another key aspect of VIV data is its spectral content. If all or most of the energy in the spectrum of the data is contained in a small frequency bandwidth, the vibrations are said to be Narrow Banded. However, if the spectrum shows the energy coming from a wide range of frequencies the data is said to be broad banded. An example of a narrow banded and broad banded spectra shown in Figure 71(b).

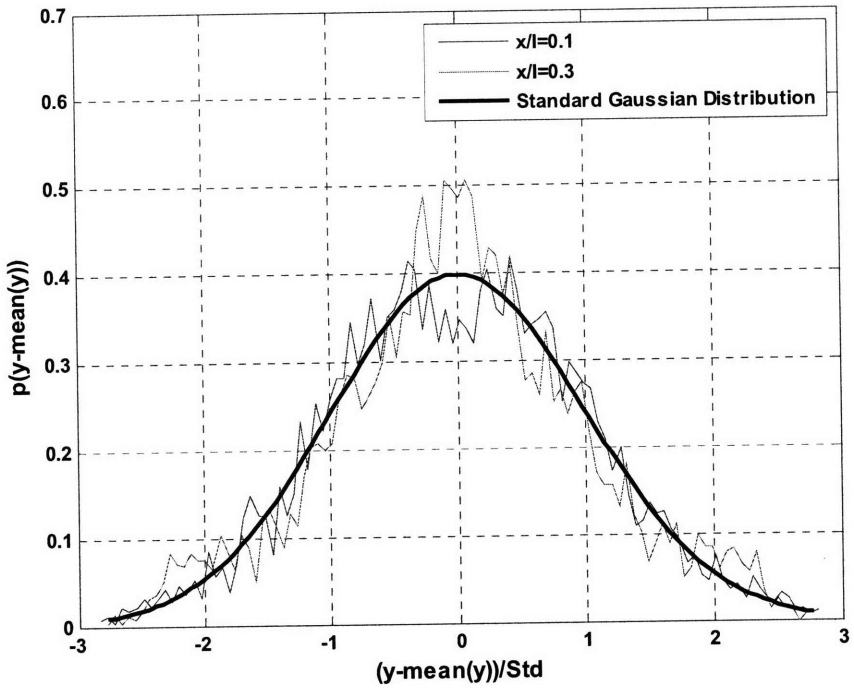

Figure 70 - Distribution of time series data generated from Shear7 output

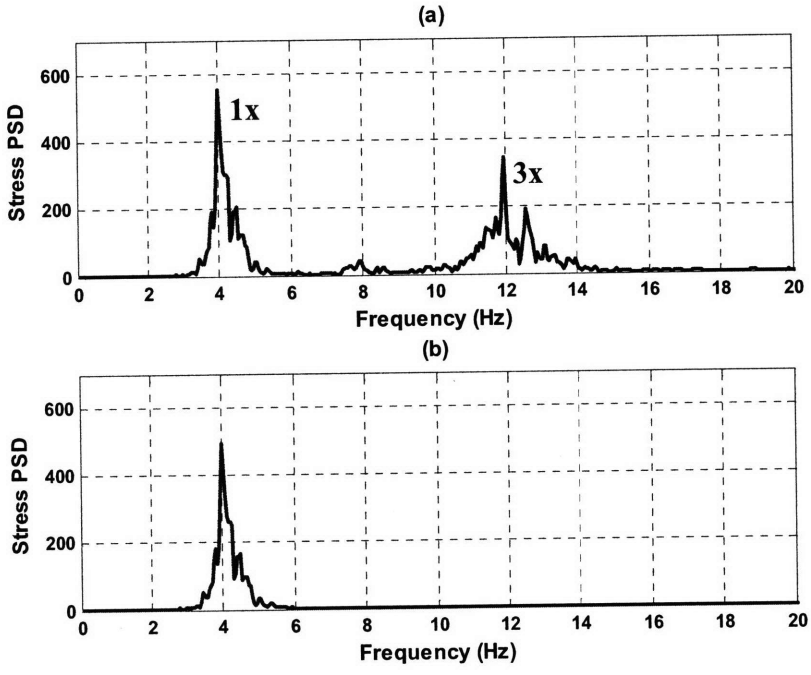

Figure 71 - (a) An example of a broadband spectrum (b) and example of a narrow band spectrum

Since VIV is essentially a resonance phenomenon, one would expect that in the regions of maximum response ("power-in" regions), most of the spectral energy would be around the local Strouhal frequency or its multiples [10]. If only the vibrations around the Strouhal frequency are considered, an assumption made in many predictive programs, the response can be considered to be narrow banded. This assumption greatly reduces the complications involved in obtaining the stress range PDF, an essential input for fatigue calculations.

Various formulations are available for the distribution of maximas of stress time series with different statistical distributions, but there are no similar formulations for stress range, which is the difference between the maxima and minima for each cycle. However, the time variation of a narrow banded spectrum can be assumed to be like a modulated sinusoid, Figure 72, and hence the stress range can be approximated as twice the stress maxima.

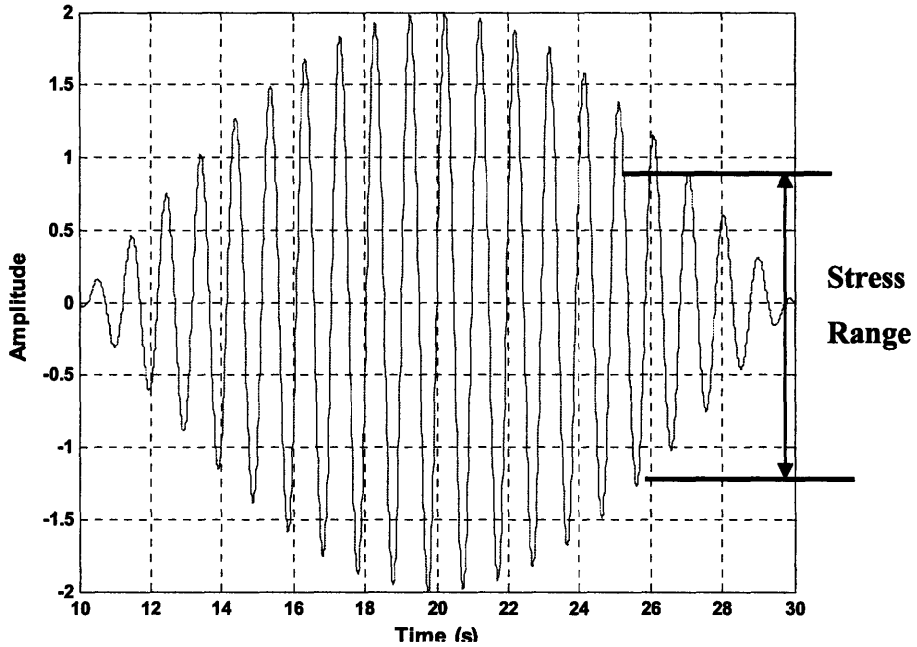

Figure 72 - Amplitude variation with time for a narrow banded spectrum

In summary, most predictive programs consider VIV to be a narrow-banded, Gaussian distributed process. Maximas of processes of this type can be shown to be Rayleigh distributed and stress ranges can be considered to be twice the maximas.

Therefore, it is common to use fatigue formulations based on the Rayleigh distribution for the stress ranges in VIV analysis.

6.3 Properties of the Gulf Stream strain data

Even though predictive programs assume VIV to be a narrow-banded Gaussian distributed process, few, if any, studies exist on the actual statistical nature of VIV. Chapter 5 discussed the higher harmonics in the Gulf Stream experiment data and showed that the strain PSD in certain regions of the pipe has a lot of energy at the higher harmonic frequencies, making the narrow-banded assumption inaccurate. Figure 73(a) is another example, this time from the first Gulf Stream experiment, where the higher harmonics contribute significantly to the total RMS strain response. The RMS strains were calculated for one quadrant, not necessarily aligned with the cross-flow or inline direction, and the contribution at the 1x frequency was obtained by filtering to remove all the frequencies that were not the fundamental frequency of vibration. Figure 73(b) shows strain response spectrum at four locations (sensor 54, 58, 62 and 66) in the region of maximum observed RMS strain, where the sensors did align with the cross-flow direction. The energy at the higher harmonics is too large to ignore, making the assumption that VIV stress response is narrow-banded inaccurate and unrepresentative of the observed data.

For these four sensor locations, the higher harmonics in the strain data were removed using filtering techniques to leave only the VIV frequencies close to the Strouhal frequency in the strain spectrum. This filtered data, the spectrum for which is narrow-banded, has a probability distribution that is significantly different from the Gaussian probability distribution (Figure 74). The data in the figure has been normalized to have a variance of 1.0 so that it can be compared with a Gaussian distribution also with variance one.

These results indicate an inaccuracy in the assumption that VIV is narrow-banded and Gaussianly distributed, which cases errors when the Rayleigh formulation is used to estimate stress range PDFs and predict VIV fatigue damage. Appendix D shows that a Weibull distribution better represents the stress range PDFs than the Rayleigh formulation.

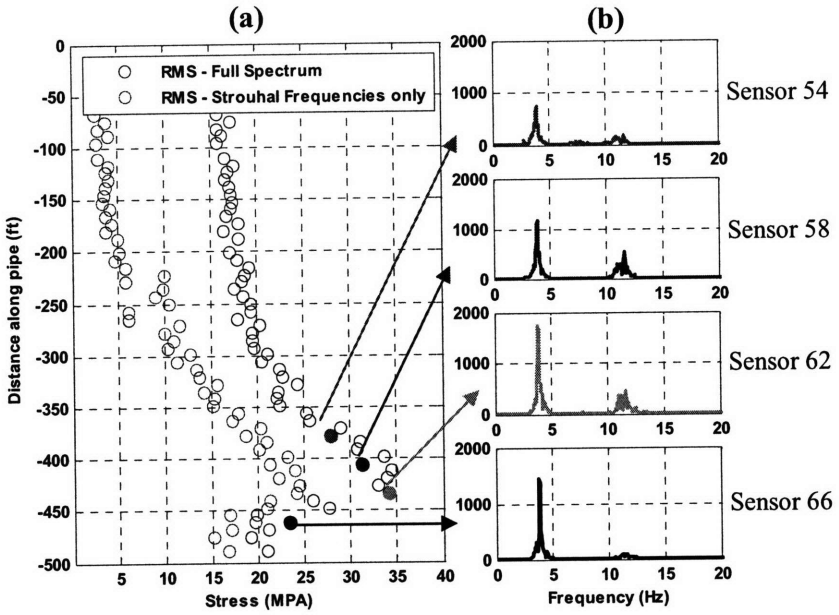

Figure 73 - Measured Strain compared to the 1x component for an example case from the first Gulf Stream experiments

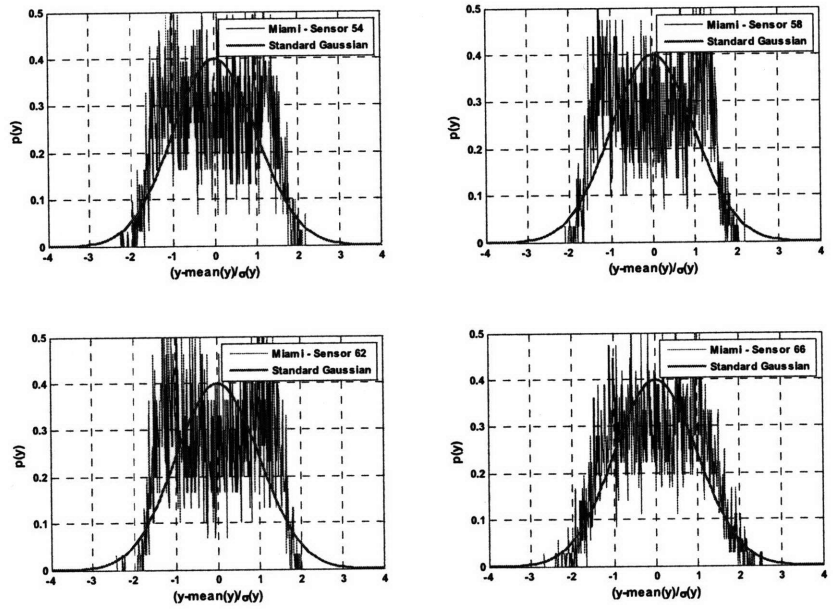

Figure 74 – The probability distribution of normalized strain amplitude (normalized using its variance) at four sensor locations. The data was first filtered to remove the higher harmonics.

6.4 In-line vs Cross-flow fatigue damage

In recent times it has become clear that for a pipe undergoing VIV, in-line motion and the strain response in the in-line direction are significant. Though research has shown that the motion response in the in-line direction is smaller than the cross-flow direction, few studies ([55]) have been performed to compare the magnitude of the in-line fatigue damage to the cross-flow fatigue damage. Table 10 shows the ratio of the maximum in-line fatigue damage to the maximum cross-flow fatigue damage for 9 different bare pipe tests from the second Gulf Stream experiments. The results indicate that it is reasonable to assume that the cross-flow fatigue damage is larger then the in-line fatigue damage for a flexible pipe undergoing VIV. A possible reason for the in-line fatigue damage to be consistently smaller could be that the maximum 2x RMS strain response and the maximum 4x RMS strain response do not happen at the same location. However, in the cross-flow direction, the maximum 1x RMS strain response occurs very close to the maximum 3x and 5x RMS strain responses. This results in the maximum fatigue damage in the cross-flow direction to be larger than the maximum fatigue damage in the in-line direction.

Table 10 – The ratio of the maximum in-line fatigue damage (at any location on the pipe) to the maximum cross-flow fatigue damage (at any location on the pipe).

Test Name	Total IL fatigue/ Total CF fatigue
20061020175715	0.59
20061020180904	0.57
20061021142015	0.80
20061023203818	0.76
20061022154633	0.89
20061023204504	0.91
20061021172823	0.89
20061021174641	1.09
20061021135143	0.65
Mean	**0.79**

6.5 Estimating cross-flow fatigue damage due to the higher harmonics

Data from the second Gulf Stream experiments provide evidence that the fatigue damage estimation process currently used by the offshore oil and gas industry makes two incorrect assumptions about the nature of the VIV stress response in the cross-flow direction. First, it assumes that the data is narrow banded, which in light of recent experiments, is shown to be inaccurate. Second, it assumes the stress response at the fundamental VIV frequency to be Gaussian distributed, which is shown to be inaccurate by the data from the second Gulf Stream experiments. These findings lead us to put forth two different methods to incorporate the higher harmonics in the predicted VIV fatigue response.

The first method predicts the fatigue damage contributed by the 1x component before the higher harmonics is incorporated using a simple amplification factor. The second method predicts the RMS stress contributions of the higher harmonics and uses broad-band formulations to convert the total response to stress range PDFs, which can then be used to estimate fatigue damage.

6.5.1 Method 1 – Using a factor to incorporate the fatigue damage due to the higher harmonics

Predictive programs like SHEAR7 assume that the 1st harmonic response is Gaussian distributed and use the Rayleigh formulation to calculate fatigue damage estimates. However, the strain data from the second Gulf Stream experiments indicates that this assumption is inaccurate and leads to an error in the predicted fatigue damage even when the predicted RMS strain response is accurate. Assuming the material to be Steel, Table 11 shows that the actual fatigue damage for the 1x harmonic, calculated using the Rainflow counting method, is less than the fatigue damage predicted using the Rayleigh formulation by a correction factor, called CF1 here. Assuming an API-X' S-N curve, CF1 has an average value of 1.47. Therefore, the cross-flow damage estimated by SHEAR7 is conservative and has to be reduced by this factor to accurately predict the fatigue damage due to the 1st harmonic. Only then can the contributions of the higher harmonics be included in the total cross-flow fatigue damage estimate.

Table 11 – The contribution of the 1st harmonic fatigue damage is overestimated when the Rayleigh formulation is used. The Rainflow method is taken as the standard for this comparison

Test Name	Rayleigh 1x fatigue/ Rainflow 1x fatigue
20061020175715	1.53
20061020180904	1.47
20061021142015	1.54
20061023203818	1.52
20061023204504	1.57
20061021172823	1.55
20061021174641	1.43
20061021135143	1.20
Mean	**1.47**

Table 12 shows the ratio of the maximum total cross-flow damage to the maximum 1x damage away from the boundary. The ratios indicate that, on average, the higher harmonics amplify damage by a factor of 27.8.

Table 12 – The amplification in fatigue damage due to the higher harmonics for 9 different bare pipe tests from the second gulf stream experiments

Test Name	Total CF Fatigue/ 1x Fatigue
20061020175715	37.65
20061020180904	35.34
20061021142015	28.49
20061023203818	42.66
20061022154633	10.05
20061023204504	27.00
20061021172823	13.48
20061021174641	31.55
20061021135143	24.20
Mean	**27.82**

$$D_{Total} = \frac{D_{SHEAR7}}{CF1} \times CF2 \tag{5.1}$$

$CF1$ = Correction factor due to over prediction of damage by the Rayleigh formulation

$CF2$ = A factor to include the effects of the higher harmonics in total cross-flow fatigue damage estimates

It was shown in Chapter 5 that the higher harmonics do not occur near the boundary. Therefore, the factor CF2 should not be applied to boundary regions where the standing wave amplifies the 1x fatigue damage but where there is little contribution from the higher harmonics.

6.5.2 Method 2 – Using broadband spectral techniques

The higher harmonic fatigue effects can also be incorporated using an empirical model for the higher harmonic RMS strain response. The higher harmonic strain component is then be combined with the predicted RMS 1x strain response to get the total cross-flow RMS strain response, which is used to calculate stress range PDFs and estimate fatigue damage. There are three important steps in this method 1) An empirical model for the higher harmonic strain response 2) Identifying a formulation that will convert the total cross-flow stress, which has broadband spectral properties, to stress range PDF 3) Developing a procedure to practically use this formulation in VIV related fatigue design.

An empirical model for the Higher Harmonics

Since there are no methods available to predict the higher harmonic component of VIV response, measured strain data from the second Gulf Stream experiment is used to develop an empirical model that allows one to estimate the higher harmonic RMS strain response in terms of the predicted RMS response at the 1st harmonic. Results in Chapter 5 showed that on average, the maximum 3rd harmonic RMS strain is 1.25 times the maximum 1st harmonic RMS strain. Similarly, on average, the maximum 5th harmonic RMS strain is 0.57 times the maximum 1st harmonic RMS strain. Further, observations suggest that the 3rd harmonic strain response was high in the reduced velocity range of 5 to 6 while the 5th harmonic strain response was high in the reduced velocity range of

5.25 to 5.75. A simple model, based on this information, for the 3rd and 5th harmonics is shown in Figure 75. The strain amplitudes are made to taper off from the region of high response to avoid discontinuities in the higher harmonic strain response.

Though the model is not based on a physical understanding of the hydrodynamics that cause the higher harmonics, it has several advantages. First, it is simple to use with predictive programs like Shear7. Second, it makes use of the predicted RMS 1x strain, which is predicted reasonably well by VIV programs in use today.

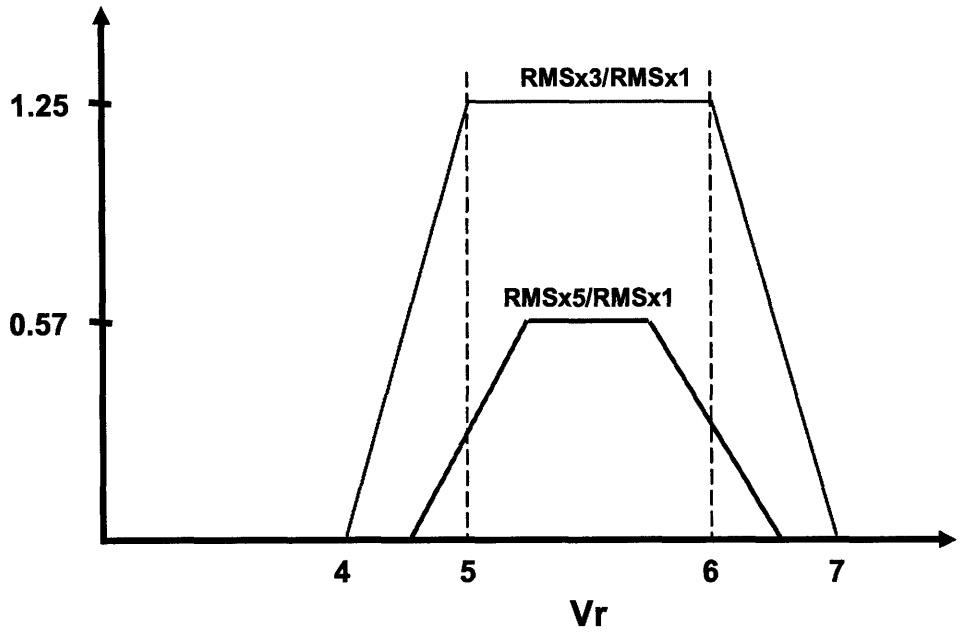

Figure 75 – A model for the strain response at the 3rd and 5th harmonic frequencies based on observed properties from the second Gulf Stream experiments.

Stress range PDFs for broadband spectra

Historically, VIV stress time histories have been assumed to be a Gaussian narrow-banded process, with energy only around the Strouhal frequency. This assumption allows the stress range PDF, $p_r(\sigma_r)$, to be represented by a Rayleigh probability distribution, which can then be used with appropriate S-N curves to predict fatigue damage.

However, VIV data from the Gulf Stream experiments is not narrow banded due to the presence of the higher harmonics. As was shown earlier, the vibrations at the Strouhal frequency are not Gaussianly distributed. However, the total VIV strain

response, which includes the higher harmonics, is Gaussianly distributed. Figure 76(a) shows an example strain PSD from the second Gulf Stream experiment which contains the vibrations at the 1x and 3x frequencies. The distribution of the response, normalized by its variance and presented in the form of probability of occurrence of strain amplitude, compares well with a Gaussian distribution with unit variance (Figure 76 (b)).

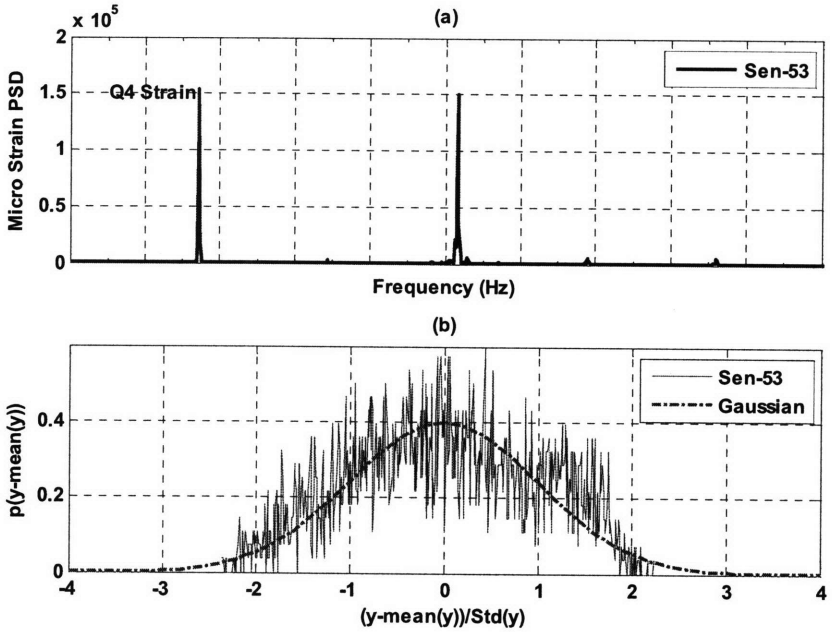

Figure 76 - The distribution of the Gulf Stream Q2 Strain data at a representative location (sensor 53 – 372.5 ft. from the top) in (a) the frequency domain using a PSD (b) time domain using the probability distribution of strain amplitude normalized by the variance of the data. Also shown in (b) is a Gaussian probability distribution (mean=0, variance=1).

Since the VIV strain response that includes the higher harmonics is a Gaussian broad-band process, the Rayleigh formulation is not an appropriate stress range PDF. Several methods exist in the literature to calculate the stress range PDFs of broadband Gaussian processes. Research [33, 45, 56, 57] suggests that method presented by Dirlik [44] is the most accurate. Unlike the Rayleigh formulation which is based only on the variance of the data (zeroth spectral moment), this formulation (Figure 77) also uses the first, second and fourth spectral moments in empirical relations to formulate the stress range PDF for a broad-band spectrum.

The Dirlik formulation uses T_C for the upcrossing period instead of T_Z where

$$T_C = \left(\frac{m_2}{m_4}\right) \quad T_Z = \left(\frac{m_0}{m_2}\right)$$

Therfore, fatigue damage is given by

$$D = \frac{T}{T_c A} \int \sigma_r^m p_{RF}(\sigma_r)\, \delta\sigma_r$$

where;

$$P_{RF}(\sigma_r) = \frac{\frac{D_1}{Q} e^{-Z/Q} + \frac{D_2 . Z}{R^2} e^{-Z^2/2R^2} + D_3 Z e^{-Z^2/2}}{2(m_o)^{1/2}}$$

$$\beta = \frac{T_C}{T_Z} = \left(\frac{m_2^2}{m_o . m_4}\right)^{1/2} \quad ; \quad X_m = \frac{T_C}{T_m} = \frac{m_1}{m_o} . \left(\frac{m_2}{m_4}\right)^{1/2}$$

$$D_1 = \frac{2(X_m - \beta^2)}{1+\beta^2} \quad ; \quad D_2 = \frac{\beta - X_m - D_1^2}{1-R} \quad ; \quad D_3 = 1 - D_1 - D_2$$

$$Q = \frac{1.25(\beta - D_3 - (D_2 R))}{D_1} \quad ; \quad Z = \frac{\sigma_r}{2\sqrt{m_o}}$$

Figure 77 – The most widely used formulation to get stress range PDFs from broadband spectra is by Dirlik and uses the zeroth, 2nd and 4th spectral moments in its formulation.

Figure 78 shows a comparison of the stress range PDF from Rainflow counting and the Dirlik method. For the same test case considered earlier in the chapter, three locations where a quadrant aligned itself with the cross-flow direction were chosen. At these locations, the stress range PDF was calculated using the Rayleigh formulation, the Dirlik formulation and the Rainflow counting method. If we consider the Rainflow method to be accurate, it is clear that the Dirlik method predicts the shape of the stress

range PDF better than the Rayleigh method. This is especially true for the low stress range oscillations, even though these low ranges do not contribute substantially to the overall fatigue damage.

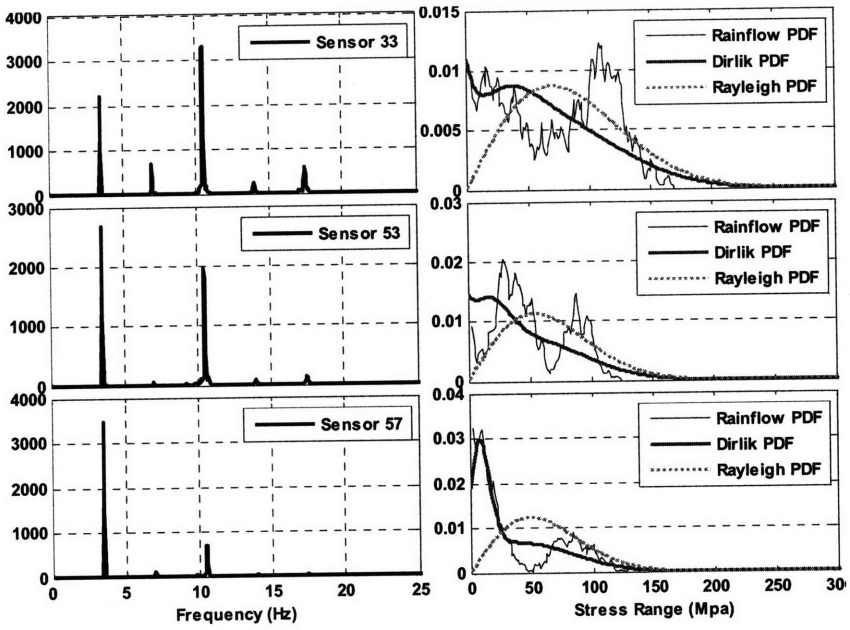

Figure 78 - Strain PSDs and corresponding stress range PDFs at 3 sensor locations (sensor 33 – 232.5 ft., sensor 53 – 372.5 ft., sensor 57 – 400.5 ft.)

Table 13 shows the comparisons of the fatigue calculations using the three methods. These values indicate that the Dirlik method predicts fatigue damage more accurately than the Rayleigh method.

Table 13 - Dirlik method predicts damage more accurately than the Rayleigh method for broadband spectra

Sensor No / Dist. Along pipe from top (ft)	Dirlik Damage / Rainflow Damage	Rayleigh Damage / Rainflow Damage
33 / 232.5	1.5014	1.7177
53 / 372.5	1.8278	2.1564
57 / 400.5	1.2467	1.4861

Using the Dirlik Spectrum in Design

Stress time series are usually not available, especially during the design phase of a project, making it difficult to include the effects of the higher harmonics in fatigue related design calculations. As the Dirlik method is more appropriate for predicting stress range PDFs when the higher harmonics are present, a method based on the Dirlik formulation and the 1x RMS strain response from a predictive program is proposed. This procedure is referred to as the "Modified Dirlik" method to distinguish it from the Dirlik formulation which uses the spectral properties from the measured spectrum.

Consider a predicted RMS stress response, S_{rms}, from a VIV prediction program like Shear7. Assuming one has a fairly accurate prediction of the 1x RMS stress response then the following method can used to estimate the spectral moments including the contributions of the 3x and 5x components.

$$\begin{aligned} m_o &= A_1 + A_3 + A_5 \\ m_1 &= A_1 f_1 + A_3 f_3 + A_5 f_5 \\ m_2 &= A_1 f_1^2 + A_3 f_3^2 + A_5 f_5^2 \\ m_4 &= A_1 f_1^4 + A_3 f_3^4 + A_5 f_5^4 \end{aligned} \tag{5.2}$$

where A_1, A_3 and A_5 are the areas under the stress spectrum corresponding to the 1x, 2x and 3x frequencies. For VIV analysis, it is known that $f_3 \sim 3*f_1$ and $f_5 \sim 5*f_1$. Further, assuming that $A_3 = h * A_1$ and $A5 = k * A_1$ where h and k are empirically determined factors, gives us a modified formulation for the stress spectral moments

$$\begin{aligned} m_o &= A_1 + hA_1 + kA_1 = (1+h+k)A_1 \\ m_1 &= A_1 f_1 + (hA_1)(3f_1) + (kA_1)(5f_1) = (1+3*h+5*k)A_1 f_1 \\ m_2 &= A_1 f_1^2 + (hA_1)(3f_1)^2 + (kA_1)(5f_1)^2 = (1+9*h+25*k)A_1 f_1^2 \\ m_4 &= A_1 f_1^4 + (hA_1)(3f_1)^4 + (kA_1)(5f_1)^4 = (1+81*h+625*k)A_1 f_1^4 \end{aligned} \tag{5.3}$$

Using $A1 = (S_{rms})^2$, where (S_{rms}) is the RMS stress of the 1x component, gives us the final form of the above formulation as

$$m_o = (1+h+k)S_{rms}^2$$
$$m_1 = (1+3*h+5*k)S_{rms}^2 f_1$$
$$m_2 = (1+9*h+25*k)S_{rms}^2 f_1^2 \quad (5.4)$$
$$m_4 = (1+81*h+625*k)S_{rms}^2 f_1^4$$

The Dirlik stress range PDF can be developed using these spectral moments, which can then be used with the appropriate S-N curve to estimate fatigue damage

The above methodology is useful because the only unknowns in this formulation are h and k, the ratios of the spectral areas under the 3x and 5x frequencies to the spectral area under the 1x frequency. The other variables are obtained from the Strouhal number and the predicted value of RMS stress of the 1x component. First, the method is checked for accuracy at the same three locations considered in Figure 78. Using Young's Modulus of Steel, Figure 79 shows that the resulting stress range PDF compares well with the Dirlik PDFs developed using the full spectrum in Figure 78. Again, sensor 33 (Q1 – 232.5 ft.), sensor 53 (Q4 – 372.5 ft.), sensor 57 (Q4 – 400.5 ft.) were chosen because they happened to be aligned with the cross-flow direction.

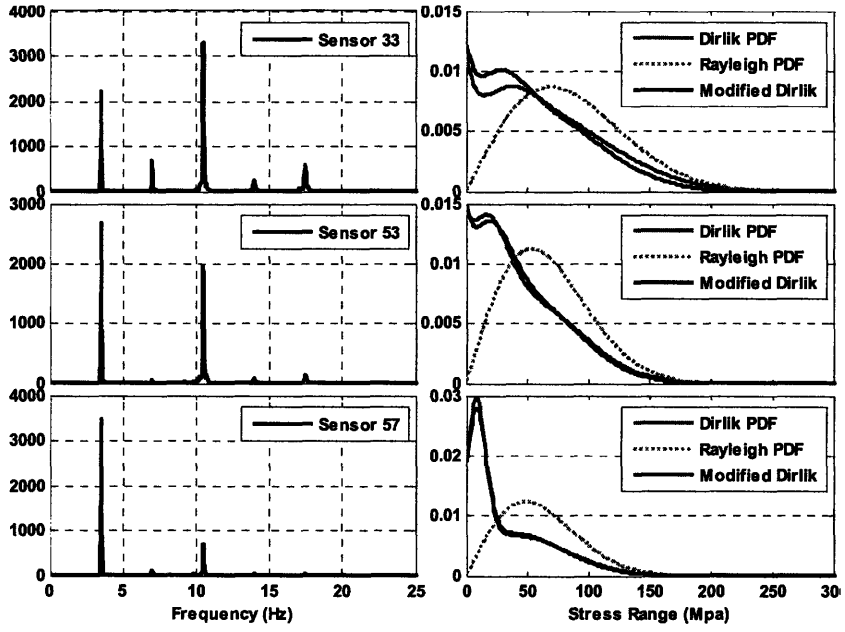

Figure 79 - Strain PSDs and corresponding stress range PDFs at 3 sensor locations.

Table 14 compares the fatigue damage obtained using the three methods. The results indicate that the modified Dirlik method provides a good estimate of the fatigue caused by the higher harmonics when compared to results from the Rainflow counting method. The simplicity of the method makes it amenable to be used with predictive programs for fatigue calculations.

Table 14 - Results using the "Modified Dirlik" approach compare well with the Dirlik method. A ratio of 1 in the table indicates an exact match with the fatigue damage estimated using the Rainflow counting method.

Sensor No / Dist. Along pipe from top (ft)	Dirlik Damage / Rainflow Damage	Modified Dirlik Damage / Rainflow Damage
33 / 232.5	1.5014	0.9665
53 / 372.5	1.8278	1.4874
57 / 400.5	1.2467	0.9854

Example Case

So far a model for the higher harmonic strain has been developed and a method is proposed which uses the Dirlik formulation, to develop the stress range PDFs for the higher harmonics. Now we put the two together to try to estimate the higher harmonic response and fatigue damage for an example case from the second Gulf Stream experiment. The example considered is Test – 20061023203818.

The model shown in Figure 75 is used with SHEAR7 V4.5 to predict the VIV strain response that includes 3rd and 5th harmonics in the cross-flow direction. For each response frequency, the 3x and 5x models shown in Figure 75 give the spatial variation of the 3x and 5x RMS strain amplitude. A time series, containing the 1x, 3x and 5x components, is constructed using the phases and amplitudes derived by Shear7. This is repeated for all the response frequencies with the time lengths of the strain time series generated each frequency determined by their probabilities of occurrence. Finally, the strain time series at each response frequencies are joined sequentially to get the strain time series of the total response, from which the total cross-flow response is computed at each spatial location as shown in Figure 80. Also shown is the predicted 1x RMS strain

response along with the measured 1x and 3x RMS strain responses. The higher harmonic strain is captured in the SHEAR 7 response.

This response is used to estimate the total fatigue damage in the cross-flow direction using the Dirlik method for stress range PDFs and the API-X' S-N curve for fatigue damage. Figure 81 shows encouraging results from the analysis because the region in peak fatigue damage, caused mainly due to higher harmonics, is estimated well in location as well as magnitude.

6.5.3 Suggested Practice for Engineers

A method is suggested for engineers who want to include the effects of the higher harmonics and are using SHEAR7 as the VIV prediction program. The proposed method can be used with other VIV programs with relevant modifications.

- Method 1 should be used to investigate if higher harmonics are a problem in the VIV design. The predicted fatigue damage from SHEAR7 is divided by 1.47 to remove the conservatism due to the assumption that the stress time history is Gaussian. The resulting spatial distribution of fatigue damage, except for the region near the boundary where standing waves are present, is multiplied by 27.8 to account for the higher harmonics. This is done for all the current profiles and the final fatigue damage is calculated using their probabilities of occurrence. If the final values of the total cross-flow fatigue damage are higher than the allowed design value, only then should the second method be used.
- The second method requires that the output from Shear7 be modified to include the effects of the higher harmonics. This is done by using simple strain prediction models for the 3^{rd} and 5^{th} harmonics to predict the total cross-flow strain response before using a the Dirlik formulation to estimate fatigue damage rate. Details of the procedure for predicting the higher harmonic strains is explained in Appendix E and can be implemented using Matlab or other programming tools. This method is more accurate because it considers the local variation of the higher harmonics.

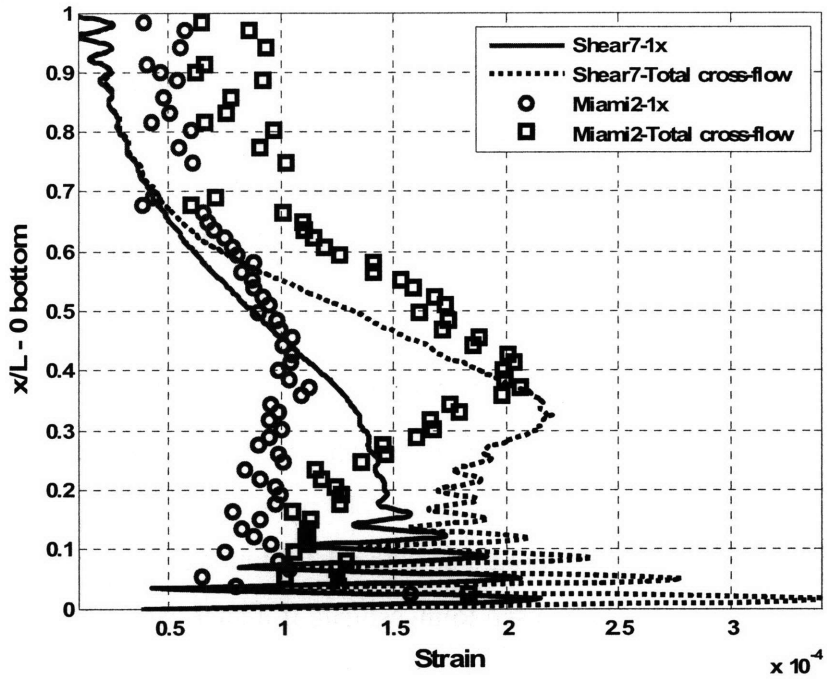

Figure 80 – Total cross-flow strain predicted using the proposed method matches well with the measured total cross-flow strain. The x-axis shows RMS strain

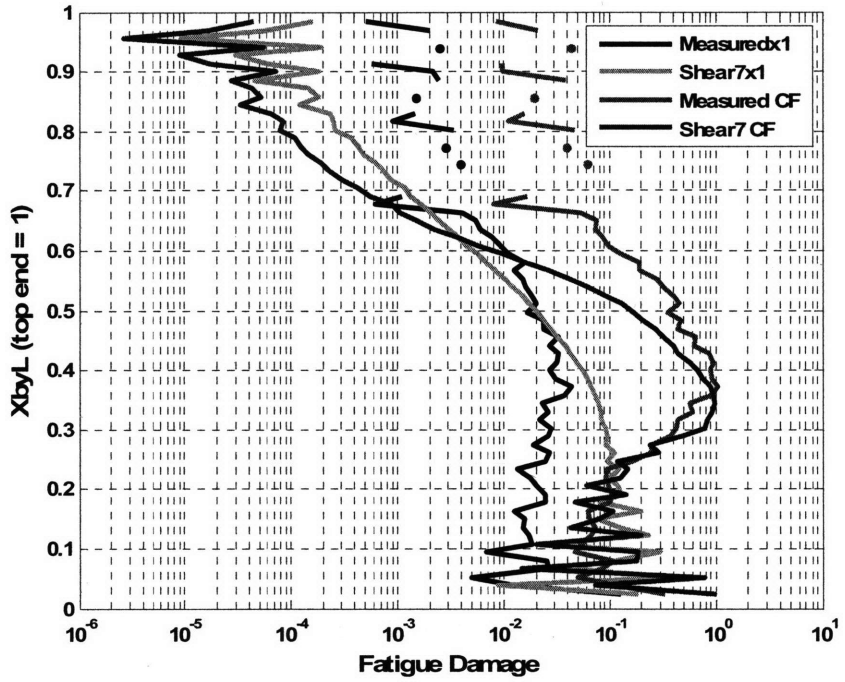

Figure 81 – The distribution of fatigue damage using SHEAR7 with the proposed method compares well with results from actual measured strain data, especially in the region of maximum damage.

6.6 Main Results and Conclusions

For the first time, a method is suggested to incorporate the effects of the higher harmonics in VIV related fatigue design. However, during the development of this method, several other important findings came to light

- The fatigue damage due to the higher harmonics is important and cannot be ignored in VIV design. On average, the higher harmonics increase the maximum measured 1^{st} harmonic fatigue damage, not considering the boundary region, by a factor of 27.8.
- The 1^{st} harmonic strain time history is narrow banded but not Gaussian, which makes the Rayleigh method inaccurate when predicting stress range PDFs. On average, the Rayleigh formulation over-predicts the damage due to the 1^{st} harmonic by factor of 1.47.
- If the higher harmonics are included in the strain spectrum, it is Gaussian but broad banded, again making the use of the Rayleigh method inaccurate. In this case, the Dirlik formulation gives more accurate stress range PDFs than the Rayleigh method.
- Two methods are proposed to incorporate the higher harmonics in design. Method 1 first reduces the damage predicted by SHEAR7 because of the conservatism built into the Rayleigh formulation and then uses experimentally determined factor to account for the effects of the higher harmonics. This method provides a maximum estimate of total cross-flow damage and can be used quickly to check if a detailed analysis is required. The second method proposes an empirical RMS strain model for the 3^{rd} and 5^{th} harmonics and uses it with the Dirlik method to estimate the total fatigue damage in the cross-flow direction. For an example case, the results match well with fatigue estimates from measured strain data.
- Finally, it is proposed that engineers use the first method to identify cases where the fatigue damage due to the higher harmonics can be a problem and then use the second method when necessary to accurately incorporate the fatigue contribution of the higher harmonics in the total estimated cross-flow fatigue damage.

7. Conclusions and Future Work

This thesis makes contributions in the in relation drag due to VIV, higher harmonic strain response in VIV and fatigue damage due to VIV.

7.1 Drag due to VIV

- A method is developed to extract the local drag coefficients using strain measurements from a densely instrumented flexible pipe undergoing VIV. This method captures the local drag coefficient accurately, both in magnitude and spatial location, and is able to detect to sudden spatial variations in local drag coefficients due to strakes or fairings or changes in the wake behavior.
- The maximum drag coefficients are likely associated with 'figure 8' displacement trajectories and occur in the region of traveling wave response. The maximum drag coefficient may not occur at the location of the maximum cross-flow displacement response.
- Even though the SHEAR7 drag formulation does not predict local drag coefficients accurately for a bare pipe undergoing VIV, it predicts well the spatially averaged drag coefficient. Therefore, even though local drag forces are inaccurate on the marine riser, predicted global drag forces are accurate.

7.2 Higher Harmonics in VIV

- The local higher harmonic response in a flexible pipe seems to be closely associated with the shape and direction of the local X,Y trajectories. In the region of high 3x buildup, the trajectories are "figure 8" patterns with upstream motion at the cross-flow extremes, while the highest 2^{nd} harmonic seems to occur near the "figure c" These observations are the first in long flexible cylinders vibrating at high mode numbers with the dominant VIV response in the form of traveling waves.
- The higher harmonics are not large near boundaries because a standing wave pattern does not allow for X,Y trajectories favorable to the formation of the higher harmonics to exist for long distances.

- On average, the maximum 3rd harmonic strain response is 1.24 (standard deviation=0.17) times the maximum 1st harmonic strain response (not considering the standing wave at the boundary) and the maximum 5th harmonic strain response is 0.57 (standard deviation=0.23) times the maximum 1st harmonic strain response (not considering the standing wave at the boundary).

7.3 Fatigue damage due to VIV

- In the region of maximum higher harmonic strain response, total fatigue damage is, on average, is about 30 times the fatigue damage due to the 1st harmonic response. However, this effect is localized and conservatisms built into predictive programs and fatigue design procedures more than account for the increase in fatigue damage.
- The largest total cross-flow fatigue damage was never found to be near the boundary because the higher harmonics are not large near the boundary. This result implies that the contributions of the higher harmonics to fatigue damage need not be considered in the region near the boundary.
- Total fatigue damage in the cross-flow direction is almost always larger than the total fatigue damage in the in-line direction. This implies that in-line fatigue related designs based on cross-flow fatigue damage results are conservative.
- Two practical methods are proposed to account for the contribution of the higher harmonics to total cross-flow fatigue damage. These methods can be implemented by engineers using tools that are currently available.

7.4 Future Work

As with any research work, this thesis solved a few problems but identified many others for future generations to work on. Some key areas for future research are :-

1. An experiment, similar to the second Gulf Stream experiment, should be conducted to investigate if the higher harmonics are suppressed in a pipe with different phase speeds in the in-line and cross-flow direction. Such a setup will not allow displacement profiles favorable to the development of higher harmonic response to exist for long lengths in the traveling wave response regime.

2. Further work is required to predict the location and magnitude of the 3rd and 5th harmonics strain responses.
3. New VIV forcing models that allow the "power-in" to be in regions of traveling wave response. Such model will be able to capture the observation that the largest cross-flow displacement response is in the traveling wave region and not the standing wave region.
4. Further research should continue to explore the relationship between local drag coefficients, local wakes, and existence of "power-in" regions.
5. More work is needed on prediction of local C_D's that are not only dependent on response amplitude-to-diameter ratios.

References

(1) Simon Oil Rig Disasters. *http://home.versatel.nl/the_sims/rig/index.htm* (accessed 12/23, **2007**).

(2) Shao, M.; Hu, H.; Li, M.; Ban, H.; Wang, M.; Jiang, J., *Karman Vortex Street Assisted Patterning in the Growth of Silicon Nanowires*, ChemComm **2007**, 793.

(3) Rayleigh, L., *The Theory of Sound*, Dover Publications, **1945**; Vol. II, pp 413.

(4) Roshko, A., *On the Development of Turbulent Wakes from Vortex Streets*, Technical Report 1191 **1954**.

(5) Jong, J.; Vandiver, J. K., *Response Analysis of the Flow-Induced Vibration of Flexible Cylinders tested at Castine, Maine in July and August of 1981*, **1983**.

(6) Jauvtis, N.; Williamson, C. H. K., *The Effect of Two Degrees of Freedom on Vortex-Induced Vibrations at Low Mass-Damping*, J. Fluid Mech. **2004**, *509*, 23.

(7) Triantafyllou, M. S.; Techet, A. H.; Hover, F. S.; Yue, D. K. P., *VIV of Slender Structures in Shear Flow;* IUTAM Conference; Rutgurs State University: New Jersey, USA, **2003**.

(8) Vandiver, J. K.; Marcollo, H.; Swithenbank, S.; Jhingran, V., *High Mode Number Vortex-Induced Vibration Field Experiments;* Proceedings at the Offshore Technology Conference; Houston, TX, USA, **2005**.

(9) Vandiver, J. K.; Swithenbank, S.; Jaiswal, V.; Jhingran, V., *DEEPSTAR 8402: Gulf Stream Experiment*, Technical Report **2007**.

(10) Vandiver, J. K.; Swithenbank, S.; Jaiswal, V.; Jhingran, V., *Fatigue Damage from High Mode Number Vortex-Induced Vibration;* Proceedings of the OMAE **2006**.

(11) Blevins, R. D., *Vortex-Induced Vibration*, Flow-Induced Vibrations, Van Nostrand Reinhold Company: New York, N.Y. **1977**; pp 44-95.

(12) Williamson, C. H. K.; Roshko, A., *Vortex Formation in the Wake of an Oscillating Cylinder*, Journal of Fluids and Structures **1988**, *2*, 355.

(13) Rayleigh, L., *On the Resultant of a Large Number of Vibrations of the same Pitch and of Arbitrary Phase*, Philosophical Magazine **1880**, *10*, 73-78.

(14) Anagnostopoulos, P., Ed., *Flow-Induced Vibrations in Engineering Practice;* Rahman, M., Satish, M. G., Eds.; International Series on Advances in Fluid Mechanics; WIT Press: Boston, USA, **2002**; Vol. Chapter 1, pp 388.

(15) Sumer, B. M.; Fredsøe, J., *Hydrodynamics around cylindrical structures*, Advanced Series on Ocean Engineering , v. 12, World Scientific: Singapore , River Edge, N.J., **1997**, pp 530.

(16) Sarpkaya, T., *A Critical Review of the Intrinsic Nature of Vortex-Induced Vibrations*, JFS **2004**, *19*, 389.

(17) Pantazoloupos, M. S., *Vortex-Induced Vibration Parameters: Critical Review*, OMAE **1994**, *1*, 199-255.

(18) Williamson, C. H. K.; Govardhan, R., *Vortex-Induced Vibrations*, Annu. Rev. Fluid Mech. **2004**, *36*, 413-455.

(19) Bishop, R. E. D.; Hassan, A. Y., *The Lift and Drag Forces on a Circular Cylinder Oscillating in a Flowing Fluid,* Proceedings of the Royal Society of London, The Royal Society: United Kingdom, **1964**, Vol. 277, pp 51.

(20) Griffin, O. M.; Ramberg, S. E., *On Vortex Strength and Drag on Bluff-Body Wakes*, JFM **1975**, *69*, 721.

(21) Milne-Thompson, L. M., Chapter 13, Theoretical Hydrodynamics, Macmillian **1960**.

(22) Kochin, N. E.; Kibel, I. A.; Roze, N. V., Chapter 5, Theoretical Hydromechanics, Interscience **1964**.

(23) Sarpkaya, T., *Transverse Oscillations of a Circular Cylinder in Uniform Flow*, Proceedings of ASME, **1978**, Vol. 104, pp 275-290.

(24) Schargel, R. S., *The Drag Coefficient of a Randomly Oscillating Cylinder in a Uniform Flow*, Massachusetts Institute of Technology, Cambridge, MA, USA, **1980**.

(25) Overvik, T., *Hydroelastic Motion of Multiple Risers in a steady Current*, Norwegian Institute of Technology, **1982**.

(26) McGlothlin, J. C., *Drag coefficients of long flexible cylinders subject to vortex induced oscillations*, Massachusetts Institute of Technology, Dept. of Ocean Engineering, **1982**.

(27) Griffin, O. M.; Vandiver, J. K., *Flow-Induced Vibrations of Taut Marine Cables and Attached Masses,* Naval Civil Engineering Laboratory Report CR 84.004., **1983.**

(28) Gopalkrishnan, R., *Vortex-Induced Forces on Oscillating Bluff Cylinders*, Massachusetts Institute of Technology, Cambridge, MA, USA, **1993**.

(29) Khalak, A.; Williamson, C. H. K., *Fluid Forces and Dynamics of a Hydroelastic Structure with very low Mass and Damping*, J. Fluid Struc. **1997**, *11*, 973-982.

(30) Khalak, A.; Williamson, C. H. K., *Motions Forces and Mode Transitions in Vortex-Induced Vibrations at Low Mass-Damping*, J. Fluid Struc. **1999**, *13*, 813-851.

(31) Schijve, J., *Fatigue of Structures and Materials in the 20th Century and the State-of-the-art*, Int J Fatigue **25**, 679-702.

(32) Shultz, W., *A History of Fatigue*, Engineering Fracture Mechanics **1996**, *54*, 263-300.

(33) Barltrop, N. D. P.; Adams, A. J., *Fatigue;* Dynamics of Fixed Offshore Structures; Butterworth and Heinemann: United Kingdom, **1991**.

(34) Miner, M. A., *Cumulative Damage in Fatigue*, Trans. ASME J. appl. Mech. **1945**, *12*, A159-A164.

(35) Matsuiski, M.; Endo, T., *Fatigue of Metals Subjected to Varying Stress-Fatigue Lives Under Random Loading*, J Japan Soc. Mech. Eng. **1969**, 37-40.

(36) Downing, S. D.; Socie, D. F., *Simple Rainflow Counting Algorithm*, Int J Fatigue **1982**, *4*, 31-40.

(37) Longuet-Higgins, M. S., *On the Statistical Distribution of the Heights of Sea Waves*, J. Mar. Res. **1952**, *11*, 245-266.

(38) Cartwright, D. E.; Longuet-Higgins, M. S., *The Statistical Distribution of the Maxima of a Random Function*, Proc. R. Soc. A **1956**, *237*, 212-232.

(39) Rice, S. O., *Mathematical Analysis of random Noise*, Bell Syst. Tech. J. **1945**, *24*, 46-156.

(40) Rice, S. O., *Mathematical Analysis of random Noise,* Bell Syst. Tech. J. **1944**, *23*, 282-332.

(41) Weibull, W., *A Statistical Distribution Function of Wide Applicability*, J. Appl. Mech. - Trans. ASME **1951**, *18*, 293-297.

(42) Wirsching, P. H.; Light, M. C., *Fatigue Under Wide Band Random Stresses*, J. Structural Division **1980**, *106*, 1593-1607.

(43) Chaudhury, G. K.; Dover, W. D., *Fatigue Analysis of Offshore Platforms Subject to Sea Wave Loadings*, International Journal of Fatigue **1985**, *7*, 13-19.

(44) Dirlik, T., *Application of Computer in Fatigue Analysis*, University of Warwick, Coventry, UK, **1985**.

(45) Bishop, N. W. M.; Sherratt, F., *A Theoretical Solution for the Estimation of 'Rainflow' Ranges from Power Spectral Density Data*, Fat. Frac. Eng. Mats. Struct **1990**, *13*, 311-326.

(46) Vandiver, J. K., *Drag Coefficients of Long Flexible Cylinders*, OTC **1983**.

(47) Aronsen, K. H., *An Experimental Investigation of In-line and Combined In-line and Cross-flow Vortex Induced Vibrations*, Norwegian University of Science and Technology, Trondheim, **2007**.

(48) Dahl, J. M., Personal Communication, **2008**

(49) Kijewski-Correa, T. L., *Full-Scale Measurements and System Identification: A Time-Frequency Perspective*, Dept. of Civil Engineering and Geological Sciences, University of Notre Dame, **2003**.

(50) Swithenbank, S., *Dynamics of Long Flexible Cylinders at High-Mode Number in Uniform and Sheared Flows*, Massachusetts Institute of Technology, Cambridge, MA, USA, **2007**.

(51) Baird, D. C., *Experimentation: An Introduction to Measurement Theory and Experiment Design;* Prentice-Hall: Englewood Cliffs, N.J., **1962**.

(52) Braaten, H.; Lie, H., *NDP Riser High Mode VIV Tests Main Report*, **2005**, *512394.00.01*, 1.

(53) Gurley, k.; Kareem, A., *Application of Wavelet Transforms in Earthquake, Wind and Ocean Engineering*, Engineering Structures, **1999**, *21*, 149-167.

(54) Vandiver, J. K., *Dimensionless Parameters Important to the Prediction of Vortex-Induced Vibration of Long, Flexible Cylinders in Ocean Currents*, Journal of Fluids and Structures, **1993**, *7*, 423-455.

(55) Baarholm, G. S.; Larsen, C. M.; Lie, H., *On Fatigue Damage Accumulation from In-line and Cross-flow Vortex-Induced Vibrations*, Journal of Fluids and Structures **2006**, *22*, 109.

(56) DET NORSKE VERITAS, *Recommended Practice: Riser Fatigue*, **2004**, *DNV-RP-F204*.

(57) Bouyssy, V.; Naboishikov, S. M.; Rackwitz, R., *Comparison of Analytical Counting Methods for Gaussian Processes*, Structural Safety, **1993**, *12*, 35-57.

APPENDIX A – Details of the Mechanical Design for the Second Gulf Stream Experiment

Experience from the first Gulf Stream experiment proved valuable in the design of the mechanical components for the second Gulf Stream experiments. There were important changes made to the spooler, top end connection and deployment method. These changes allowed the deployment and spooling-in operations to be performed faster, enabling more tests to be done during the experiment. Further, it also allowed for an incident free experiment with no fiber breaks and larger allowed top angles (ie larger tow velocities).

The Spooler

The spooler, shown in Figure 82, was manufactured in Houston by CPC Petrochem. It consisted of a 10 ft diameter, 4 ft wide drum on which the experiment pipe was wrapped. Transportation issues and maximum strain considerations dictated the diameter of the drum. The top end assembly, consisting of the fiber optic termination box, the load cell, and the U-Joint, needed to lie flat on the drum so that no bending moment was transferred to any of the components. A ramp was designed to support the top end assembly and prevent damage due to bending. Figure 83 (b) shows the top end assembly when stowed on the ramp.

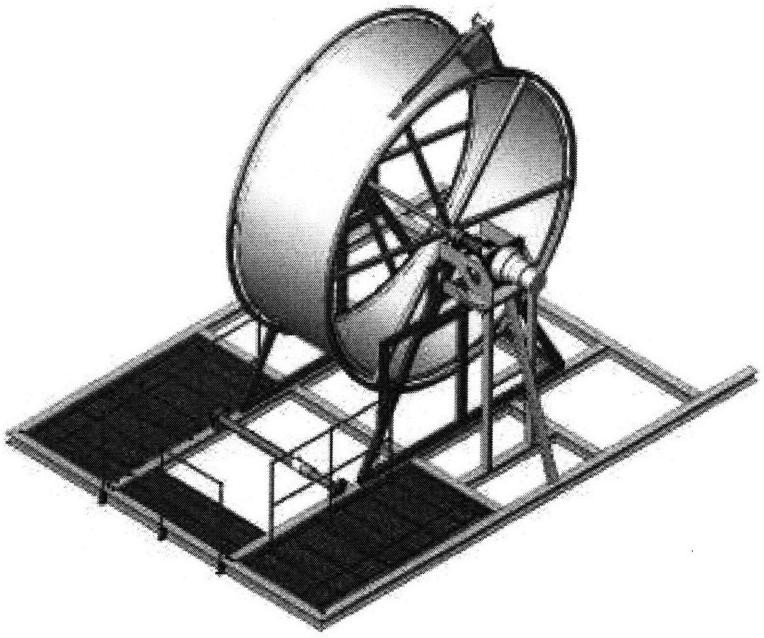

Figure 82 - 3D model of the spooler and base structure

The weight of the spooler was distributed on the deck using an assembly of beams that aligned with the deck longitudinal and transverse beams of the Walton Smith. The assembly was constructed using 6" I-beams that were welded to the deck. The spooler was secured to the bottom beams using a frame of smaller I-beams.

The Top End connection

The top end setup was modified for the second Gulf Stream experiments to address issues noticed during the 2004 tests. The most important change was made to the way the pipe was hung when deployed. A U-Joint was used in the first Gulf Stream experiment to provide free rotation of the top end of the pipe. However, at high current speeds, the top U-Joint reached its' maximum design angle thus preventing free rotation at the top. Design changes were made in the second Gulf Stream experiments to prevent this from occurring. The new design allowed the mean top angle to be taken by a collar rotating on a bar, leaving only the dynamic component to be handled by the U-Joint. Since the dynamic component of the tilt angle was much smaller than the mean tilt angle, the U-Joint was able to operate well below its' angle design limit. The strategy proved very effective in the field providing for a robust system where maximum tow speeds were not limited by the U-Joint.

The top assembly comprised of two distinct setups. The first setup consisted of components that made up the connection from the collar to the top end of the pipe. This layout is shown the sketch below. This whole setup, including the collar, was wrapped with the pipe on to the spooler for stowage. The setup after deployment and during stowage on the drum is shown in Figure 83. The second setup was the bar assembly used when the pipe was deployed. The sketch shown in Figure 84 shows the details of the two setups and how they are connected when the pipe is deployed.

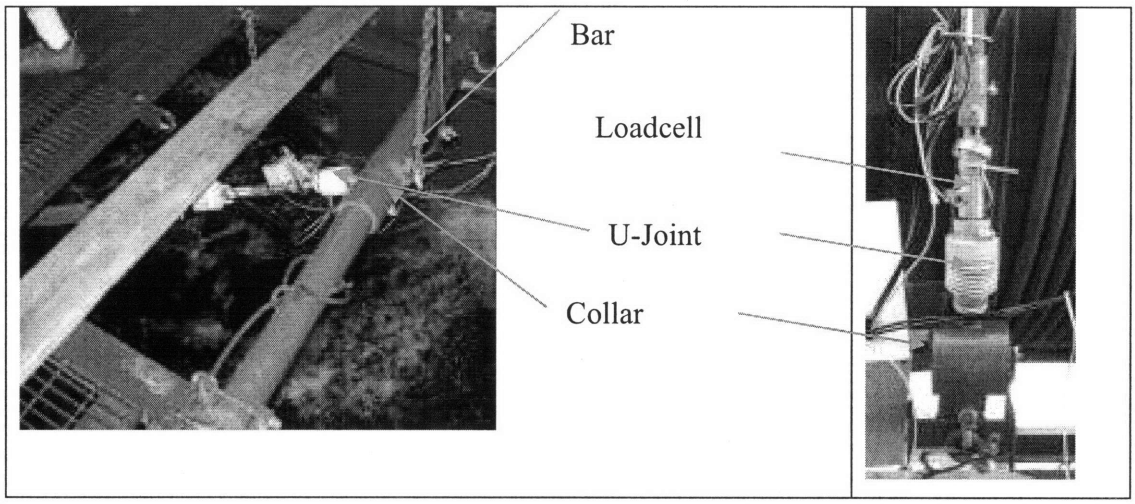

Figure 83 - The top end connection when (a) deployed (b) stowed on the drum

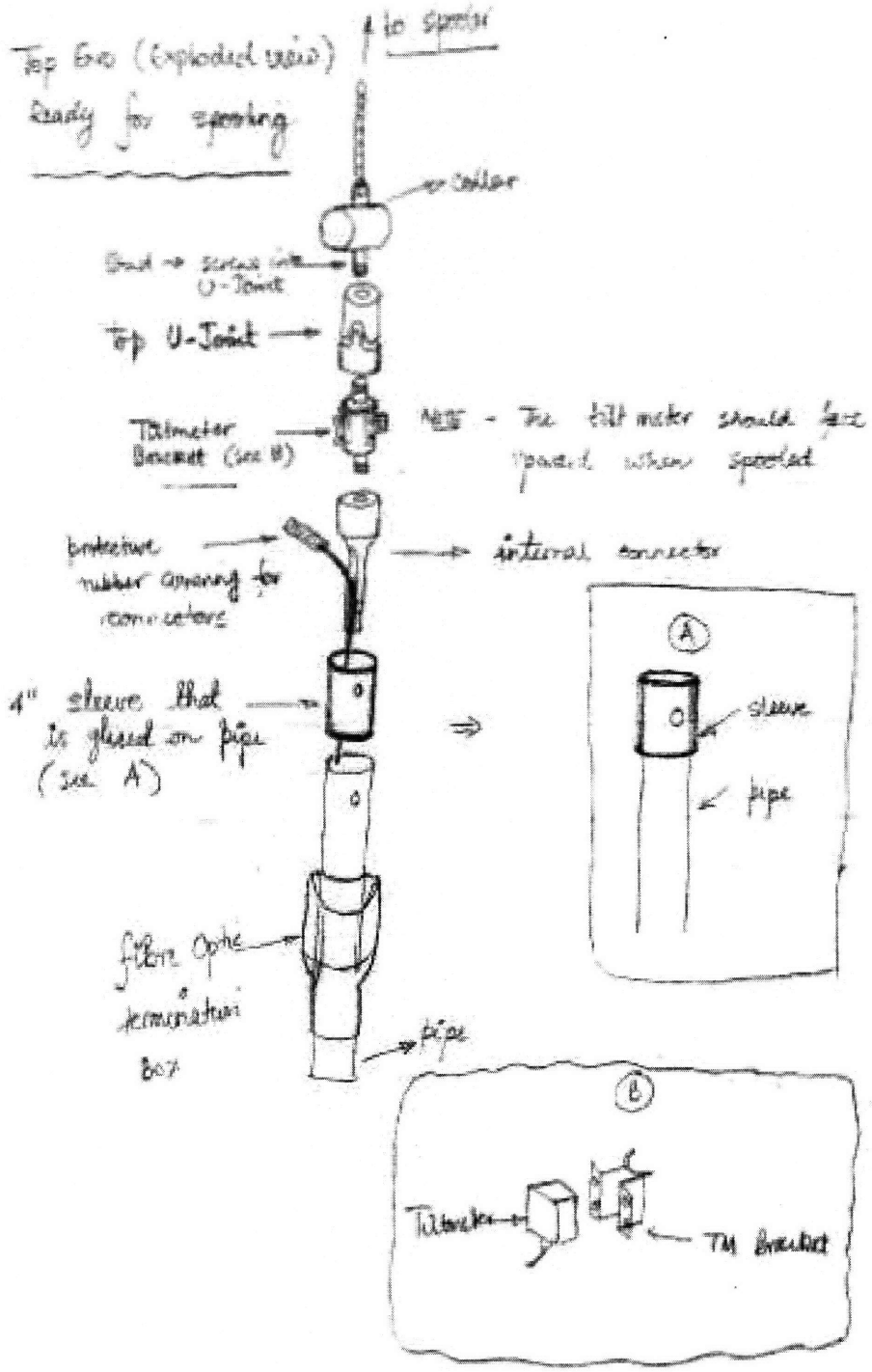

Figure 84 - Sketch of the top end connection

When the pipe was deployed, it was spooled out till the collar was at the level of the work deck. At this point, the weight of the pipe was being taken by the chains connecting the collar to the spooler. The bar assembly was then installed with the bar going through the collar and secured in the cradles at the edge of the moon pool using 3/8" bolts (Figure 85(a)). The chains were slacked and the weight of the pipe assembly was transferred to the bar. Also shown in Figure 85(b) is the collar rotating over the bar.

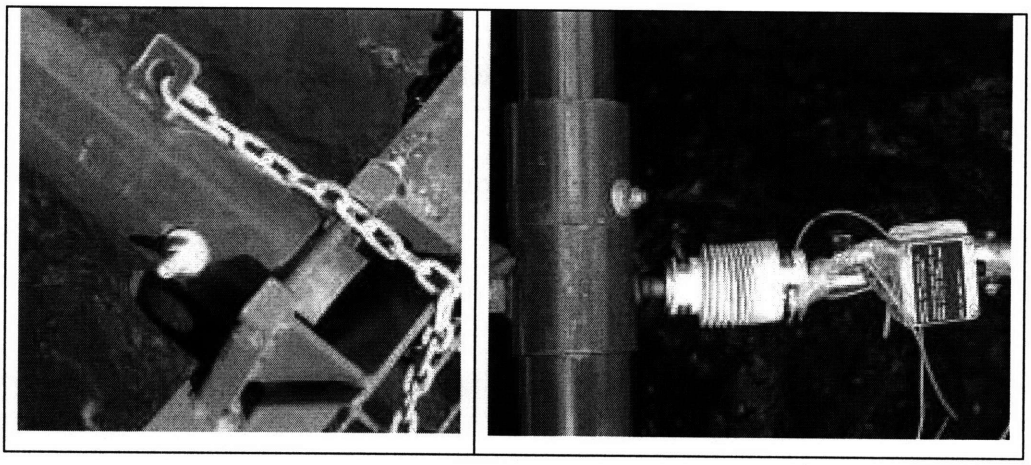

Figure 85 - (a) Details of the cradle and bolt mechanism to keep the bar secure during the tests (b) Details of the collar-bar setup during operation

The installation process was followed in reverse while recovering the pipe. The weigh was taken by the chains attached to the spooler. The bar was then removed and stowed on deck. The pipe was then ready to be recovered.

Bottom End Connections

The bottom end connection was similar to the one used in the first Gulf Stream experiment. A Rail Road wheel (RRW) weighing over 800 lb was used to provide the tension in the pipe. The weight of the RRW was taken by the spindle as shown in Figure 86. The spindle in turn connected to the bottom U-Joint. The Pipe and the U-Joint were attached using a connector and a sleeve as shown in Figure 87.

The spindle was welded to improve its strength to ensure it does not fail due to the static and dynamic load of the RRW. The friction between the RRW the spindle was large enough that no additional means of securing the RRW was required.

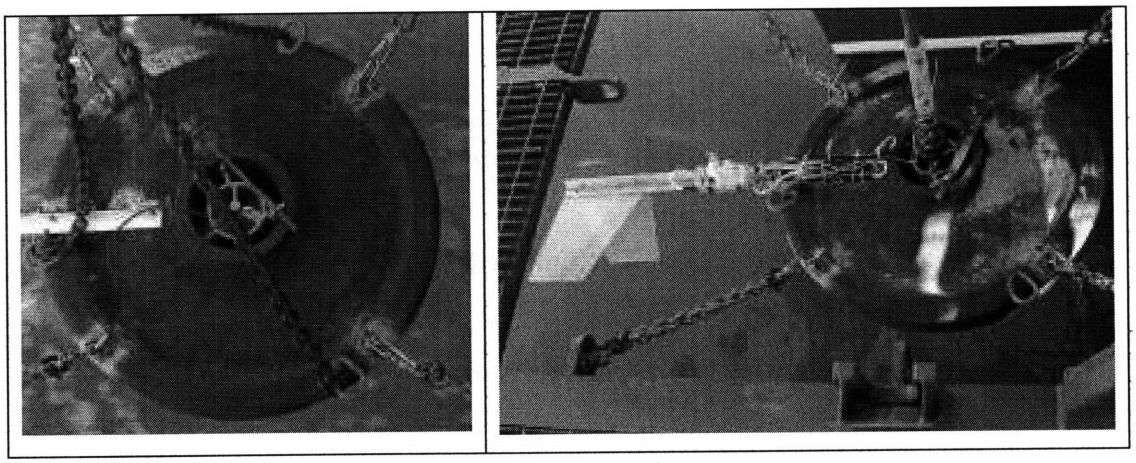

Figure 86 – (a) RailRoad Wheel with the spindle in position (b) The bottom end connection during the experiments.

A Kevlar coated cable consisting of seven copper wires was connected the current meter, pressure gauge and direction indicator to the National Instruments Data Acquisition System (NI DAS) on the deck.

The bottom U-Joint mated with the stud at the top of the spindle. The connection was secured using a ½" bolt. The other end of the U-Joint mated with a stainless steel internal connector. The internal connector and the end of the pipe were attached using a sleeve secured in place using ⅜" bolts.

Figure 86 (a) shows the setup during the experiments with the RRW attached to the spindle. Figure 86 (b) shows that the bottom end connection as put together during the experiments. It also shows the fin that was mounted on the RRW to stabilize it during the experiments. The direction indicator and the pressure gauge were attached to the fin. Figure 87 details the bottom end connection setup (except for the Rail Road Wheel).

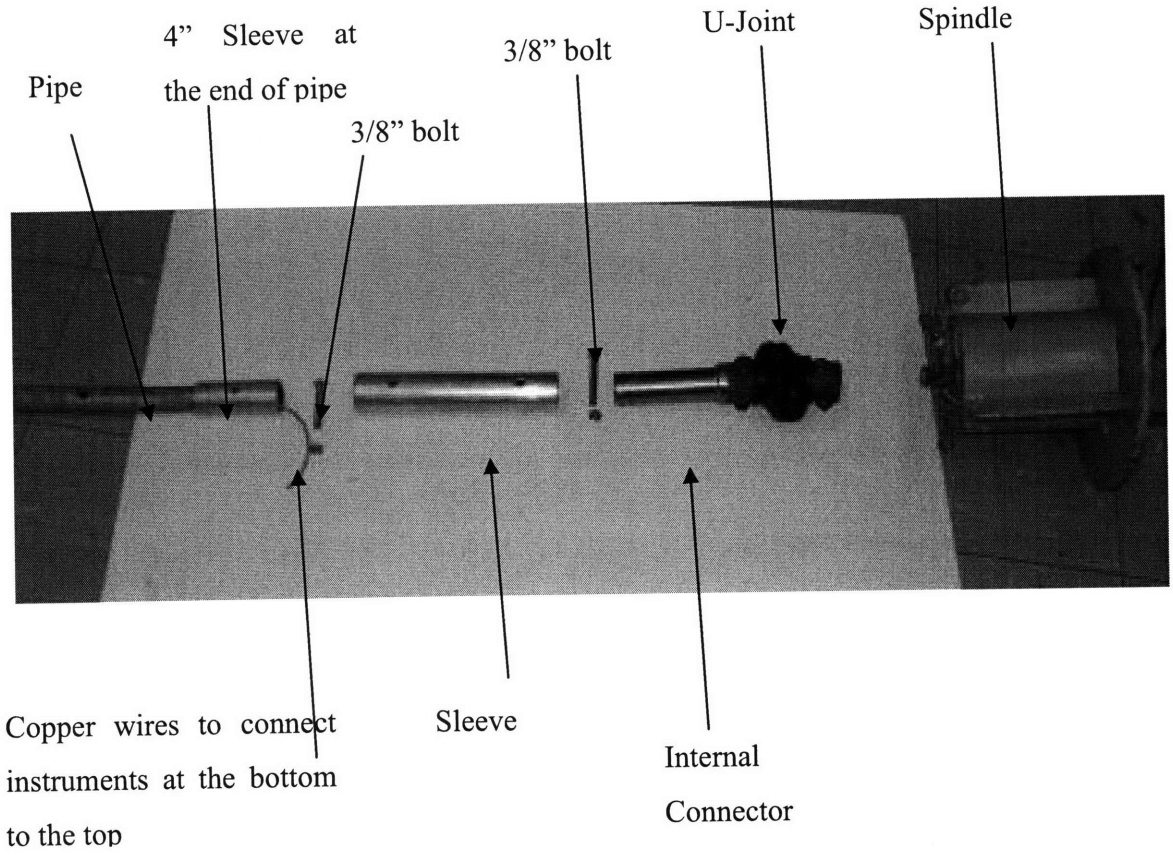

Figure 87 - Bottom connection details

A list of the bottom end components is shown in Table 15. The table also gives some details of each of the components.

RailRoad Wheel - 825 lb bottom weight (not shown in figure)
Spindle
Bolt to secure Spindle with U-Joint - 1/2" bolt, 3.143" length (tip to tip)
U-Joint -
Internal connector – Stainless steel with slot on the side for the Kevlar cable.
Bolt to secure U-Joint to sleeve - 1/2" bolt, 3.143" length (tip to tip)
Sleeve - 1.67 ID, slides over internal connector and pipe
Bolt to secure Sleeve and Internal connector - 3/8" bolt, 2.94" length (tip to tip)
Pipe with 4" sleeve glued to it at the end.
Bolt to secure Sleeve and bottom end of pipe - 3/8" bolt, 2.94" length (tip to tip)

Table 15 - List of components that make up the bottom connection

Appendix B – Depth Sensor

Pressure Transducer

A transducer was used to monitor the hydrostatic pressure at the depth of the railroad wheel. The pressure was used to determine the depth of the railroad wheel below the free surface. The pressure transducer is shown in Figure 6. It was mounted inside of the aluminum pressure housing shown in Figure 5. The transducer was screwed into a threaded hole which penetrated the case and was exposed to external pressure. The threads were backed up by an O-ring seal which prevented flooding of the casing. The same casing contained the electronics supporting a device for determining the relative direction between the fin on the railroad wheel and the current. This device is described after the pressure transducer discussion

Figure 88 – Aluminum casing for pressure transducer

The pressure transducer was manufactured by Cooper Instruments. The specifications for the transducer are as follows:

Model number: PTG-402

Full Scale Range: 300 psi

Error: 0.5 % F.S. Amplified

Excitation: 10-28 VDC

Output: 4-20 mA

The output of the transducer is a current. In order to record the output as a voltage, a circuit was designed so that the current passes through a precision 100 D resistance. The voltage drop across this resistance was recorded as the transducer reading.

The equation for conversion from voltage to depth is given by:

Depth (feet) = [V (volts) − 0.365]*412.448(ft / volt)

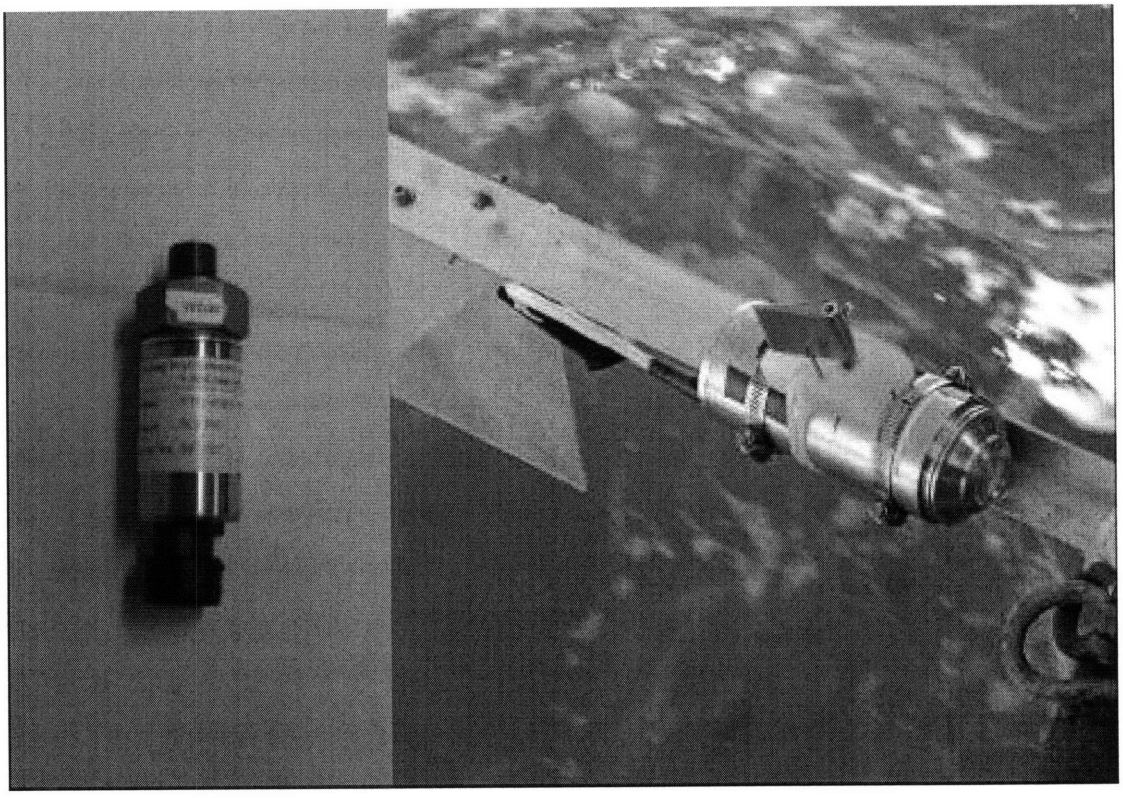

Figure 89 – (left) Pressure transducer (right) direction vane and pressure transducer installed on the Rail Road Wheel fin angle.

Direction Vane

The direction vane consisted of an integrated circuit sensor (Honeywell HMC-1501 Angular Sensor) which measures the orientation of any imposed magnetic field. The sensor was installed on a circuit board housed inside the aluminum bottle. The magnet was installed outside of the bottle on a shaft which supported the vane and rotated with the vane, as it aligned itself with the local flow. When the flow direction changed, the vane realigned itself to the flow and in the process changed the orientation of the magnet with respect to the sensor mounted on the circuit board inside of the bottle. The voltage output of the sensor changed with the orientation of the magnet on the rotating shaft. The relationship between the output and the orientation of the vane is shown in Figure 7.

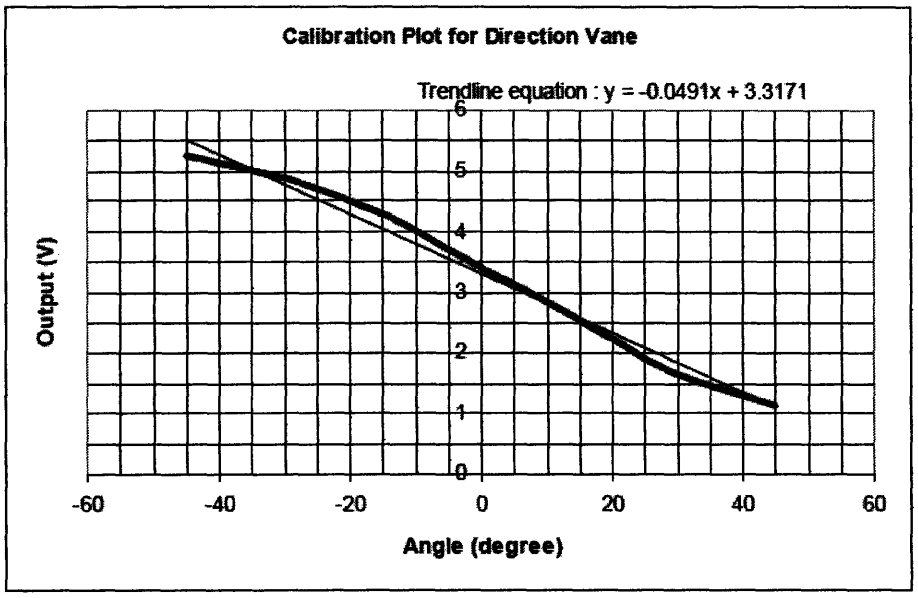

Figure 90 – Calibration Curve for Direction Vane

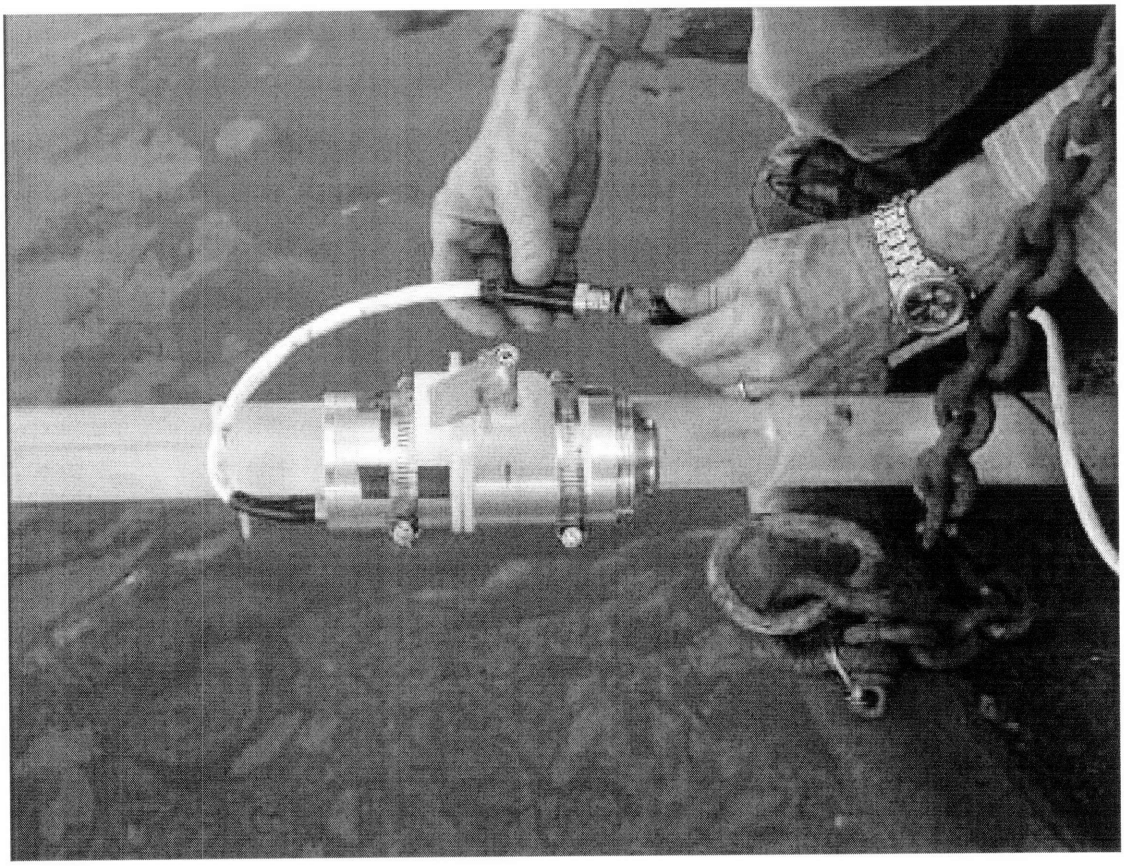

Figure 91 – Bottom End Connections

Appendix C – More results on the Higher Harmonics in VIV

There are many correlations that were evaluated for the higher harmonics. The important results are presented in the main body of the report. The rest are shown in this appendix.

3rd harmonic

Orientation in relation to the 1st harmonic

In VIV literature, the 3rd harmonic forcing, and hence response, has been assumed to occur in the cross-flow direction where it adds to 1st harmonic frequency response. However, results from the second Gulf Stream experiment indicate that the 3rd harmonic is not perfectly aligned with the direction of the 1st harmonic response. Figure 92 shows the distribution of the 1st and 3rd harmonic RMS strains along the length of the pipe for two orthogonal quadrants from Test - 20031023205043. Due to the twist in the optical fibers introduced during the pipe manufacturing process, none of the fibers were aligned with the cross-flow and in-line directions for the entire length of the pipe, as evident by the large changes in strain magnitude in the Q1 and Q4 RMS strain as they align and move away from the cross-flow direction. In the range of z/L=0.2 to z/L=0.3, the 1st harmonic strain response, shown in (a), is perfectly aligned with the fibers in Q4. However, the 3rd harmonic, shown in (b), has significant RMS strain response in both Q1 and Q4, showing that the response is not aligned with the 1st harmonic response. In this case, the 3rd harmonic response and the 1st harmonic response are about 20 degrees apart.

In spite of this we will assume that the third harmonic acts exactly in the cross-flow direction for two main reasons. First, the angle that the 3rd harmonic response makes to the cross-flow direction, and hence the 1st harmonic response, is small. Therefore, assuming that it acts exactly in the cross-flow direction helps simplify calculations without introducing much error. Second, the error introduced by this assumption makes the calculations of total RMS cross-flow strain, and of fatigue life, conservative.

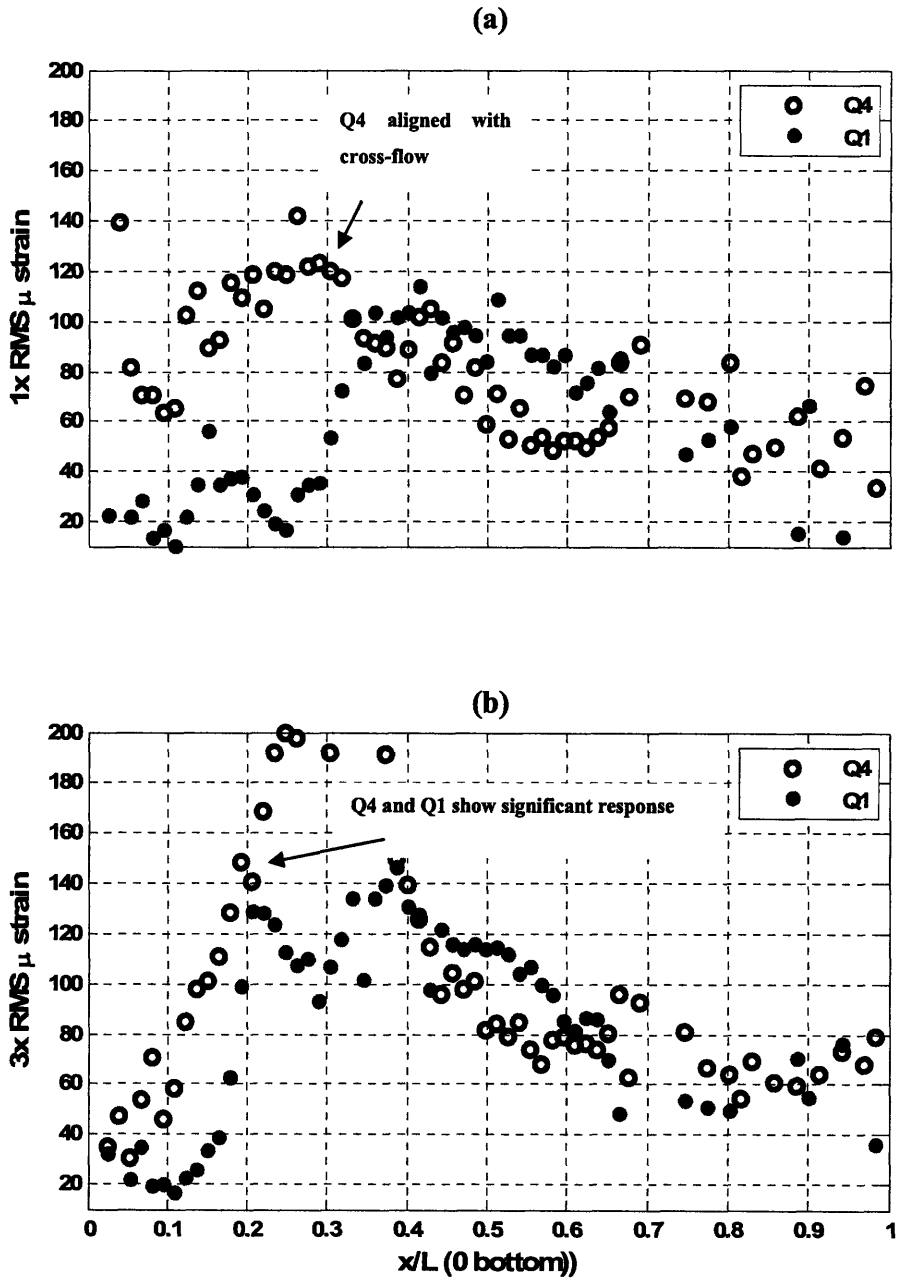

Figure 92 – (a) 1x RMS micro strains from two orthogonal quadrants (Q1 and Q4) and (b) 3x RMS micro strains from the same two orthogonal quadrants.

Phase Relationships

The second Gulf Stream experiments confirmed recent observations by Mukundan (verbal communication) that the 3rd harmonic is phase locked to the 1st harmonic. A simple method to explore the phase relationship is to plot the filtered 3rd harmonic strain

time history against the filtered 1st harmonic strain time history. If a pattern develops and repeats itself, as shown in Figure 93, it indicates that the phase of the 3rd harmonic relative to the 1st harmonic does not change over time, making the 3rd harmonic phase locked to the 1st harmonic. Further, if the same pattern is seen in multiple tests it signifies that a specific phase relationship exits between the 3rd harmonic and the 1st harmonic. In this case, the phase angle between the 1x and 3x components is zero.

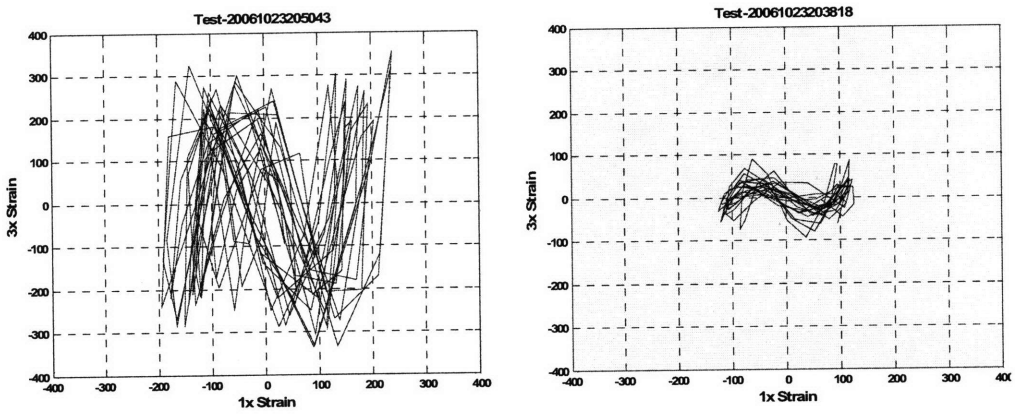

Figure 93 – When the 3rd harmonic strain time series is plotted agaist the 1st harmonic strain time series in steady-state regions, the shapes remains constant in time indicating that the 3rd harmonic is phase locked to the 1st harmonic.

Research by Dahl (Dahl, 2008) indicates that the 3rd harmonic forcing occurs when the pipe interacts with the vortices in its wake in a particular manner. Dahl, in tests with rigid cylinders, observes that a specific displacement trajectory of the pipe leads to an enhanced 3rd harmonic forcing and the data from the second Gulf Stream experiments confirms this. Figure 94 shows the X,Y trajectories for a three second period at the location corresponding to the peak RMS 3x strain in two separate tests conducted during the second Gulf Stream experiments. The direction of motion can be obtained by joining the dots from the largest to the smallest. The motion indicates a phase difference of around 45 degrees, a little less in (a) and a little more in (b), between the in-line and cross-flow displacement time series. Other tests have shown phase differences anywhere from close to 0 degrees to close to 90 degrees in the region of maximum 3x RMS strain response. This observed phase difference is consistent with the findings of Dahl in carefully done laboratory experiments, where he found the largest 3rd harmonic response at a 45 degree phase difference.

The relationship of the phase between the in-line and cross-flow motion in a traveling wave is studied in detail later in the chapter. (X,Y trajectories for many 1x and 2x phase differences are shown in Figure 49)

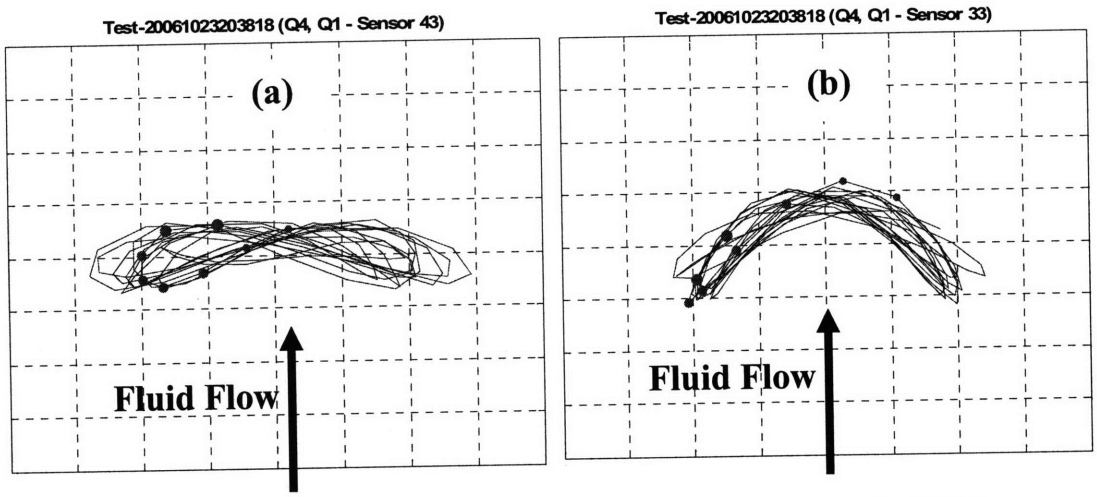

Figure 94 – The X,Y trajectories when the region of maximum 3x RMS response shows a phase difference of around 180 degrees between the inline and cross-flow motion.

When the normalized maximum RMS strains of the 3rd harmonic were studied Figure 94 shows the results from tests carried out on three separate days, and each mark corresponds to a particular test. The figure shows that there is only a moderate correlation between the 1x peak RMS and the 3x peak RMS normalized strain response, given by rho=0.68, indicating that in flexible risers, a large response at the fundamental frequency of vibration does not always translate to a large response at the 3rd harmonic.

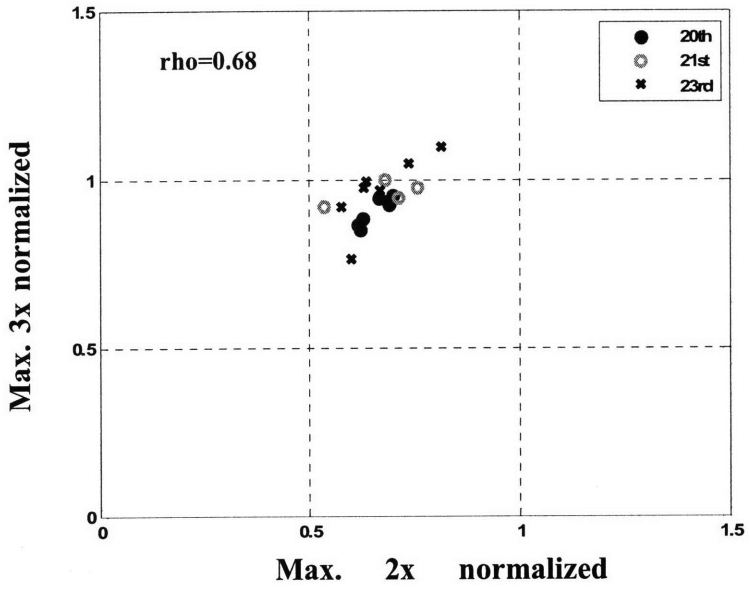

5th Harmonic

Correlation plots

The 1x and 3x harmonics were obvious choices to look for trends because they occur in the cross-flow direction and their RMS strain peaks occur spatially close to each other. Figure 59 (a) shows the variation of the RMS strain at the 5th harmonic with RMS strain at the 1st harmonic. There are no clear trends that exist as shown by the correlation coefficient of 0.36. A similar result is found when the 5th harmonic RMS strain is plotted against the maximum 3rd harmonic RMS strain, though the correlation coefficient value of 0.62 is misleading because it indicates a slight trend when Figure 59 (b) indicates none. These plots imply that a strong response at the 3x frequency or the 1x frequency does not necessarily imply a strong response at the 5x frequency.

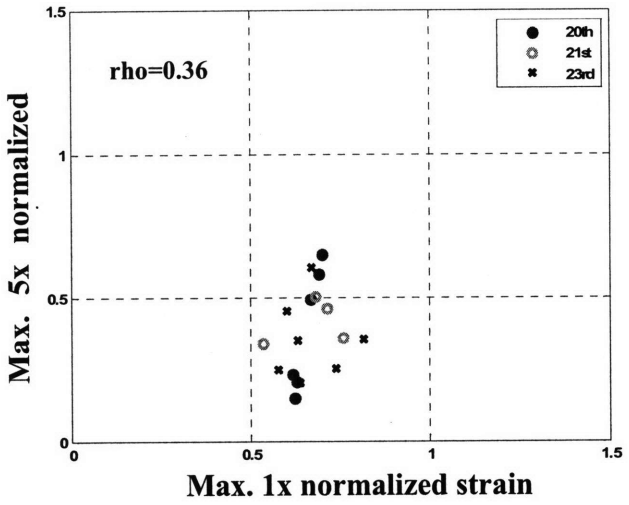

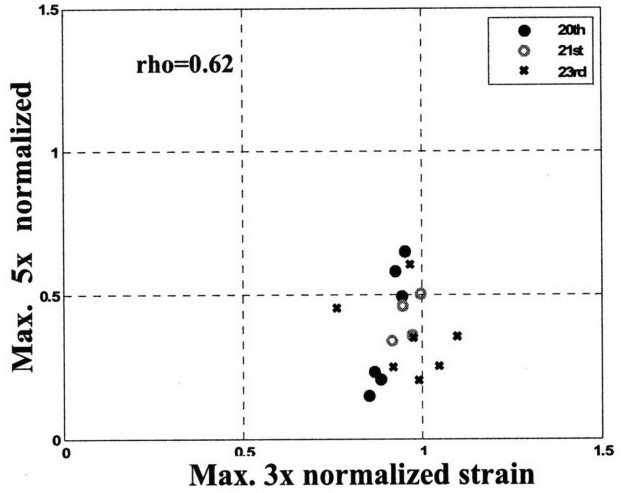

2nd harmonic

Magnitude

Similar to the analysis done for the 3x magnitudes, two different methods were used to estimate the observed maximum 2x RMS strain response. The first used the same eleven full tests used for the analysis of the 3x observed magnitudes. They represent a mean estimate of the measured 2x maximum RMS strain response (Table 16). The second method used steady-state cases to get conservative estimates of the 2x maximum RMS strain response, shown in Table 17. In each case the ratio 2x-to-1x, defined as the maximum measured 2x RMS strain response for a test divided by the maximum measured 1x RMS strain response for that test, is calculated and the mean value and standard deviation used as suggested values to be used for engineers.

Table 16 – The 2x-to1x ratio for full tests provides the a mean estimate of the strain response at the 2x harmonic in terms of the measured or estimated 1x response.

Test name	Ratio
20061023203818	1.23
20061023204504	1.29
20061023205043	1.21
20061023205557	1.47
20061022154633	1.20
20061022153702	1.66
20061022153003	1.41
20061023204504	1.29
20061020182045	1.21
20061020175715	1.29
20061020174124	1.32
20061020172900	1.17
Mean Value	**1.31**
Standard Deviation	0.14

Table 17 – The 2x-to1x ratio for steady-state regions provide another estimate of the strain response at the 2x harmonic in terms of the measured or estimated 1x response.

Test name	Start Sec	Stop Sec	Ratio
20061020175715	0	35	1.25
20061020175715	125	155	1.36
20061020180904	35	65	1.20
20061021142015	1	35	1.08
20061023203818	110	170	1.16
20061021174641	20	50	1.29
		Mean Value	**1.22**
		Standard Deviation	0.10

Phase Relationships

Previous research has indicated that the response at the 1x frequency and the response at 2x frequency are phase locked. This is seen in the observed figure 8's in field

and laboratory experiments. The second Gulf Stream experiments also observed this phase locking in the form of a particular shape, not always the figure 8's, being repeated in time in the steady-state regions. In particular, the region of maximum 2x response was observed when the phase difference between the 1x and 2x frequencies was 90 degrees, leading to a figure 'c' pattern. Figure 95 shows the X,Y trajectories for two different tests in the region of the maximum observed 2x RMS strain. Instead of displacement, it plots the 1x strain time series against the (2x/4) strain time series, where the factor 4 comes in when displacement at the 2nd harmonic is converted to 2nd harmonic strain, hence making the plots equivalent to a X,Y displacement plot. The figure 'c' pattern is seen in all of them. Later in this chapter, the phase difference is shown to change in a traveling wave, resulting in changes to the maximum observed RMS 2x response.

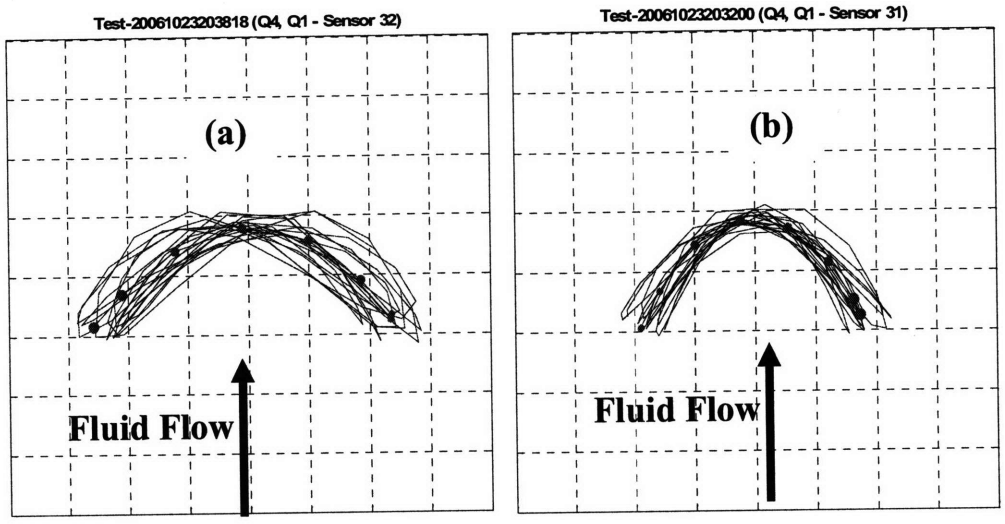

Figure 95 – The X,Y trajectories in the region of maximum 2x response for (a) Bare Pipe test 20061023203818 and(b) Bare pipe test 200610233200. The plots show a 'figure c' pattern.

4th Harmonic

The amplitude of the 4th harmonic, like the 5th harmonic can be calculated in two ways. The first is by using the steady-state cases to estimate the 3x maximum response as a multiple of the 1st harmonic. The second is to use smaller test regions, where the fundamental VIV frequency shifts around and does not allow the 4th harmonic to develop fully but are more representative, according to some newly published research

[Susan's thesis], of VIV response in real current situations. The results using both methods are shown in Table 18 and

Table 18 – The 4x-to-1x ratio for the 4th harmonic for steady state cases shows the a high mean value but also a large standard deviation

Test Name	Start Sec	Stop Sec	Ratio
20061020175715	0	35	1.38
20061020175715	125	155	1.07
20061020180904	35	65	1.34
20061021142015	1	35	1.69
20061023203818	110	170	1.93
		Mean Value	**1.48**
		Standard Deviation	0.33

Table 19 - The 4x-to-1x ratio for the 4th harmonic using unsteady cases shows a smaller mean value but the standard deviation is still large

Test Name	Start Sec	Stop Sec	Ratio
20061020172900	25	35	0.83
20061020174124	27	32	0.33
20061020174124	83	88	0.23
20061020174124	142	148	0.38
20061020175715	10	30	0.96
20061020175715	132	142	0.77
20061021140802	107	112	0.47
20061021142015	42	47	0.66
20061021174641	110	115	0.60
20061021174641	22	27	0.73
20061023203200	160	170	0.55
20061023203818	17	22	0.90
20061023203818	62	67	0.34
20061023204504	27	35	0.41
20061023204504	140	150	0.32
20061023205043	52	58	0.58
		Mean Value	**0.57**
		Standard Deviation	0.23

Figure 96 shows that the maximum 4th harmonic response, like the maximum 5th harmonic response, depends on the shear in the current.

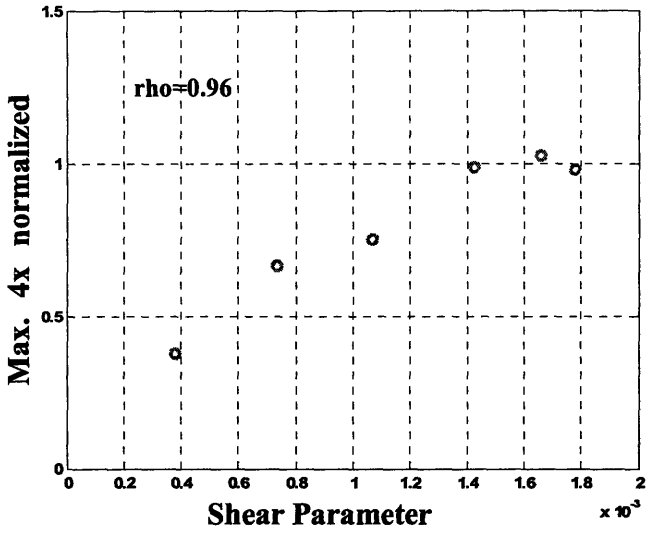

Figure 96 – Maximum normalized 4x RMS strain shows good correlation with the shear parameter

Appendix D – Weibull Distribution to represent the 1st harmonic stress range

Since the Miami data was available as a time series, a probability distribution of the stress ranges can be obtained using Rainflow counting methods. This method, first proposed by Matsuishi and Endo {{39 Matsuiski, M. 1969; }}, is generally regarded by research community as giving the most consistent results for fatigue stress range probabilities. In my analysis, I have used the Wave Analysis for Fatigue and Oceanography (WAFO) Matlab toolbox developed by Lund Institute of Technology in Sweden to determine the stress range probabilities.

Figure 97 shows that the stress range PDFs, for the stress time histories discussed in Figure 74, obtained using the Rainflow counting technique do not compare well with those obtained using the Rayleigh formulation. The Rayleigh formulation does not accurately predict the stress range with the highest probability of occurrence and, more importantly, predicts a larger probability than the Rainflow method for the occurrence of very large stress ranges. This error in the probabilities of occurrence of the large stress ranges is particularly troubling because they contribute disproportionately to the fatigue damage of the pipe. Table 20 shows that the estimated fatigue life calculated using the Rayleigh PDF overestimates fatigue damage by a factor of 1.6 when compared to the results obtained using the Rainflow counting method.

Table 20 – Fatigue damage calculations that use the Rayleigh method to calculate stress range PDFs produce overly conservative results for the 1x VIV data measured during the Gulf Stream experiments.

Sensor No / Dist. Along pipe from top	Rayleigh Damage/ Rainflow Damage
54/-377.2	1.55
58/-405.3	1.62
62/-433.4	1.63
66/-461.5	1.61

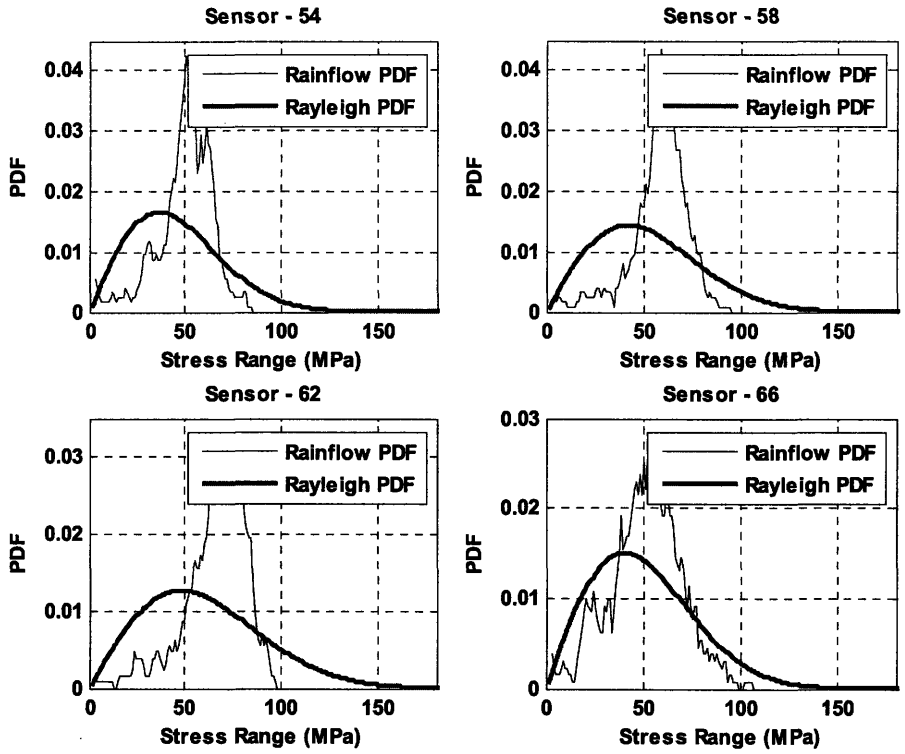

Figure 97 – Comparison of Rainflow cycle counting and Rayleigh PDF's for stress range distributions

The difference in the stress range PDF's shown in Figure 97 is to be expected because the data, as shown previously, is not Gaussian distributed. This necessitates the use of statistical distributions that predict the maxima of non-Gaussian distributions for calculating stress range PDFs. In this study, a two parameter Fisher-Tippet type III distribution, also known as the Weibull distribution, is used. The mathematical formulation for the distribution is shown below

$$W(k,\lambda) = \frac{k}{\lambda}\left(\frac{x}{\lambda}\right)^{k-1} e^{-(x/\lambda)^k}$$

The Rayleigh distribution is a special case of the Weibull distribution, with the parameters k = 2 and $\lambda = \sqrt{2}\, std(x)$ where $std(x) = \sqrt{m_o}$, m_o denotes the area under the spectrum.

The Weibull distribution parameters were obtained by minimizing error in the fatigue damage predicted using the stress range PDF from the Weibull formulation and the

fatigue damage estimate using the stress range PDF from the Rainflow counting method. In a parametric analysis k and λ were varied so as to minimize the objective function, shown in Equation

(1.1)

$$\text{Objective Function}=(1-\frac{Fat(W(k,\lambda))}{Fat(\text{Rainflow})})$$

where

$Fat(W(k,\lambda)$ – Fatigue Damage estimate based on Weibull function with parameters k and .

$Fat(\text{Rainflow})$ – Fatigue damage estimate based on Rainflow cycle counting method. (1.1)

As an example, the values of the objective function are shown in Figure 98 for the four locations considered in Figure 97. The values of k and λ that give a zero value of the objective function are the desired parameters. The results show that there are many possible combinations of k and λ that minimize the objective function. However, each pair has a different sensitivity to error. Having a low sensitivity to error becomes the criteria for choosing the final k and λ combination. For example, based on these results, k =2 and λ =0.8m_o is an acceptable combination of the parameters. However, near the region of minimum error, the rate of change of error is large, which means that if the measured data is actually represented by a Weibull distribution with parameters k=2+Δk and λ =0.8m_o+$\Delta\lambda$ where Δk and $\Delta\lambda$ are small, the error in the fatigue life estimation is going to be large. Accounting for error sensitivity, k =4 and λ =1.1m_o were chosen for the best parameters for the Weibull distribution.

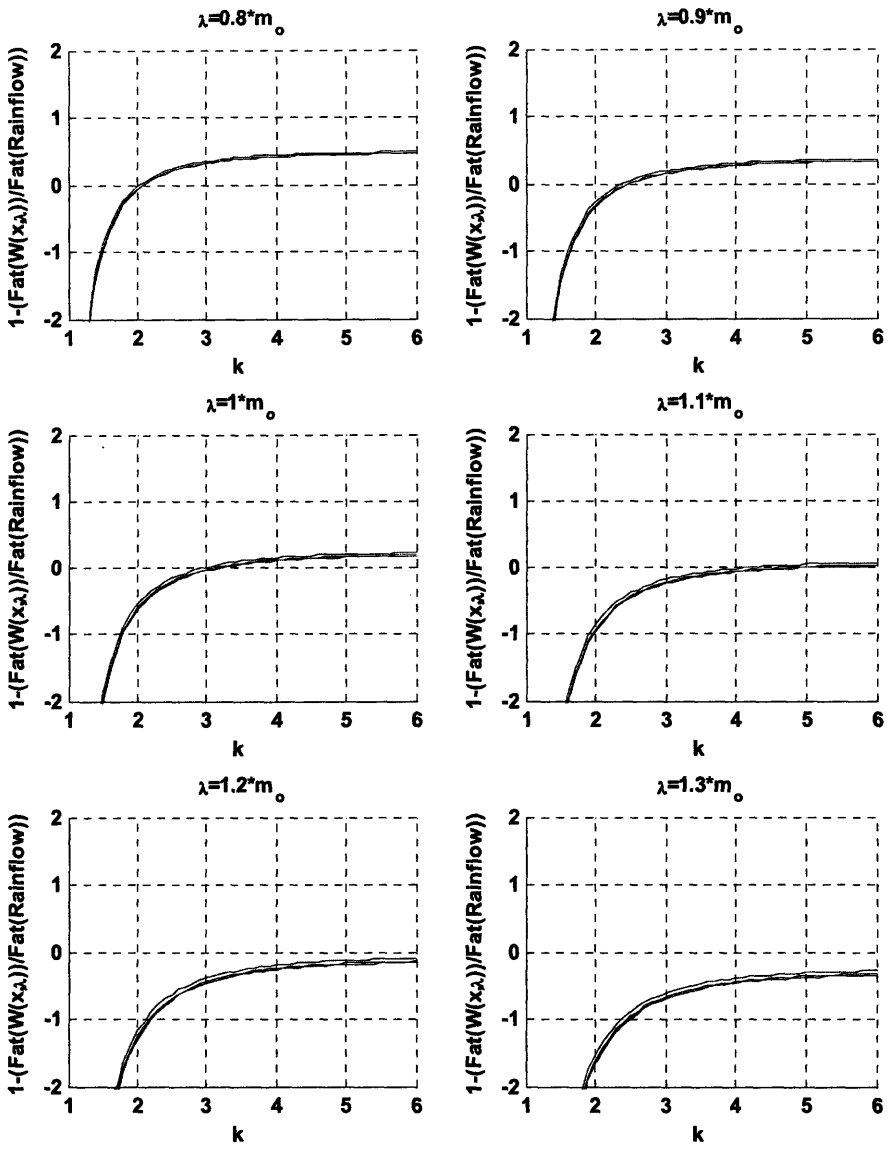

Figure 98 - Variation of Fatigue damage with k for different values of λ

The Weibull distribution, with k =4 and λ=1.1mo, compared well with the Rainflow probability distribution at the four different sensors locations studied in earlier figures. Figure 99 shows the Rainflow cycle stress range PDF and the stress range PDF's obtained using the above mentioned Weibull distribution. Also shown is the Rayleigh PDF, which is the current formulation used in the oil and gas industry. The better match of the Weibull distribution is clear from the plots.

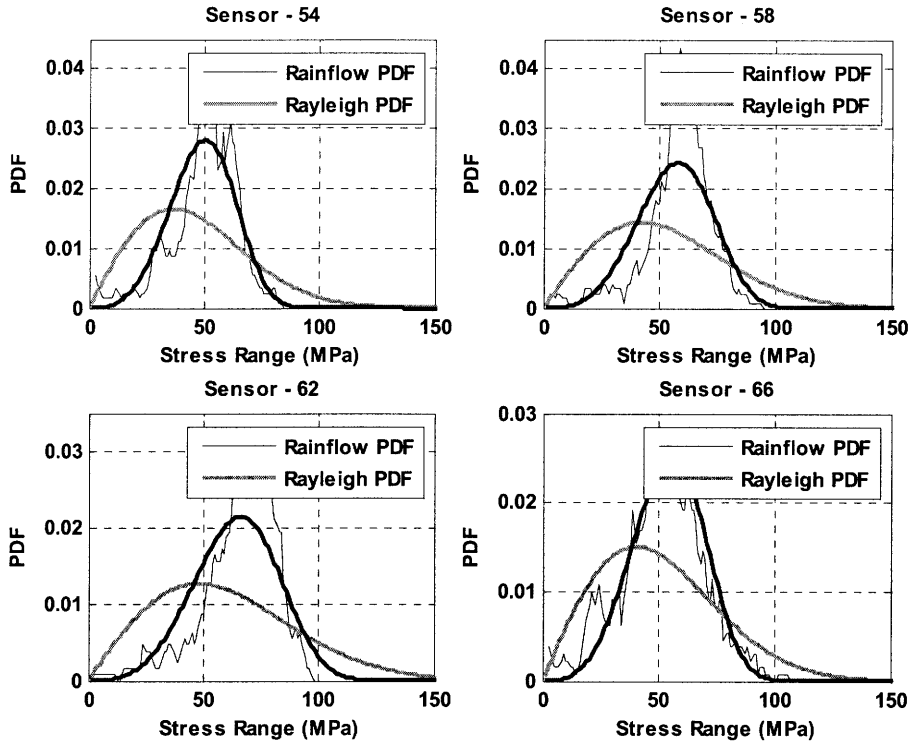

Figure 99 - A comparison of the stress range PDFs shows that the Weibull distribution with k=4 and $\lambda = 1.1 m_0$ is a better approximation of the stress range PDF obtained from Rainflow counting methods.

Using an API-X' SN curve and these stress range PDFs, fatigue damage was calculated for the four cases. The estimates from the Weibull distribution match closely those obtained using the Rainflow counting PDF, as shown in Table 21.

Table 21 - Weibull distribution, with k =4 and $\lambda = 1.1 m_0$, predicts fatigue damage better than the Rayleigh method when compared to the Rainflow counting method. A value of 1.0 in the table would indicate an exact match with the Rainflow fatigue damage estimate.

Sensor No / Dist. Along pipe from top	Rayleigh Damage/ Rainflow Damage	Weibull Damage/ Rainflow Damage
54/-377.2	1.55	1.02
58/-405.3	1.62	1.06
62/-433.4	1.63	1.07
66/-461.5	1.61	1.05

An example from the second Gulf Stream test

Test 20061023203818 from the second Gulf Stream experiments was used to validate the proposed Weibull distribution. The strain time series data from all the sensors in quadrant 1 was filtered to remove the higher harmonics leaving only the vibrations corresponding to the fundamental frequency of vibration. These filtered time series measurements were then used to calculate stress range PDFs at 4 different locations on the pipe. Figure 101(a) shows the distribution of RMS strain for two orthogonal quadrants, Quadrant 1 and Quadrant 4. Also shown in (b) is the current profile for the experiment and the locations of the sensors where the PDFs were calculated.

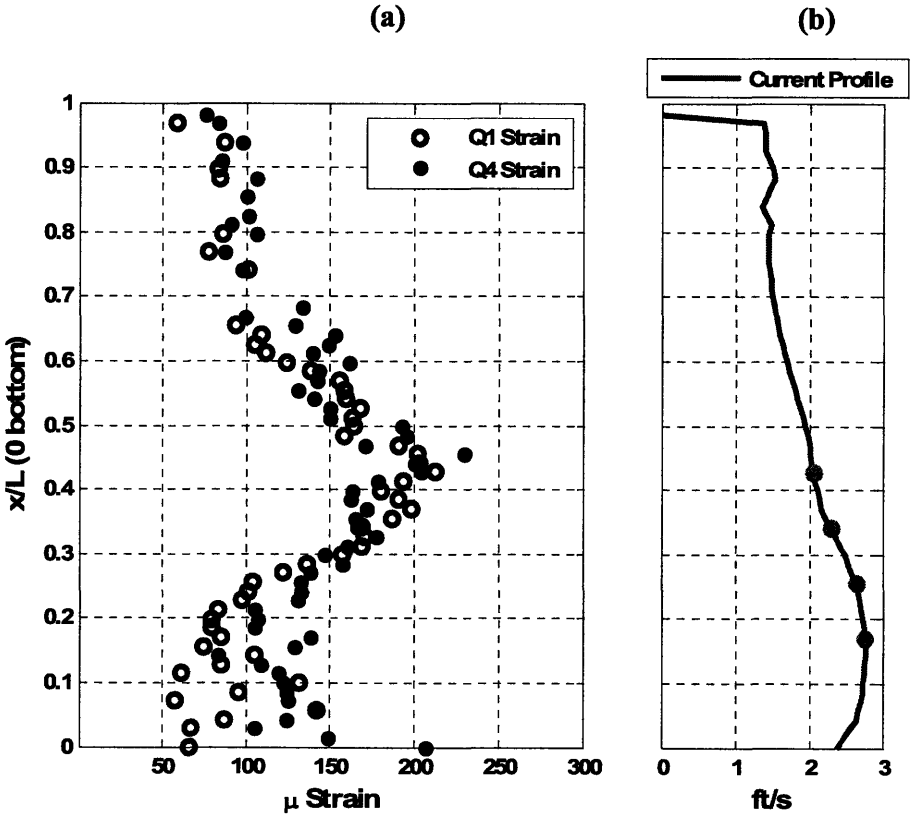

Figure 100 - The RMS micro strain from Test – 20061023203818 for Q2 and Q1 shows the region of maximum strain around the center of the pipe. (b) The mean normal current profile for the experiment with the green dots showing the four locations that were studied in detail.

As mentioned in the earlier sections, the twist in the fiber optics resulted in a change of orientation with axial distance along the pipe. The strain spectrum for Q1 at the four

locations mentioned above is shown in Figure 101. The presence of all the harmonics in the spectra indicates that they were not aligned with either the in-line or cross-flow direction. Also shown are the strain spectra of the filtered signal, where everything except the vibrations at the fundamental frequency of vibration has been removed. This filtered data was used for the calculating the stress range PDFs.

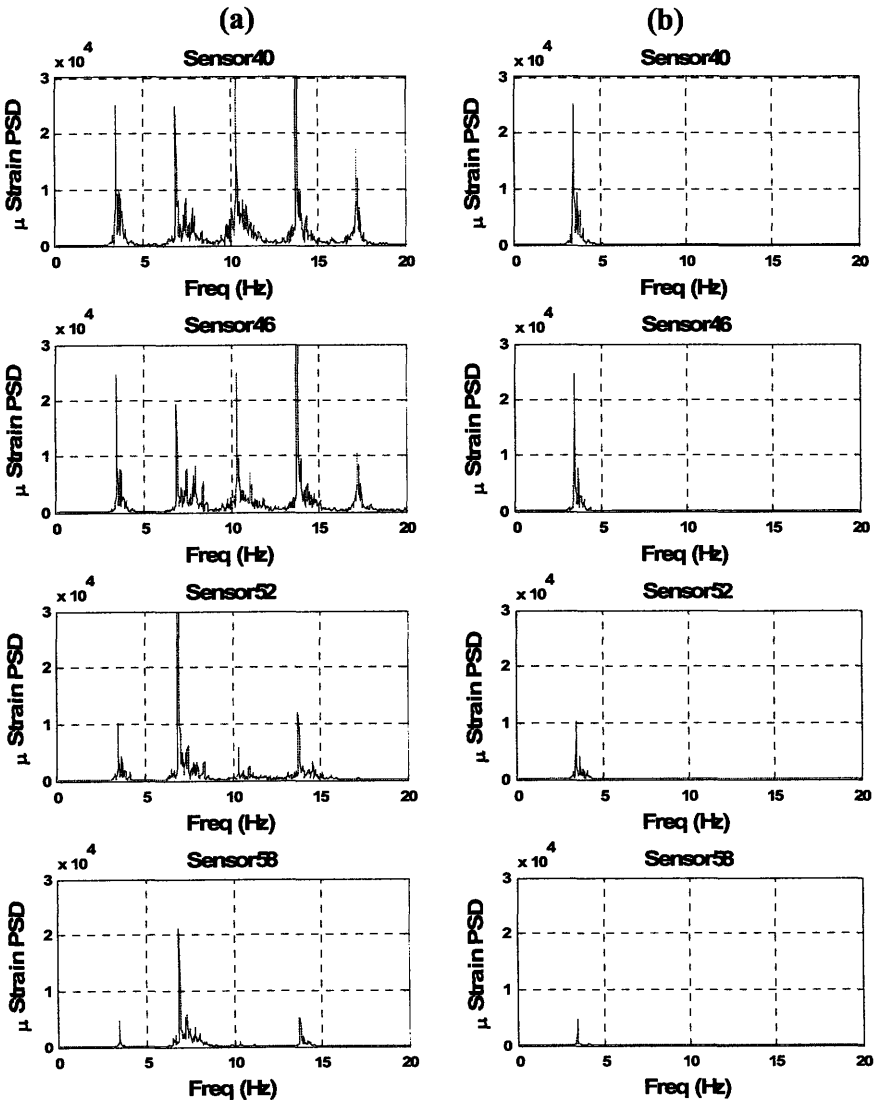

Figure 101 – (a) Spectra at four different locations from Test – 20061023203818 shows the presence of the higher harmonics. (b) Filtered spectra that were used to check the accuracy of the proposed Weibull stress range PDFs.

The stress range PDFs are computed at the four locations using the three methods discussed earlier, Rainflow counting, Rayleigh formulation and the proposed Weibull formulation. Once again the Rainflow counting method is considered as the benchmark, and is used to compare the other two formulations. The results are shown in Figure 14. The Stress range PDF from the Weibull formulation is a better fit to the Rainflow stress range PDF than the Rayleigh formulation.

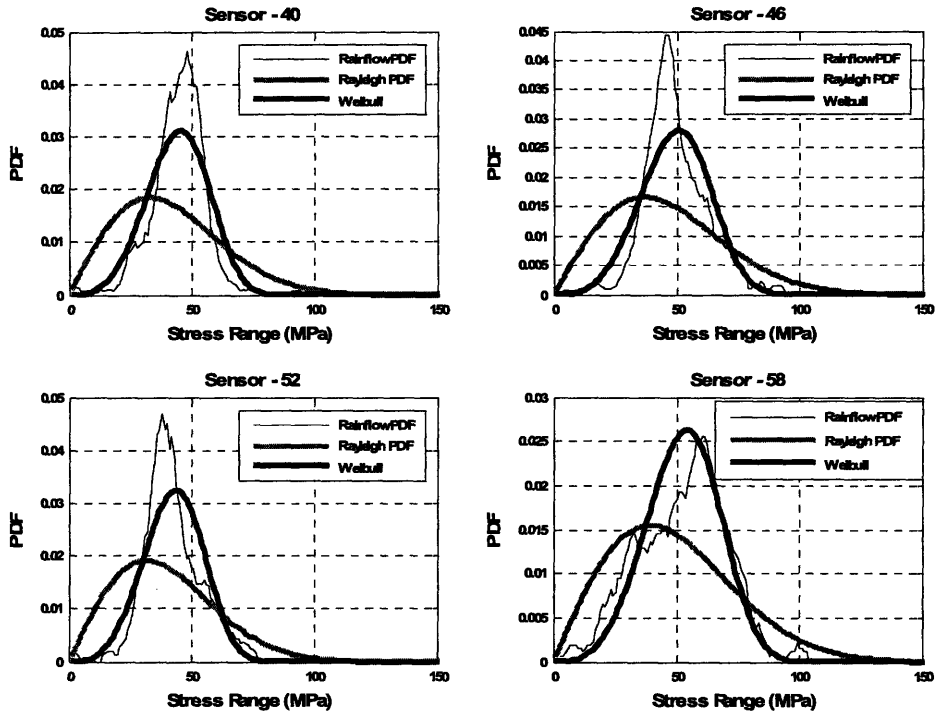

Figure 102 - The stress range PDFs from the proposed Weibull distribution matches those obtained from Rainflow counting methods. The four locations correspond to sensors 40 (-281.6 ft), 46 (-323.6 ft), 52 (-365.6 ft) and 58 (-407.6 ft).

These stress range plots can now be used to calculate the fatigue damage using the S-N curve method. Using the API-X' curve, fatigue damage estimates were compared and the results are tabulated in

Table 22. The accuracy of the predictions made by the Weibull formulation is significantly better than the Rayleigh formulation. In

Table 22, sensor 58, which shows the maximum error for the Weibull distribution, is removed from the region of maximum fatigue damage. This is clear in Figure 101 which shows that there is very little energy at the fundamental frequency of vibration in the data from sensor 58.

Table 22 - A comparison of fatigue life estimates at four sensor locations for Test – 20061023203818 from the second Gulf Stream experiments. The table indicates that the Weibull distribution predicts fatigue damage more accurately than the Rayleigh method when compared to the Rainflow counting method. (k =4 and =1.1mo)

Sensor No / Dist. Along pipe from top	Rainflow Damage/Rayleigh Damage	Rainflow Damage/Weibull Damage
40/-281.6	0.68	1.038
46/-323.6	0.68	1.045
52/-365.6	0.68	1.035
58/-407.6	0.76	1.17

Appendix E – Modeling the higher harmonic strain response in SHEAR7

SHEAR7 version 4.5 incorporates the concept of "timesharing" for the first time in VIV prediction {{43 Swithenbank, S. 2007; }}. "Timesharing" assumes that the overall VIV response of the riser is composed of response at many different frequencies occurring at different times. Therefore, at each time instant, the response is at only one frequency. At each timesharing frequency ω_1, SHEAR7 calculates the RMS displacement response which can be represented by Equation (1.1)

$$y_1 = A_1(z)\sin(\omega_1 t + \alpha_1) \tag{1.1}$$

Curvature can be calculated as

$$(y_1)_{zz} = (A_1(z))_{zz}\sin(\omega_1 t + \alpha_1) \tag{1.2}$$

As strain $\varepsilon = (y_1)_{zz} \times \frac{D}{2}$ and denoting $S_1(z) = A_1(z)_{zz} \times \frac{D}{2}$;

$$(y_1)_{zz} \times \frac{D}{2} = S_1(z)\sin(\omega_1 t + \alpha_1) \tag{1.3}$$

SHEAR7 also calculates the axial distribution of reduced velocity ($V_r(z)$) corresponding to ω_1. Using $V_r(z)$ and the models for the 3rd and 5th harmonics suggested in Chapter 5, the strain response for the 3rd and 5th harmonics can be estimated. The models presented in Chapter 5 represent expected RMS 3rd and 5th harmonic strain responses in terms of the RMS 1st harmonic strain response and have a V_r dependence.

If $S_3(z)$ is the 3rd harmonic strain amplitude then the strain time history at the 3rd harmonic can be represented as

$$(y_3)_{zz} \times \frac{D}{2} = S_3(z)\sin(\omega_3 t + \alpha_3)$$

As $\omega_3 = 3\omega_1$ (1.4)

$$(y_3)_{zz} \times \frac{D}{2} = S_3(z)\sin(3\omega_1 t + \alpha_3) \tag{1.5}$$

Similarly for the 5th harmonic;

$$(y_5)_{zz} \times \frac{D}{2} = S_5(z)\sin(5\omega_1 t + \alpha_5) \tag{1.6}$$

The final strain response for timesharing frequency ω_1 including the higher harmonics can be written as :-

$$(y)_{zz} \times \frac{D}{2} = S_1(z)\sin(\omega_1 t + \alpha_1) + S_3(z)\sin(3\omega_1 t + \alpha_3) + S_5(z)\sin(5\omega_1 t + \alpha_5) \tag{1.7}$$

The response from all *n* time sharing frequencies is combined to produce the final strain response time histories.

$$\sum_{i=1}^{n}((y)^i_{zz} \times \frac{D}{2}) = \sum_{i=1}^{n} S^i{}_1(z)\sin(\omega^i{}_1 t + \alpha^i{}_1) + S^i{}_3(z)\sin(3\omega^i{}_5 t + \alpha^i{}_3) + S^i{}_5(z)\sin(5\omega^i{}_5 t + \alpha^i{}_5)$$